21815

NATIONAL LIBRARY
OTTAWA

BIBLIOTHÈQUE NATIONALE
OTTAWA

CANADA

NAME OF AUTHOR........Peter C Flynn........

TITLE OF THESIS........Studies of Supported........
........Metal Catalysts........
....

UNIVERSITY...of Alberta........

DEGREE FOR WHICH THESIS WAS PRESENTED....Ph. D........

YEAR THIS DEGREE GRANTED.....1974........

Permission is hereby granted to THE NATIONAL LIBRARY OF CANADA to microfilm this thesis and to lend or sell copies of the film.

The author reserves other publication rights, and neither the thesis nor extensive extracts from it may be printed or otherwise reproduced without the author's written permission.

(Signed)........Peter C Flynn........

PERMANENT ADDRESS:

........11403 92 St........
........Edmonton Alta T6G 0Z6
....

DATED...Oct 25.......19 74

NL-91 (10-68)

THE UNIVERSITY OF ALBERTA

STUDIES OF SUPPORTED METAL CATALYSTS

BY

© PETER C. FLYNN

A THESIS
SUBMITTED TO THE FACULTY OF GRADUATE STUDIES AND RESEARCH
IN PARTIAL FULFILMENT OF THE REQUIREMENTS FOR THE DEGREE
OF DOCTOR OF PHILOSOPHY

DEPARTMENT OF CHEMICAL ENGINEERING

EDMONTON, ALBERTA
FALL, 1974

THE UNIVERSITY OF ALBERTA

FACULTY OF GRADUATE STUDIES AND RESEARCH

The undersigned certify that they have read, and recommend to the Faculty of Graduate Studies and Research, for acceptance, a thesis entitled "STUDIES OF SUPPORTED METAL CATALYSTS" submitted by PETER C. FLYNN in partial fulfilment of the requirements for the degree of Doctor of Philosophy.

Sieghard Wanke
(Supervisor)

Michel Boudart
(External Examiner)

Henry W. Habgood

A E Mather

Dalla Lana

M L Wayman

Date Oct. 25, 1974

ABSTRACT

Supported metal catalysts provide an economical way of utilizing noble metals as commercial catalysts. In this work two methods of characterizing such catalysts, electron microscopy and selective gas adsorption, have been studied in detail. These two techniques have been employed in following the sintering behavior of a variety of Pt/Al_2O_3 catalysts. A model for sintering of supported metal catalysts has been developed.

The accuracy of particle size distributions determined from electron micrographs was examined from both theoretical and experimental points of view. Particle detectability and apparent size were found to be sensitive functions of defocus, and hence of elevation of particles in the specimen. Contrast has been shown to vary with orientation of both particles and support material. Sources of contrast inherent in the support in the sub-nm range have been illustrated. It is concluded that particle size distributions become increasingly subject to error as the fraction of particles with sizes below about 2.5 nm increases.

The nature of adsorbed oxygen on Pt/Al_2O_3 supported catalysts and the reaction on the surface of oxygen with hydrogen have been studied. Gas uptake data show that a repeated (H_2-O_2) titration step leads to subsequent enhancement of the hydrogen adsorbed on the surface, and a retardation of subsequent oxygen uptake. The enhancement is correlated to the ratio of initial hydrogen to initial oxygen uptakes, which in turn depends on the dispersion of the platinum crystallites.

IR spectra of CO adsorbed on catalysts with preadsorbed oxygen reveal two types of adsorbed oxygen species. Type I forms during room temperature adsorption, while Type II is found after high temperature adsorption and repeated (O_2-CO) treatment. Type II adsorbed oxygen is not observed after repeated (H_2-O_2) treatments, and hence is ruled out as a cause of enhancement. H_2O generated during the titration step is postulated as a possible cause of the enhancement/retardation effect.

An interparticle transport model for the sintering of supported metal catalysts has been developed. The model postulates escape of atoms from crystallites to the support surface, rapid migration of these atoms along the surface, and their recapture by crystallites upon collision. A reduction in surface energy provides the driving force for transfer of metal from small to large particles. The model has been solved by finite difference methods and applied to several theoretical particle size distributions (PSD). The model predicts an increase in the rate of sintering as the width of the initial PSD increases. The rate of sintering also increases as the surface velocity and the metal loading increase. Sintering behavior is sensitive to the activation energy and temperature. Under certain conditions substantial redispersion is predicted. The model can account for power-law orders from < 2 to > 13, as observed experimentally. Power-law order increases with PSD width and with increases in mean crystallite size.

Changes in the dispersion of supported Pt/Al_2O_3 catalysts following reduction and a variety of thermal treatments have been monitored by gas uptake and electron microcopy. Evidence of redispersion was

found after sintering of one catalyst in oxygen at 450° to 600°C. Sintering is found to be sensitive to gas atmosphere and metal loading. Addition of a portion of presintered catalyst containing large Pt particles increased the rate of sintering of a catalyst. From electron micrographs of the same catalyst area before reduction and after reduction and various thermal treatments, it was concluded that Pt agglomeration occurs during all these steps. Some Pt crystallites remain in a fixed location during reduction and thermal treatments.

ACKNOWLEDGEMENTS

In the last three years I have incurred a number of personal debts, far too many to be acknowledged here in any complete fashion. I would like to single out, however, and thank:

- the International Nickel Company for two years of support as an Inco Graduate Fellow, and the National Research Council of Canada for partial support of this work.
- Eichi Kikuchi, whose company I enjoyed for two years as a co-worker and friend.
- Linda Stolee, who typed the text, and Gertrude Herzberg, who proofread it.
- Charlie Richmond, the best neo-Freudian clinical psychologist I know, and Fraser Russell, who was such a help in my getting to the University of Alberta in the first place.
- Peter Turner, who patiently taught and re-taught how to use the electron microscope.
- Finally, and most of all, Sieg Wanke, an excellent scientist and human being who contributed so much to making this thesis enjoyable.

TABLE OF CONTENTS

Page

CHAPTER 1 INTRODUCTION 1

1.1 Supported Metal Catalysts 1

1.2 Measurement of Metal Dispersion and Crystallite Size 3

1.2.1 X-Ray Diffraction Line Broadening 4

1.2.2 Electron Microscopy 4

1.2.3 Gas Chemisorption 5

1.3 Sintering of Supported Metal Catalysts 7

1.4 References 8

CHAPTER 2 EXPERIMENTAL PROCEDURES 9

2.1 Catalyst Preparation 9

2.2 Gas Adsorption by Dynamic (Flow) System 9

2.3 Electron Microscopy 13

2.4 Other Measurements 15

2.5 References 15

CHAPTER 3 THE LIMITATION OF THE TRANSMISSION ELECTRON MICROSCOPE FOR CHARACTERIZATION OF SUPPORTED METAL CATALYSTS 17

3.1 Survey 17

3.2 Specimen Characteristics 18

3.3 Theory of Image Generation 21

3.3.1 Phase Contrast 22

3.3.2 Diffraction Contrast 26

3.4 Microscope Use 26

3.5 Results and Discussion 29

TABLE OF CONTENTS (continued)

Page

CHAPTER 3 continued

3.5.1 Calculated Image Profiles 29

3.5.2 Variation of Contrast and Apparent Size with Defocus 29

3.5.3 The Effect of Tilt on Contrast 44

3.5.4 Contrast Structure in the Support Material 48

3.6 Conclusions 50

3.7 References 52

CHAPTER 4 THE TITRATION REACTION ON SUPPORTED Pt CATALYSTS 54

4.1 Survey 54

4.2 Experimental Results 57

4.2.1 Isotherms and Isobars of Oxygen and Hydrogen 57

4.2.2 Hydrogen Titration of Oxygen Adsorbed at Elevated Temperatures 62

4.2.3 IR Spectra of CO Adsorbed on Pt with O_2 Preadsorbed at Various Temperatures 62

4.2.4 Gas Uptakes in Titration Sequences 66

4.2.5 Long Titration Sequence 72

4.2.6 IR Spectra of CO Adsorbed on Pt After Repeated Sequences of (O_2-CO) and (O_2-H_2) Treatments 75

4.3 The Origin of the Enhancement Effect 77

4.4 Conclusions 84

TABLE OF CONTENTS (continued)

Page

CHAPTER 4 continued

4.5 References 85

CHAPTER 5 A MODEL OF SUPPORTED METAL CATALYST SINTERING 87

5.1 Survey 87

5.2 Proposed Model 93

5.2.1 Escape of Metal Atoms from Crystallites 93

5.2.2 Migration of Metal Atoms Over Support Surfaces 99

5.2.3 Capture of Atoms by Metal Crystallites 99

5.2.4 A Summary of the Model 100

5.3 Method of Solution 101

5.3.1 Solution for $\alpha/S_o > 10^{12}$ m^{-2} 102

5.3.2 Solution of $\alpha/S_o < 10^{12}$ m^{-2} 104

5.4 Description of Cases Investigated 105

5.4.1 Crystallite Size Distributions 105

5.4.2 Parameter Values 106

5.5 Results and Discussion 106

5.5.1 Effect of Initial PSD on Rate of Sintering 106

5.5.2 The Effect of Surface Mobility and Metal Loading on Sintering Behavior 116

5.5.3 The Effect of E_a/RT on Sintering Behavior 118

5.5.4 The Order of Sintering 121

TABLE OF CONTENTS (continued)

Page

CHAPTER 5 continued

5.5.5 Application of the Model to an Experimental Case 125

5.5.6 The Possibility of Multiple Mechanisms 129

5.6 Conclusions 129

5.7 Nomenclature 131

5.8 References 132

CHAPTER 6 EXPERIMENTAL STUDIES OF SINTERING OF SUPPORTED PLATINUM CATALYSTS 135

6.1 Survey 135

6.2 Results 138

6.2.1 Constant Time/Variable Temperature Treatments 138

6.2.2 Variable Time/Constant Temperature Treatments 142

6.2.3 Catalyst Mixture Experiments 143

6.2.4 Effect of Reduction and Sintering on Individual Metal Particles 148

6.3 Discussion 161

6.4 Conclusions 164

6.5 References 165

APPENDIX A EXPERIMENTAL CONDITIONS 167

A-1 Catalysts and Preparations 167

A-2 Gas Adsorption System 168

TABLE OF CONTENTS (continued)

Page

APPENDIX A continued

A-2.1 Calibration, Accuracy, and Sample Calculations 168

A-2.2 The Effect of Reduction and Outgassing Times on Gas Uptakes 177

A-2.3 Effect of Rate of Addition of Oxygen on Oxygen Uptake 181

A-2.4 Experimental Conditions and Results 186

APPENDIX B CALCULATION OF PHASE CONTRAST IMAGES 208

APPENDIX C CALCULATION OF A SINTERING HISTORY 215

LIST OF FIGURES

Figure		Page
2.1	Schematic Diagram of the Dynamic Adsorption System	10
3.1	Schematic Cross Section of Typical Specimen Grid	20
3.2	Schematic Diagram of Optical Diffraction Micrograph Resolution Test, and Optical Diffraction Pattern From Micrograph of Thin Carbon Film	28
3.3	Calculated Image Intensity Profile for a Single Atom	30
3.4	Three Calculated Image Intensity Profiles for a Single Atom	32
3.5	Calculated Maximum Image Intensity as a Function of Defocus for the One and Seven Atom Cases	33
3.6	Calculated Maximum Image Intensity as a Function of Defocus for the Three and Four Atom Cases	34
3.7	Calculated Apparent Image Size as a Function of Defocus	37
3.8	Two Calculated Image Intensity Profiles for the Four Atom Case	38
3.9	Micrographs of a Pt/Al_2O_3 Catalyst Showing the Effect of Defocus Change on Image Contrast	39
3.10	Variation of Measured Particle Size with Defocus for Three Through Focus Series of Micrographs of a Pt/Al_2O_3 Catalyst	41
3.11	Variation of Measured Particle Size with Defocus for Three Through Focus Series of Micrographs of a	

LIST OF FIGURES (continued)

Figure		Page
	Pt/Al_2O_3 Catalyst	42
3.12	Variation of Measured Particle Size with Defocus for Three Through Focus Series of Micrographs of a Pt/Al_2O_3 Catalyst	43
3.13	Micrographs of a Pt/Al_2O_3 Catalyst Showing the Effect of Tilt on Image Contrast	47
3.14	Micrographs of a Pt/Al_2O_3 Catalyst Showing the Effect of Tilt on Contrast	49
3.15	Micrograph of Pure Al_2O_3 ("Alon") Specimen Showing the Contrast Inherent in the Support	49
4.1	Oxygen Isotherms for a 2.03% Pt on Alon Catalyst	59
4.2	Oxygen and Hydrogen Isobars for Three Different Pt/Al_2O_3 Catalysts	60
4.3	Variation of the 2060-80 and 2120 cm^{-1} Bands from CO Adsorbed on Pt/Al_2O_3 Catalysts with Different O_2 Preadsorption Temperatures	64
4.4	Influence of Evacuation on the 2060-80 and 2120 cm^{-1} Bands	67
4.5	Hydrogen Enhancement Ratio (H3/H1 or H2/H1) as a Function of the Ratio of Initial Hydrogen Uptake to Initial Oxygen Uptake (H1/O1)	71
4.6	Variation of Initial Uptake Ratio (H1/O1) with Catalyst Dispersion as Measured by Hydrogen Uptake (H1)	73
4.7	Long Term Titration	74

LIST OF FIGURES (continued)

Page

Figure

4.8 The Effect of (CO-O_2) Cyclic Treatment 76

4.9 The Effect of (O_2-H_2) Cyclic Treatment 78

5.1 Electron Micrographs of 4.76% Pt on Alon Alumina After Various Pretreatments 90

5.2 Particle Size History for Selected Individual Particles 110

5.3 Particle Size History for Selected Individual Particles 111

5.4 Effect of Initial Particle Size Distribution on the Rate of Sintering 113

5.5 Cumulative Particle Size Distribution as a Function of Time 114

5.6 Cumulative Particle Size Distribution as a Function of Time 115

5.7 Effect of Surface Mobility of Metal Atoms on Support 117

5.8 Effect of E_a/RT on Sintering Behavior 119

5.9 Effect of E_a/RT on Sintering Behavior 120

5.10 Effect of Mean Crystallite Size on Power-Law Order 123

5.11 Effect of Particle Size Distribution Width on Power-Law Order 124

5.12 Cumulative Particle Size Distribution History Predicted by Model for the Initial Distribution 126

5.13 Predicted Dispersion as a Function of Time for the Initial Distribution of Wynblatt and Gjostein[5.3] 127

LIST OF FIGURES (continued)

Page

Figure

5.14 A Power-Law Order Test of the Calculated Dispersion History for the Initial Distribution of Wynblatt and Gjostein[5.3] 128

6.1 Effect of Treatment Temperature on Metal Particle Size Range, Measured from Electron Micrographs 139

6.2 Effect of Treatment Temperature on Metal Dispersion for 0.5% Pt on Al_2O_3, Measured by Gas Uptake 141

6.3 Particle Size Distribution from Electron Micrographs of a Sintered Engelhard 0.3% Pt on Al_2O_3 Catalyst 144

6.4 Low Magnification Micrographs from Grid 6 152

6.5 Micrographs from Grid 4 154

6.6 Micrographs from Grid 7 155

6.7 Micrographs from Grid 2 156

6.8 Micrographs from Grid 1 157

6.9 Micrographs from Grid 6 160

A-1 Output from Thermal Conductivity Cell from Run 112 175

LIST OF TABLES

Table		Page
1.1	Rapid Decrease in Dispersion as Metal Crystallite Size Increases	2
3.1	Theoretical Defocus Windows for Dark Contrast for Various Atomic Clusters	35
3.2	Calculated Image Intensity and Apparent Size Over a Range of Defocus and Apertures	45
4.1	Description of Catalysts	58
4.2	O_2 Adsorption Uptakes as a Function of Temperature and Room Temperature H_2 Titration and Adsorption Uptakes	61
4.3	H_2 and O_2 Adsorption and Titration Uptakes	69
4.4	Hydrogen Enhancement and Oxygen Retardation During Titration	81
5.1	Relative Rate of Loss of Atoms per Crystallite as a Function of Crystallite Size as Estimated by the Kelvin Equation	98
5.2	Data for Generation of Particle Size Distributions	107
5.3	Parameter Values Used in Study	108
6.1	Effect of Addition of a Portion of Presintered Catalyst on the Sintering Rate of a 2.03% Pt on Alon Catalyst	147
6.2	Grid Treatments	149
A-1	O_2 Calibration of Sample Loop Size	169
A-2	Hydrogen Calibration	172
A-3	Contents of Partial O_2 Pulses	173

LIST OF TABLES (continued)

Table		Page
A-4	Sample Calculations, Run 112	176
A-5	Effect of Reduction Conditions on Gas Uptake	178
A-6	Effect of Outgassing Time on Gas Uptake	180
A-7	Effect of Pulse Dilution on Oxygen Uptake	183
A-8	Oxygen and Hydrogen Uptakes for Stream and Pulse Addition of Initial Oxygen	185
A-9	Results from Dynamic Adsorption System	189
B-1	Atom Coordinate Positions Used in EMCON	209
B-2	Parameters Used in EMCON	210

CHAPTER 1

INTRODUCTION

1.1 Supported Metal Catalysts

The catalytic properties of metals have been known for over 100 years. Early applications of metal catalysts were generally confined to laboratory research studies, particularly in organic synthesis reactions. Since problems of scale economy or catalyst life are generally not critical in synthesis studies, catalysts were generally used in pure metallic form.

In this century, however, and particularly since the Second World War, metal catalysts have found increasing application in large scale industrial processes. Reactions such as hydrocarbon hydrogenation and dehydrogenation, partial oxidation, and petroleum reforming are all examples of standard manufacturing processes utilizing supported metal catalysts. In plant operation, catalyst expense and durability become extremely critical and this cost/lifetime pressure led to the development of supported metal catalysts.

A supported metal catalyst generally consists of a relatively stable porous base (carbon or a metal oxide such as alumina or silica) on which small crystals of the metal are grown. Group V11b metals (Fe, Co, Ni, Ru, Rh, Pd, Os, Ir, and Pt) are the most common metals supported in this fashion. The metal is generally added to the support by immersing the support in a salt solution, evaporating to dryness, and then either reducing the metal salt directly or converting it to the metal oxide in an oxygen atmosphere and then reducing the metal oxide. The resulting metal crystallites may vary in size from 200 nm or more to smaller than 1 nm.

The economic value of supported metal catalysts may be readily shown. In purchasing metal, a user pays by bulk; in using the metal as a solid catalyst in a gas phase reaction, he utilizes only those metal atoms which "see" the gas, i.e. surface atoms. The ratio of surface metal atoms to total metal atoms, known as the dispersion ratio, thus measures efficiency of utilization of the expensive metal. Table 1.1 shows the rapid decrease in dispersion as metal crystallite size increases.[1.1]

Table 1.1: Rapid Decrease in Dispersion as Metal Crystallite Size Increases

# of Atoms in edge of crystallite	Crystallite size, nm (based on platinum)	Dispersion
2	0.78	1.000
5	1.95	0.780
10	3.89	0.490
18	7.00	0.300

Thus use of 7 nm metal particles "wastes" 70% of the total metal atoms, which are unable to participate in the reaction. By way of further illustration, a platinum metal cube with a 1 mm edge has a dispersion of about one one-millionth, so 99.9999% of the metal atoms do not contact the gas.

Attempts to physically disperse metal catalysts through grinding or precipitation of a metal sponge (black) prove unsuccessful for two reasons: first, particles even in the 100 nm range are such a fine dust that containment within a reactor is difficult; second, even at moderate temperatures the metal particles, even in a sponge, tend to reagglomerate to larger crystallites. Use of a supporting material reduces both of these effects. In general metal crystallites adhere quite firmly to the supporting material, and thus catalyst loss in the product is negligible. In addition, the support holds small crystallites at a distance and retards sintering, the name given to the process of metal crystallite growth. Thus the support stabilizes highly dispersed metals and allows economical use of expensive metal catalysts in large scale industrial processes. Generally, the support is inert and does not influence the reaction, although petroleum reforming is a notable exception to this rule.

1.2 Measurement of Metal Dispersion and Crystallite Size

As outlined above, metal dispersion, a function of the metal crystallite size, is an extremely critical parameter of a supported metal catalyst. In addition to the problem of efficient use of metal atoms, detailed above, a second factor makes dispersion significant. Boudart[1.2] has identified two types of catalytic reactions, facile and demanding. In the former, the reaction rate varies directly as the surface area of the catalyst; in the latter, the reaction rate per unit *surface area of metal* depends upon the crystallite size. For example, van Hardeveld and van Montfoort[1.3] demonstrated that the nitrogen adsorption activity per unit surface area of a nickel on silica catalyst was highest when crystallite sizes were 2 to 7 nm.

Thus knowledge of average metal particle size and particle size distribution are important in characterizing a supported metal catalyst. Three techniques have been employed in the determination of the size of the metal crystallites, and each will be briefly described here, along with advantages and disadvantages.

1.2.1 X-Ray Diffraction Line Broadening

Klug and Alexander[1.4] explain the theory behind use of x-ray line broadening in determining small crystal sizes. Briefly, an x-ray diffraction peak for a given crystal plane broadens as the crystal size in the sample decreases. The peak width difference between large crystals (width determined by instrumental response) and small crystals (additional width due to crystallite size) may be related to an average crystallite size. Smith[1.5] indicates that an average size

$$\bar{d} = \frac{\Sigma n_i d_i^4}{\Sigma n_i d_i^3} \qquad 1.1$$

is obtained, where $\bar{d}$ is the average size obtained by this method and n_i is the number of particles in the size interval centered on d_i. Fourier analysis of the broadened diffraction curve yields some information on the particle size distribution of the sample.

However, the great drawback of x-ray diffraction line broadening is its inability to detect particles of a very small size. While some authors[1.6, 1.7] reported detection of 3 nm particles and smaller, it is generally accepted[1.8] that particles less than 5 nm will not be detected by x-ray line broadening and thus will not be included in the average particle diameter. Since 5 nm represented a median to upper limit of the metal crystallite sizes of typical interest in this research, x-ray techniques have not been employed.

1.2.2 Electron Microscopy

Adams *et al.*[1.7] and Moss[1.9] gave some of the first descriptions of the use of the electron microscope in determining particle sizes in supported metal catalysts. Since then numerous investigators have utilized electron microscopy to determine particle size distributions. The primary advantage of electron micrograph analysis is that the data are in the form of a distribution, rather than an average particle size.

Chapter 3 examines in detail the accuracy and validity of particle size distributions determined by electron micrographs of catalyst specimens. It is concluded that even under ideal conditions the computation of accurate particle counts is questionable when the size of particles counted drops below 2.5 nm.

1.2.3 Gas Chemisorption

The third means of determining relative particle sizes in a supported metal catalyst is through measurement of the gas chemisorbed on the metal surface. One advantage of the method is immediately evident--it measures how the catalyst will interact with a feed stream in reactor conditions. Since all metal atoms that interact with the gas are detected, this method "sees" particles of all sizes, even atomically dispersed metal.

Three methods are available for determination of chemisorbed uptake, the classical volumetric method using a vacuum rack, a dynamic adsorption system and the gravimetric balance. Dorling[1.10] reviews each method. The classical volumetric approach provides greater accuracy and allows ready determination of isotherms (uptake versus pressure at a variety of temperatures). However, it is more time consuming and involves a higher capital investment than the dynamic method. Samples require two determinations, one measurement of gas uptake on the supported metal catalyst and one on a support blank so that physical adsorption effects may be eliminated.

The dynamic method's primary advantages are atmospheric operation (*i.e.*, it does not require a high vacuum system), and elimination of support correction; these two factors allow more rapid analysis of gas uptake. The system employed in this research will be briefly detailed in Chapter 2.

The gravimetric method actually weighs a small catalyst sample and records weight increases due to gas adsorption. This method also involves high capital cost, and is also difficult to apply for hydrogen adsorption because of the low mass of the adsorbate atom compared to the sample. The gravimetric technique has found widest application with heavier adsorbed gases such as carbon monoxide and hydrocarbons.

Whatever the method of its determination, the uptake is related to an average size through an adsorption stoichiometry and a crystal-shape model. The most generally assumed models for stoichiometry are either one atom of oxygen or one atom of hydrogen per exposed metal surface atom; both have been reported and used by various workers. Crystallites may be modeled in a variety of ways, for example, as spheres, as cubes, as octahedra, as cubo-octahedra, etc. Each of these models predicts a dispersion (fraction of atoms that are at the surface) as a function of particle size. Van Hardeveld and Hartog[1.11] summarize these models; deviations among the various models are small.

Thus, by assuming an adsorption stoichiometry, the absolute number of surface metal atoms may be determined from the measured adsorbed gas uptake. The absolute number of total metal atoms is known from the catalyst composition and weight, so the dispersion may be readily calculated. From the dispersion, a surface average diameter is determined.

The surface average diameter, $\bar{d}$, determined in this fashion, is related to the particle size distribution by the relation.[1.11]

$$\bar{d} = \frac{\Sigma n_i d_i^3}{\Sigma n_i d_i^2} \qquad 1.2$$

Chapter 4 examines in greater detail the uptake of hydrogen and oxygen on support Pt catalysts. Anomalies in the titration reaction (consumption of adsorbed oxygen by gaseous hydrogen, or vice versa) are discussed in detail.

1.3 Sintering of Supported Metal Catalysts

Although a support material helps to stabilize metal dispersion as compared to pure metal catalysts, changes in the dispersion of supported metal catalysts still occur. This effect is known as sintering; loss of dispersion via this process is one of the major factors limiting the life of supported metal catalysts. Where supported metal catalysts are envisioned in high temperature situations (such as automotive exhaust mufflers), problems of dispersion maintenance are especially critical.

The physical mechanisms accounting for sintering have not yet been established. In Chapter 5 an existing model advanced to explain sintering behavior is reviewed, and an alternate model postulating surface diffusion of atoms is advanced. This atomic surface diffusion model is solved and applied to a number of situations of catalytic interest. The effect of the model parameters on the predictions for sintering behaviour is detailed. Finally, in Chapter 6 experimental evidence of sintering is presented and discussed in light of the theoretical models.

1.4 References

1.1 Poltorak, O.M. and Boronin, V.S., Russian Journal of Physical Chemistry 40, 11, 1436-1445 (1966).

1.2 Boudart, M., Aldag, A., Benson, J.E., Dougharty, N.A., and Harkins, C.G., J. Catal. 6, 92, (1966).

1.3 Van Hardeveld, R., and van Montfoort, A., Sur. Sci. 4, 3-6 (1966).

1.4 Klug, H.P. and Alexander, L.E., "X-Ray Diffraction Procedures", John Wiley and Sons, Inc., New York, 1954, Chapter 9.

1.5 Smith, W.L., Warren Spring Laboratory Report LR 145(CA), Department of Trade and Industry (London), 1970.

1.6 Schlosser, E.G., Chem. Ing. Tech. 39, 409 (1967).

1.7 Adams, C.R., Benesi, H.A., Curtis, R.M. and Meisenheimer, R.G., J. Catal. 1, 336, (1962).

1.8 Kral, H., Z. Phys. Chem. (Frankfort am Main) 48, 129 (1966).

1.9 Moss, R.L., Platinum Metals Rev. 11, 141, (1967).

1.10 Dorling, T.A., Warren Spring Laboratory Report LR 144(CA), Department of Trade and Industry (London), 1971.

1.11 Van Hardeveld, R. and Hartog, F., Sur. Sci. 15, 189 (1969).

CHAPTER 2

EXPERIMENTAL PROCEDURES

2.1 Catalyst Preparation

Commercial and prepared catalysts were used in this work. Engelhard 0.3% and 0.5% Pt on Al_2O_3 catalysts (all catalyst concentrations are reported by weight), and 0.5% Rh on Al_2O_3 were used after overnight reduction at 500°C.

Prepared catalysts were made with two Al_2O_3 supports, Kaiser 201 spheres (8-10 mesh) and Alon^R, a fine alumina manufactured by the Cabot Corporation. In each case the support was wetted by a solution of chlorplatinic acid (H_2PtCl_6), then dried at 110°C. The catalyst was then given a mild reduction at 250°C, which converted the metallic salt to metal. Details of the preparation are given in Appendix A, Section 1. Before gas uptake measurement the catalyst was further reduced in H_2 at 500°C. Catalyst loadings from 0.10% to 4.76% were prepared in this fashion. Bond[2.1], Dorling[2.2], and Gil'debrand[2.3] give a broader discussion of various supported metal catalyst preparation techniques.

2.2 Gas Adsorption by Dynamic (Flow) System

Figure 2.1 shows a flow plan of the dynamic system used in this work for adsorption measurements. The catalyst sample was inserted in a Vycor glass tube, allowing heating to 800°C. The catalyst remained under a constant flow of an inert carrier gas (generally helium) during uptake measurements. Gases to be adsorbed (generally H_2 or O_2)

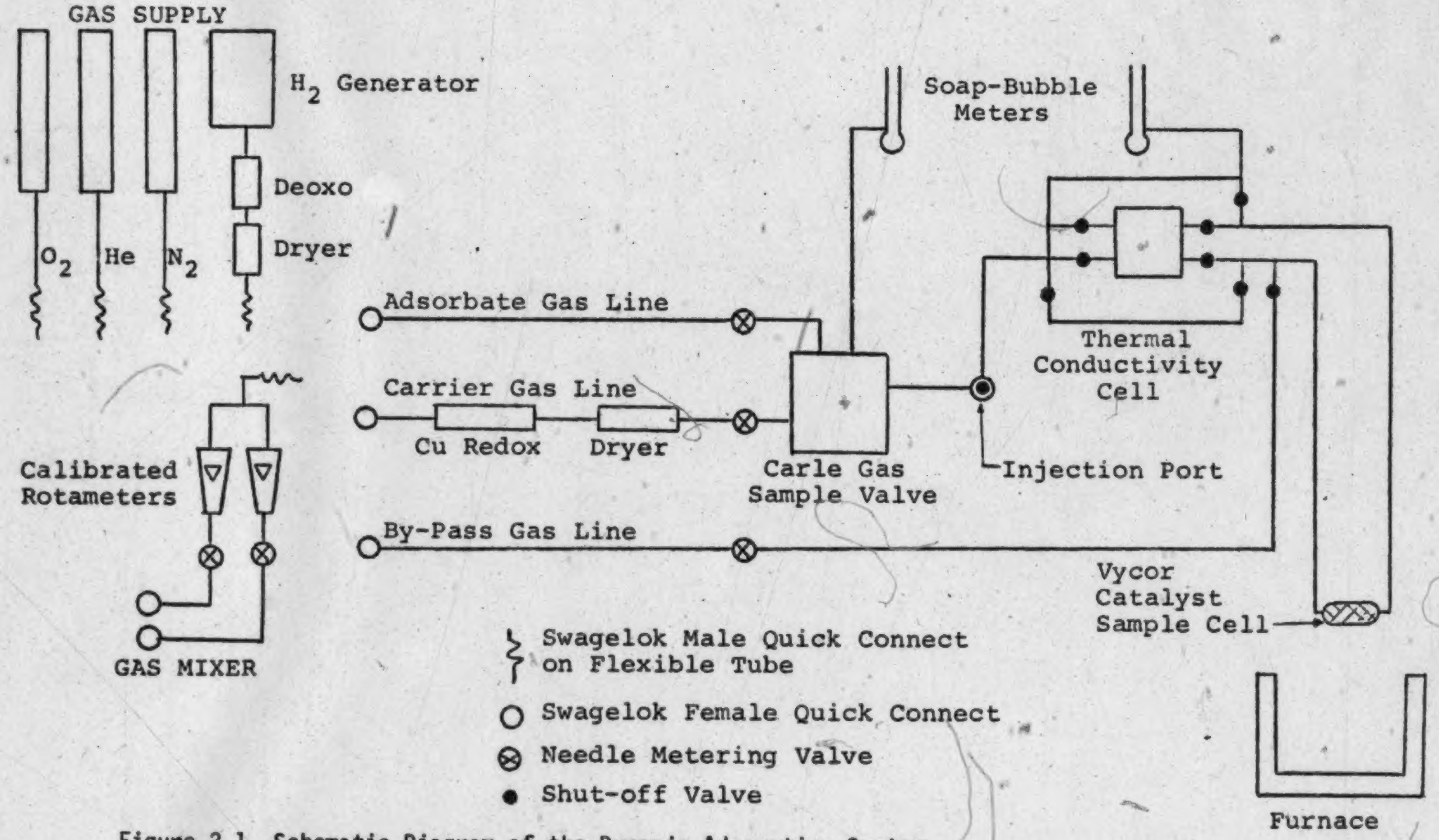
GAS SUPPLY
O_2
He
N_2
H_2 Generator
Deoxo
Dryer
Calibrated Rotameters
GAS MIXER
Adsorbate Gas Line
Carrier Gas Line
Cu Redox
Dryer
By-Pass Gas Line
Carle Gas Sample Valve
Soap-Bubble Meters
Thermal Conductivity Cell
Injection Port
Vycor Catalyst Sample Cell
Furnace
Swagelok Male Quick Connect on Flexible Tube
○ Swagelok Female Quick Connect
⊗ Needle Metering Valve
● Shut-off Valve

Figure 2.1 Schematic Diagram of the Dynamic Adsorption System

were flowed through a calibrated sample loop; switching of the sample valve (Carle Instrument Co, Fullerton, Cal; catalogue #2014) thus injected a pulse of known content in the carrier gas stream. Provision of two calibrated rotameters allowed dilution of the sample gas by the carrier gas. Thus a range of pulse sizes could be generated. Gas connections were through flexible Swagelok Quick-connects, eliminating the danger of leakage through pressurized valves. Carrier and sample gas flow rates were measured by bubble flow meters.

The catalyst could be inserted in a temperature controlled furnace or in various temperature baths, thus allowing uptake as a function of temperature to be readily determined. The furnace was a Thermolyne Model 86 (Sybron Co, Dubuque, Iowa) modified to allow introduction of the Vycor tube holding the catalyst. Temperature was controlled by a Thermo Electric 400 temperature controller (Thermo Electric Co, Saddle Brook, N.J., Model No. 3242200) attached to an iron-constantan thermocouple in the vicinity of the catalyst. A second thermocouple was inserted into the furnace and its output recorded as a check on the internal temperature. In practice control was within 5°C, with little overshoot when a sample was inserted in a hot furnace (<20°C) and no overshoot on cold starts.

Standard adsorption temperatures were: -98°C (a methanol ice bath made by stirring liquid N_2 into a Dewar flask containing methanol; 0°C (ice bath); 96-97°C (boiling distilled H_2O); and 203°C (in the furnace). Room temperature runs were made by inserting the tube in an H_2O filled beaker; room temperatures varied from 22° to 24°C. Reduction was generally effected at 500°C, followed by helium outgassing for one or two hours at 500°C. One requirement of a dynamic system is a high purity carrier gas, since even traces of adsorbents such as carbon monoxide or oxygen in the carrier gas will accumulate on the sample. In this system the carrier gas is first passed over a mixed reduction-oxidation catalyst (supported Cu/CuO) prepared according to the method of Meyer and Ronge[2.4]. Contamination of a carrier gas by H_2 or O_2 after passage over this bed of less than 0.4 ppm was determined by the above authors, and confirmed in this laboratory from a long term degassing study described in Appendix A, Section 2. Water is removed after the carrier gas purification step by a molecular sieve column. The by-pass gas line allows bypassing of the purification catalyst during oxidation or reduction of the sample catalyst. Valving was included to allow bypassing of the thermal conductivity cell when desirable.

Hydrogen used in this work was formed in a Matheson H_2 Generator and further purified by passing over an Englehard Deoxo hydrogen purifier. The gas was dried over a molecular sieve column before introduction to the catalyst. Oxygen and nitrogen were Linde prepurified grade, 99.995% and 99.997% pure, respectively. Instrument grade helium supplied by Canadian Liquid Air was further purified, as described above, before use.

The size of the input pulse of oxygen was established by comparison to a known volume of gas injected by syringe; use of the ideal gas law enabled calculation of the moles of oxygen per pulse. In all runs the flow of O_2 through the sample loop was held constant to ensure identical pulse sizes. Hydrogen content in the sample loop under standard flow conditions was determined by pressure measurements in the sample loop; comparison to the pressure during oxygen flow allowed the H_2 content to be calculated by the ideal gas law. Details of the calibration are given in Appendix A, Section 2.

The output pulse was measured by thermal conductivity cell (Gow-Mac Instrument Co, Madison, N.J., cell model 10-785, with Rhenium-Tungsten filaments, powered by a Gow-Mac Power supply, model 40-001) and recorded on a chart recorder. Mechanical integration of peaks by a Disc Integrator was used to calculate the size of the output pulse. In standard operation pulses of adsorbate gas were passed over the catalyst until a steady state output size was achieved (presumed to be identical to the input pulse). Comparison of partial output peaks to the area of the final output peak enabled calculation of the total output of adsorbate gas. The amount adsorbed on the catalyst surface was determined by difference between input and output.

Appendix A, Section 2, details studies of the variation of gas uptake in standard operation of the flow system. The influence of reduction time, outgassing time, rate of adsorbent admission and other parameters on gas uptake is also reviewed.

This flow system for chromatographic pulse measurement of gas uptakes on catalysts is similar to that described by Freel and others [2.5-2.8]. Chromatographic desorption measurement systems[2.9, 2.10] and chromatographic breakthrough systems utilizing a constant flow of adsorbent gas[2.11] have also been described.

2.3 Electron Microscopy

The electron micrographs used in this work were recorded on a JEM 100 B Microscope in the University of Alberta Department of Physics. The microscope was equipped with a goniometer (tilting) stage, and was capable of resolving the 0.34 nm spacings in graphitized carbon. All images were recorded in the bright field mode using a 100 KV accelerating voltage (λ = 3.7 pm). The maximum magnification recorded on the negative was 330,000, although further increases were obtained through photographic enlargement.

For analysis of pretreated catalyst specimens, samples were crushed into a fine powder and suspended in an inert solvent, then dropped onto a copper grid covered with a "holey" carbon film. The latter was prepared by condensing water droplets in a film of dissolved plastic. Specifically, a pre-soaped dry glass slide was dipped into a 0.1% solution of formvar in chloroform ($CHCl_3$). Water was added to the slide by breath or as a mist from sprayer. As the solvent evaporated and the plastic film hardened, holes were left whose size could be roughly controlled by the preparation conditions[2.12, 2.13]. The plastic film was then floated off onto water, and electron microscope grids placed on it. The film was then picked up by adhesion to a piece of paper or plastic sheet. After drying, the film covered grids were coated with a thin layer of evaporated carbon to conduct electrons and strengthen the film. When the suspended catalyst was dropped on the film, portions of the catalyst extended over the holes, so that any effects of the carbon film on the image contrast were avoided. Astigmatism was corrected at maximum magnification, and very low contamination rates were achieved through use of the standard decontamination device.

For *in situ* reduction and sintering studies, where the catalyst was treated after placement on the electron microscope grid, two modifications were employed. First, a tungsten grid was used, because of its greater strength at sintering temperatures. Second, in order to improve film stability the plastic film was dissolved after being carbon-coated; as a result, "holey" carbon films were prepared which were stable for some time at 500°C in an inert atmosphere.

2.4 Other Measurements

In conjunction with our studies of the titration reaction over supported Pt catalysts, Dr. Eichi Kikuchi measured gas uptakes on a static system and IR spectra. These data are presented in Chapter 4.

The static apparatus was a conventional high vacuum glass volumetric adsorption system. The catalyst was typically reduced in hydrogen at 500°C for two hours and then evacuated for another two hours at that temperature.

IR measurements were carried out on a 2.03% Pt on Alon catalyst. IR transparent wafers were prepared by pressing a finely crushed powder in a one inch diameter die at pressures of 12 tons/in^2. The catalyst wafer was placed in an *in situ* infrared cell with sodium chloride windows. Pretreatment conditions were identical to those for the static measurements described above. Subsequent IR spectra were recorded at room temperature on a Perkin-Elmer Model 621 spectrophotometer, using a similar cell without a catalyst wafer in the reference beam.

2.5 References

2.1 Bond, G.C., "Catalysis By Metals", Academic Press, London, 1962.

2.2 Dorling, T.A., Warren Spring Laboratory Report LR 144(CA), Department of Trade and Industry (London), 1971.

2.3 Gil'debrand, E.I., Int. Chem. Eng. 6, 3, 449 (1966).

2.4 Meyer, F.R., and Ronge, G., Angew. Chem. 52, 637 (1939).

2.5 Freel, J., J. Catal. 25, 139 (1972).

2.6 Roca, F.F., de Mourgues, L, and Trambourze, Y., J. Gas Chromatog. 6, 161 (1968).

2.7 Brooks, C.S., and Kehrer, V.J., Anal. Chem. 41, 1 (1969).

2.8 Gruber, H.L., Anal. Chem. 34, 13, 1828 (1962).

2.9 Hunt, C.E., J. Catal 23, 93 (1971).

2.10 Piringer, O., and Tataru, E., J. Gas Chromatog. 2, 323 (1964).

2.11 Mears, D.E., and Hansford, R.C., J. Catal. 9, 125 (1967).

CHAPTER 3

THE LIMITATION OF THE TRANSMISSION ELECTRON MICROSCOPE FOR CHARACTERIZATION OF SUPPORTED METAL CATALYSTS

3.1 Survey

In the last fifteen years the electron microscope has found increasingly widespread application for the characterization of supported metal catalysts[3.1-3.7]. A principle aim in such studies is the determination of the metal dispersion (the ratio of surface to total metal atoms) which can be calculated if the metal particle size distribution is known, and if a particle geometry is assumed. Electron microscopy has been used to provide direct determination of the size distribution from the images of the metal particles, as discussed in Chapter 1.

The claimed resolution in images of supported metal catalysts has gradually increased, to the point where the detection of 0.4 nm particles and calculated average particle sizes of less than 2 nm have been reported[3.3, 3.6, 3.7]. Such particle size distributions obtained by electron microscopy are based on three implicit assumptions, namely:

a) the size of a metal particle is equal to the size of its image recorded on the micrograph (corrected for magnification);

b) detection of a particle of a given size implies that all particles of that size and all larger particles are being detected;

c) image contrast of the metal particles is distinguishable from contrast arising from the support material.

These assumptions are consistent with the use of a simple mass-thickness interpretation of image contrast in the electron microscope.

It is clear that the correctness of these assumptions is important, since particle size distributions determined from micrographs have often been used to confirm a proposed adsorption stoichiometry for the selective adsorption of gases on supported catalysts[3.3, 3.6]. This latter technique, thus calibrated, has been used for routine determination of metal dispersions.

Recent work on the bright field imaging of atoms and atomic clusters using conventional high resolution instruments[3.8, 3.9, 3.10] has emphasized the importance of careful image interpretation, using theories which take into account the defects of the imaging lens[3.11]. On the basis of such results and of the characteristics of the specimens involved, it was suspected that none of the above assumptions was necessarily valid, particularly for smaller metal particles, and that limits should be determined for both the smallest reliable particle size and the smallest reliable difference between the size of two particles.

In this chapter the results of an investigation into the contrast characteristics of images of platinum particles supported on alumina are presented. The qualitative predictions of both the phase contrast and of the diffraction contrast mechanisms of image contrast have been confirmed by experiments in which the variations in image contrast of specimen particles has been studied as the focus or specimen orientation were varied. The results confirm that the three assumptions listed are not correct for the conditions typical in high resolution microscopy of supported metal catalysts.

3.2 Specimen Characteristics

Crucial to these considerations are the characteristics of the catalyst as a specimen for high resolution microscopy. The metal particles vary from atomic clusters (consisting of a small number of atoms, or possibly single atoms), to true microcrystallites with diameters of the order of 10 nm. The fact that the larger metal particles are crystalline, with the same face-centered cubic structure as bulk material, has been established by x-ray diffraction[3.1] and by analysis of dark-field micrographs[3.12]. At the other extreme, Prestridge and Yates[3.13] have presented micrographs in which images of clusters of a few rhodium atoms have been identified. In these same micrographs, however, may be observed the strong contrast from the silica support.

The metal particles are supported on silica or alumina particles which are usually porous assemblages of irregularly shaped crystals containing defects, of which some are inherent in the crystal structure. Crushing the catalyst to a powder generally results in clumps of support particles of varying thicknesses greater than 30 nm.

The supporting material is in turn placed on microscope grids in various ways; only in the recent work of Freel[3.3] and Prestridge and Yates[3.13] have "holey carbon" support films been used, to eliminate any possibility of interference from the granular image detail observed in continuous amorphous support films (see, for example, Thon[3.14]). From stereoscopic images it is observed that there is typically a range of elevations in the direction of the electron beam of order 100 nm, often between two apparently adjacent alumina particles. This specimen elevation, illustrated in Figure 3.1, imposes a different focus condition upon various particles imaged in the same micrograph. Thus, within any one micrograph there will be a range of values of defocus (deviation from perfect focus), and within two micrographs of similar regions the

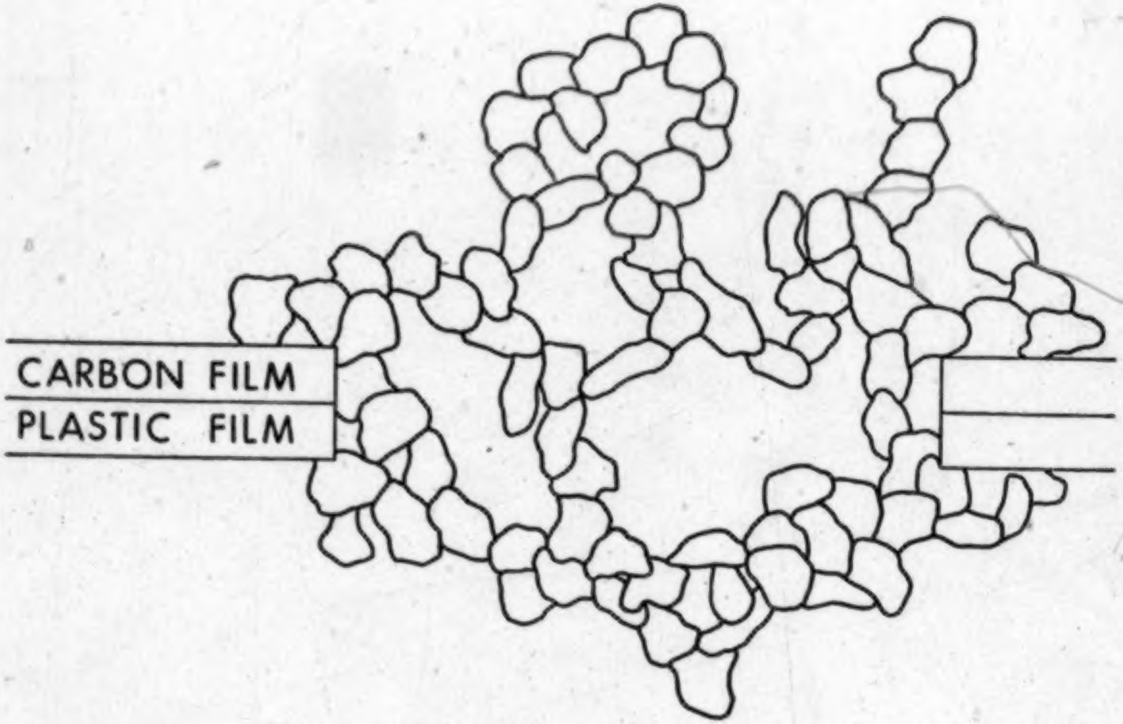
CARBON FILM
PLASTIC FILM

Figure 3.1 Schematic cross section of typical specimen grid, showing clumping of support particles. Depth in the beam direction of order 100 nm.

range of defocus values will in general be different.

For the imaging of small atomic clusters, considerable efforts have been made to minimize the background contrast produced by the supporting film (see, for example [3.8]). Such films are essentially flat and only a few nm thick. Clearly the typical catalyst specimen is far from ideal in that the support imposes appreciable background contrast and holds the metal particles at different elevations.

Finally it may be noted that the support particles, and hence the metal particles are oriented at random. Therefore any image contrast effects which are sensitive to the orientation of the electron beam may be expected to contribute to variations in contrast between otherwise identical particles.

3.3 Theory of Image Generation

It is clear from the characteristics of the specimens that more than one mode of image contrast formation must be considered. For the very small metal particles (clusters of atoms) the *phase contrast* mechanism will operate. However, for larger metal particles in which a definite crystalline structure has developed, the scattering process will be best described in terms of Bragg diffraction giving rise to *diffraction contrast*. This will apply also to the essentially crystalline support particles.

We have therefore considered the implications of each of these contrast theories in what follows. There will of course be a gradation from one of these extremes to the other, but for the present purpose the intermediate case need not be considered. It was found necessary to perform fairly detailed calculations of phase contrast in order to evaluate the variation of image size with defocus. However the qualitative features of diffraction contrast are sufficiently well documented, so that additional calculations were not required.

3.3.1 Phase Contrast

The contrast of an image obtained in the conventional transmission electron microscope is best understood by considering the situation in the back focal plane of the objective lens, where the Fraunhofer diffraction pattern of the electron wave emerging from the specimen is formed. The objective aperture placed in this plane cuts off from the image that part of the wave corresponding to electrons which are scattered through an angle greater than that subtended by the aperture. But in addition, the spherical aberration and the defocus of the lens have the effect of changing the phase of the wave in the back focal plane, through the "contrast transfer function", which depends also on the electron wave length and the scattering angle. Thus, even with a large objective aperture, the microscope will not image faithfully detail smaller than 1 or 2 nm. (For recent reviews of this theory see Thon[3.14] and Hawkes[3.15]).

The way in which the phase contrast transfer function removes certain spatial frequencies from the image while changing (including reversing) the relative phases of others has been established by Thon, using amorphous thin carbon films[3.14]. In order to be able to interpret the images of particles smaller than a few nanometers, the effects of lens defects must be included in suitable theoretical calculations of image contrast. This was first done by Scherzer[3.11]; more recently Reimer[3.10] and Hall and Hines[3.9] have made detailed calculations of the contrast of single atoms and clusters of atoms. (The atom is considered to change the phase but not the amplitude, of the electron wave.) Their results show that the optimum defocus values, at which maximum contrast is expected, vary with cluster size, and that for exact focus the contrast may be too low to detect. Hall and Hines[3.9] obtained through focal series of images of gold particles (on an almost structureless graphite support) which confirmed their predictions.

In order to evaluate the effects on apparent particle size of the lens defects, we have computed image profiles of atoms and atomic clusters using the formulation of Eisenhandler and Siegel[3.16]. Their solution employs a real atomic scattering factor, values of which are readily available (for example, [3.17]). This approach assumes a phase shift of $\pi/2$ upon scattering, a less accurate approach than that of Hall and Hines[3.9], who used a complex atomic scattering factor with the correct phase shift due to scattering. However, their results show that the discrepancies between the two calculations are not significant for the qualitative results in which we are interested. In these calculations, the intensity at the point (x_i, y_i) in the image plane (scaled to unit magnification) is given by

$$| \Psi (x_i, y_i) |^2 = 1 + \frac{4\pi}{\lambda} (1 - \beta^2)^{-\frac{1}{2}} R(x_i, y_i) \qquad 3.1$$

where

$\psi (x_i, y_i)$ = the wave function of the scattered electron

λ = electron wave length, set by the voltage

$(1 - \beta^2)^{-\frac{1}{2}}$ = relativistic correction; β is the electron velocity expressed as a fraction of the speed of light.

For a single atom, $R(x_i, y_i)$ is given by

$$R(x_i, y_i) = \int_0^{\alpha_{max}} f_0(\sin(\tfrac{\alpha}{2})/\lambda) \cos\left[\frac{\pi}{2} - \frac{2\pi}{\lambda}\left(\frac{C_s\alpha^4}{4}\right) + \frac{2\pi}{\lambda}\left(\frac{\Delta f\alpha^2}{2}\right)\right] J_o\left(\frac{2\pi\alpha r_i}{\lambda}\right) \alpha d\alpha \qquad 3.2$$

where

α = scattering angle (α_{max} is determined by the objective aperture)

f_o= atomic scattering factor for electrons

C_s= spherical aberration constant

Δf= defocus

J_o= zero order Bessel function

r_i= radial position in image plane from scattering center

$(r_i=(x_i{}^2 + y_i{}^2))$.

For multiple atom cases, the Bessel function term above is replaced by the expression

$$\sum_{n=1}^{\text{all atoms}} J_o \left(\frac{2\alpha\pi}{\lambda}\left((x_i + x_n)^2 + (y_i + y_n)^2\right)^{\frac{1}{2}}\right) \qquad 3.3$$

where

x_n, y_n are the locations in the object plane of the various scattering atoms.

The term $\cos\left[\frac{\pi}{2} - \frac{2\pi}{\lambda}\left(\frac{C_s\alpha^4}{4}\right) + \frac{2\pi}{\lambda}\left(\frac{\Delta f\alpha^2}{2}\right)\right]$ is the phase contrast transfer function of the lens, and contains the phase changes imposed on the scattered electron wave within the lens by spherical aberration and defocus.

In order to assess the variation in image intensity for particles of different sizes, four cases were evaluated. These were arbitrarily chosen as a single atom, a three atom planar array, a four atom pyramidal array, and a seven atom planar hexagonal array. For the multiple atom cases, the scattering centers (atoms) were separated by 0.275 nm, and the intensity profiles were computed along a radius which ran through a non-central atom. Test calculations along a radius running between two non-central atoms gave similar intensity profiles with slightly different spacings.

The calculations were performed using relativistic Hartree-Fock atomic scattering factors for gold[3.17]. Values for C_s (1.6 nm) and α_{max} (0.0125 rad) were chosen to be typical for a high resolution microscope at 100 KV (λ = 3.7 pm). Since a range of defocus values are expected within an image, the calculations were performed for Δf values from -200 to +400 nm in 20 nm steps.

In addition, the single atom case was evaluated over the defocus range -20 to +200 nm for four other values of α_{max}. These calculations were designed to test the effect of aperture size on phase contrast effects.

The R integral, equation 3.2, was iteratively evaluated, with a minimum of 200 steps to α_{max}, by the IMSL DRMBIU subroutine. Evaluation of ψ^2 at intervals of 0.5 nm to a total of 10 nm allowed determination of the phase contrast image profile, *i.e.* the image intensity as a function of spatial location in the image plane. Contrast, defined as the difference in intensity between image point and background divided by background intensity, is given ψ^2-1. The program for calculation of intensity profiles, along with details of parameters used, is shown in Appendix B.

3.3.2 Diffraction Contrast

For larger specimen structures the phase contrast calculation is invalid, because multiple scattering and diffraction effects become significant. Once the metal particles reach a size of 2-3 nm diameter, Bragg diffraction effects should dominate in the scattering process, and the use of standard multibeam dynamical calculations (see for example Hirsch *et al.*[3.18]) is appropriate. The diffraction pattern from a single crystal consists of a series of discrete spots corresponding to diffraction from various planes in the crystal. In the back focal plane the objective aperture intercepts all except the directly transmitted beam, giving rise to bright field diffraction contrast: the variation in the intensity of the directly transmitted beam from point to point across the crystal surface. The theory then predicts a fairly sensitive dependence of image contrast on the thickness and orientation of the crystal[3.18], but a reduced sensitivity of contrast to defocus as compared with phase contrast images[3.9].

3.4 Microscope Use

In order to test these theoretical predictions, two series of experiments were performed. The phase contrast effects were examined by taking through focal series of each of a number of areas for both Pt/alumina and pure alumina specimens. Diffraction contrast effects were observed by imaging the same field a number of times, tilting the specimen through a known angle between each set of through focus exposures.

The astigmatism correction was checked for selected cases and the transfer characteristics of the lens were determined approximately from through focal series of images of thin amorphous carbon which were analysed using a simple optical diffractometer[3.14]. The optical diffraction pattern reveals which spatial frequencies are present in the image, and which have been filtered out by phase cancellation (the contrast transfer function is zero for certain values of α). An example is show in Figure 3.2, along with a schematic of the resolution test apparatus. The distance from the central spot is proportional to the inverse of the spatial separation, and may be calibrated by imaging a known mesh. Accounting for magnification, the spatial scattering passed unfiltered for this particular pattern was calculated as 0.55, 0.67, 0.89 nm and greater than 1.17 nm with filtering effects between these values. Alternate frequencies passed by the lens are reversed in phase relative to their original values. For this particular case, no meaningful detail less than 0.55 nm was transmitted by the lens, thus representing a limit to resolution. Elliptical rings indicate the presence of astigmatism in the objective lens which had not been completely corrected.

The objective apertures available subtended angles of approximately 0.01, 0.006, and 0.003 radians. The first of these, a 60 nm aperture, was used for most of the work reported, since the project was concerned with the imaging of the smallest particles and atomic clusters. This aperture removes from the image information concerning spacings smaller than 0.37 nm, and is therefore large enough for phase contrast. On the other hand, all Bragg diffracted beams (except one) are intercepted, giving rise to diffraction contrast from the crystalline particles. The exception in our studies was the 111 reflection of γ-Al_2O_3, for which d_{111} is 0.456 nm. Lattice fringes of this spacing were often

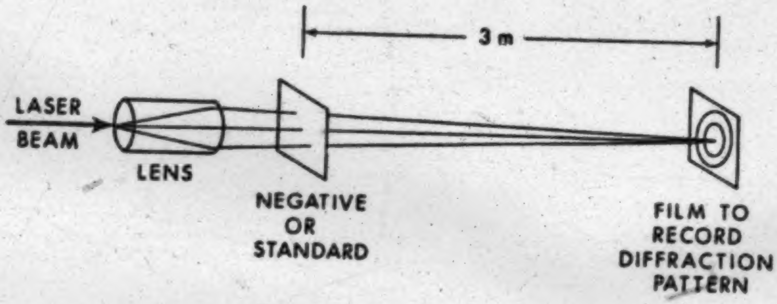
3 m
LASER BEAM
LENS
NEGATIVE OR STANDARD
FILM TO RECORD DIFFRACTION PATTERN

MICROGRAPH RESOLUTION TEST

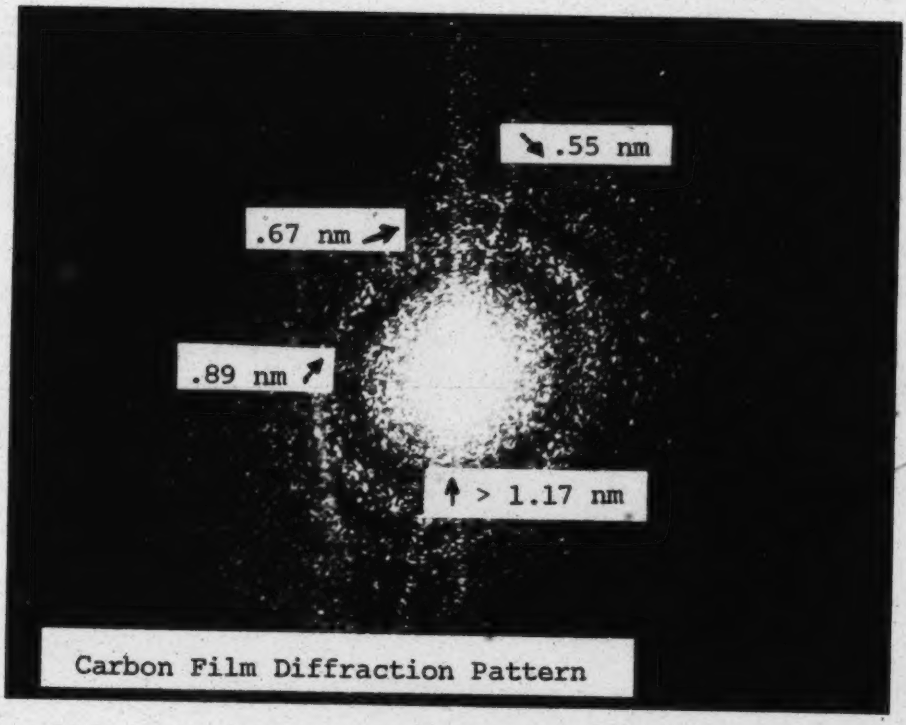
.55 nm
.67 nm
.89 nm
> 1.17 nm
Carbon Film Diffraction Pattern

Figure 3.2 Schematic diagram of optical diffraction micrograph resolution test, and optical diffraction pattern from micrograph of thin carbon film, illustrating the elimination of certain spatial frequencies from the image.

observed and were used as an internal magnification standard. The smaller apertures were used to verify the predicted effects of lower α_{max} values on image resolution.

3.5 Results and Discussion

3.5.1 Calculated Image Profiles

Solution of the phase contrast equation generates an image intensity profile; the result for a single atom and a defocus of 180 nm is shown in Figure 3.3. In order to compute detectability and size as a function of defocus, we assumed limits for distinguishable contrast, and took the width of the central peak (d_0 in Figure 3.3) as the apparent size. Following Eisenhandler and Siegel[3.16], 5% light or dark maximum contrast was assumed to be necessary for detection: if the maximum intensity was between 0.95 and 1.05 the size was set for zero.

The arbitrary nature of these assumptions is evident. Other size definitions could have been used, such as the diameter at 5% contrast ($d_{0.95}$ in Figure 3.3). A different detectability limit would alter the sizes determined; under some conditions images can have bright and dark rings surrounding the central peak, with obvious complications in defining size. These and other factors would be critical if one attempted to deduce the actual size of a cluster (number of atoms), for which one would require to know the defocus value for each particle in the image. It is important to emphasize, however, that the assumption of different detectability limits or size definitions in no way affects the qualitative results of the present studies, which apply in general irrespective of the optical constants of the particular microscope being used.

3.5.2 Variation of Contrast and Apparent Size with Defocus

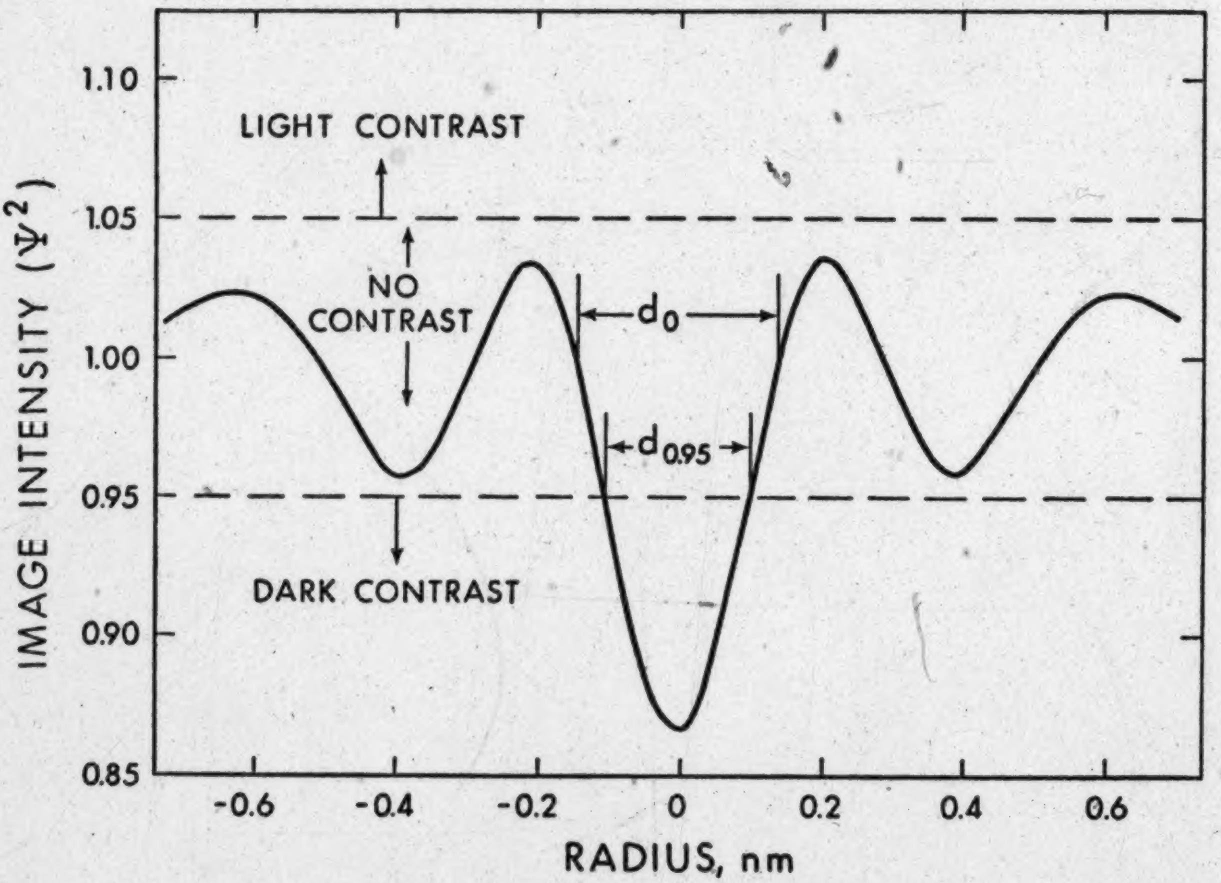

Figure 3.3 Calculated image intensity profile for a single atom at a defocus of 180 nm. Dashed lines are detectability limits; two size parameters are shown.

The character of an image profile is a sensitive function of focus, and can shift from light, through undetectable to dark, as shown in Figure 3.4. The three profiles are for a single atom with defocus values of 140 nm, 160 nm and 180 nm.

Figures 3.5 and 3.6 show the calculated maximum image intensity of the four clusters of atoms as a function of defocus. It is evident that all four clusters will be detectable, as light or dark regions depending upon the defocus. In addition, it is evident that the range of defocus over which the arrays will appear as a region of dark contrast, the "window size", increases as the number of atoms in the cluster increases. Table 3.1 shows the calculated window sizes for the four cases.

In order to relate these results to micrographs of supported metal catalysts, the geometry of the specimen must be considered. Referring to Figure 3.1, the specimen in the region of a hole in the grid consists of an irregular stacking of catalyst fragments, with a typical depth (measured from the image shift after tilting the specimen through a known angle) of greater than 50 nm. This depth imposes an immediate restraint on any micrograph, for the defocus over the specimen has a range equal to the depth. A large crystallite in the specimen will have dark contrast regardless of its spatial position and defocus, because of the diffraction contrast mechanism. Small metal clusters, however, have a contrast which is extremely sensitive to the defocus, and thus only some regions of the specimen may be so situated as to provide dark phase contrast for these small particles.

Calculated apparent size of metal clusters is also a sensitive function of the defocus, as shown for the three and seven atom cases in

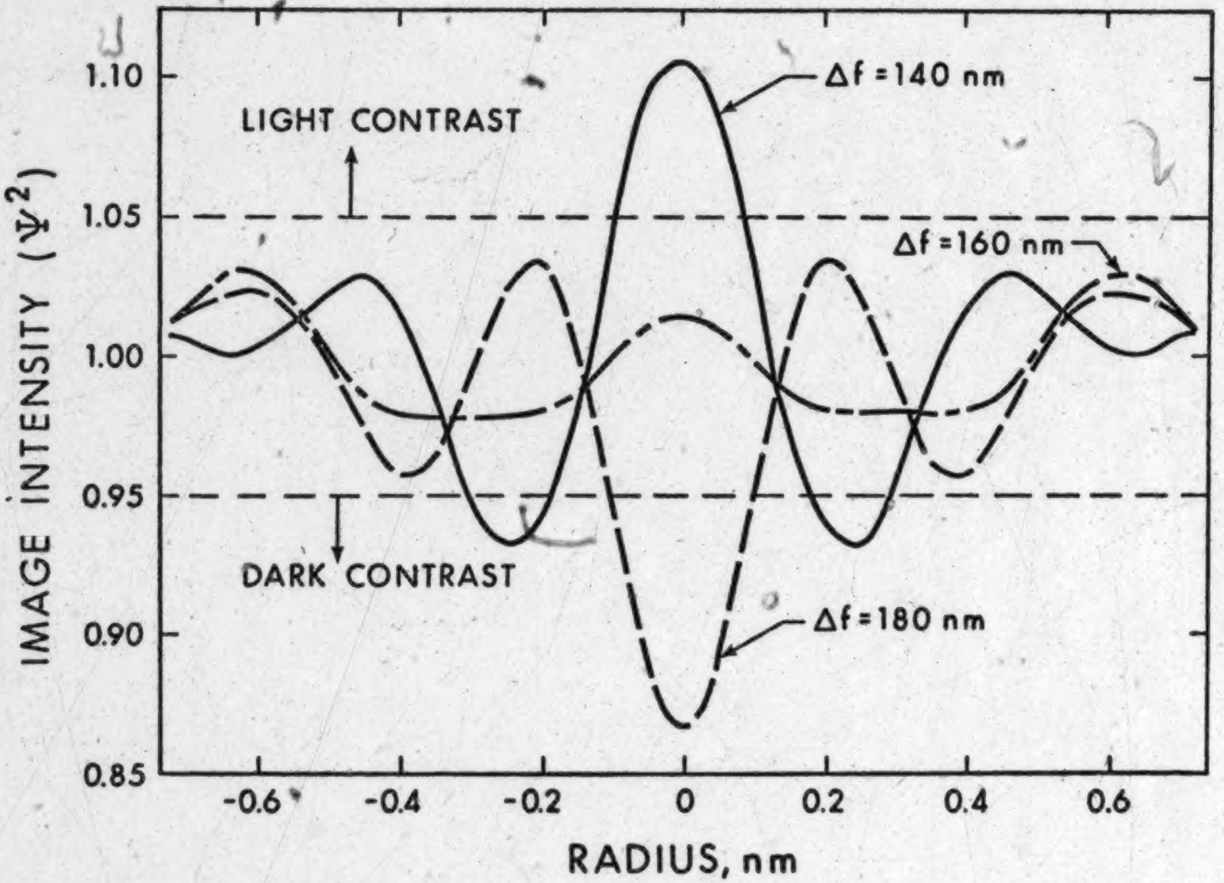

Figure 3.4 Three calculated image intensity profiles for a single atom, showing the sensitivity of the image to changes in defocus.

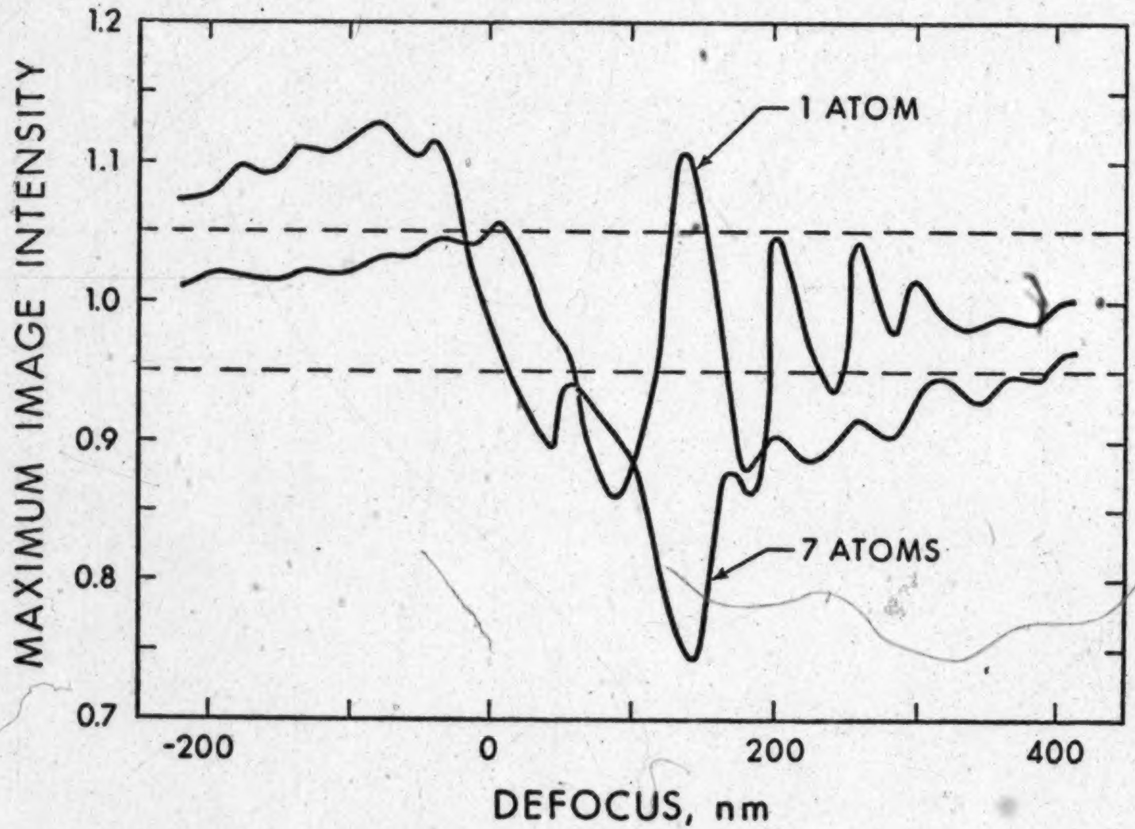

Figure 3.5 Calculated maximum image intensity as a function of defocus for the one and seven atom cases. All atom clusters will give detectable dark contrast only over a selected range of defocus values.

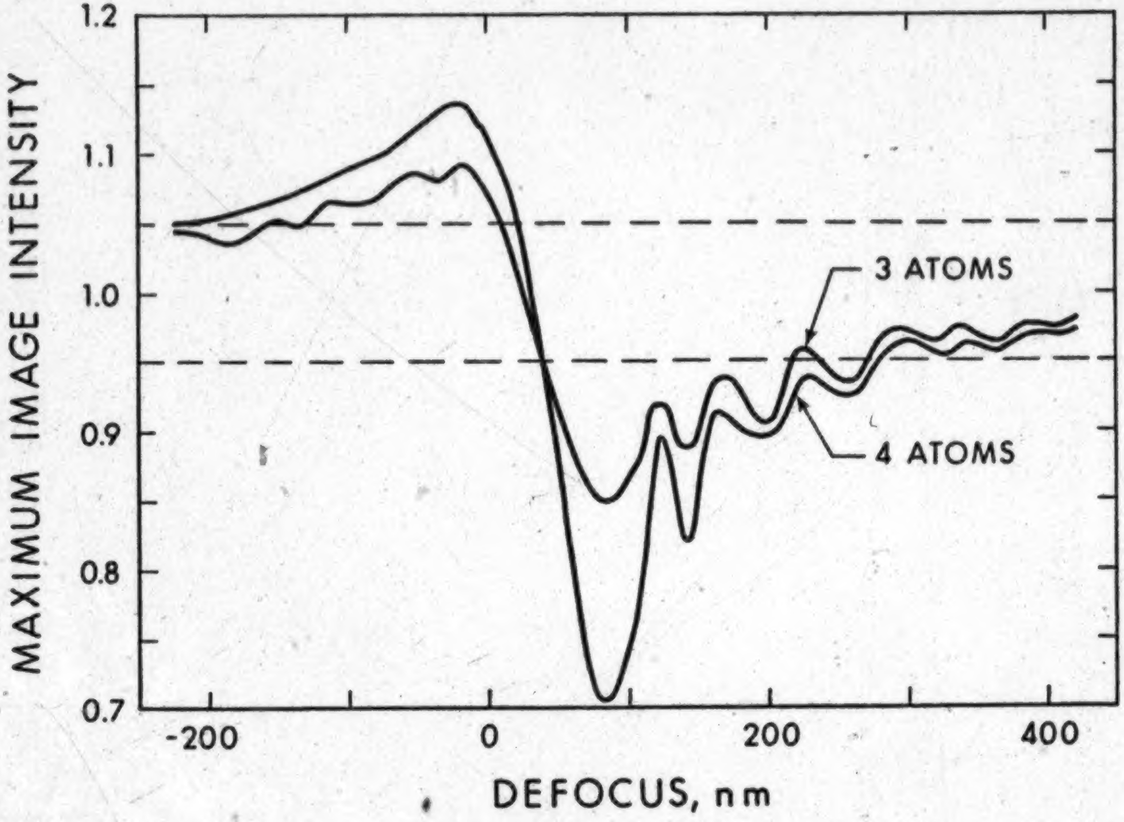

Figure 3.6 Calculated maximum image intensity as a function of defocus for the three and four atom cases. All atom clusters will give detectable dark contrast only over a selected range of defocus values.

Table 3.1: Theoretical Defocus Windows for Dark Contrast for Various Atomic Clusters (C_s = 1.6 mm, λ = 3.7 pm)

Case	Windows
1 atom	60-120; 150-195; 235-250
3 atoms	45-215; 240-275
4 atoms	40-280
7 atoms	10-390

Figure 3.7. Even in the region where clusters give dark contrast, the sharpness and diameter of their images varies strongly with defocus. Thus, again returning to an actual catalyst specimen, identical small metal particles at different elevations in the specimen would be expected to have varying image sizes, because the variation in defocus for these particles is equal to their differences in elevation in the specimen. Similarly, identical particles imaged in different micrographs would in general appear of different sizes because of differences in defocus.

An extreme case of the deviation in calculated image appearance with defocus for the four atom case is shown in Figure 3.8. A 60 nm change in defocus changes the image from a dark region of 0.8 nm apparent diameter, to a ringed dark-light pattern, with an apparent size for the inner dark region of 0.4 nm.

Analysis of a series of micrographs of a 4.76% Pt on Alon catalyst confirms that for small contrast regions detectability and apparent size are a sensitive function of the defocus. Figure 3.9 shows micrographs of identical areas of catalyst at various values of defocus. (Reproduction may have reduced the quality of the micrograph; prints are available on request from the author.) Between the two micrographs shown in Figure 3.9 (a) there is a difference in defocus of 80 nm. Regions "a" and "d" show the distortion of apparent shape effected by the defocus change. The dark region "a" appears to resolve into two crystallites in the right hand micrograph, while the shape of particle "d" is substantially altered. The region of contrast above "c" is enhanced in the right hand picture. Regions "b", "e", "f" and "g" show the fine contrast detail which alters with

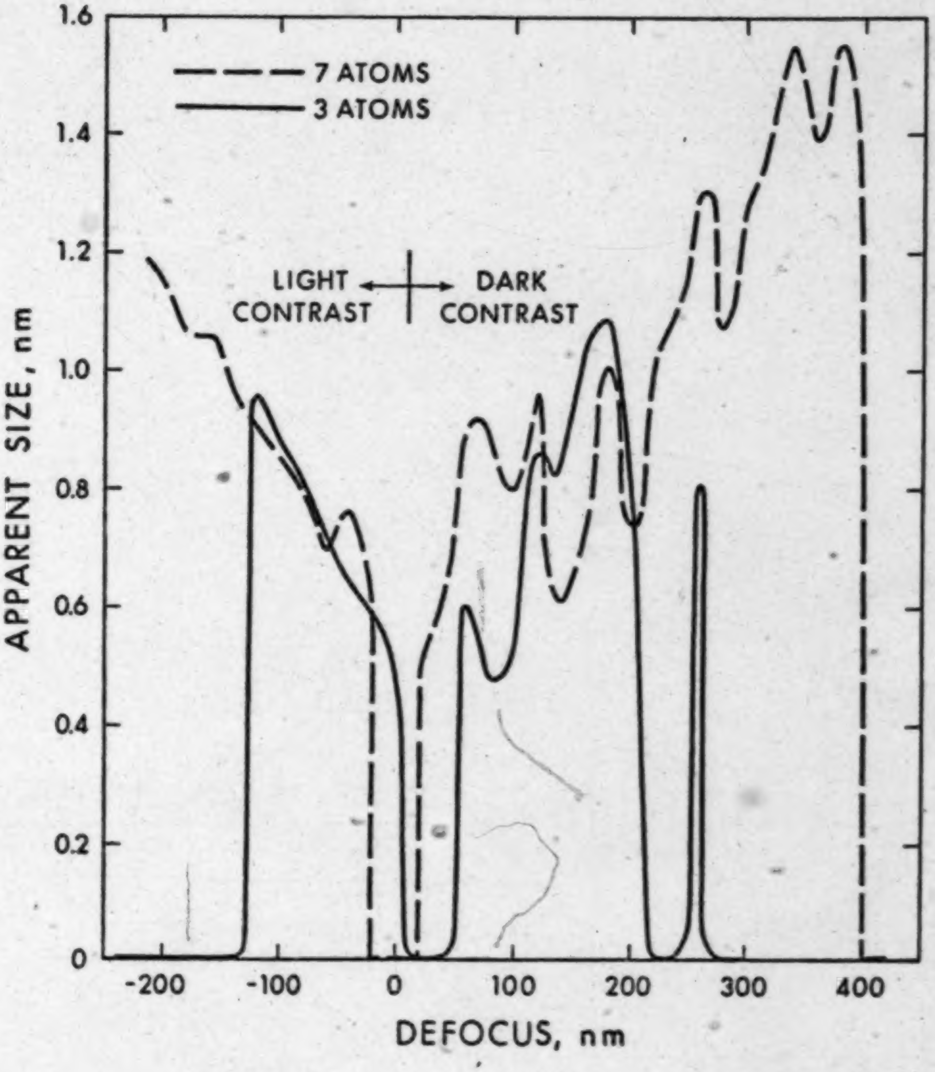

Figure 3.7 Calculated apparent image size as a function of defocus. The size of the image is not a simple function of the size of the specimen particle.

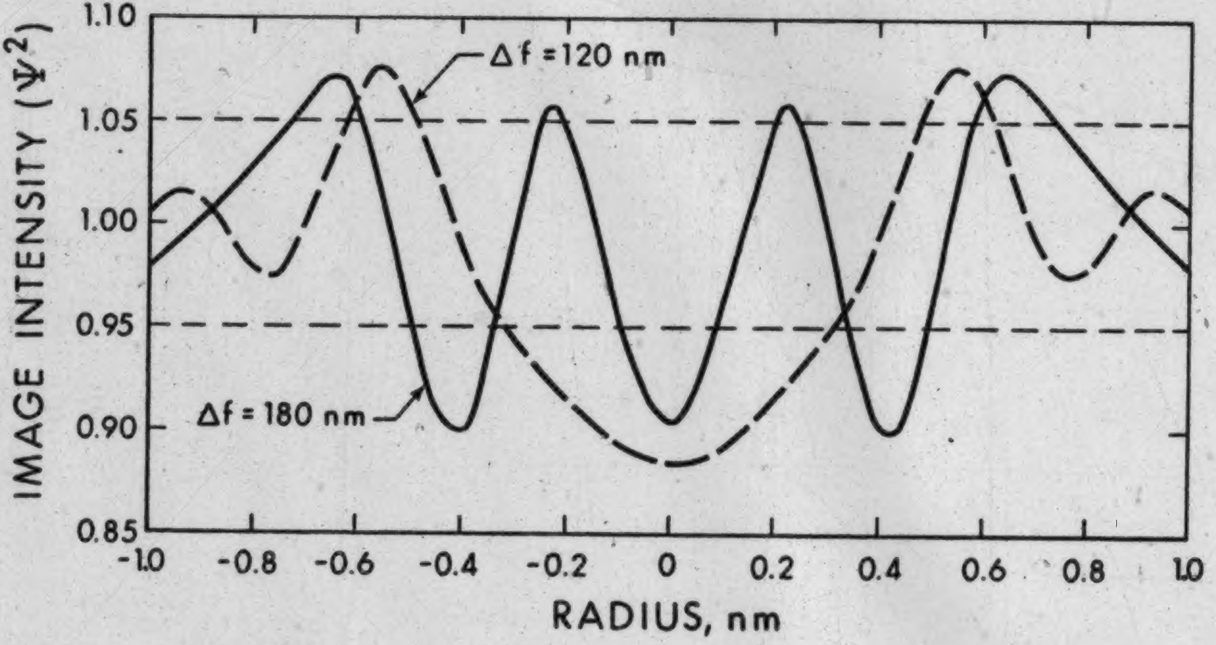

Figure 3.8 Two calculated image intensity profiles for the four atom case, showing the sensitivity of apparent image size to defocus.

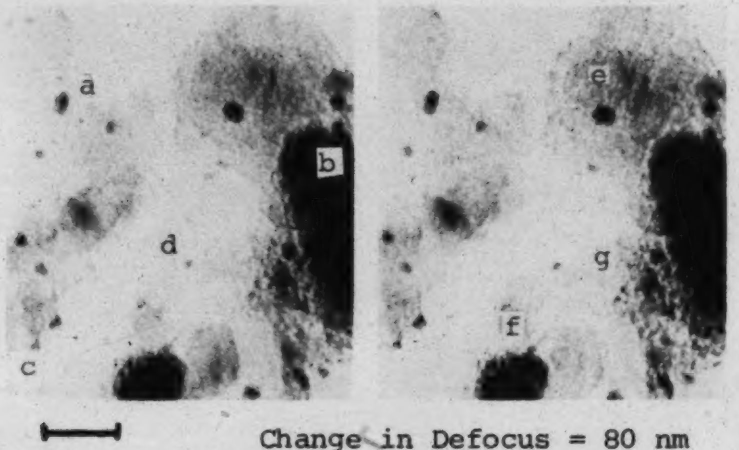
a
b
c
d
e
f
g
10 nm

Change in Defocus = 80 nm

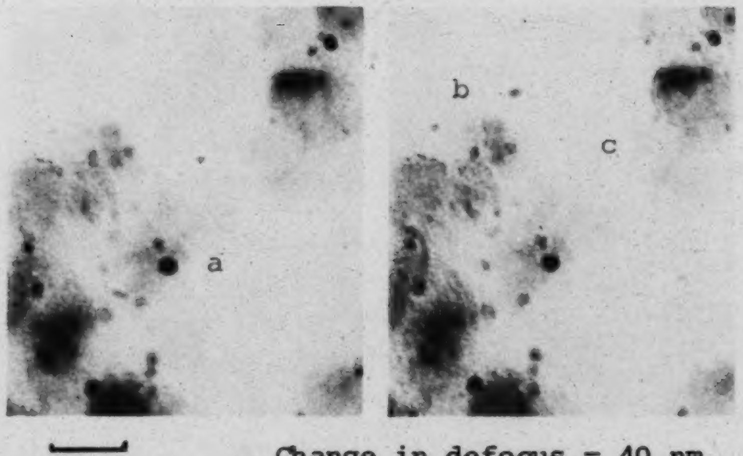

Change in defocus = 40 nm

Figure 3.9 (a), (b). Micrographs of a Pt/Al_2O_3 catalyst showing the effect of defocus change on image contrast.

defocus; in each region particular sub-nanometer structure is apparent or highlighted in one micrograph, but not in the other. Similar effects are observable near regions "a", "b" and "c" in Figure 3.9 (b), for which the change in focus is 40 nm.

The fact that it is not possible to decide from such micrographs whether this fine contrast arises from platinum particles or from the substrate is discussed later.

Measurements of apparent image size were made for a number of particles in each micrograph of a through focal series. The results are plotted in Figures 3.10, 3.11 and 3.12 for three separate fields of view, and it is evident that "window sizes" are smaller and relative fluctuations in apparent sizes greater, for the smaller contrast regions. These results confirm the qualitative predictions made on the basis of the phase contrast calculations (see Figures 3.5 and 3.6 and Table 3.1).

These results make it quite clear that the number of particles which will be detected in a standard size analysis will depend upon the average defocus value of the micrograph as a whole, and on the particular defocus range existing within the micrograph. Identical small particles at different elevations in the specimen will have different apparent sizes, or may not be detectable simultaneously. The observed variation in apparent size of up to 1 nm imposes an uncertainty on measured sizes which implies that for analysis of size distribution, division of sizes into classes which differ by less than 1 nm is not warranted.

As aperture size is reduced, calculations indicate that the variation in image intensity and apparent size decreases, but at the expense

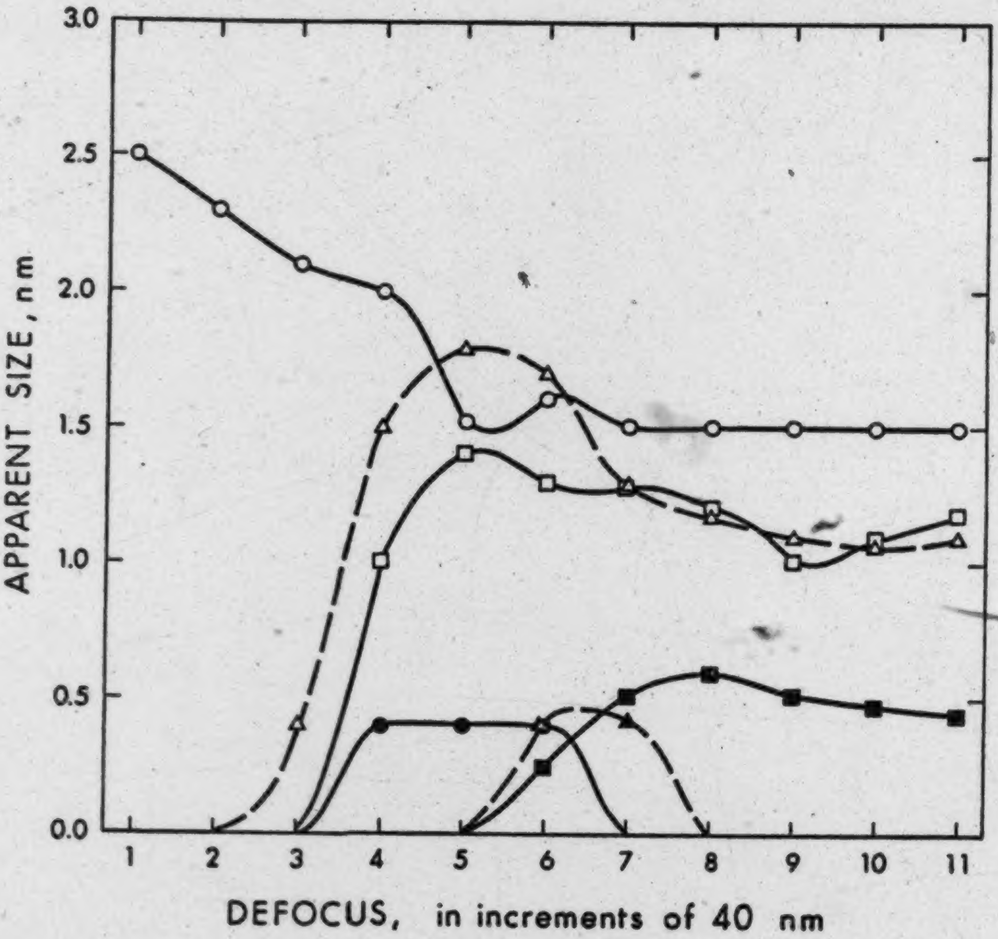

Figure 3.10 Variation of measured particle size with defocus for three through focus series of micrographs of a Pt/Al_2O_3 catalyst. Zero values mean that the particle was not detected.

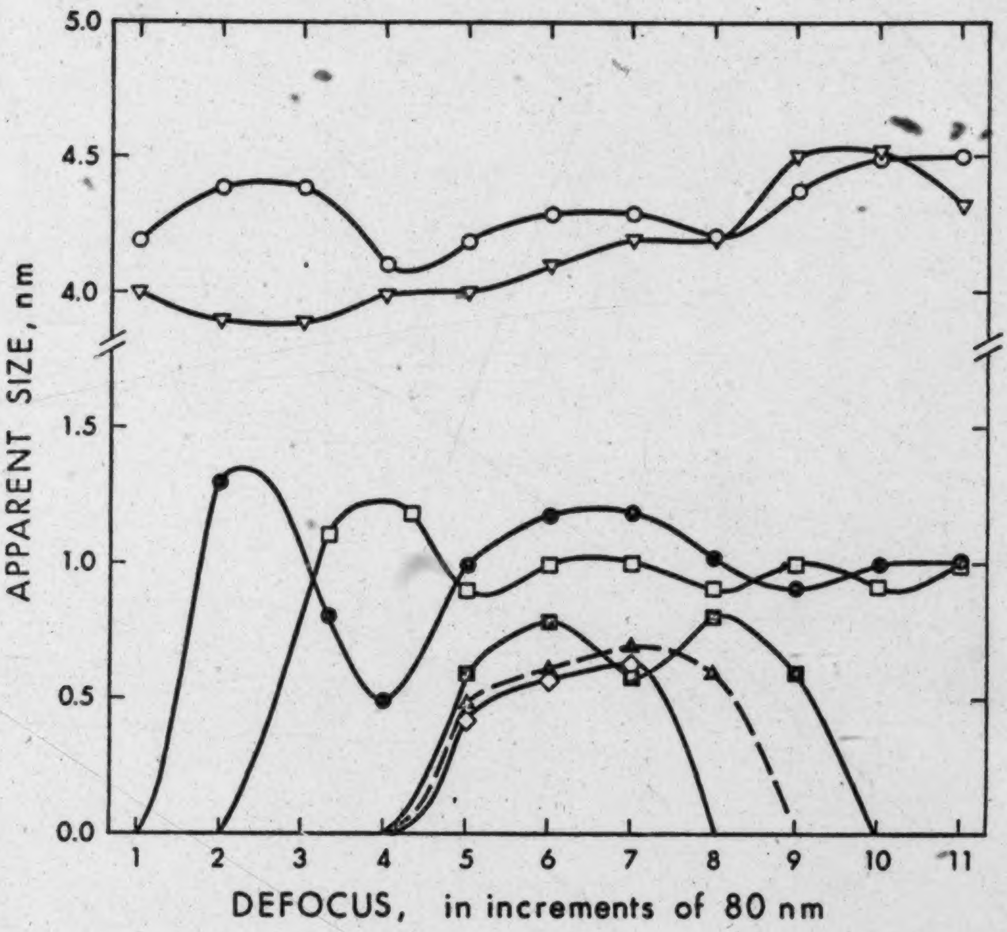

Figure 3.11 Variation of measured particle size with defocus for three through focus series of micrographs of a Pt/Al_2O_3 catalyst. Zero values mean that the particle was not detected.

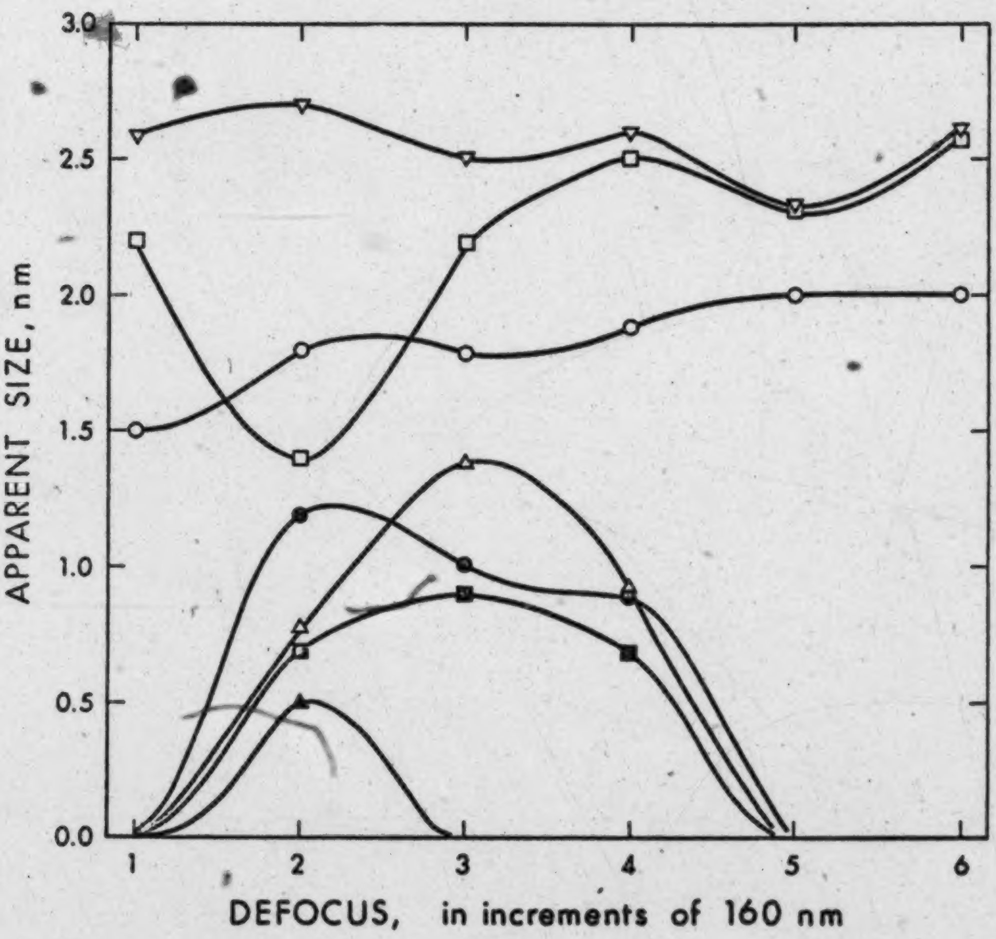

Figure 3.12 Variation of measured particle size with defocus for three through focus series of micrographs of a Pt/Al_2O_3 catalyst. Zero values mean that the particle was not detected.

of contrast and size information[3.9]. This is shown in Table 3.2, where for the single atom case the maximum image contrast and apparent size are shown over a defocus range for varying apertures, and hence varying values of α_{max}. For the α_{max} value of 0.005 radians, no contrast above 5%, light or dark is realized in this defocus range, while for a very small aperture giving an α_{max} of 0.00125 radians, even 0.1% contrast is not achieved. As the aperture is decreased, the image size increases, until for the smallest aperture, the atom, if detected, would appear to be greater than 2 nm in size. Thus variations in image appearance with defocus are reduced by smaller apertures, but at the cost of image intensity and size definition of the image.

Through focal series of images were recorded of the same specimen area for apertures subtending angles of 0.01, 0.006, and 0.003 radians. The predicted loss of resolution was observed with some very small regions of dark contrast, clearly resolved in the image recorded with an α_{max} of 0.01, but being progressively washed out through lower contrast and increased size as the aperture size was reduced.

It may be noted that if one is not concerned with detection of particles less than about 2 nm, the use of smaller apertures is probably advantageous. The variation of intensity with defocus is reduced for smaller apertures and the diffraction contrast of particles is greater, although we still observed some variation of apparent size with defocus.

3.5.3 The Effect of Tilt on Contrast

The sensitivity of the contrast of both metal microcrystallites and support particles to the orientation of the electron beam was investigated using the high resolution tilting holder. Micrographs of

Table 3.2: Calculated Image Intensity and Apparent Size Over a Range of Defocus and Apertures

aperture, μm	40		32		16		8		4	
α_{max}, radians	0.0125		0.0100		0.0050		0.0025		0.00125	
defocus, nm	I_{max}[a]	do[b]	I_{max}	do	I_{max}	do	I_{max}	do	I_{max}	do
-20	1.039	0.56	1.051	0.56	1.017	0.70	1.001	1.44	1.000	2.0
0	1.053	0.50	1.036	0.52	1.007	0.66	1.001	1.30	1.000	2.0
20	1.037	0.40	1.035	0.40	0.996	0.86	0.999	1.46	1.000	2.0
40	1.005	0.14	1.023	0.22	0.986	0.76	0.999	1.45	1.000	2.0
60	0.950	0.56	0.943	0.56	0.976	0.75	0.998	1.45	1.000	2.0
80	0.860	0.43	0.847	0.45	0.969	0.75	0.997	1.45	1.000	2.0
100	0.868	0.46	0.867	0.48	0.964	0.76	0.997	1.45	1.000	2.0
120	0.954	0.80	0.993	0.74	0.961	0.78	0.996	1.45	1.000	2.0
140	1.105	0.26	1.060	0.26	0.962	0.80	0.995	1.45	1.000	2.0
160	1.014	0.18	1.003	0.12	0.965	0.86	0.995	1.44	1.000	2.0
180	0.865	0.30	0.944	0.40	0.970	0.92	0.994	1.44	1.000	2.0
200	0.049	0.20	0.972	1.20	0.977	1.04	0.994	1.45	1.000	2.0

a - calculated so that background intensity is 1.0

b - in nm

a specimen being tilted differ not only in angle of orientation to the electron beam, but also differ slightly in the defocus condition. This latter occurs because during tilting the specimen shifts physically in the object plane, and an exact restoration of the previous defocus value is impossible. However variations in regions of contrast greater than 2 to 3 nm can be attributed to orientation effects since phase contrast effects become minimal at these sizes.

The micrographs in Figure 3.13 show identical specimen areas with a variation in tilt angle. In Figure 3.13 (a), a tilt change of 15° significantly alters the appearance of the metal particles. The particle in region "a" disappears in the right hand micrograph, while a third crystallite in region "c" is more clearly evident in the right hand micrograph. The two particles in region "b" appear as one in the right hand micrograph possibly due to superposition. The sensitivity of support contrast to orientation is evident to the right of region "c". Similarly, in Figure 3.13 (b) several contrast alterations are evident with a tilt change of 7°. The relative contrast of the two particles in region "a" changes, revealing the sensitivity of contrast to orientation. A contrast region to the right of region "c" is not detected in the right hand micrograph. In regions "b" and "d", the background contrast is reduced substantially as a result of tilt; in region "b" this results in highlighting of a particle virtually obscured in the left hand photograph.

The simultaneous variations in support and metal particle image contrast again raises questions about the reliability of single micrograph particle size distribution analysis. The variation in orientation leads to a change in apparent contrast of a particle. For larger

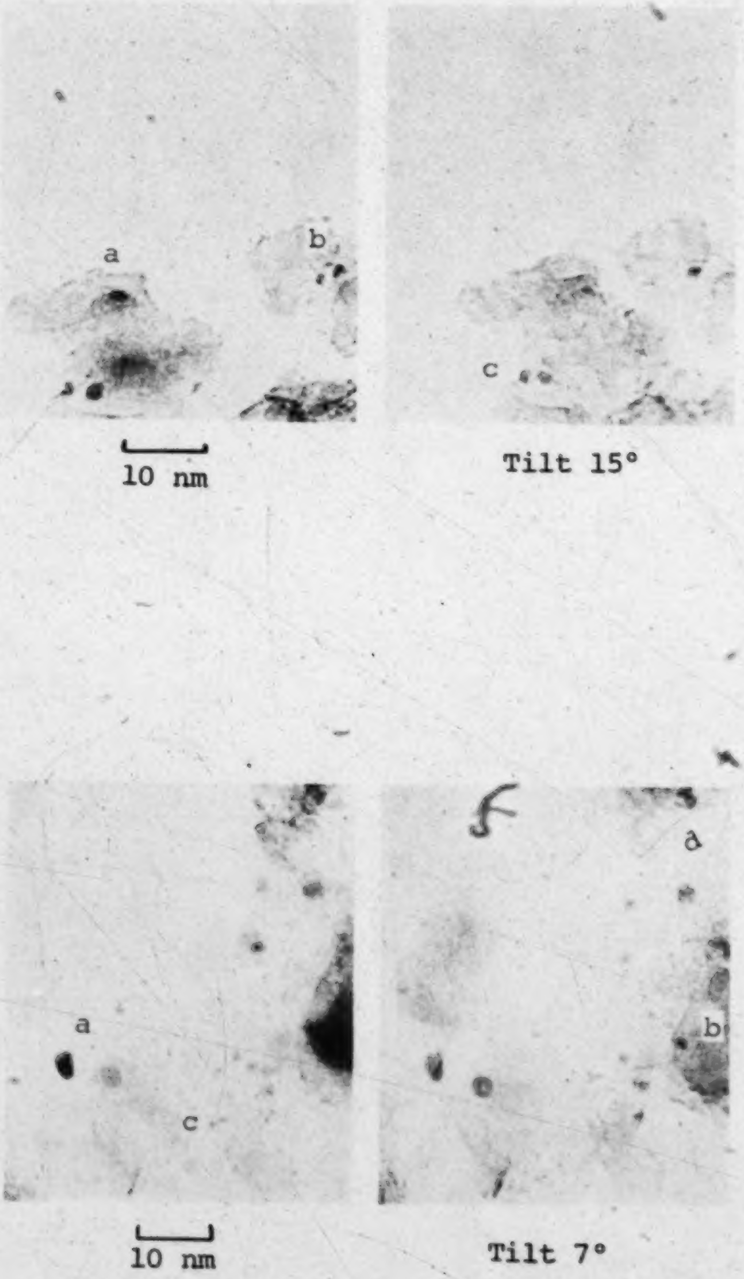
a
b
c
10 nm
Tilt 15°
a
c
a
b
10 nm
Tilt 7°

Figure 3.13 (a), (b). Micrographs of a Pt/Al_2O_3 catalyst showing the effect of tilt on image contrast.

particles, this contrast change would not be sufficient to prevent detection, but for smaller particles the orientation clearly can prevent their being included in a particle count. Since a typical supported metal catalyst contains particles at all orientations, the danger of miscount is evident.

3.5.4 Contrast Structure in the Support Material

An additional concern in assessing the accuracy of particle size distribution analysis is the distinguishability of small crystallite images from the contrast inherent in the support. Typical support materials, such as alumina or silica, have a highly irregular structure leading to high surface areas. This irregularity is a desired feature for catalysts, allowing a large gas-solid interface and a high dispersion of metal. Diffraction evidence from alumina support materials confirms a fine polycrystalline structure.

The polycrystalline irregular structure leads to considerable contrast variation in the micrograph of alumina itself. Such contrast structure is on a small (down to 0.5 nm) scale, and is particularly evident in regions of crystal overlap.

Figure 3.14 demonstrates this effect. The left hand micrograph shows two regions of catalyst at different elevation. In the right hand micrograph, the grid has been tilted through 25° so that these regions now overlap. Considerable contrast structure is evident along the line of overlap which does not arise from the presence of metal crystallites detectable in the left hand micrograph. This contrast structure is indistinguishable in a standard micrograph from that which is generated by small crystallites. Examination of micrographs of pure

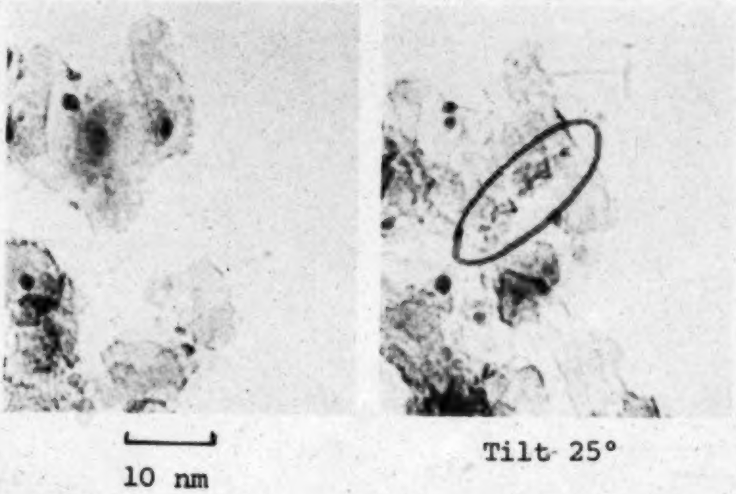

Figure 3.14 Micrographs of a Pt/Al_2O_3 catalyst showing the effect of tilt on contrast. Note fine contrast structure along overlap region in the right hand micrograph.

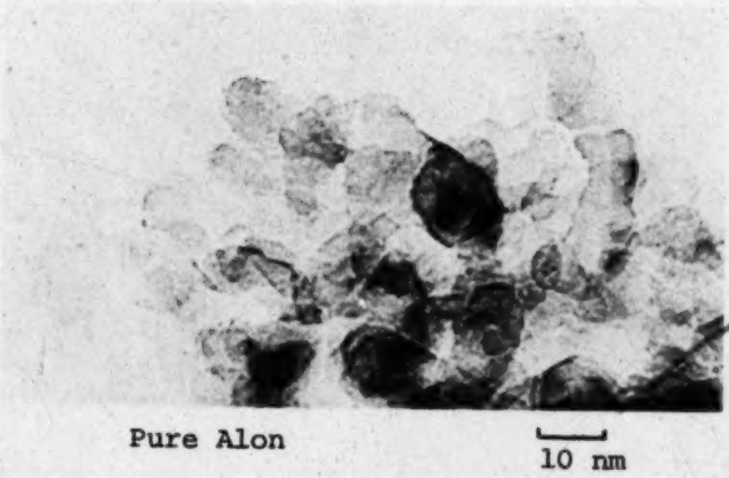

Figure 3.15 Micrograph of pure Al_2O_3 ("Alon") specimen showing the contrast inherent in the support.

Alon, with no platinum added, show this fine contrast structure, again particularly in overlap and boundary regions; Figure 3.15 illustrates this.

The inherent support contrast structure limits the lower size limit to which particle size analysis may be extended. Even where microscope resolution is better than 1 nm, distinction of metal particle from support contrast in this size range is virtually impossible in a single bright field micrograph.

3.6 Conclusions

A number of conclusions concerning the determination of particle size distribution of supported metal catalysts from electron micrographs emerge from the work reported in this chapter.

1. For metal particles below 2 nm in diameter:

   a) Because of the phase contrast mechanism, detection is a sensitive function of the defocus and hence of the spatial elevation in the specimen. As metal clusters get smaller, the defocus range over which they are detectable as a region of dark contrast decreases;

   b) Apparent size is a sensitive function of defocus, since the microscope "filters" certain spatial frequencies and thus distorts the images. Thus identical clusters will have apparent images which vary with their spatial elevation in the specimen, within a single field of view. Identical particles in separate micrographs could appear to have differing sizes because of different settings of the objective focus. Further, variation in apparent particle size of up to 1 nm suggests this value as the lowest meaningful division of diameters in a particle size distribution;

c) An inherent contrast is generated by the use of irregular polycrystalline supports. Particularly for metal particle images below 1 nm, distinction of particle images from background contrast is virtually impossible within a single bright field micrograph.

2. For larger metal particles, identical crystallites can have markedly different contrast due to different orientation to the electron beam.
3. For all sizes of metal particle, the effects of overlap, and the orientation sensitivity of the contrast of the support material, can seriously affect size analysis. Certain combinations of particle/support orientation make the particle undetectable.

It is evident that these conclusions are incompatible with the assumptions implicit in some applications of particle size distribution analysis of supported metal catalysts. Clear evidence of the detection of a crystallite of a given size does not imply that all crystallites of that size and larger are being detected, because of contrast window and orientation factors. Small image sizes cannot in general be directly correlated to the particle size in the specimen, preventing computation of a meaningful average size for catalysts containing small metal particles. Analysis of such catalysts is further complicated by the difficulty of distinguishing metal contrast from inherent support contrast.

These conclusions draw into question the extension of particle size analysis into the sub-nm size range; they further imply that analysis of micrographs cannot currently provide a definitive test of adsorption stoichiometries for small crystallites[3.6]. As a general rule we would argue that particle size distributions become increasingly unreliable as the size of particles counted extends below 2.5 nm. While micrographs can give evidence of smaller particles, detection and accurate identification of all particles of a size below 2.5 nm is extremely unlikely.

It should be emphasized, however, that the present studies have been concerned only with the use of conventional high resolution transmission electron microscopes, using standard bright field imaging. There are a number of other imaging techniques which may prove more suitable after similar detailed evaluation. The use of dark-field images, which have proved valuable for the detection of single heavy atoms[3.21], and for relatively large supported metal particles[3.22] may show promise for high resolution work. An even more promising possibility in the long term may well be the use of scanning transmission instruments of the type developed by Crewe and his colleagues[3.23] which permit a range of new contrast mechanisms to be applied.

3.7 References

3.1 Adams, C.R., Benesi, H.A., Curtis, R.M. and Meisenheimer, R.G., J. Catal. 1, 336 (1962).

3.2 Cormack, D., and Moss, R.L., J. Catal. 13, 1 (1969).

3.3 Freel, J., J. Catal. 25, 139 (1972).

3.4 Moss, R.L., Platinum Metal Rev. 11, 141 (1967).

3.5 Pope, D., Smith, W.L., Eastlake, M.J. and Moss, R.L., J. Catal. 22, 72 (1971).

3.6 Wilson, G.R. and Hall, W.K., J. Catal. 17, 190 (1970).

3.7 Wilson, G.R., and Hall, W.K., J. Catal. 24, 306 (1972).

3.8 Formanek, H., Mueller, M., Hahn, M.H. and Koller, T., Naturwiss. 58, 339 (1971).

3.9 Hall, C.R. and Hines, R.L., Phil. Mag. 21, 1175 (1970).

3.10 Reimer, L., Z. Naturforsch A 24, 377 (1969).

3.11 Scherzer, O., J. App. Phys. 20, 20 (1949).

3.12 Avery, N.R. and Sanders, J.V., J. Catal. 18, 129 (1970).

3.13 Prestridge, E.B. and Yates, D.J.C., Nature 234, 345 (1971).

3.14 Thon, F., "Electron Microscopy in Material Science", (Eds. Valdre, V. and Zichichi, A.), p. 570, Academic Press, New York, 1971.

3.15 Hawkes, P.W., "Electron Optics and Electron Microscopy", Taylor and Francis Ltd., London, 1972.

3.16 Eisenhandler, C.B. and Siegel, B.M., J. Appl. Phys. 37, 4, 1613 (1966).

3.17 Doyle, P.A. and Turner, P.S., Acta Cryst. A 24, 390 (1968).

3.18 Hirsch, P.B., Howie, A., Nicholson, R.B., Pashley, D.W. and Whelan, M.J., "Electron Microscopy of Thin Crystals", Butterworths, London, 1965.

3.19 Fukami, A. and Adachi, K., J. Electronmicros. 14, 112 (1965).

3.20 Fukami, A., Adachi, K. and Katok, M., J. Electronmicros. 21, 19 (1972).

3.21 Hashimoto, H., Kumao, A., Hino, K., Yotsumoto, H. and Ono, A., Jap. J. Appl. Phys. 10, 1115 (1971).

3.22 Fornwalt, D.E. and Kinoshita, K., Micron. 4, 99 (1973).

3.23 Crewe, A.V. and Wall, J., Optik 30, 461 (1970).

CHAPTER 4

THE TITRATION REACTION ON SUPPORTED Pt CATALYSTS

4.1 Survey

As discussed in Chapter 1, gas adsorption on metal surfaces has become a fairly standard technique for the determination of the dispersion of supported metal catalysts. Conversion of a corrected volumetric gas uptake to a metal surface area or dispersion requires the assumption of a stoichiometry of adsorption. In light of the current controversy over an appropriate stoichiometry, detailed below, experiments were designed to explore the adsorption of oxygen and hydrogen, and their interaction on the surface of a supported Pt catalyst. The IR spectra and static system gas uptake results reported in this chapter were recorded by Dr. E. Kikuchi, and then combined with the flow system gas uptake results for interpretation.

In their studies of low concentration supported Pt catalysts, Benson and Boudart[4.1] proposed that H_2 titration of adsorbed O_2 would increase the sensitivity of measurement. In interpreting their results they used the stoichiometry

$$\mathrm{Pt}_{\overline{\mathrm{surf}}}\,\mathrm{O} + \frac{n}{2}\,\mathrm{H}_2 \rightarrow \mathrm{H}_2\mathrm{O} + \mathrm{Pt}_{\overline{\mathrm{surf}}}\,\mathrm{H}_{(n-2)} \tag{4.1}$$

with an n value of 3, but Mears and Hansford[4.2] found n values closer to 4. Wilson and Hall[4.3] proposed to resolve this discrepancy by postulating that n is 3 for large crystallites, but incomplete surface coverage by O_2 on small crystallites leads to apparent n values of 4 for highly dispersed catalysts. Dalla Betta and Boudart[4.4] similarly found that small platinum clusters on Y zeolite took up less oxygen per surface atom than larger platinum crystals. Like Wilson and Hall, they attributed this phenomenon to the relative electron deficiency of small particles as compared to large ones. Basset *et al.*[4.5] studied heats of adsorption and reaction for both the titration of oxygen, equation 4.1, and the titration of adsorbed hydrogen

$$\mathrm{Pt}\underset{\mathrm{surf}}{\text{—}}\mathrm{H} + \frac{m}{2}\,\mathrm{O}_2 \rightarrow \mathrm{H}_2\mathrm{O} + \mathrm{Pt}\underset{\mathrm{surf}}{\text{—}}\mathrm{O}_{(m-\frac{1}{2})} \qquad 4.2$$

They also found an n value of 3 for large metal particles, and calculated low heat of adsorption values (about 18 kcal/mole) for the capture by the support of the H_2O generated during titration.

A preliminary survey of titration data in this laboratory showed considerable deviation from the simple stoichiometric picture presented by equations 4.1 and 4.2. Initial hydrogen uptakes generally exceeded initial oxygen uptakes. By "initial" we mean the gas adsorbed on the "degassed" catalyst surface, as compared to that calculated as remaining on the surface after a titration step, which we refer to as secondary, tertiary, etc. uptakes. In addition, the secondary or tertiary uptakes of gases differed from the initial uptake of the same gas on a "degassed" surface. We frequently observed that

$$H_A' > H_A \qquad 4.3$$

$$\text{and } O_A' \le O_A \qquad 4.4$$

where H_A' and O_A' are the uptakes of hydrogen and oxygen after titration, corrected for the amount of gas consumed to form water, and H_A and O_A are initial gas uptakes. Thus titration seems to enhance the adsorption of hydrogen and to retard the adsorption of oxygen on Pt-on-alumina catalysts.

In this chapter the deviations from a simple constant stoichiometry are documented by static and flow system gas uptake data. The data of other authors are also summarized. Three possible explanations of the deviations are discussed: a modification of the surface area, as proposed by Darensbourg and Eischens[4.6], the formation of more than one type of adsorbed oxygen species, and a promotion/retardation effect stemming from the water generated during the titration. IR spectroscopy was used to examine the nature of the surface oxygen species during adsorption and titration.

Infrared spectroscopy has been applied extensively to study adsorbed species on catalysts. Heyne and Tompkins[4.7] have recorded IR spectra of CO adsorbed on silica-supported Pt pretreated with oxygen at 300°C. They observed two different kinds of CO adsorbed on platinum sites: one on platinum metal (2080 cm^{-1}), the other on platinum ion (2120 cm^{-1}). They also found that oxygen adsorbed on platinum metal could be removed by carbon monoxide (as carbon dioxide), while that on platinum ion could not. Primet *et al.*[4.8] concluded from their IR study that a part of the surface platinum adsorbs both oxygen and carbon monoxide on the same site, and gives an IR absorption band of C=O stretching shifted to 2120 cm^{-1}. They showed that such species $\mathrm{Pt}{<}^{O}_{CO}$ could be obtained even at room temperature by repeated (O_2-CO) treatment.

These investigations with IR spectroscopy indicate that the adsorption of oxygen on Pt is not simple: namely there are at least two different kinds of adsorbed species of oxygen. In this work, volumetric uptake data has been supplemented by an IR study of the nature of the surface oxygen species after repeated O_2-CO and O_2-H_2 treatments, and after O_2 adsorption at temperatures from 25°C to 500°C.

4.2 Experimental Results

Table 4.1 shows the details of the catalysts used in this work. For both the static and flow system, gas uptakes were measured at room temperatures except as noted in the text.

4.2.1 Isotherms and Isobars of Oxygen and Hydrogen

Figure 4.1 illustrates typical isotherms of oxygen uptake obtained with the static system at temperatures from 25°C to 500°C for catalyst I. The adsorption isotherm was extrapolated to zero pressure to obtain the adsorbed amount of oxygen on platinum.

Figure 4.2 shows oxygen and hydrogen uptakes as a function of temperature measured in the static system for catalysts E and I, and in the flow system for catalyst A. Hydrogen uptakes were remeasured at room temperature after reducing the sample used for the measurement of each static oxygen adsorption isotherm (Table 4.2). For catalyst I, reduction at 500°C was enough to restore the original hydrogen uptake value. On catalyst E, however, subsequent hydrogen uptakes were found to be depressed by 24.4% and 35.4% after oxygen adsorption measurements at 400°C and 500°C, respectively. Assuming that these decreases in hydrogen uptake resulted from a decrease in metal surface area, oxygen uptakes at these temperatures were corrected and the corrected values are shown in Figure 4.2 by the dotted line.

Oxygen uptakes were found to increase with increasing uptake temperature, while hydrogen uptakes decreased. In the room temperature region hydrogen uptake is higher than oxygen uptake for both catalysts A and E, as measured by both systems.

Table 4.1: Description of Catalysts

Catalyst	Pt Content (wt%)	Type of Support
A	0.5	Engelhard (Lot #18-381)
B	0.5	(1)
C	0.5	(2)
D	0.5	(3)
E	4.76	Alon (4)
F	2.46	Alon
G	0.10	Alon
H	1.00	Alon
I	2.03	Alon
J	1.61	Kaiser 201 alumina
K	2.03	Kaiser 201 alumina

(1) same as catalyst A except sintered for 16 hours in O_2 at 450°C

(2) same as catalyst A except sintered for 16 hours in O_2 at 600°C

(3) same as catalyst A except sintered for 16 hours in O_2 at 700°C

(4) Registered trademark of Cabot Corp.

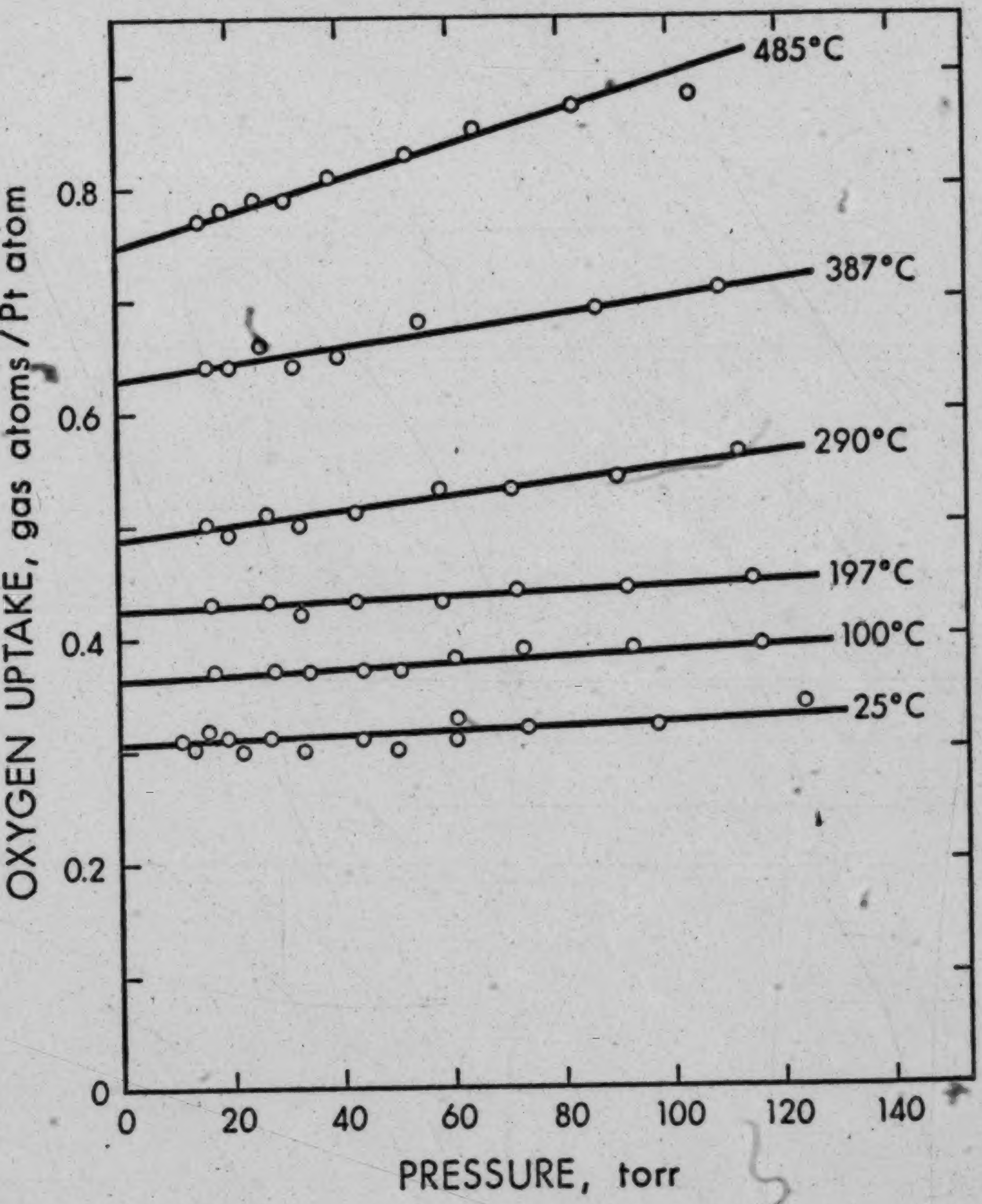

Figure 4.1 Oxygen isotherms for a 2.03% Pt on Alon catalyst

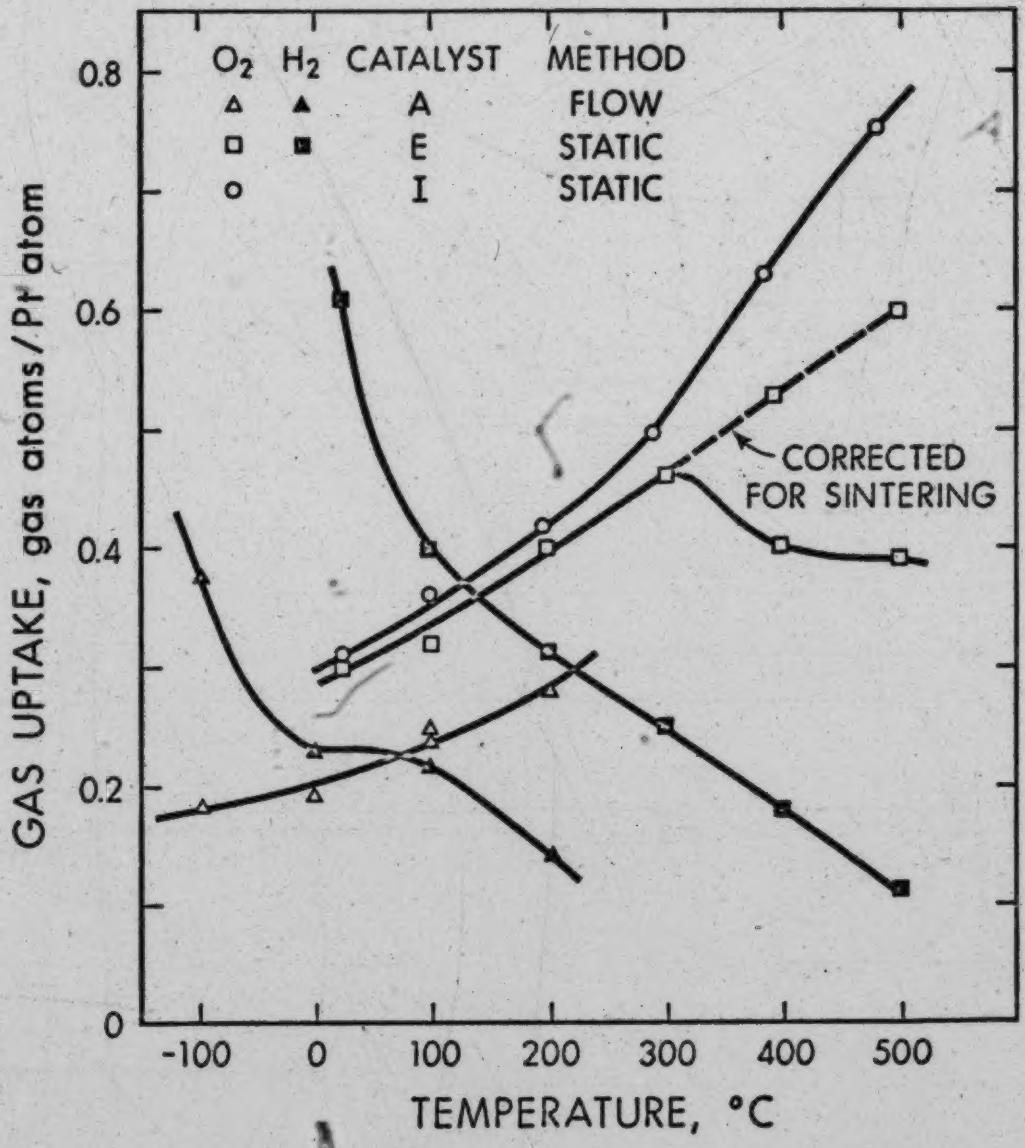

Figure 4.2 Oxygen and hydrogen isobars for three different Pt/Al_2O_3 catalysts.

Table 4.2: O_2 Adsorption Uptakes as a Function of Temperature and Room Temperature H_2 Titration and Adsorption Uptakes

Catalyst	*Oxygen adsorption* Temp°C	Uptake (atoms/atom)	Room temperature *hydrogen titration* Uptake (atoms/atom)	HT/OA	Subsequent room temperature hydrogen adsorption uptakes (atoms/atom)
I	RT	0.31	1.39	4.48	0.73
	100°C	0.36	1.49	4.14	0.72
	197	0.42	1.69	4.12	0.73
	290	0.49	1.72	3.44	--
	387	0.63	1.62	2.57	0.73
	485	0.75	0.96	1.30	0.74
E	RT	0.30	1.32	4.40	0.61
	100	0.32	1.13	3.53	--
	200	0.40	1.30	3.25	--
	300	0.46	1.31	2.85	0.60
	395	0.40	1.04	2.60	0.45
	500	0.39	0.72	1.85	0.39

4.2.2 Hydrogen Titration of Oxygen Adsorbed at Elevated Temperatures

Experiments were designed to test the reactivity of oxygen adsorbed at various temperatures with gaseous hydrogen. Oxygen was added at 100 torr to catalysts E and I at temperatures from 25°C to 500°C, following which the catalyst was evacuated for one-half hour and cooled to room temperature. Hydrogen titration uptakes were then measured. Oxygen and hydrogen titer uptakes are shown in Table 4.2.

These data suggest that oxygen adsorbed at higher temperatures is less reducible by hydrogen at room temperature than the oxygen adsorbed at 25°C. Oxygen adsorbed at elevated temperatures may form a new type of surface species or may oxidize metal below the surface layer. This phenomenon was further studied by IR spectroscopy.

4.2.3 IR Spectra of CO Adsorbed on Pt with O_2 Preadsorbed at Various Temperatures

IR transparent discs of catalyst I were contacted with O_2 at temperatures from 25 to 500°C in the *in situ* IR cell. Following O_2 adsorption (100 torr O_2 pressure) the sample was cooled to room temperature, the cell was evacuated and the catalyst was contacted with CO, at 100 torr, for two hours. IR spectra, following these treatments, showed absorption bands with maxima near 2120, 2060-80, 1800, 1640, 1480 and, 3600 cm^{-1}. The last four bands correspond to those observed by Parkyns[4.11] when CO_2 was adsorbed on alumina. Eischens and Pliskin [4.12], in their study of CO adsorption on supported Pt, observed bands at 2060-80 and 1800 cm^{-1}, which they attributed to the linear and bridged forms of adsorbed CO. Heyne and Tompkins[4.7] and Primet *et al.* [4.8] observed a band at 2120 cm^{-1} when CO was contacted with a catalyst which had previously been exposed to oxygen. Their interpretation as to the nature of the bond responsible for this band differs; the former workers attribute it to CO adsorbed on Pt ions while the latter assign it to CO adsorbed on a Pt atom which also has an adsorbed oxygen atom.

In our work the bands at 1480, 1640 and 3600 cm^{-1}, and part of the band at 1800 cm^{-1}, are probably due to the interaction of CO_2, formed by the oxidation of CO with adsorbed O_2, with the alumina support. CO adsorbed on Pt, probably in the bridged structure, also contributes to the band at 1800 cm^{-1} since it is present when CO is adsorbed on a freshly reduced sample. When oxygen was introduced at room temperature to a freshly reduced sample onto which CO has been adsorbed, the absorption bands at 2060-80 cm^{-1} and near 1800 cm^{-1} decreased in intensity, and a new band developed at 2120 cm^{-1}. This new band is the one also observed by Heyne and Tompkins[4.7] and Primet *et al.*[4.8]. The intensity of the 2060-80 cm^{-1} band initially decreased rapidly, but it did not disappear completely over a period of several hours unless the catalyst was heated to 100°C. Heyne and Tompkins[4.7] reported that this band rapidly disappeared completely at room temperature. This difference is possibly due to the different support, as postulated by Eischens and Pliskin[4.12], or it may be caused by differences in Pt crystallite sizes.

The band at 2120 cm^{-1} was also observed when CO was introduced to the catalyst which had preadsorbed oxygen at elevated temperatures. This is illustrated in Figure 4.3. The intensity of this band increased with increasing temperature of oxygen adsorption up to 400°C, then decreased when O_2 was preadsorbed at 500°C. The 2060-80 cm^{-1} band, however, continually decreased with increasing oxygen adsorption

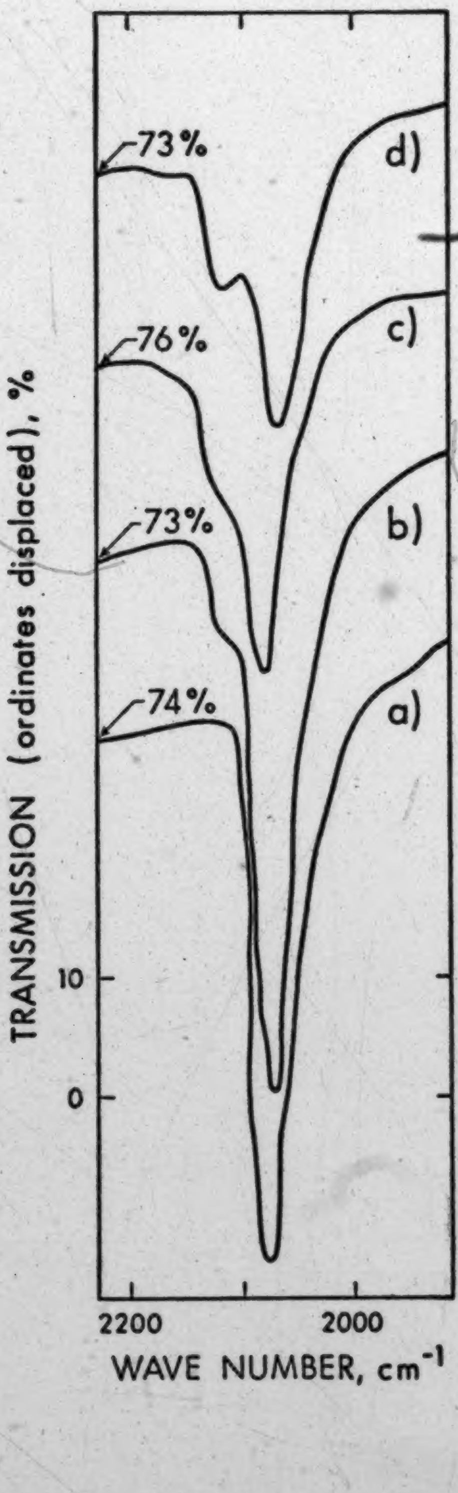

Figure 4.3 Variation of the 2060-80 and 2120 cm^{-1} bands from CO adsorbed on Pt/Al_2O_3 catalysts with different O_2 preadsorption temperatures.
a) freshly reduced sample b) O_2 preadsorbed at 200°C
c) at 400°C d) at 500°C

temperature. These results suggest that oxygen is taken up by supported platinum on at least two different sites. One site which gives the 2060-80 cm^{-1} band when CO is admitted, is generally associated with adsorption of oxygen on a platinum atom. This species of oxygen is readily removed by CO in a reaction to form CO_2, and the band thus arises from CO adsorbed on the "clean" site. The second site for adsorbed oxygen, which gives rise to the 2120 cm^{-1} band when CO is introduced, has been associated with platinum ion, or a platinum atom which simultaneously adsorbs CO and oxygen. This second species of oxygen is thus less reactive with CO, and is formed more extensively as the temperature of oxygen adsorption increases up to 400°C. For convenience we refer to this second species of adsorbed oxygen as Type II oxygen, and to the previously described site as Type I. However, it should be emphasized that the exact character of the sites is not definitively established.

The 2120 cm^{-1} Type II band decreases when the sample is treated with hydrogen at room temperature and is recontacted with CO. At the same time the 2060-80 cm^{-1} Type I band increases, suggesting that hydrogen is capable of reducing some Type II sites to metallic platinum which subsequently adsorbs CO. However, the higher the temperature of oxygen preadsorption, the less reducible the Type II oxygen becomes.

A series of experiments was designed to further investigate the nature of the two oxygen sites. Oxygen was adsorbed on two freshly reduced samples of catalyst I, at room temperature for one sample and 400°C for the other. Subsequently both samples were evacuated at 400°C for 16 hours. The sample that had O_2 adsorbed at room temperature did not show any further O_2 uptake when oxygen was readmitted at room temperature. However, the other sample took up 21.5% of the original O_2 uptake when oxygen was readmitted at 400°C. These results suggest that oxygen may be more easily removed from Type II sites, formed at 400°C, than from Type I sites, which predominate in O_2 adsorption at 25°C. The removal could be either desorption or migration into the metal to form a bulk oxide.

In other experiments CO spectra were recorded of two samples of catalyst I after adsorption of O_2 at 400°C, one after one-half hour evacuation, and the other after a 16 hour evacuation. The spectra, shown in Figure 4.4, again indicate a sizeable decline in Type II sites, but almost no change in Type I sites. Similarly, a spectrum recorded after O_2 adsorption at room temperature followed by 16 hour evacuation at 400°C shows only a slight decrease in the 2075 cm^{-1} peak from the Type I site, and no evidence of a peak at 2120 cm^{-1}.

These results not only suggest that oxygen is removable from Type II sites far more readily than from Type I sites, but also indicate that Type II species are not formed from adsorbed Type I species. Heating in vacuum a sample on which O_2 had been adsorbed at room temperatures to temperatures (400°C) where Type II sites are formed does not generate Type II oxygen. Thus Type II sites may be formed only by contact with gaseous oxygen or, as will be subsequently shown, during cyclic treatment at room temperature with CO and O_2.

4.2.4 Gas Uptakes in Titration Sequences

Table 4.3 shows the results from a number of titration sequences in both directions (*i.e.* O_2-H_2-O_2 and H_2-O_2-H_2). While the trend is

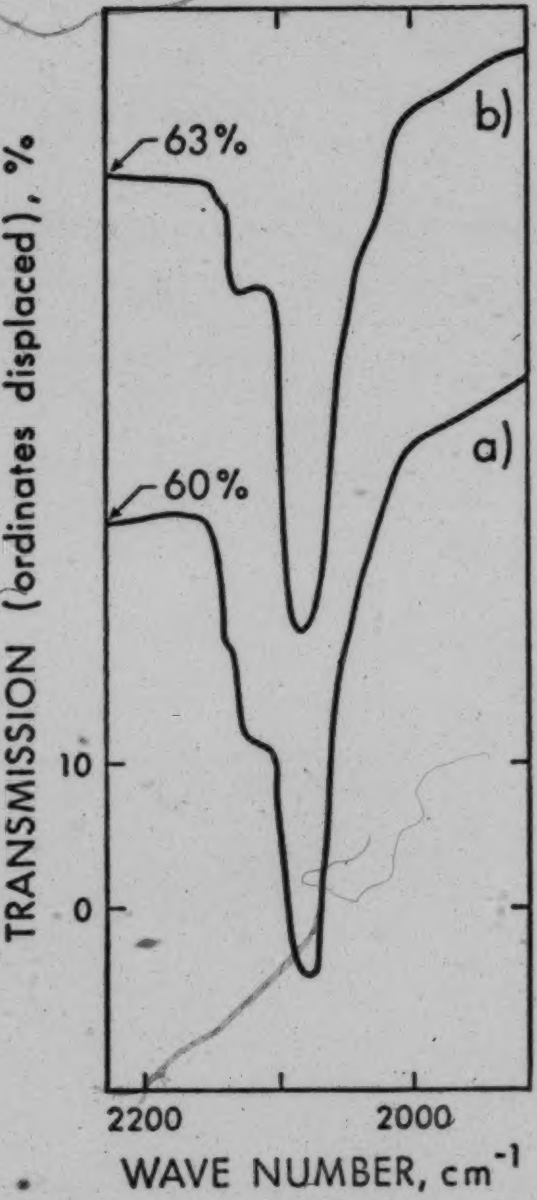

Figure 4.4 Influence of evacuation on the 2060-80 and 2120 cm^{-1} bands. O_2 preadsorbed at 400°C

a) evacuated one-half hour b) evacuated 16 hours.

not universal, it is evident that secondary and tertiary hydrogen uptakes (H2' and H3') are generally higher than the initial hydrogen uptake, while secondary and tertiary oxygen uptakes (O2' and O3') are generally less than or equal to the initial oxygen uptake. (See Table 4.3 for nomenclature.) A survey of other reported titration data [4.2, 4.3, 4.5, 4.13, 4.14] showed that only Wilson and Hall report instances where secondary hydrogen uptake is substantially lower than the initial hydrogen uptake.

Figure 4.5 shows a plot of the post-titration hydrogen enhancement (H2'/H1 or H3'/H1) as a function of the hydrogen uptake to oxygen uptake (H1/O1) ratio. This plot includes the data of Wilson and Hall[4.3, 4.13] and Basset *et al.*[4.5] as well as our own. The data of Gruber[4.14] was excluded because oxygen uptake was measured at a different temperature (350°C) than the hydrogen uptake, and samples were evacuated at 500°C between titrations.

Two interesting observations emerge from inspection of Figure 4.5. First, all of the points from these experiments which show a hydrogen enhancement factor less than unity were recorded at 0°C or were sintered in O_2 before measurement. For all room temperature measurements of non-sintered specimens, secondary and tertiary hydrogen adsorption is higher than the initial hydrogen uptakes. One titration sequence (Run 83) was run in a methanol ice bath (-98°C). The tertiary hydrogen adsorption is only 10% of the initial uptake, which we postulate arises from the fact that generated H_2O freezes and blocks access to the metal surface. The 0°C points similarly may experience some surface blockage, leading to lower enhancement ratios than occur in titrations at room temperature or higher.

Table 4.3: H_2 and O_2 Adsorption and Titration Uptakes

Run	Catalyst	Temperature	H1	O2	H3	O1	H2	O3	H1/O1	H_2 Adsorption Ratios H3' : H2' : H1	O_2 Adsorption Ratios O3' : O2': O1	Comments
----	I	RT	0.73	0.58	1.42	0.31	1.39	0.63	2.36	1.35:1.05:1	0.77:0.68:1	1
----	E	RT	0.60	0.55	1.31	0.35	1.34	0.54	1.71	1.35:1.07:1	0.63:0.71:1	1
----	K	RT	1.08	0.80	1.86	0.36	1.86	0.88	3.00	1.25:1.05:1	0.86:0.72:1	1, 2
83	A	-98°C	0.38	0.35	0.36					0.09:----:1		3
56 & 57	A	0°C	0.22	0.29		0.18	0.58		1.26	1.01:1	0.97:1	
58 & 59	A	0°C	0.23	0.29		0.18	0.60		1.33	1.07:1	0.99:1	
86	A	97°C	0.22	0.36	0.77					1.63:----:1		
87	A	206°C	0.14	0.39	0.81					1.19:----:1		
60 & 61	B	0°C	0.32	0.34		0.20	0.70		1.59	0.95:1	0.92:1	
62 & 63	C	0°C	0.27	0.32		0.20	0.57		1.37	0.63:1	0.90:1	
64 & 65	D	0°C	0.09	0.12		0.08	0.25		1.11	0.92:1	0.88:1	
79 & 80	E	RT	0.37	0.42	0.90	0.26	0.91	0.42	1.42	1.17:1.09:1	0.86:0.90:1	
81 & 82	F	RT	0.39	0.46	0.96	0.25	0.96	0.48	1.53	1.09:1.17:1	1.01:1.07:1	
104 & 105	F	RT	0.30	1.34	0.77	0.16			1.90	1.30:----:1	1.21:1	4
106	F	RT	0.36	0.43	0.86					1.01:----:1		
90 & 90a	G	RT	0.40	0.61	1.32	0.27	1.10	0.64	1.49	1.25:1.40:1	1.51:1.52:1	5
77	H	RT	0.16	0.46	0.97							
70 & 71	J	0°C	0.28	0.26		0.12	0.48		2.28	0.87:1	1.01:1	
74 & 74a	J	RT	0.22	0.22	0.46	0.12	0.46		1.84	1.10:1.04:1	0.93:1	
75	J	RT	0.22	0.22	0.44					1.06:----:1		6

Table 4.3 (continued)

Nomenclature:

HX and OX are measured H_2 and O_2 uptakes in gas atoms per Pt atom for step 'X' in the titration sequence, e.g., for the series H_2-O_2-H_2-O_2 the corresponding uptakes are H1, O2, H3, and O4, for the series O_2-H_2-O_2-H_2 the uptakes are O1, H2, O3, and H4. HX' and OX' are the H_2 and O_2 adsorption uptakes for step 'X' calculated from the measured total uptakes.

Comments:

1. Data obtained in static system; all other results are from flow system.
2. Evacuated at 500°C for 6 hours prior to adsorption measurements.
3. Results not included in Figure 4.5 and 4.6.
5. Catalyst charge (3g) wetted by injecting 0.5 cc of degassed H_2O into the carrier gas after pretreatment and prior to adsorption measurements.
6. Run 34 extended for 14 (O_2-H_2) cycles (Results shown in Figure 4.7).

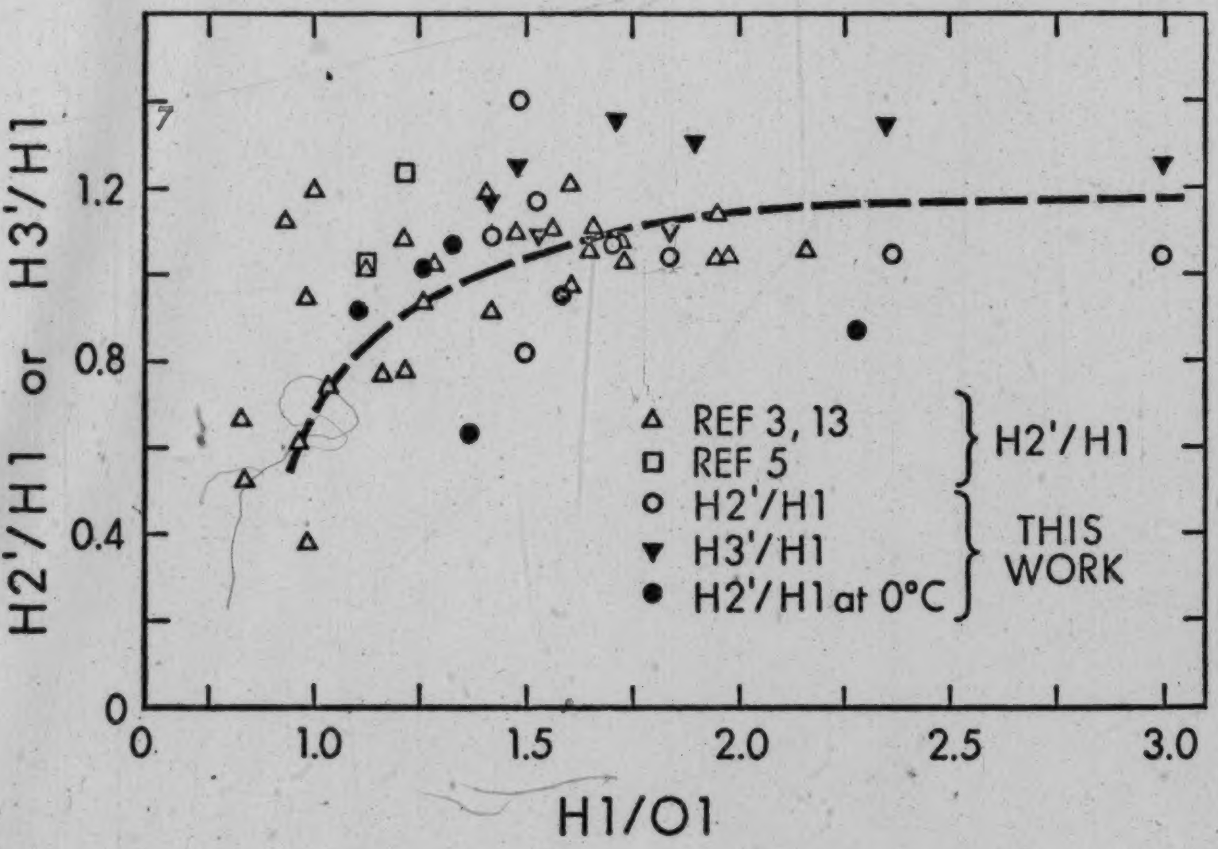

Figure 4.5 Hydrogen enhancement ratio (H3/H1 or H2/H1) as a function of the ratio of initial hydrogen uptake to initial oxygen uptake (H1/O1).

Second, Wilson and Hall's data reveals cases where low enhancement factors are observed. All of these points occur where the initial hydrogen uptake is less than about 1.3 times the initial oxygen uptake. Finally, a check of Wilson and Hall's pretreatment conditions indicates that all their points showing enhancement ratios less than unity had been exposed to air or hydrogen at temperatures of 545°C or higher, with most treated at temperatures greater than 600°C. Thus from Figure 4.5 the trend is evident that catalysts which have initial hydrogen uptakes greater than about 1.3 times the initial oxygen uptakes tend to show enhancement of hydrogen adsorption after one or two titrations, particularly at room temperatures and higher.

Figure 4.6 shows a plot of the ratio of initial hydrogen uptake to initial oxygen uptake (H1/O1) versus the catalyst dispersion as measured by hydrogen uptake (H1). Again, the data of Wilson and Hall [4.3, 4.13] and Basset *et al.*[4.5] are included. While considerable scatter is evident in the data, a trend to a higher H/O ratio with increasing dispersion (smaller particle size) is evident. Thus, as Wilson and Hall suggest, chemisorption data supports a variable stoichiometry, with hydrogen and oxygen uptakes being about the same only on larger platinum crystallites.

4.2.5 Long Titration Sequence

One experiment (Run 75) on catalyst J was extended for a total of 14 (O_2-H_2) titration sequences. Figure 4.7 shows the resulting uptakes of titered oxygen and hydrogen, as well as the ratio of hydrogen uptake to oxygen uptake for each step. The final HT/OT ratio does not approach 2.0 as predicted by stoichiometric considerations,

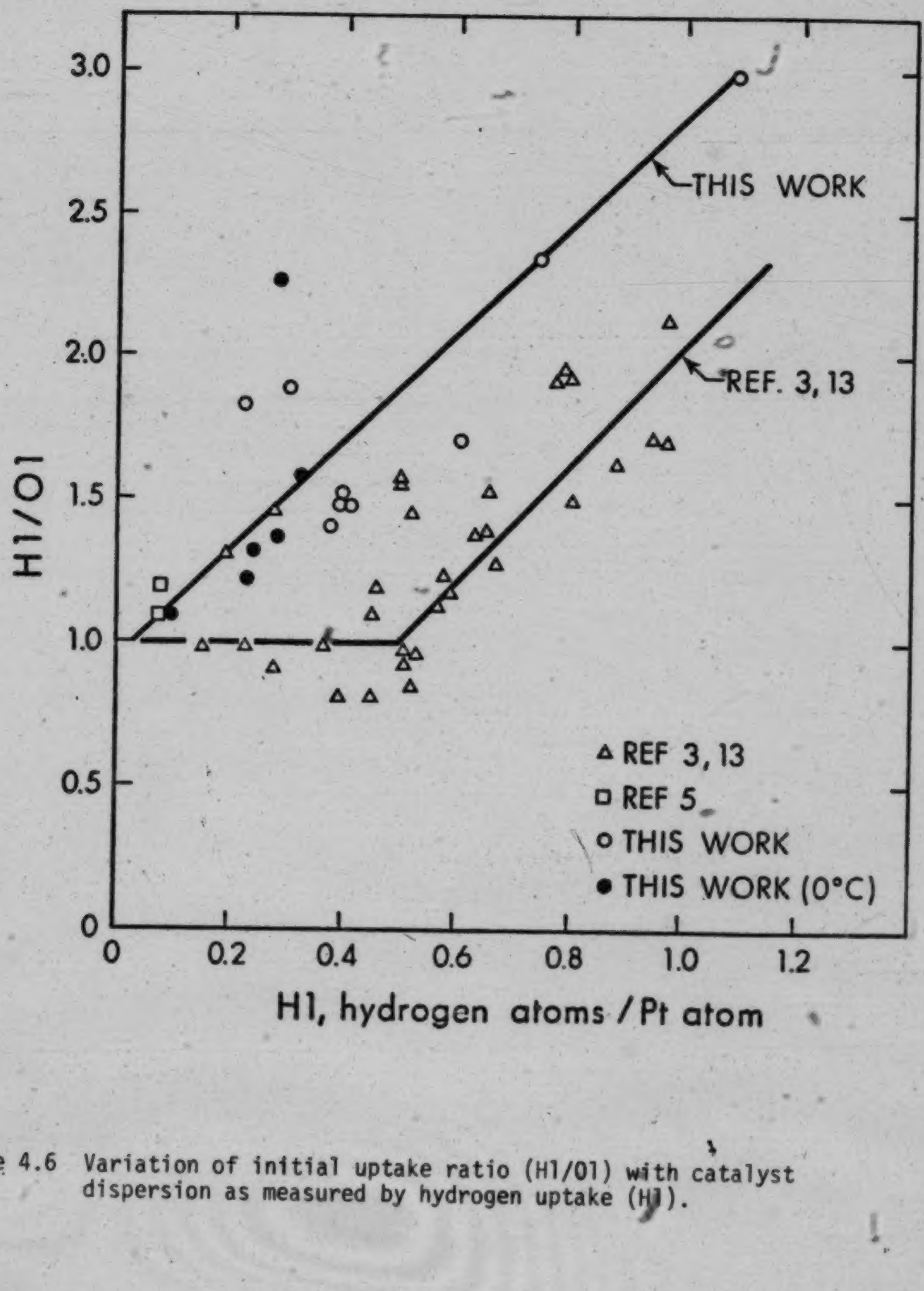

Figure 4.6 Variation of initial uptake ratio (H1/O1) with catalyst dispersion as measured by hydrogen uptake (H1).

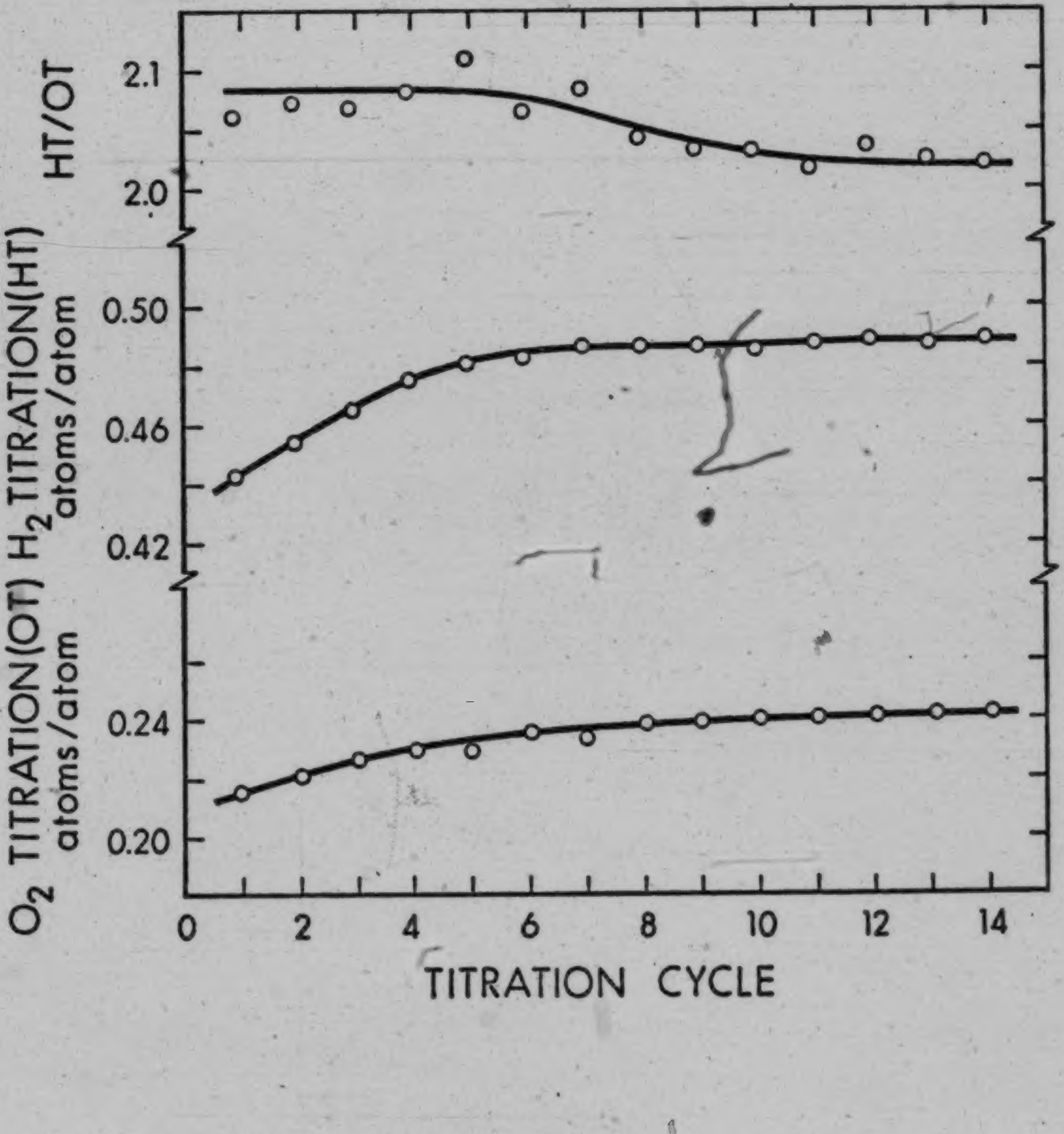

Figure 4.7 Long term titration: plot of
a) oxygen titer uptake b) hydrogen titer uptake, and
c) the ratio HT/OT for each titration cycle.

but rather is asymptotic to about 2.02. This 1% factor could well arise from the failure of the flow system to detect a small portion of the hydrogen which is reversibly adsorbed and "bleeds" off. However, it is evident that hydrogen adsorption enhancement continues through the first 8 titration sequences, and thus this effect is not restricted only to the first titrations.

4.2.6 IR Spectra of CO Adsorbed on Pt After Repeated Sequences of (O_2-CO) and (O_2-H_2) Treatments

a) (O_2-CO) cycles

Oxygen (100 torr) and carbon monoxide (100 torr) were cyclically introduced, at room temperature with evacuation for one-half hour between cycles, to catalyst I, and IR spectra were recorded after each addition. Figure 4.8 shows some of the recorded spectra.

After the second CO adsorption the 2070-75 cm^{-1} band reached a maximum, and subsequent (O_2-CO) sequences caused this band to decrease in intensity. On the other hand, the 2120 cm^{-1} band increased with cyclic treatment. Thus repeated (CO-O_2) treatments generate increasing amounts of Type II surface adsorbed oxygen, which is not reduced by the next CO titer.

When freshly reduced catalyst I was contacted for 17 hours with oxygen at room temperature, subsequent CO treatment did not generate the 2120 cm^{-1} Type II oxygen band. Thus it is the cyclic treatment with CO which promotes the formation of the Type II site, rather than the time of contacting with O_2. When hydrogen was introduced at room temperature to a cyclically treated catalyst, the 2120 cm^{-1} band decreased but was not totally reduced. The 2070-75 cm^{-1} band shifted

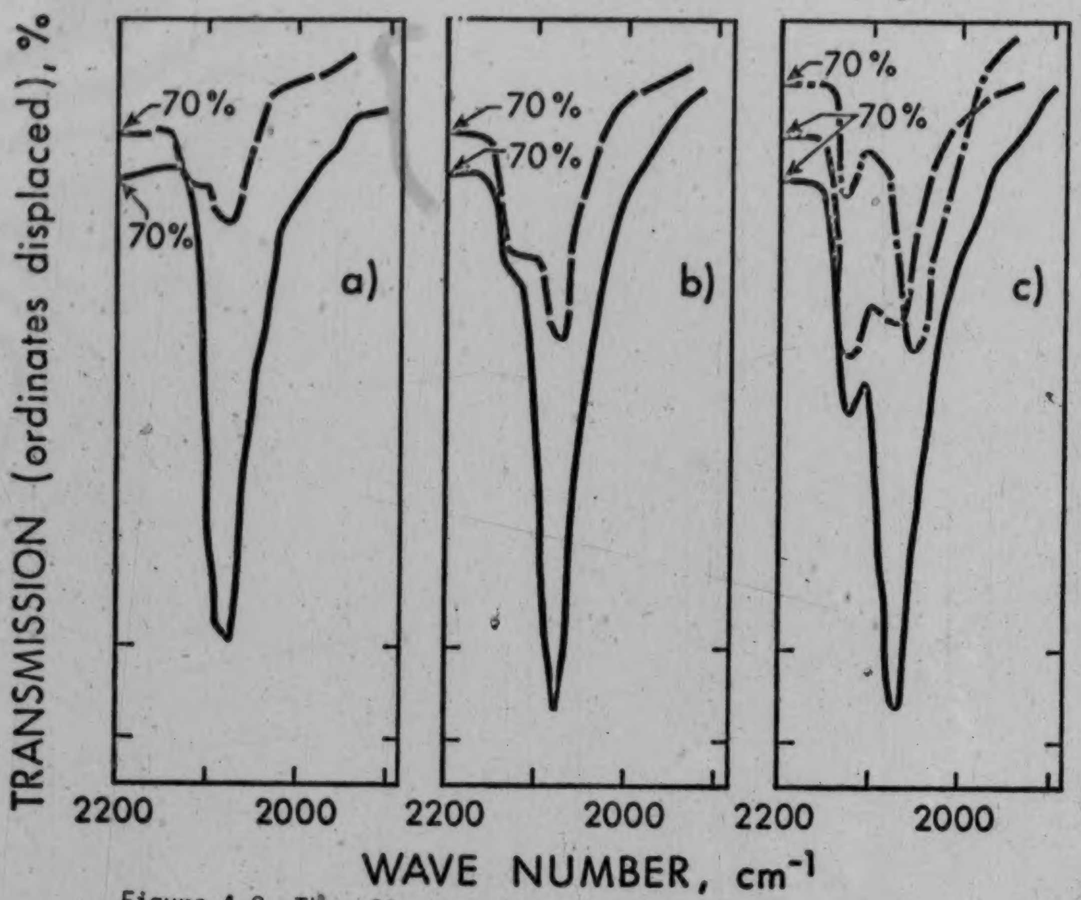

Figure 4.8 The effect of (CO-O_2) cyclic treatment:

a) 1st cycle b) 3rd cycle c) 6th cycle.

(— CO adsorption; - - - O_2 treatment; —· —· —· H_2 treatment) to lower frequency ($\Delta\nu$=20 cm^{-1}).

b) (O_2-H_2) cycles

In these experiments fresh catalyst was contacted with oxygen, then hydrogen, and then CO was introduced to the cell and the spectra recorded. Typical results are shown in Figure 4.9. As found by Darensbourg and Eischens[4.6], the 2070-75 cm^{-1} band is enhanced by subsequent treatments. In addition, we observed the band to shift to 2060 cm^{-1} ($\Delta\upsilon$=15 cm^{-1}). This shift is almost identical to the shift observed by Primet *et al.*[4.8] when water was added to their CO adsorption system. We thus tentatively ascribe the shift to a modification of adsorbed CO electronic properties arising from the H_2O generated during titration.

Evidence of H-O-H bending, in the 1630 cm^{-1} band shown in Figure 4.9, further demonstrates the presence of water. Also, absorption in the 3500-3800 cm^{-1} region, due to alumina OH groups, increased with increasing number of O_2-H_2 cycles, indicating that some of the generated H_2O was being taken up by the alumina.

The 1835 cm^{-1} band was enhanced by repeated O_2-H_2 cycles, as shown in Figure 4.9. This was not observed in the cyclic O_2-CO treatment. The most outstanding difference, however, between the two treatments is that the 2120 cm^{-1} band, attributed to Type II oxygen, was not detected in the cyclic (O_2-H_2) treatment, even after six cycles.

4.3 The Origin of the Enhancement Effect

Enhancement of hydrogen uptake following titration is demonstrated by the results in Table 4.3 and Figure 4.5. It may be argued that this apparent increase is due to incomplete H_2 desorption during the

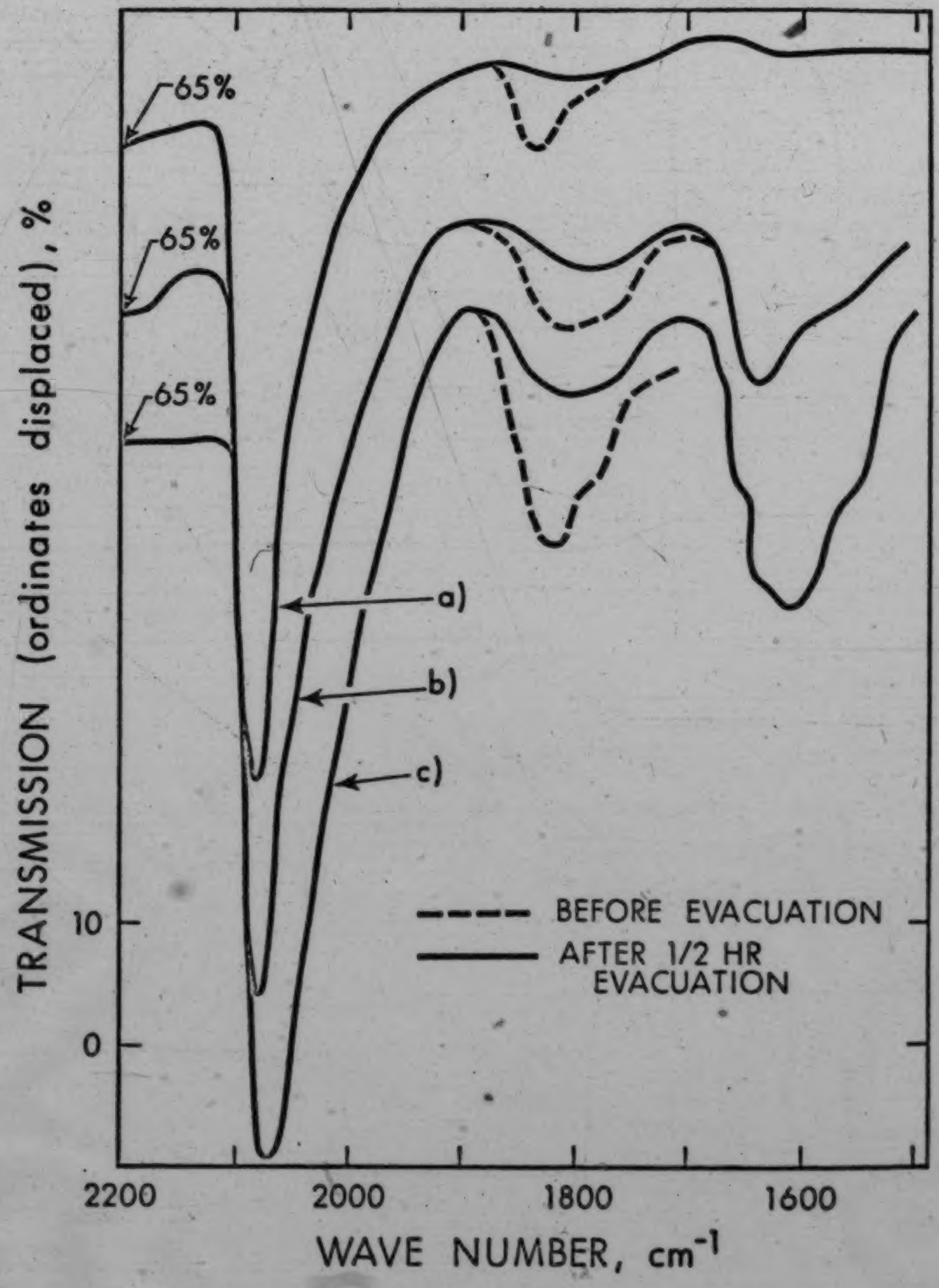

Figure 4.9 The effect of (O_2-H_2) cyclic treatment:
a) CO adsorption on the reduced catalyst b) after 1st cycle c) after 5th cycle.

relatively short degassing periods after reduction (1 to 2 hours at 500°C). However, an absolute measure of enhancement or retardation, independent of initial surface hydrogen coverage, can be calculated, as shown in equations 4.5 to 4.10.

$$\mathrm{Pt{-}H_x} \xrightarrow{\frac{H1}{2}\,H_2} \mathrm{Pt{-}H_a} \xrightarrow{\frac{O2}{2}\,O_2} \underset{+\frac{a}{2}\,H_2O}{\mathrm{Pt{-}O_b}} \xrightarrow{\frac{H3}{2}\,H_2} \underset{+b\,H_2O}{\mathrm{Pt{-}H_c}} \tag{4.5}$$

$$\mathrm{Pt{-}H_x} \xrightarrow{\frac{O1}{2}\,O_2} \underset{+\frac{x}{2}\,H_2O}{\mathrm{Pt{-}O_d}} \xrightarrow{\frac{H2}{2}\,H_2} \underset{+d\,H_2O}{\mathrm{Pt{-}H_e}} \xrightarrow{\frac{O3}{2}\,O_2} \underset{+\frac{e}{2}\,H_2O}{\mathrm{Pt{-}O_f}} \tag{4.6}$$

where 'x' is the number of H_2 atoms remaining on the platinum per platinum atom after evacuation, and 'a', 'b', 'c', 'd', 'e', and 'f' are the number of hydrogen or oxygen atoms adsorbed per platinum atom at various stages in the titration sequences. (All stoichiometric coefficients in these equations are expressed in terms of *total* metal atoms, hence they are not an absolute surface stoichiometry.) The absolute enhancement in H_2 adsorption is given by (c-a) and (e-a). According to Equation 4.5

$$(c-a) = H3 - 2(O2) \tag{4.7}$$

and from Equations 4.5 and 4.6

$$(e-a) = H2 - 2(O1) - H1 \tag{4.8}$$

Similarly, the retardation of O_2 adsorption is given by

$$(d-f) = \frac{H2}{2} - O3 \tag{4.9}$$

and

$$(d-b) = O1 + \frac{H1}{2} - O2 \tag{4.10}$$

The values of (c-a), (e-a), (d-f) and (d-b) obtained from our data are tabulated in Table 4.4. The results indicate a general enhancement of H_2 uptakes during titration and a retardation of O_2 uptakes. Thus the variation in adsorption stoichiometry which we observed during titration is not attributable to insufficient degassing.

Darensbourg and Eischens[4.6] noted H_2 enhancement in their IR studies of supported Pt catalysts, and attribute it to an increase in metal surface area arising from the room temperature reduction of the adsorbed oxygen. In examining our results, we have considered this hypothesis and others: the creation of different species of surface oxygen, as occurs during repeated (CO-O_2) treatments, and an influence from the water generated during titration.

The primary difficulty with an interpretation of increased surface area following titration is that it fails to explain the retardation or lack of enhancement of oxygen uptake noted during titration. In some cases the reduction in O_2 uptake exceeded 35% on the second titer (O3') and 30% on the first titer (O2'). It is difficult to conceive of an alternate increase in surface area during a hydrogen titration, followed by a decrease in surface during an oxygen titer. For this reason we conclude that a simple physical size explanation for hydrogen enhancement is not satisfactory.

It is evident from the IR results that the two CO bands may be correlated with two different oxygen adsorption sites. The Type II site associated with the 2120 cm^{-1} band appears after high temperature adsorption of oxygen, but is also generated during room temperature repeated (O_2-CO) treatment. Once formed, this Type II site is not totally reducible by hydrogen at room temperature. (Total reduction is observed

Table 4.4: Hydrogen Enhancement and Oxygen Retardation During Titration

Run	Temperature	H_2 enhancement		O_2 retardation	
		H atoms / Pt atom		O atoms / Pt atom	
		(c-a)	(e-a)	(d-f)	(d-b)
---	R.T.	0.26	0.04	0.07	0.10
---	R.T.	0.21	0.04	0.13	0.10
---	R.T.	0.26	0.06	0.05	0.10
83	-98°C	-0.34			
56 & 57	0°C		0.03		0.005
58 & 59	0°C		0.02		0.001
86	+97°C		0.04		
87	+206°C		0.02		
60 & 61	0°C		-0.02		0.02
62 & 63	0°C		-0.06		0.02
64 & 65	0°C		-0.01		0.01
79 & 80	R.T.	0.06	0.02	0.04	0.03
81 & 82	R.T.	0.03	0.07	-0.002	-0.02
104 & 105	R.T.	0.09			
106	R.T.	0.005			
90 & 90a	R.T.	0.10	0.16	-0.09	-0.14
77	R.T.	0.05			
70 & 71	0°C		-0.04		
74 & 74a	R.T.	0.02	0.01		0.01
75	R.T.	0.01			

at 150°C). However, the Type II sites decrease substantially during high temperature evacuation, while Type I sites do not.

Given these results for (O_2-CO) treatment, we speculated that cyclical (O_2-H_2) treatment at room temperature might similarly generate the second type of oxygen site. If these sites could still adsorb hydrogen, then enhanced hydrogen and retarded oxygen uptakes could be explained. However, CO adsorption after repeated (O_2-H_2) treatments gave no evidence of the 2120 cm^{-1} band. We therefore do conclude that Type II sites are not generated during titration sequences. This does not, of course, imply that other surface complexes may not be formed which account for the H_2 enhancement/O_2 retardation effect.

Another factor to be considered in titration anomalies is the effect of the water generated. The results presented in Tables 4.3 and 4.4 indicate that at temperatures of 0°C and below both H_2 and O_2 adsorption may be retarded. This may be due to incomplete reaction during titration and/or blockage of the Pt surface by H_2O. At room temperature and above H_2 adsorption is enhanced and O_2 adsorption is retarded. This may be caused by an alteration of the Al_2O_3/Pt interaction due to the H_2O/Al_2O_3 interaction in the vicinity of Pt crystallites. From IR evidence we concluded that some of the water is taken up by the support. However, the water affects CO adsorbed on Pt sufficiently to generate a shift in the 2075 cm^{-1} band, also observed by Primet *et al.*[4.8]. This indicates a change in the electronic properties of the platinum.

The changes in H_2 and O_2 adsorption uptakes are much more marked for the static results than for the dynamic ones. The presence of the carrier gas in the dynamic measurements may facilitate the movement of water from the Pt surfaces to areas of the support sufficiently removed from the Pt crystallites so as to reduce the effect of water on subsequent adsorptions.

It is impossible to duplicate post-titration wetting conditions by addition of H_2O to a fresh catalyst, because during titration water is generated only at the platinum crystallite locations. However, one experiment (Runs 104 and 105) was made on catalyst F in which a 3.1 g catalyst charge was wetted by one-half cc of degassed distilled H_2O. While this major dose of water caused both initial hydrogen and intial oxygen uptakes to decrease, the oxygen decrease (37%) was greater than the hydrogen decrease (20%). Thus for the wetted catalyst, the H1/O1 ratio was 1.90, compared to 1.53 for the dry sample, again indicating that wetting more greatly retarded oxygen uptake. While this single result is by no means conclusive, it suggests that investigation of the effect of wetting on gas uptakes warrants further investigation.

It is easy to postulate an influence of crystallite size on the effect of H_2O on gas uptakes. Primet *et al.*[4.8] attributed the shift of the 2075 cm^{-1} band in CO adsorption on a wetted catalyst to the electronic donation from the water to the platinum crystallite. Both Wilson and Hall[4.3] and Boudart and Dalla Betta[4.4] have cited the relative electron deficiency of small platinum crystallites in explaining oxygen uptake differences among catalysts of varying dispersion. If the water does act as an electron donor, it could affect the smaller crystallites more significantly than the larger ones. Thus the mechanism of uptake enhancement/retardation may be electronic, rather than physical blocking of the surface sites as cited for the -98°C results.

The other interesting point to emerge from this study is a dependence of the relative uptakes of hydrogen and oxygen, as measured by the ratio H1/O1, on the dispersion. Wilson and Hall[4.3] first noted this in accounting for the discrepancy between Benson and Boudart's[4.1] and Mears and Hansford's[4.2] titration stoichiometries. In Figure 4.5, it is evident that Wilson and Hall's data predict the start of a deviation between hydrogen and oxygen uptakes as the dispersion measured by H_2 adsorption exceeds about 0.3. Our data and that of Basset *et al.*[4.5] indicate that hydrogen and oxygen uptakes differ over the entire dispersion range. This discrepancy may well be attributable to Wilson and Hall's generally more severe pretreatment conditions.

Wilson and Hall used particle size distribution analysis of electron micrographs to attribute the deviation of hydrogen and oxygen uptakes in small particles to Pt_2O_{surf} stoichiometry on small platinum particles. They argued that evidence points to an H/Pt_{surf} ratio of unity regardless of metal particle size. Dalla Betta and Boudart[4.4] also conclude that oxygen uptake on small particles is less than 1 oxygen per surface metal atom, based on calculations of the size of particles in the cages in a Y zeolite. In our experiments we did not attempt to independently determine hydrogen and oxygen adsorption stoichiometries through separate measurement of crystallite size. Rather, we only note the influence of dispersion, and hence particle size, on the relative uptakes of the two gases.

4.4 Conclusions

Titration of adsorbed hydrogen and oxygen on supported platinum catalyst generally results in enhanced post-titration adsorbed hydrogen values, and reduced post-titration adsorbed oxygen values. The enhancement occurs over a variety of catalyst loadings and temperatures, and is correlated with the ratio of initial hydrogen and oxygen uptakes, decreasing as H1/O1 approaches unity.

Explanation of the enhancement through modified surface areas, according to Darensbourg and Eischens[4.6], does not satisfactorily account for a reduced oxygen uptake. Explanation through the formation of Type II oxygen sites, as occurs in the (O_2-CO) reaction is also unsatisfactory since there is no evidence of Type II sites in O_2-H_2 titration sequences. The addition of H_2O to catalysts appears to retard subsequent oxygen uptake more than hydrogen uptake. More experimentation is necessary to confirm whether the water generated during titration is the key factor in enhancement.

Type II sites associated with the 2120 cm^{-1} band are formed during O_2 adsorption at elevated temperatures, and during repeated (O_2-CO) treatments at room temperature. They are not formed by room temperature O_2 adsorption or by repeated (H_2-O_2) treatments. Once formed, the sites are not completely reducible by hydrogen at room temperature but do disappear in H_2 at 150°C. The sites are not formed from Type I adsorbed oxygen, even after *in vacuo* heating of Type I adsorbed oxygen.

The ratio of initial hydrogen uptake to initial oxygen uptake on supported platinum catalysts depends upon the dispersion of the catalyst. Relative to oxygen, hydrogen uptake increases with the metal dispersion.

4.5 References

4.1 Benson, J.E., and Boudart, M., J. Catal. 4, 704 (1965).

4.2 Mears, D.E., and Hansford, R.C., J. Catal. 9, 125 (1967).

4.3 Wilson, G.R., and Hall, W.K., J. Catal. 17, 190 (1970).

4.4 Dalla Betta, R.A., and Boudart, M., Proc. V Int. Cong. Catal, 1972, North-Holland, 2, 96 - 1329.

4.5 Basset, J.M., Theolier, A., Primet, M., and Prettre, M., Proc, V Int. Cong. Catal, 1972, North-Holland, 2, 63 - 915.

4.6 Darensbourg, D.J., and Eischens, R.P., Proc. V. Int. Cong. of Catal., 1972, North-Holland, 1, 21 - 371.

4.7 Heyne, H., and Tompkins, F.C., Trans. Farad. Soc. 63, 1274 (1967).

4.8 Primet, M., Basset, J.M., Mathieu, M.V., and Prettre, M., J. Catal. 29, 213 (1973).

4.9 Freel, J., J. Catal. 25, 139 (1972).

4.10 Meyer, F.R., and Ronge, G., Angew. Chem. 52, 637 (1939).

4.11 Parkyns, N.D., J. Chem. Soc. (A), 410 (1969).

4.12 Eischens, R.P., and Pliskin, W.A., Advan. Catal. and Relat. Subj. 10, 1 (1958).

4.13 Wilson, G.R., and Hall, W.K., J. Catal. 24, 306 (1972).

4.14 Gruber, M.L., J. Phys. Chem. 66, 48 (1962).

CHAPTER 5

A MODEL OF SUPPORTED METAL CATALYST SINTERING

5.1 Survey

The overall process resulting in a change in metal dispersion of supported metal catalysts during use or treatment at elevated temperatures is called sintering. Since, in general, sintering results in a loss of catalytic activity, an understanding of the processes occurring during sintering is of importance in the design of catalysts with improved stability. Unfortunately, there is insufficient direct evidence to establish the mechanism of supported metal catalyst sintering.

Ruckenstein and Pulvermacher[5.1, 5.2] have carried out a detailed analysis of the sintering process by means of a model which envisages the sintering process as a migration of metal particles over the support surface, followed by the fusion of metal crystallites upon collision. Their results showed that the rate of metal surface area change is given by an equation of the form

$$\frac{dS}{dt} = -KS^{n} \qquad 5.1$$

where the value of n varies between 2 and 8, depending on whether the rate of fusion (particle sintering) or the rate of surface diffusion of metal crystallites is rate controlling. Recently, Wynblatt and Gjostein[5.3] in their sintering studies of supported Pt found the value of n to be $\simeq$13. They proposed an equation, based on the concept of a nucleation barrier, to explain this large value of n. In their formulation, the resulting equation being somewhat similar to that of

Somorjai[5.4], the constant K in equation 5.1 decreases exponentially with increasing average particle radius, r, *i.e.*

$$K = B \exp(-Ar/RT) \qquad 5.2$$

Wynblatt and Gjostein did not compare the predictions with experiment, but planned to pursue this in the future.

The model of Ruckenstein and Pulvermacher[5.1, 5.2], besides being unable to account for the above mentioned large value of n, encounters other difficulties in being unable to explain some of the experimental observations made during sintering studies. These include:

1. Under certain conditions, generally in an oxidizing atmosphere, metal dispersion increases during high temperature treatment[5.5-5.8]. A simple crystallite diffusion model of sintering process cannot account for increases in metal surface area, although Ruckenstein and Pulvermacher propose to discuss crystallite separation in a future work.
2. The high activation energies observed for the sintering process, up to 70 kcal/gmole for Pt on Al_2O_3[5.9], are difficult to account for on the basis of the fusion of two adjacent metal crystallites. (Ruckenstein and Pulvermacher do not quantitatively discuss the activation energies of crystallite surface diffusion and particle sintering.)
3. The continued growth of metal particles to the extent that the metal particle size is of the order of the support particle size is difficult to explain on the basis of metal crystallite migration. Figure 5.1 illustrates this from electron micrographs of catalyst treated in this laboratory. The specimen is an impregnated 4.76% Pt on Alon alumina catalyst. The support consists

Figure 5.1: Electron micrographs of 4.76% Pt on Alon alumina after various pretreatments, showing formation of large Pt crystallites.

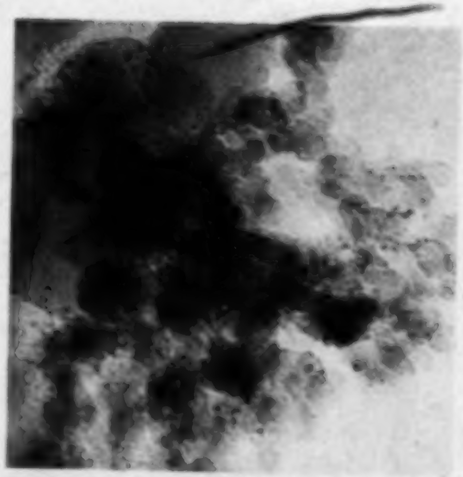

Unreduced

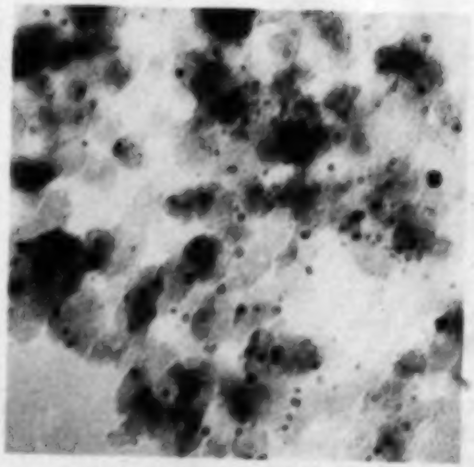

Reduced at 250 °C

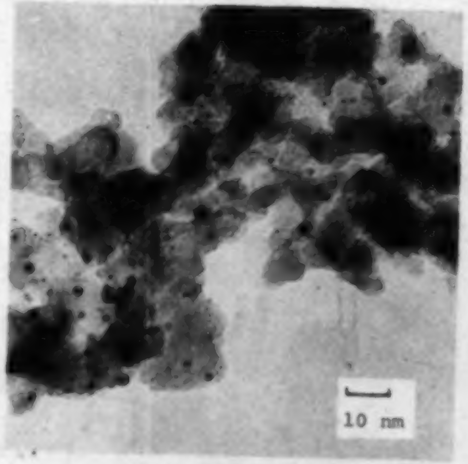

Heated in O_2 at 500 °C

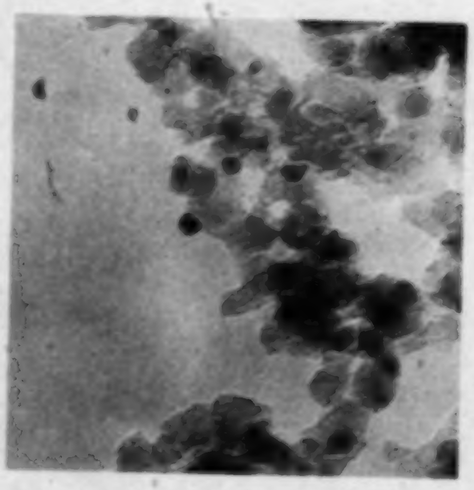

Heated in O_2 at 550 °C

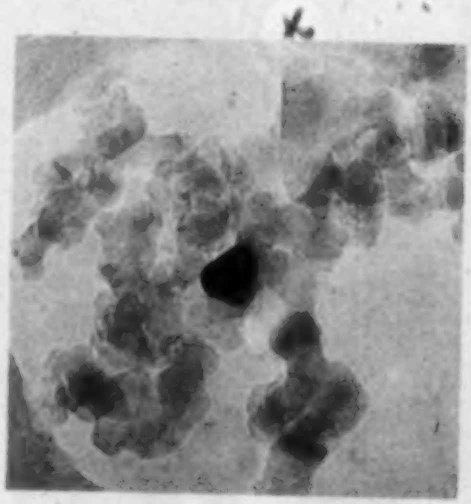

Heated in O_2 at 600 °C

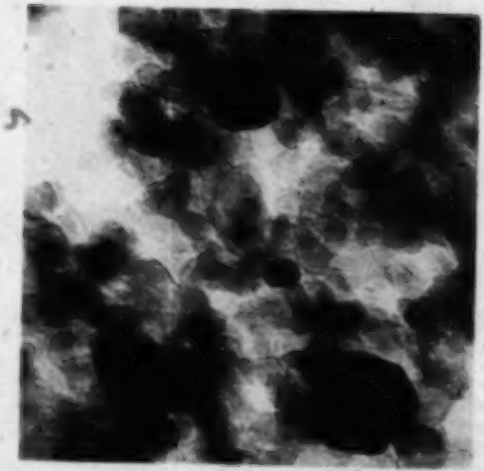

Heated in O_2 at 700 °C

of 10 to 30 nm discrete alumina particles which agglomerate upon wetting. The various micrographs show platinum particle sizes after impregnation, after reduction in hydrogen in mild conditions (250°C), and after 16 hr treatment in an O_2 atmosphere with temperatures ranging from 500 to 700°C.

It is evident that the platinum continues to grow in size on the Alon support even when it reaches 30 nm particle sizes, exceeding the average size of the particles in the support. The occurrence of this growth by crystallite transport over long distances of the irregular support, by diffusion from one Alon particle to the next, seems highly unlikely. A transfer of atomic or molecular metal species, either across the bridge where the support particles contact or through desorption, vapor phase transport, and readsorption, seems a far more plausible hypothesis for the formation of these large particles.

4. Despite the frequent citing of crystallite migration as a sintering mechanism (*e.g.*[5.1, 5.2, 5.10, 5.11 5.12]), there is little concrete evidence of motion over the appreciable distances needed to account for sintering of supported metal catalysts. For example, in *in situ* film growth studies by transmission electron microscopy Pashley *et al.*[5.13] observed small reorientations, such as rotations of the order of 1°, when particles merged. However, they did not report significant crystallite motion. Phillips *et al.*[5.12] cite crystallite diffusion in interpreting their electron micrographs. However, the authors were not able to describe their observations by their proposed model. In particular, Figures 1 and 2 of reference [5.12] are odd in that larger particles (~100 nm)

appear to move more rapidly than smaller particles (~5 nm).

Wynblatt and Gjostein[5.14] observed minimal migration, less than 10 nm in 16 hours at 1000°C in a hydrogen atmosphere, for Pt particles of an average size of 7.5 nm on an Al_2O_3 substrate. They conclude that particle migration is too slow a process for particle sizes greater than 5 nm to account for observed sintering rates. Geus' review[5.10] makes it evident that most evidence of substantial crystallite motion is inferential.

It should be noted that the conditions in which crystallite diffusion is cited as a mechanism in film growth are drastically different from those in typical supported metal catalyst sintering studies: first, temperatures are generally 200 to 500°C lower in film growth studies; second, coverage of the support is typically about 0.1 to 0.5 in film growth studies, while typical catalysts have about 10^{-3} times that coverage of support by metal; and finally, typical film growth supports are smooth, often cleaved planes, while typical catalyst supports are polycrystalline and highly irregular. Thus even if definitive evidence of crystallite diffusion at film growth conditions is obtained, the translation of this mechanism to supported metal catalyst sintering would not necessarily follow.

In light of these difficulties in interpreting experimental evidence of sintering via the model of diffusing crystallites, we have looked to alternate mechanisms to account for the sintering phenomenon. In this chapter a model for the sintering of supported metal catalysts is developed based on individual metal atoms leaving the metal crystallites, migrating over the support and being captured by metal crystallites upon collision. This approach is by no means devoid of conceptual difficulties, but it can account for a variety of experimental observations of sintering.

5.2 Proposed Model

The mechanism of supported metal catalyst sintering in the proposed model is postulated to consist of three steps: one, individual metal atoms (or molecules such as PtO in an oxygen atmosphere) move from the metal crystallite to the surface of the support; two, the metal atoms migrate over the support surface; and three, the migrating atoms are either captured by collision with a metal crystallite or are immobilized by a drop in temperature or by encountering an energy well on the support surface. Each of these three steps will be discussed in detail.

5.2.1 Escape of Metal Atoms from Crystallites

Previous workers considering metal migration and particle agglomeration have generally discounted the possibility of loss of individual atoms, due to the large activation energy, E_a, that this step would require. The heat of sublimation of platinum, for example, is 135 kcal/gmole[5.15]. Arguing by extension from measurements on other metals, Geus[5.10] estimated the dissociation of a pair of Pt atoms to be about 65 kcal/gmole. Thus most investigators of nucleation effects (*e.g.* ref.[5.10-5.13, 5.16-5.19]) have concluded that for metals such as Bi, Au, Ag, Pt, etc. the dissociation of atoms from clusters of larger than a few atoms is neglectably small. Similarly, the forces between particle and support are presumed to be van der Waals type only, so that heat of adsorption, H_a, of single metal atoms is taken to be less than 20 kcal/gmole.

Supported metal catalyst sintering is generally observed at temperatures of 800 - 1000°K, which is higher than typical nucleation study temperatures of 500 - 600°K. At these temperatures, an activation energy of less than 60 to 75 kcal/gmole is necessary if a process is to occur with a significant rate. Thus the large sublimation energy and presumed low interaction of metal with support appear on first glance to rule out escape of metal atoms to the support surface from metal crystallites as a plausible mechanism.

However, Geus' extensive review[5.10] of data observed in metal film formation studies indicates that several factors may substantially increase the interaction between metal and support surface. In advancing this model we suggest that localized metal-support interactions are sufficiently large to reduce the net energy difference between an atom in the crystallite and an atom on the surface to the required value less than 75 kcal/gmole.

The presence of oxygen has been reported by many authors to significantly increase the interaction of metal crystals and oxide supports[5.10]. Formation of a metal oxide layer at the support surface is believed to result in a strong chemical interaction, thought to involve metal incorporation in the support structure. For nickel, iron, chromium and titanium ageing in air at room temperature has been observed to substantially increase the adherence of metal particles on films. This type of strong interaction between metal and support, not necessarily reversible by reduction, could readily enhance removal of a metal atom from the particle to the surface. (In certain atmospheres the escaping metal species would presumably be molecular rather than atomic.)

A second factor explored by Geus[5.10] which increases localized metal-support interaction is the presence of defects in the support structure. The well known decorating effect, where crystals are seen to nucleate in the region around defects, is attributed to the favorable energetics of adatom adsorption in these regions. Thus again metal escape from particle to support surface can be enhanced in localized regions by the presence of defects.

Finally, Geus[5.10] reviews evidence that impurities on the support surface increase the interaction of metal and support. The presence of cracking products of hydrocarbons or of carbon has been found to increase the localized adatom population. The role of such impurities in serving as a bridge for the "spillover" of adsorbed gases from metal to surface has been discussed[5.20]. By increasing metal-support interaction, such impurities may also help to bridge the spillover of metal atoms to the support.

These arguments for loss of metal atoms to the support surface are admittedly tenuous. However, they point to an interaction far more complex than the van der Waals forces cited in ruling out the possibility of particle dissociation. Because of the large heat of condensation of metals, and their ready mobility on support surfaces, no direct measurement of the heat of adsorption of Pt on typical supports is possible[5.10]. Phillips *et al.*[5.12] found that an H_a of 35 kcal/gmole for Au on SiO was required to explain their results in terms of their particle migration model. Tabatadze *et al.*[5.21] measured the conductance of metal oxides during the adsorption of noble metals. They observed large changes in conductance as long as metal atoms were supplied to the oxide surface. Their results indicate a strong electronic interaction of single metal atoms with the oxide surfaces which disappears once these atoms aggregate to form metal crystallites. This indirect evidence supports conclusions from nucleation and film growth studies that forces other than van der Waals are involved in the adsorption of metal atoms on oxide surfaces.

The reduction in surface energy is the driving force for the transfer of metal from smaller to larger crystallites. We are interested in obtaining an approximate relationship for the rate of loss of metal atoms from a crystallite to the support as a function of crystallite size. The Kelvin equation relates the spreading pressure, ϕ, to the crystallite radius, r, by

$$\phi = \phi_0 \exp(\beta/r) \qquad 5.3$$

where the value of β depends on the shape of the crystallite, the metal-support contact angle, the metal-support and metal-vapor interfacial energies, the metal molar volume, and the temperature. For a specific support/metal system, at a constant temperature, the value of β should be relatively constant.

At equilibrium the rate at which a crystallite captures atoms is proportional to $r\phi$, and therefore the rate of atom loss, $\frac{dL_i}{dt}$, is also proportional to $r\phi$. The rate of loss is independent of whether or not the system is in equilibrium if energy transfer is not controlling. Hence the ratio of the rates of loss for two crystallites of different size is given by

$$\left(\frac{dL_1}{dt}\Big/\frac{dL_2}{dt}\right) = \frac{r_1\phi_1}{r_2\phi_2} = \frac{r_1}{r_2}\exp\left[\beta\left(\frac{1}{r_1} - \frac{1}{r_2}\right)\right] \qquad 5.4$$

The Pt/Al_2O_3 contact angle is ∿90°, and therefore the crystallites were taken to be hemispheres. For this case the value of β is defined by

$$\beta = \frac{(\gamma_1 + 2\gamma_2)V}{RT} \qquad 5.5$$

where γ_1 and γ_2 are the Pt - Al_2O_3 and Pt - atmosphere interfacial energies, V is the molar volume of Pt, and T was taken as 1000°K. In order to assess the range in reported values of γ (*e.g.*[5.22, 5.23]) and the variation of Pt species (such as metallic Pt, PtO, etc.), three values of β, ranging from 4 to 6 nm, were employed in calculating relative rates of loss by equation 5.4. In Table 5.1 the rates of atom loss relative to a crystallite with a diameter of 25 nm are reported for the three cases over the size range 2 to 50 nm.

From the values reported in Table 5.1, it is evident that in the size range of interest in sintering studies the rate of loss of atoms from a crystallite may reasonably be approximated as independent of the crystallite size. The variation in loss is less than 30% up to 30 nm, except for very small particles where equation 5.3 predicts questionably high values of ϕ/ϕ_0. Accordingly, we have modeled the rate of loss of atoms from the ith particle as

$$\frac{dL_i}{dt} = A\, e^{-E_a/RT} \qquad 5.6$$

where $\frac{dL_i}{dt}$ is the rate of transfer of atoms to the surface, A is an arbitrary constant, and E_a is the activation energy required to move from a particle to the surface. For particle sizes above 30 nm the surface energy and size variance of the rate of loss do not compensate

Table 5.1: Relative Rate of Loss of Atoms per Crystallite as a Function of Crystallite Size as Estimated by the Kelvin Equation (Normalized to 25 nm Diameter Crystallites)

Crystallite diameter nm	Case I $\beta = 4.0$ nm	Case II $\beta = 5.0$ nm	Case III $\beta = 6.0$ nm
2	3.17	7.96	19.97
4	0.86	1.31	1.99
6	0.66	0.85	1.10
8	0.63	0.75	0.89
10	0.65	0.73	0.82
12	0.68	0.74	0.81
15	0.74	0.78	0.83
18	0.82	0.84	0.87
20	0.87	0.88	0.90
25	1.00	1.00	1.00
30	1.14	1.12	1.11
40	1.42	1.38	1.34
50	1.70	1.64	1.57
100	3.15	2.96	2.79

for each other, and the assumption of a constant loss rate, equation 5.6, becomes increasingly subject to error.

5.2.2 Migration of Metal Atoms Over Support Surfaces

The extensive work on nucleation and film growth leaves little doubt about the mobility of atoms on supports, even at temperatures much lower than those encountered during supported metal catalyst sintering[5.10-5.13, 5.16-5.19]. The atoms may be considered as a two-dimensional gas, in which case their speed is given by

$$v = \left(\frac{\pi k_B T}{2m} \right)^{\frac{1}{2}} \tag{5.7}$$

or the motion may be described by the jumping from one surface site to next which is described by

$$v = a\, \nu \exp(-E_s/RT) \tag{5.8}$$

It should be noted that E_s, the activation energy for surface diffusion, is not necessarily equal to E_a, but is generally considerably smaller than E_a.

In the present model it is immaterial whether equation 5.7 or 5.8 is used, but equation 5.8 illustrates that a drop in temperature could readily immobilize surface atoms if certain sites on the support surface have large values of E_s. We presume a surface velocity rapid enough, at sintering temperatures, to lead to a uniform concentration of free surface metal atoms on the support surface.

5.2.3 Capture of Atoms by Metal Crystallites

Upon collision of a migrating atom with a metal crystallite, the atoms may become incorporated in the crystallite. The rate at which a crystallite gains metal atoms by this process depends on the concentration of metal atoms on the support surface, the velocity of these atoms, and the effective diameter of the crystallite, D_i, *i.e.*,

$$\frac{dG_i}{dt} = \alpha \frac{v}{N_t} \frac{F_s}{S_o} D_i \qquad 5.9$$

where α = sticking probability of an atom colliding with a crystallite (assumed to be independent of D)

N_t = total metal atoms

S_o = support area per metal atom

F_s = number of atoms migrating on support with an area $N_t S_o$ (*i.e.* $\frac{F_s}{N_t S_o}$ is the concentration of atoms on support surface)

Once the atom has become attached to the periphery of the particle it can migrate over the metal surface and become part of the crystal. The surface self diffusion rates of metals are generally quite large, the activation energy for Pt only being 26 kcal/gmole[5.24], and the resulting crystals should be three-dimensional rather than metal islands on the support.

5.2.4 A Summary of the Model

The net rate of change of the number of atoms in the ith particle is given by

$$\frac{dN_i}{dt} = \frac{dG_i}{dt} - \frac{dL_i}{dt} \qquad 5.10$$

which, according to equation 5.3 and 5.6 may be written as

$$\frac{dN_i}{dt} = \alpha\, v \frac{F_s}{N_t S_o} D_i - A\, e^{-E_a/RT} \qquad 5.11$$

The rate of change of the number of migrating surface atoms is given by the material balance

$$\frac{dF_s}{dt} = \sum_{i=1}^{M} \left(\frac{dL_i}{dt} - \frac{dG_i}{dt} \right) = - M A e^{-E_a/RT} + \alpha v \frac{F_s}{N_t S_o} \sum_{i=1}^{M} D_i \qquad 5.12$$

where M is the number of metal crystallites on the support of area $N_t S_o$.

This model of supported metal catalyst sintering may be likened to an evaporation condensation process among multisized droplets. In that case the variation in vapor pressure among drops of different size leads to a transfer of liquid from smaller to larger droplets. By our sintering model a single particle on a support surface would establish an equilibrium concentration of metal atoms migrating along the surface. With several particles of different size, however, the surface concentration is not equilibrated with each particle, and thus growth or decay in individual particle sizes occurs. Because smaller crystallites would equilibrate with higher concentrations of migrating surface atoms than larger crystallites, the larger crystallites grow at the expense of the smaller.

5.3 Method of Solution

Equations 5.11 and 5.12 were written in the following finite-difference form for solution

$$\Delta N_i = \left(\alpha v \frac{\overline{F}_s}{N_t S_o} D_i - A e^{-E_a/RT} \right) \Delta t \qquad 5.13$$

$$\Delta F_s = - \sum_{i=1}^{M} \Delta N_i \qquad 5.14$$

where $\overline{F}_s$ = arithmetic average of F_s during time increment Δt and v is given by equation 5.7. In the above formulation the constant α includes the reduction in the velocity of migrating atoms, v, due to an activation energy for surface diffusion. The support surface area per metal atom, S_o, is related to the metal loading of the catalyst. For example, $S_o = 10\ \text{nm}^2/\text{atom}$ corresponds to a catalyst containing ∿ 1 wt % Pt on a support having an area of 300 m^2/g.

Two methods of solution for equations 5.13 and 5.14 were employed, depending on the value of $\frac{\alpha}{S_o}$ (v being given by equation 5.7 and F_s/N_t, the fraction of atoms migrating on the support, being determined in part by the value of $\alpha v/S_o$).

5.3.1 Solution for $\alpha/S_o > 10^{12}\ m^{-2}$

For values of $\alpha/S_o > 10^{12}\ m^{-2}$ it was found that F_s is always small, $F_s \approx 0$, and the approximation $\sum_{i=1}^{M} \Delta N_i = 0$ could be made. This condition corresponds to rapid rates of surface atom migration and capture compared to the rate at which atoms leave crystallites. For this situation, the rate at which a crystallite captures atoms, assuming all crystallites are equally accessible to migrating atoms, is proportional to diameter, D_i. Equations 5.13 and 5.14, for this case, reduce to

$$\Delta N_i = \left(\frac{M\,D_i}{\sum_{i=1}^{M} D_i} - 1\right) A\, e^{-E_a/RT}\, \Delta t \qquad 5.15$$

The values of N_i, for all particles, as a function of time can readily be computed by a single-step method (Euler's formula) once a relationship between D_i and N_i is chosen. In this work we described the crystallites as fcc cubes and used the equations of van Hardeveld and Hartog[5.25] to determine the total number of atoms, N_i, and the number of atoms, $N_{s,i}$, at the surface of each crystallite, *i.e.*

$$N_i = 0.5 + 0.5\,[1 + 2q]^3 \qquad 5.16$$

and

$$N_{s,i} = 12q^2 + 2 \qquad 5.17$$

for $q \geq 1$

where

$$q = \frac{(\ell_i - a_o)}{\sqrt{2}\,a_o}$$ (*i.e.* the number of atoms along the edge of cube minus one)

ℓ_i = the length of the edge of cube

a_o = atomic diameter (0.277 nm for Pt)

The effective diameter, D_i, of a crystallite for the capture of migrating atoms was taken as

$$D_i = 4(\ell_i + a_o) \qquad 5.18$$

By starting with a given particle size distribution, *i.e.* ℓ_i for all particles at time = 0, equation 5.15 was used to obtain N_i's as a function of time. The corresponding dispersion, D, was calculated by

$$D = \frac{\sum_{i=1}^{M} N_{s,i}}{\sum_{i=1}^{M} N_i} \qquad 5.19$$

Any crystallites for which N_i became <14 (*i.e.* $q < 1$) during a time interval were considered to have disappeared, and the remaining atoms in these crystallites were distributed among the remaining crystallites in the following time increment in proportion to their size.

5.3.2 Solution for $\alpha/S_0 < 10^{12}$ m^{-2}

Equations 5.13 and 5.14 were solved by a trial and error for these cases. The number of atoms, F_s, was taken as zero at time equal to zero. In order to avoid oscillatory values of F_s in the initial time increments a heating period was incorporated in the calculations. The temperature was increased from 300 K to the desired final temperature over a period of one hour in 0.01 hour increments. The trial and error procedure used to calculate N_i and F_s at time $t' = t + \Delta t$ was as follows:

1. The value of F_s at t' was guessed (*i.e.* ΔF_s for Δt).
2. N_i was computed for each particle using equation 5.13

$$(\overline{F}_s = F_s\big|_t + \frac{\Delta F_s}{2}).$$

3. ΔF_s was computed using equation 5.14.
4. If ΔF_s from step 1 differed from ΔF_s by step 3 by less than 0.1 atoms and if $F_s\big|_t + \Delta F_s$ was ≥ 0 calculation proceeded to the next time increment; if the difference was > 0.1 steps 1 to 3 were repeated, with the new ΔF for step 1 being estimated using the magnitude of the difference as a guide.

If only a negative value of F_s (physically impossible) at t' could satisfy the above conditions, the size of Δt was decreased to one-tenth of its value and steps 1 to 4 were repeated. If any N_i became < 14, these N_i were added to F_s in the next time increment.

The dispersion for this case was calculated in a manner analogous to equation 5.19, except that F_s was included in the number of metal surface atoms, *i.e.*

$$D = \frac{F_s + \sum_{i=1}^{M} N_{s,i}}{\sum_{i=1}^{M} N_i} \qquad 5.20$$

A value of 0.1 hour for Δt was used for the computations. Calculations using a Δt of 0.017 hour yielded essentially the same results. The complete programs used for each case are attached in Appendix C.

5.4 Description of Cases Investigated

5.4.1 Crystallite Size Distributions

The initial (zero-time) particle size distributions (PSD) were generated in the following manner:

1. the maximum and minimum size of particles in the distribution was chosen (ℓ_{max} and ℓ_{min}),
2. the size range was split into K equal size increments of size $\Delta\ell$,
3. the number of particles, P_k, was specified for each size increment,
4. the size of each particle was calculated by

$$\ell_i = \ell_{min} + (k-1)\Delta\ell + \left(\frac{j-1}{P_k}\right)\Delta\ell \qquad 5.21$$

for $k = 1$ to $K + 1$ and $j = 1$ to P_k for each k. Where $i = j + \sum_{m=o}^{k-1} P_m$ with $(P_o = 0)$, $P_{K+1} = 1$ was included to obtain a particle of size ℓ_{max}. This procedure results in $\sum_{k=1}^{K+1} P_k$ particles all having a different size.

Two general types, I and II, of PSD were generated by this procedure. The Type I distribution is approximately Gaussian in nature, and Type II is skewed with a large fraction of small particles. The values of ℓ_{min}, ℓ_{max}, k and P_k used to generate the specific PSD are given in Table 5.2.

The PSD listed in Table 5.2 contain 121 particles, except 8 and 9 which contain 122. In these two distributions one large particle (10 nm) was added to PSD 1 and 7. To check the sensitivity of the calculations to the number of particles present, calculations were carried out with PSD for which the values of P_k for k = 1 to K were doubled (P_{K+1} was kept equal to one). These calculations showed that as long as the remaining number of particles was $\geq$ 7 the dispersion as a function of time remained unaltered.

5.4.2 Parameter Values

The values of parameters used in solving equations 5.13 and 5.14 (or equation 5.15) for the specific cases reported in the next section are listed in Table 5.3. Although many other combinations of parameters were examined the cases listed illustrate the general behaviour of the model. It should be mentioned that, although all the cases listed used a value of $A = 8 \times 10^{13}$ sec^{-1}, the results are readily extended to lower values of A (significantly higher values of A are physically unlikely). Thus, for a specific PSD and fixed values of T and α/S_0, the dispersion as a function of time is determined by the value of A $\exp(-E_a/RT)$, *i.e.*, $A = 1.65 \times 10^7$ sec^{-1} and $E_a/RT = 15.0$ is equivalent to $A = 8 \times 10^{13}$ sec^{-1} and $E_a/RT = 35.0$ (Case 1).

5.5 Results and Discussion

5.5.1 Effect of Initial PSD on Rate of Sintering

From equation 5.11 it is evident that for a certain value of D_i, and the corresponding crystallite size, ℓ_i, according to equation 5.18,

Table 5.2: Data for Generation of Particle Size Distributions

Distribution Number	ℓ_{min} (nm)	ℓ_{max} (nm)	Type	Dispersion
1	2.70	3.30	I	0.35
2	2.10	3.90	I	0.34
3	1.20	4.80	I	0.31
4	2.960	3.065	I	0.35
5	2.00	12.50	I	0.13
6	5.00	15.50	I	0.10
7	1.50	4.29	II	0.35
8*	1.50	4.29	II	0.28
9*	2.70	3.30	I	0.29

Type I

$$P_k = \begin{cases} k \text{ for } k = 1 \text{ to } 10 \\ 10 \text{ for } k = 11 \text{ and } 12 \\ 22 - k \text{ for } k = 13\text{-}21 \\ 1 \text{ for } k = 22 \end{cases}$$

Type II

k	1	2	3	4	5	6	7	8	9	10
P_k	20	20	18	16	14	12	10	7	3	1

* one 10 nm particle was added to these distributions to simulate a bimodal distribution.

Table 5.3: Parameter Values Used in Study

Case Number	E_a/RT	T(K)	$\frac{\alpha}{S_o}$ (m^{-2})
1	35.0	1000	1×10^{12}
2	35.0	1000	2×10^{7}
3	33.3	900	1×10^{12}
4	33.0	900	2×10^{7}
5	31.6	950	1×10^{12}
6	31.6	950	2×10^{9}
7	31.6	950	2×10^{7}
8	31.6	950	4×10^{6}
9	31.6	950	2×10^{6}
10	30.0	1000	1×10^{12}
11	30.0	1000	2×10^{7}
12	27.5	1000	1×10^{12}

$A = 8 \times 10^{13}$ sec^{-1} for all cases the net rate of growth is equal to zero. Particles with sizes larger than this 'critical' size will grow while smaller particles will shrink. This critical size is given by

$$\ell_{CRIT} = \frac{A\ N_t\ S_o}{4\alpha\ v\ F_s}\, e^{-E_a/RT} - a_o \qquad 5.22$$

or according to equation 5.15

$$\ell_{CRIT} = \frac{\sum_{i=1}^{M} D_i}{4M} - a_o = \frac{\sum_{i=1}^{M} \ell_i}{M} \qquad 5.23$$

As sintering progresses the number of particles, M, decreases and the number of free surface atoms decreases as well. This results in an increase in ℓ_{CRIT} as sintering progresses, and crystallites which initially grow in size will eventually decay.

Figure 5.2 and 5.3 shows the particle size history for individual particles of the same initial size for PSD 1 and 9, Case 3. PSD 1 and 9 are the same except one 10 nm particle has been added to PSD 1 to get PSD 9. The effect of the added 10 nm particle is evident when comparing Figures 5.2 and 5.3. This large particle captures many of the migrating atoms, resulting in an increased rate of sintering.

The effect of large particles or broad initial PSD on the rate of sintering is further illustrated in Figure 5.4 where the normalized dispersion D/D_o is shown as a function of time for various initial PSD. The addition of one large particle (10 nm) to PSD 7 (i.e. to get PSD 8) significantly increases the rate of sintering. PSD 1 to 4 are all Type I distributions with a mean crystallite size of 3.0 nm, but the size range ($\ell_{max} - \ell_{min}$) varying from 0.105 nm (PSD 4) to 3.50 nm (PSD 3).

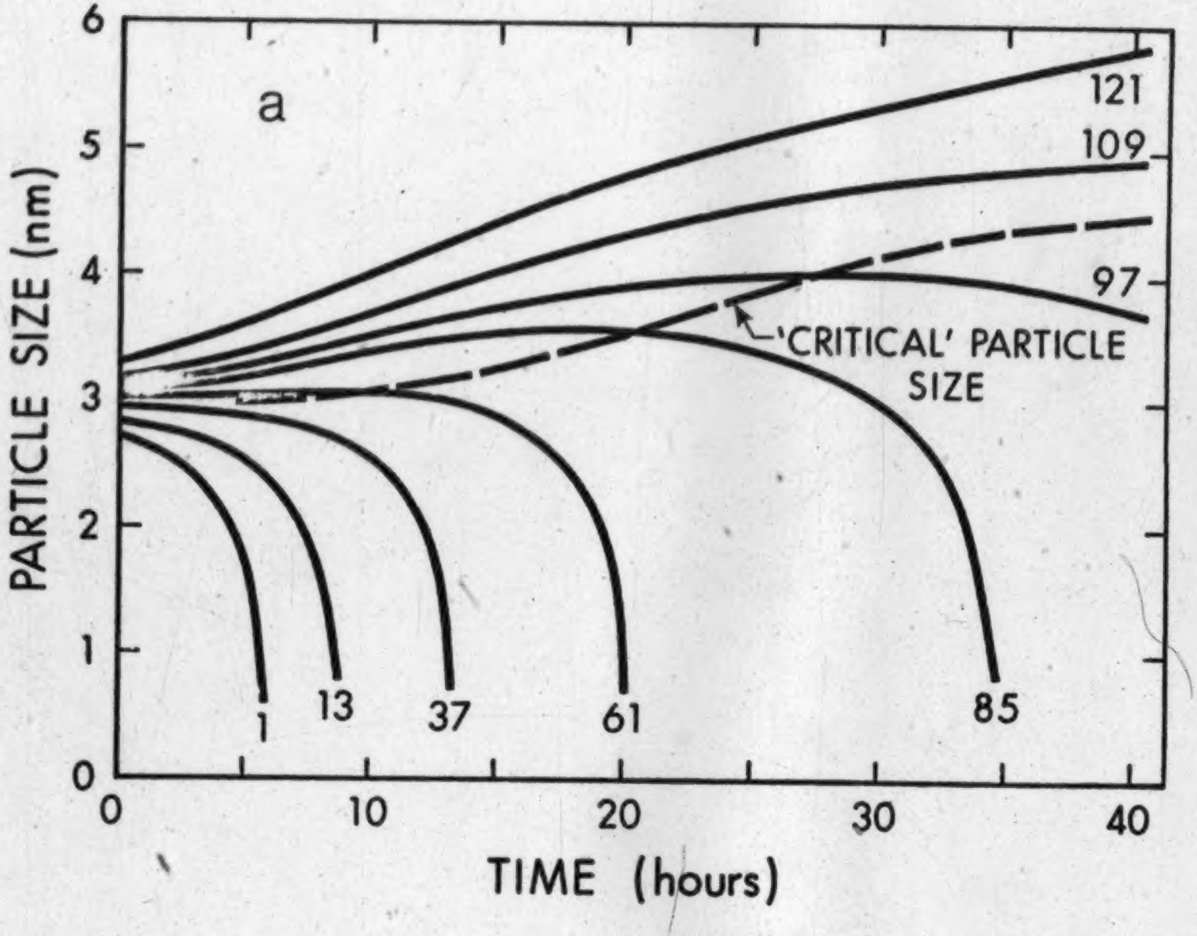

Figure 5.2: Particle size history for selected individual particles, PSD1, Case 3. (Number is i, the particle number is the PSD.)

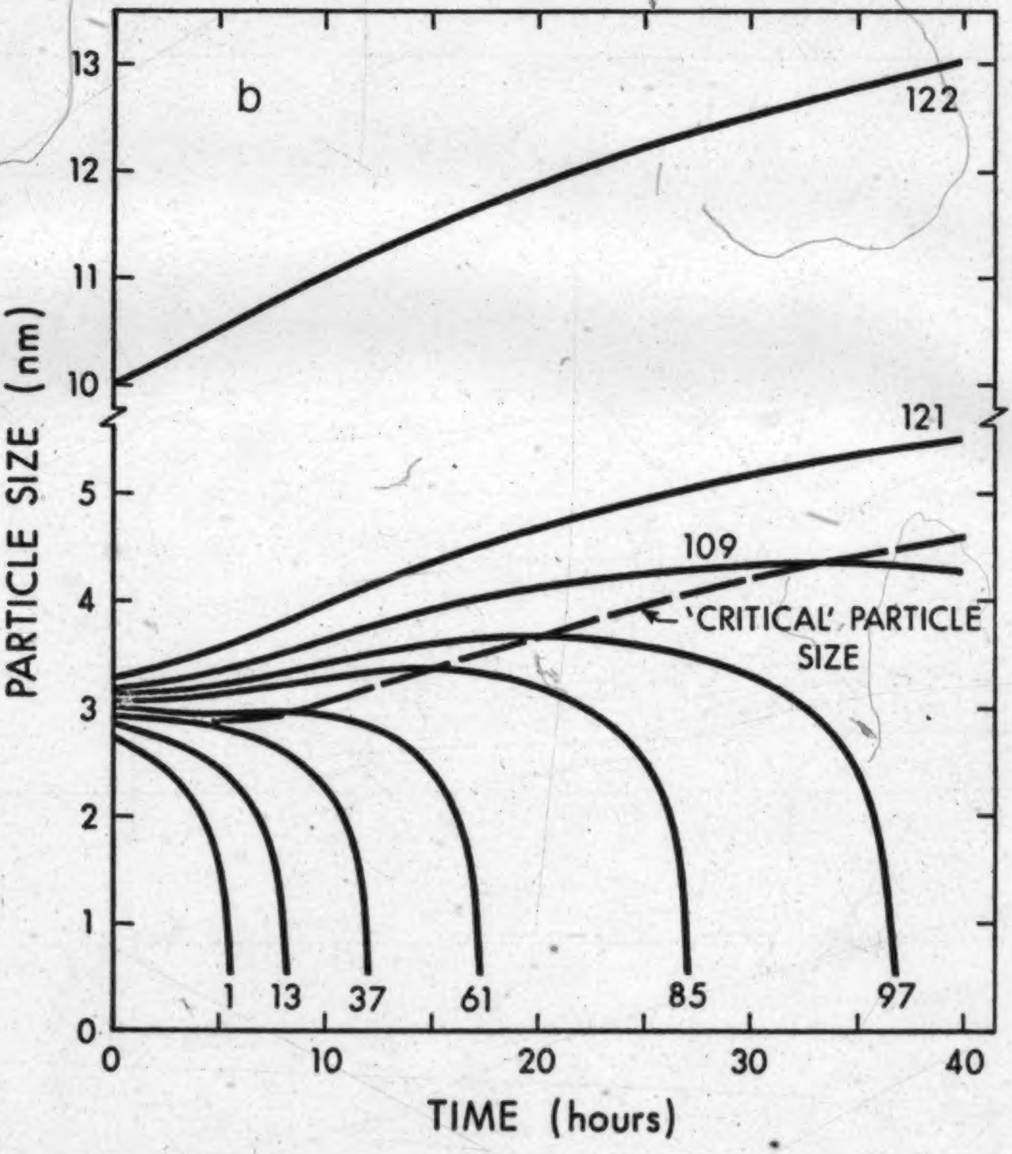

Figure 5.3: Particle size history for selected individual particles, PSD9, Case 3. (Number is i, the particle number is the PSD.)

The rate of sintering, as shown in Figure 5.4, is larger for the broader distribution in an initial period of about 10 hours. The reduced rate of sintering for narrow distributions occurs because in the initial stages of sintering these distributions are becoming gradually broader without the disappearance of particles. The narrow size range does not generate a substantial driving force for transfer of metal from the smaller to the larger particles.

Figures 5.5 and 5.6 show the cumulative distribution function F as a function of time for Type I and II initial distributions. This illustrates the spreading of the distributions with time. In each case, as sintering progresses the model predicts the presences of particles smaller than the initial minimum size. During early stages of sintering the broadening, and specifically the decay of a substantial fraction of the particles to smaller sizes, is evident. This prediction of the presence of small particles at all stages of sintering is one significant difference between the proposed interparticle transport model and the crystallite diffusion model[5.1, 5.2]. The latter model does not allow for formation of particles smaller than the initial minimum size, nor does it predict the type of induction period for narrow PSD shown in Figure 5.4. Further, it predicts that sintering would occur with a unisized distribution (practically unattainable), whereas the model developed here predicts that such a distribution would not sinter because of an absence of a driving force for interparticle transport. Some experimental evidence exists that even in heavily sintered samples small crystallites are still present[5.26]. Further experiments that follow the nature of the particle-size-distribution broadening would be useful in elucidating the mechanism of sintering.

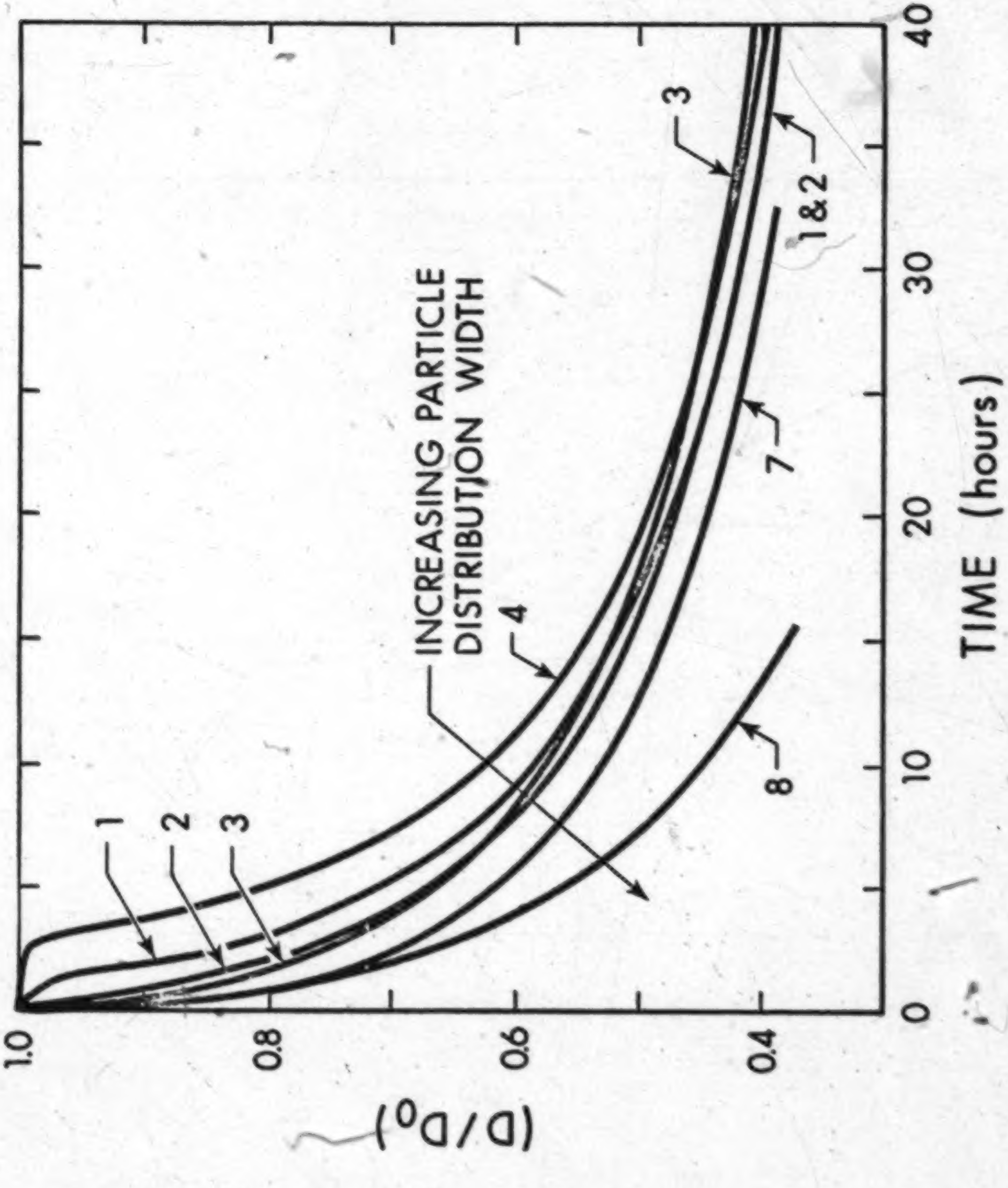

Figure 5.4: Effect of initial particle size distribution on the rate of sintering (Case 5, the numbers identify the PSD).

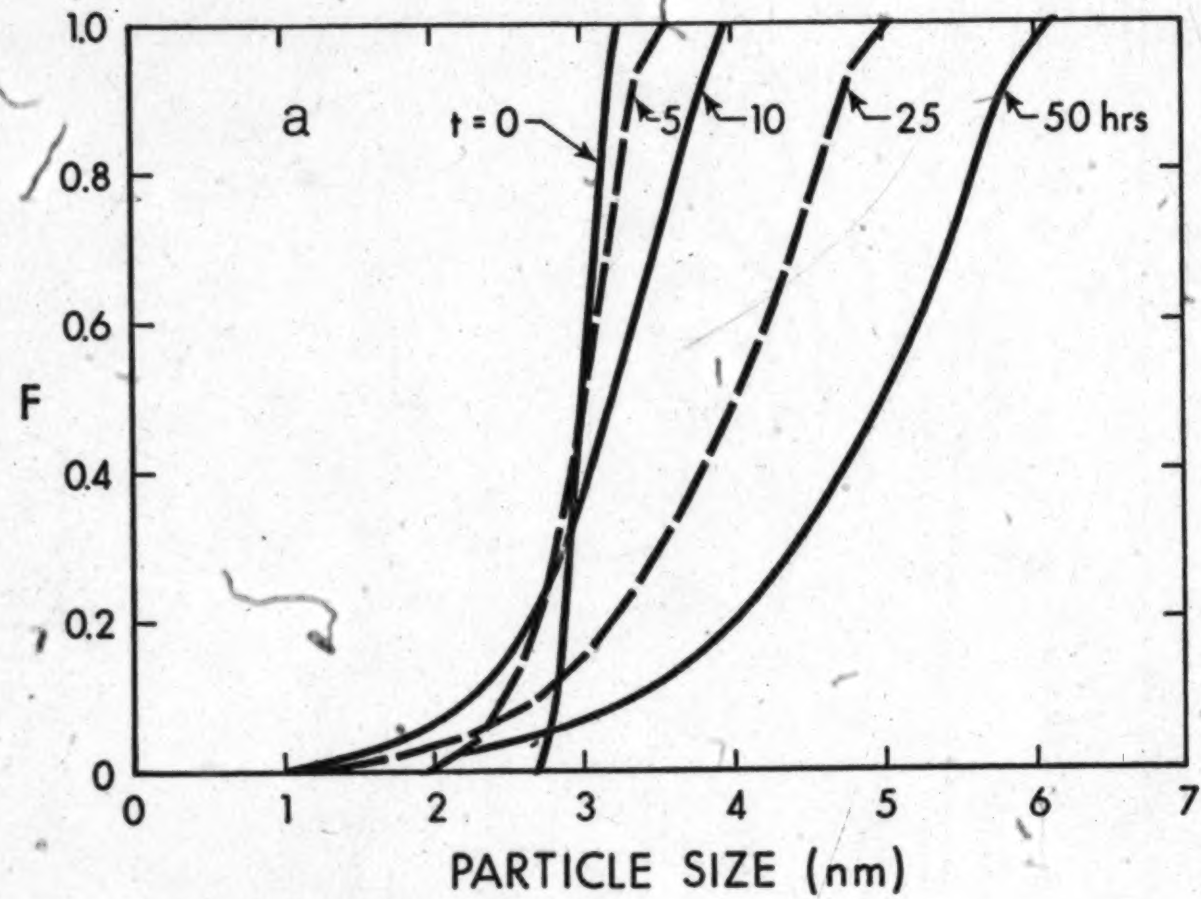

Figure 5.5: Cumulative particle size distribution as a function of time, showing the broadening of the initial distribution, PSD1, Case 3.

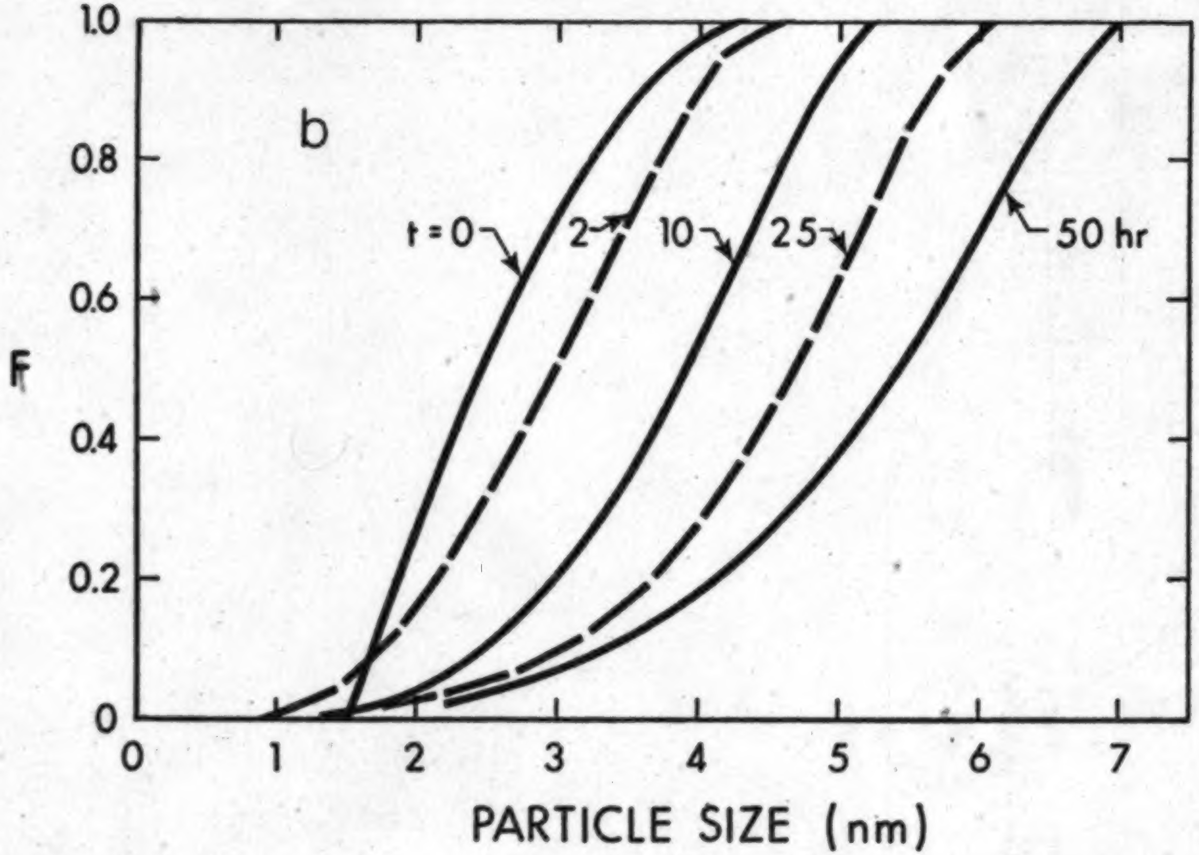

Figure 5.6: Cumulative particle size distribution as a function of time, showing the broadening of the initial distribution, PSD2 Case 3.

5.5.2 The Effect of Surface Mobility and Metal Loading on Sintering Behavior

If no initial free surface atoms are postulated, then during the early stages of sintering the value of F_s grows as particles lose atoms to the surface and relatively few are captured by crystallites. The parameter α/S_0 determines the extent to which surface atoms are captured, and hence the size of F_s. The increases in dispersion (defined by equation 5.20) shown in Figure 5.7 are due to this increase in F_s.

For large values of α/S_0, corresponding to high metal loadings (*i.e.* small values of S_0) or high velocity of migration, the number of migrating surface species approaches zero and the rate of sintering is controlled by the loss from particles only. In these cases, the rise in dispersion due to the surface species is negligible, and this model does not predict any redispersion of metal.

Lower values of α/S_0, however, can account for significant redispersion. The lower values could arise from lower metal loadings or a reduced velocity of migrating species (larger E_s). In such cases a significant amount of free surface atoms builds up, leading to higher dispersions and reduced overall rates of sintering. Redispersion could occur through cooling of a sintering sample during this period of growth in number of free surface atoms. If the migrating atoms were frozen as single atoms or small particles during cooling, the increased dispersion would remain. Experimental evidence[5.27] indicates that rapid cooling does give higher dispersions after sintering treatments than slow cooling. Figure 5.7 shows that for α/S_0 values less than about 2×10^6 m^{-2} the capacity of the surface to accomodate free surface atoms exceeds the number of atoms present, and thus all the particles disappear.

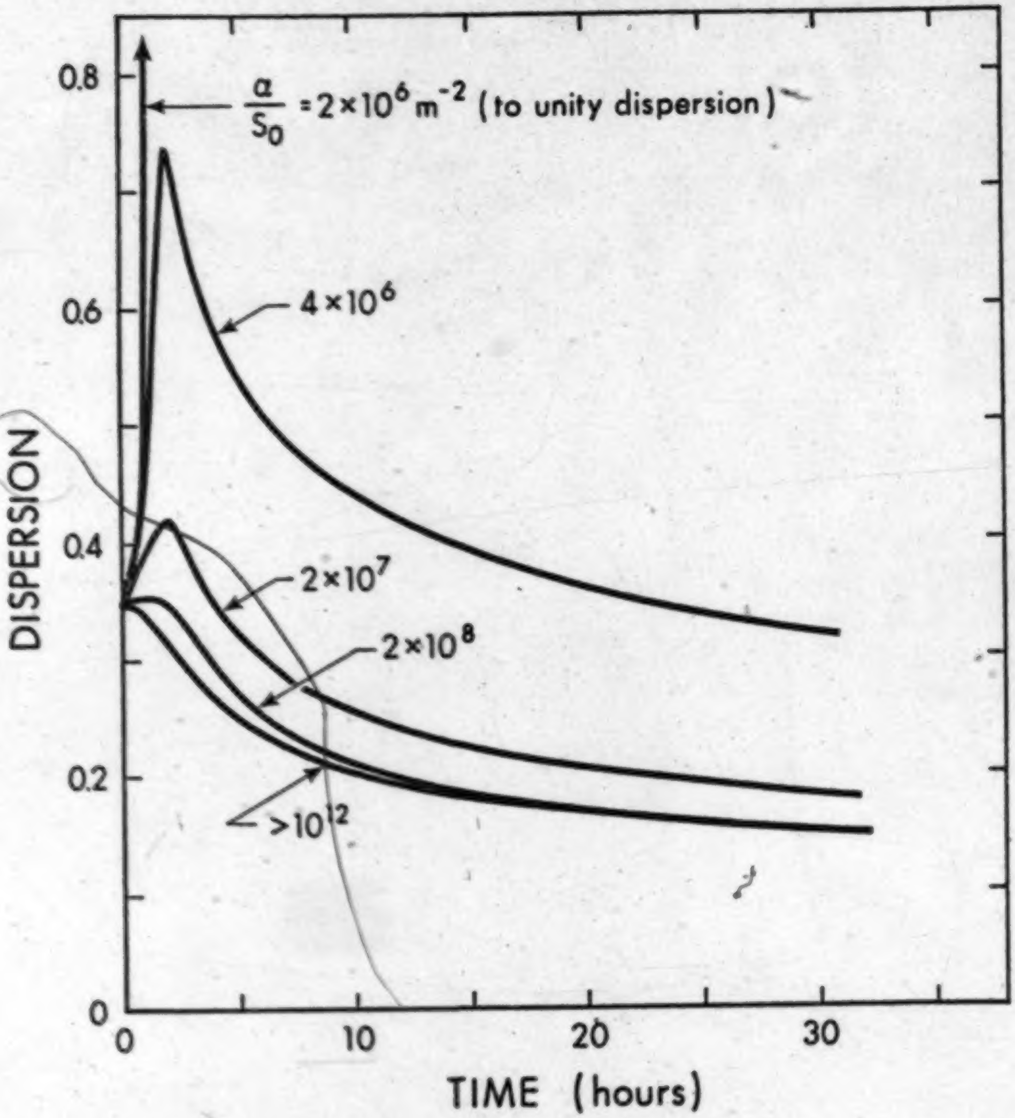

Figure 5.7: Effect of surface mobility of metal atoms on support, and metal loading, on sintering behavior. (PSD1, Cases 5 to 9.)

The predictions of the model as α/S_0 becomes smaller may become unreliable because the assumption that the surface concentration of migrating atoms is position independent is no longer valid at low migration rates. The extent of the error introduced by this approximation has not been investigated.

5.5.3 The Effect of E_a/RT on Sintering Behavior

Figure 5.8 shows, for the case where α/S_0 is large and the free surface atoms are rapidly captured, the influence on sintering behavior of variations in E_a/RT. The plots correspond to either a change in temperature or in the activation energy. For instance, if E_a is taken as 60 kcal/gmole, the curves in Figure 5.8 would represent temperatures ranging from about 850°K ($E_a/RT = 35$) to 1100°K ($E_a/RT = 27.5$). If the temperature is postulated as 1000°K, the curves represent activation energies from 55 to 70 kcal/gmole.

As would be expected for such large activation energies, the sintering behavior is extremely sensitive to variations in temperature. Sintering is extremely slow for $E_a/RT = 35.0$, with less than 10% loss of dispersion in 40 hours, while for $E_a/RT = 27.5$, sintering is extremely rapid, resulting in the transfer of all the metal in the initial 121 particles to a single large particle within 5 hours.

Similar trends are evident, as shown in Figure 5.9, when values of α/S_0 are lower and a significant surface concentration of migrating atoms is present. In this case, however, a lower value of E_a/RT, corresponding to higher temperatures or a lower activation energy, affects not only the rate of sintering but also the extent of initial redispersion. While lower values of E_a/RT lead eventually to more rapid sintering, the

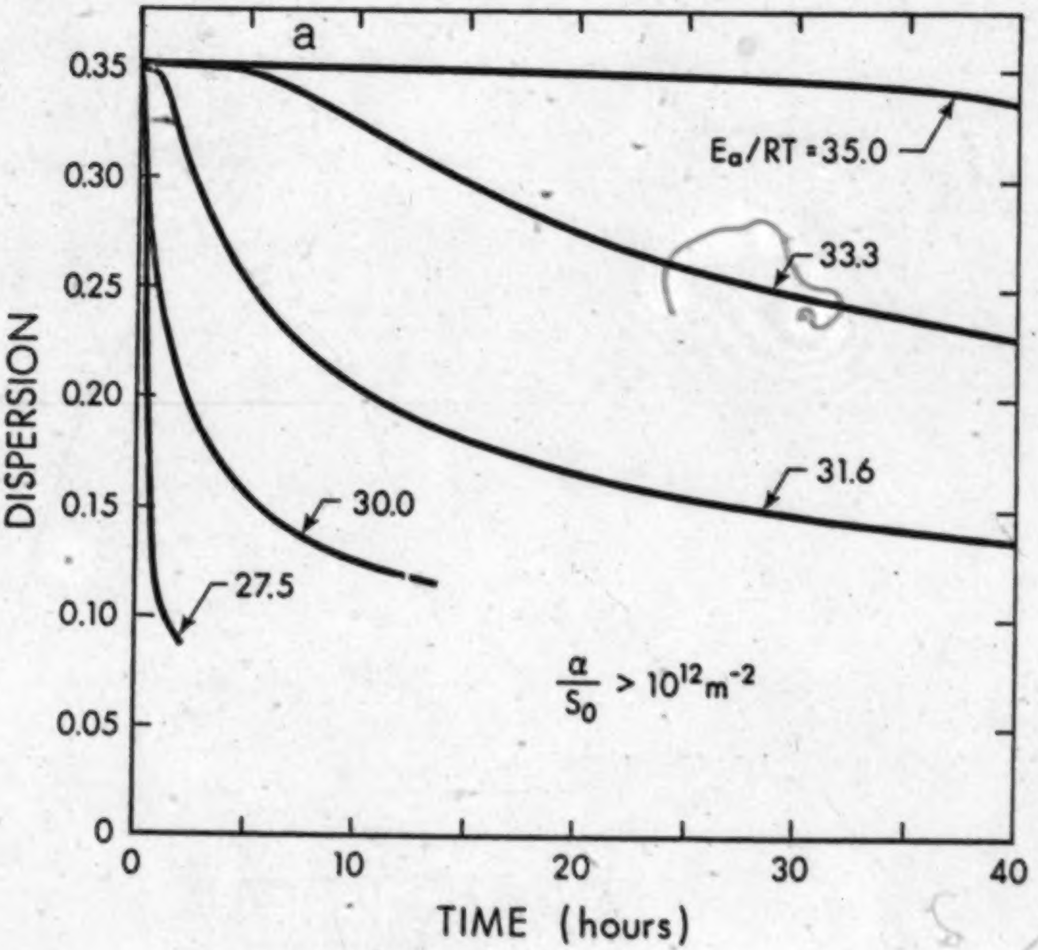

Figure 5.8: Effect of E_a/RT on sintering behavior, PSD1, high value of α/S_0, Cases 1, 3, 5, 10 and 12.

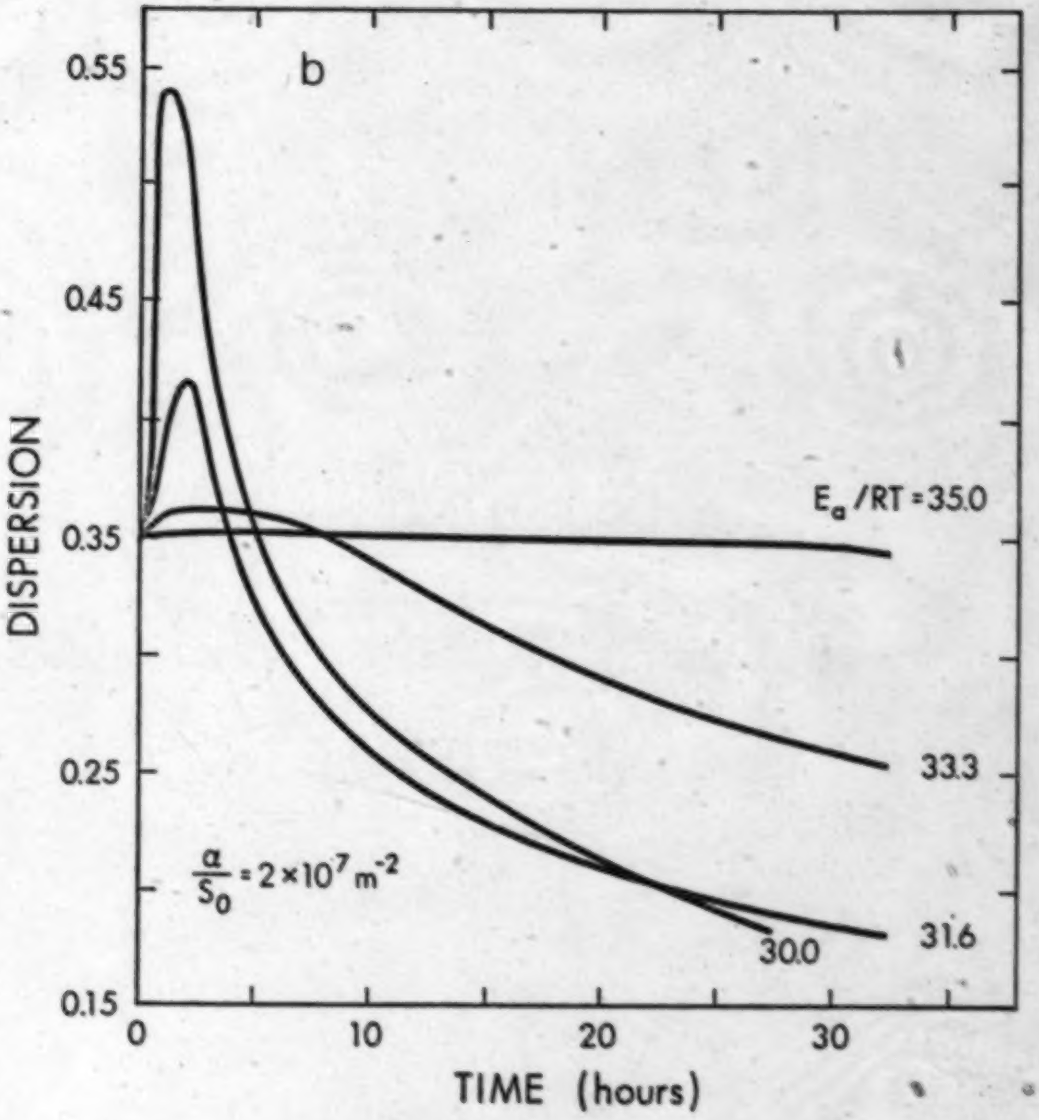

Figure 5.9: Effect of E_a/RT on sintering behavior, PSD1, low value of α/S_0, Cases 2, 4, 7 and 11.

initial rise means that for a period of time the dispersion is lower for higher E_a/RT values.

Changes in atmosphere would affect the activation energy for metal movement from the particle to the support surface. The actual species leaving would probably differ in oxidizing and reducing atmospheres. In the former case a metal oxide molecule would probably be the migrating species. Oxidizing atmospheres are found to enhance interactions between metal and support[5.10], and thus could lower the activation energy of escape. The pre-exponential factor, A, could also be affected. It is possible that in the case of oxidizing atmospheres the rate determining step in the sintering process is the formation of the surface oxide species since oxygen adsorption on metals such as Pt is an activated process. Different atmospheres could also affect the velocity of migration along the surface, *i.e.* changes in the activation energy for surface migration, a factor included in the parameter α discussed above.

5.5.4 The Order of Sintering

Several authors (*e.g.* [5.3, 5.9]) have fit experimental data of sintering to a power-law model of the form

$$\frac{dD}{dt} = -KD^n \qquad 5.24$$

where D is the dispersion and K and n are constants. Values of n from 2 to 13 have been reported.

The rate of change of dispersion has been fitted to equation 5.24 to determine the range of n values predicted by the proposed model. One immediate difficulty with the power-law model is its inability to account for an initial period of redispersion as the surface atoms concentration builds up. Accordingly, we have fitted only those data for the regions where the dispersion is decreasing. If equation 5.24 is valid, then a plot of $(D_0/D)^{n-1}$ versus time will result in a straight line with an intercept of unity ($n \neq 1$). Figure 5.10 shows these plots for PSD 5 and 6. These distributions are identical, except the mean size is displaced by 3.0 nm. The behavior of PSD 5 (mean size = 7.25 nm) is well fitted by an n value of 6, while PSD 6 (mean size = 10.25 nm) is well fitted by an n value of 3. This tendency of decreasing values of n with increasing mean particle sizes for symmetrical PSD was observed for several other PSD.

Figure 5.11 illustrates the effect of PSD width on the value of n for PSD with the same mean size (PSD 1 and 2). Neither case is well described by the power-law model, but the narrow PSD 1 shows very low values of n (< 2) at times < 15 hours. This is the result of the 'induction' period for the sintering behavior of narrow PSD that has been discussed previously. As PSD 1 broadens with time (see Figure 5.5) the value of n increases and at even larger values of time n decreases. A similar, but less marked, trend is observed with PSD 2. Not only does n vary with the extent of sintering, but the value of n also depends on the width of the initially symmetric PSD.

The inability of the power-law model to describe the progress of sintering over wide variations of D/D_0 is well recognized[5.3, 5.4]. It is evident that the sintering process should depend on the nature of the PSD and not only on the dispersion. The proposed model predicts the nature of the dependence of n on PSD, but experimental determinations of n as a function of PSD are not presently available.

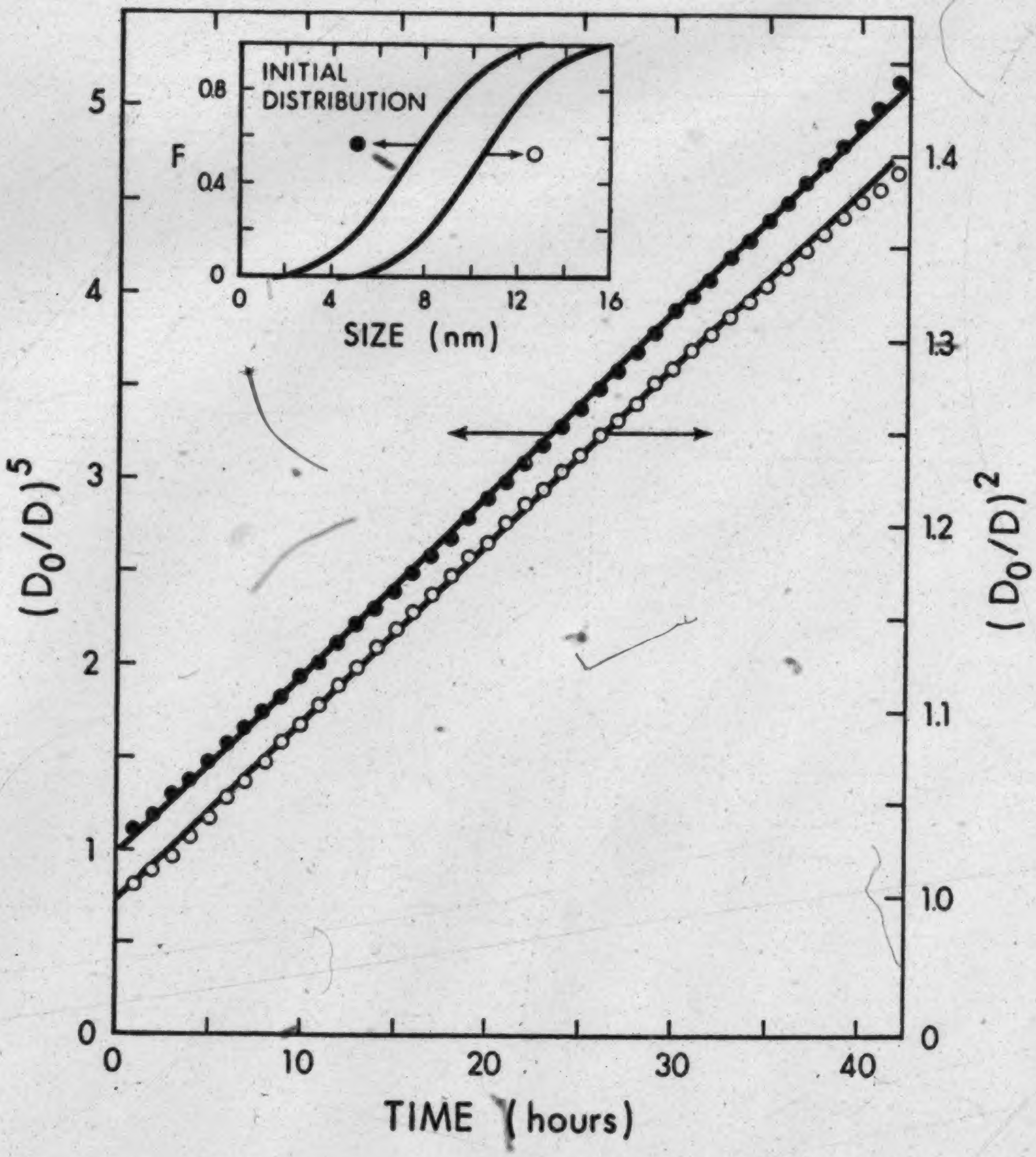

Figure 5.10: Effect of mean crystallite size on power-law order (Case 5; ● PSD5, o PSD6).

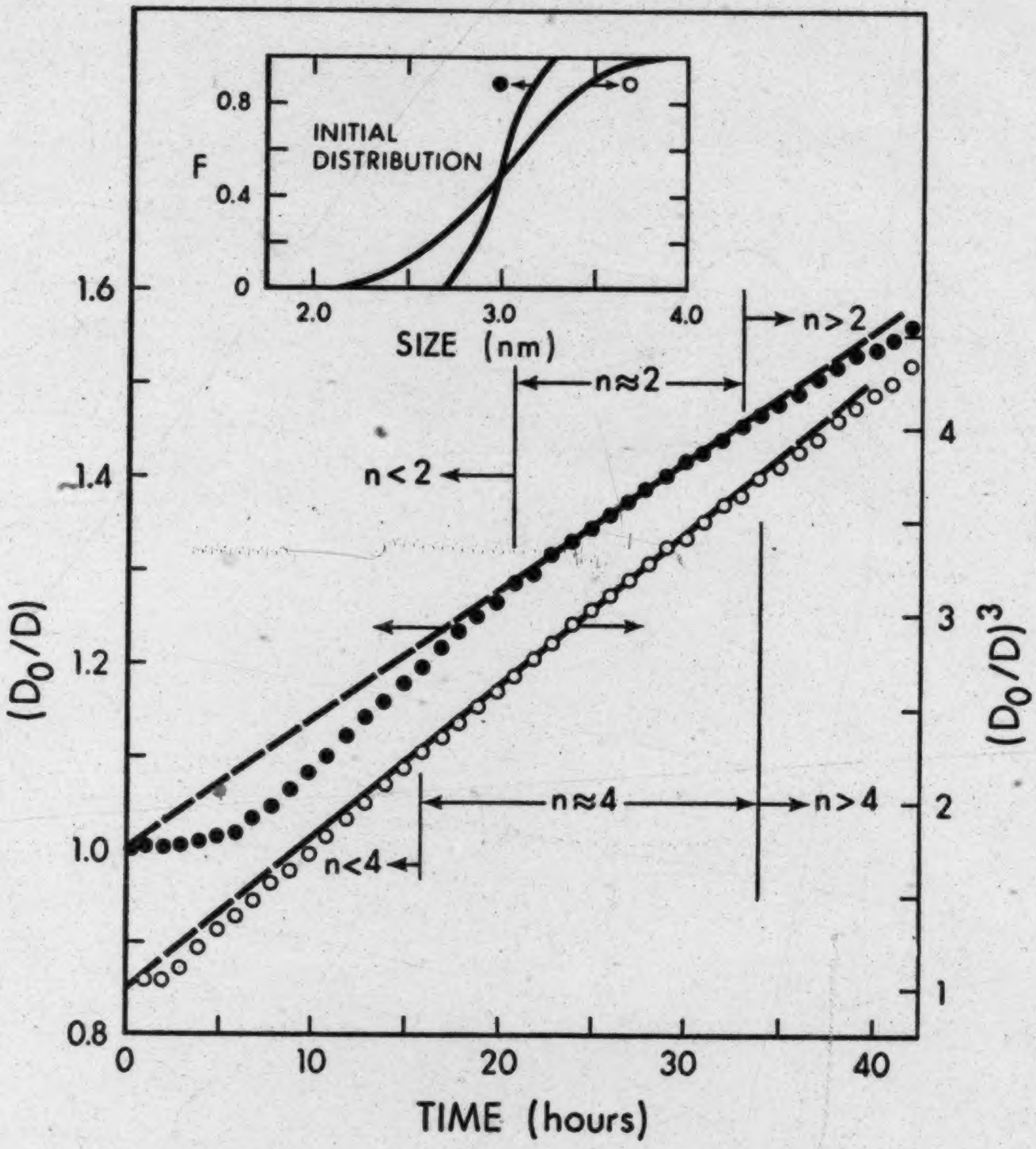

Figure 5.11: Effect of particle size distribution width on power-law order (Case 3; ● PSD1, o PSD2).

5.5.5 Application of the Model to an Experimental Case

To test the ability of the proposed model to describe some experimetal sintering data we chose the data of Wynblatt and Gjostein[5.3]. An approximate initial PSD was obtained by measuring the size of approximately 200 particles in Figure 1a of reference 5.3. The distribution was adjusted to yield an average initial dispersion of 6.7% corresponding to the average particle radius of ∿ 8.0 nm reported by Wynblatt and Gjostein. The resulting bimodal PSD is shown in Figure 5.12 (line at $t = 0$)

Equation 5.15 (*i.e.* $\alpha/S_0 > 10^{12}\ m^{-2}$) was used to predict the PSD as a function of time. The value of E_a/RT was adjusted until the predicted dispersion at 15 hours was equal to 5.4% (corresponding to the reported average radius of 10 nm after 15 hours). The value of E_a/RT that gave this desired result was 29.5, corresponding to an activation energy of 57 kcal/gmole at 973°K. The predicted PSD and dispersion as a function of time for this case are shown in Figure 5.12 and 5.13 respectively. Fitting the dispersion versus time results by equation 5.24 resulted in values of $n = 13$ at $t < 17$ hours, to $n = 4$ for $t = 25$ to 50 hours. This is illustrated in Figure 5.14.

This result agrees well with the experimentally observed n value of 13[5.3]. The initially broad and bimodal PSD is responsible for high value of n at low time. As sintering progresses the bimodal nature of the distribution becomes less pronounced and at $t \approx 20$ hours the PSD is approximately symmetric. As the PSD becomes more symmetric the value of n starts to decrease rapidly and changes from 13 to 4. To further test the validity of the model initial PSD and PSD as sintering progresses should be determined experimentally and compared to predictions.

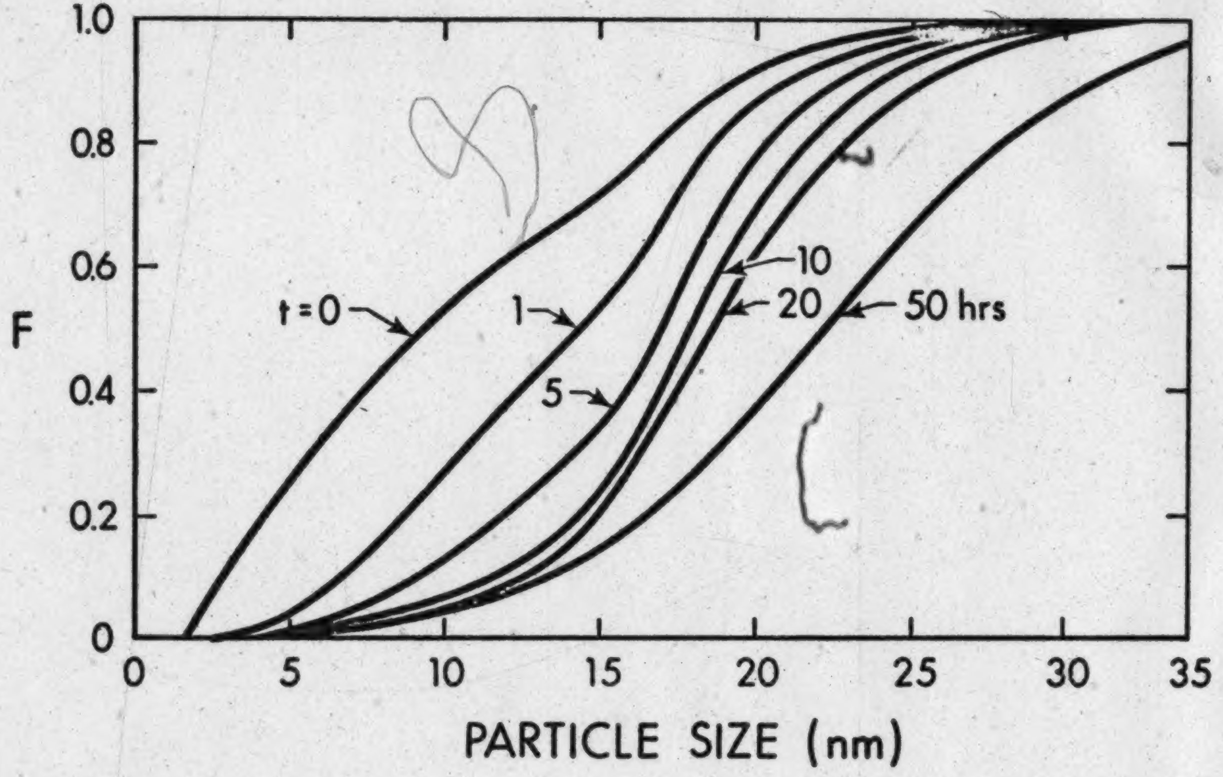

Figure 5.12: Cumulative particle size distribution history predicted by model for the initial distribution (approximate) of Wynblatt and Gjostein (Ref. 5.3).

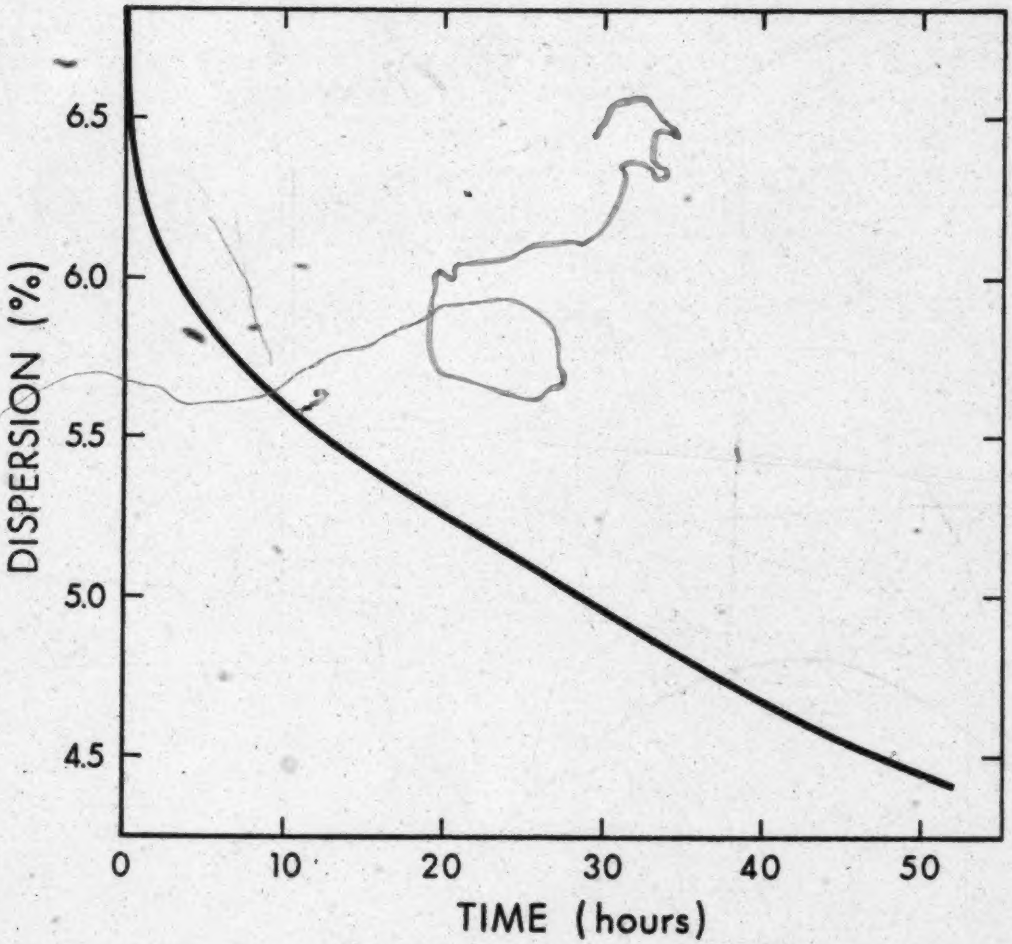

Figure 5.13: Predicted dispersion as a function of time for the initial distribution of Wynblatt and Gjostein[5.3].

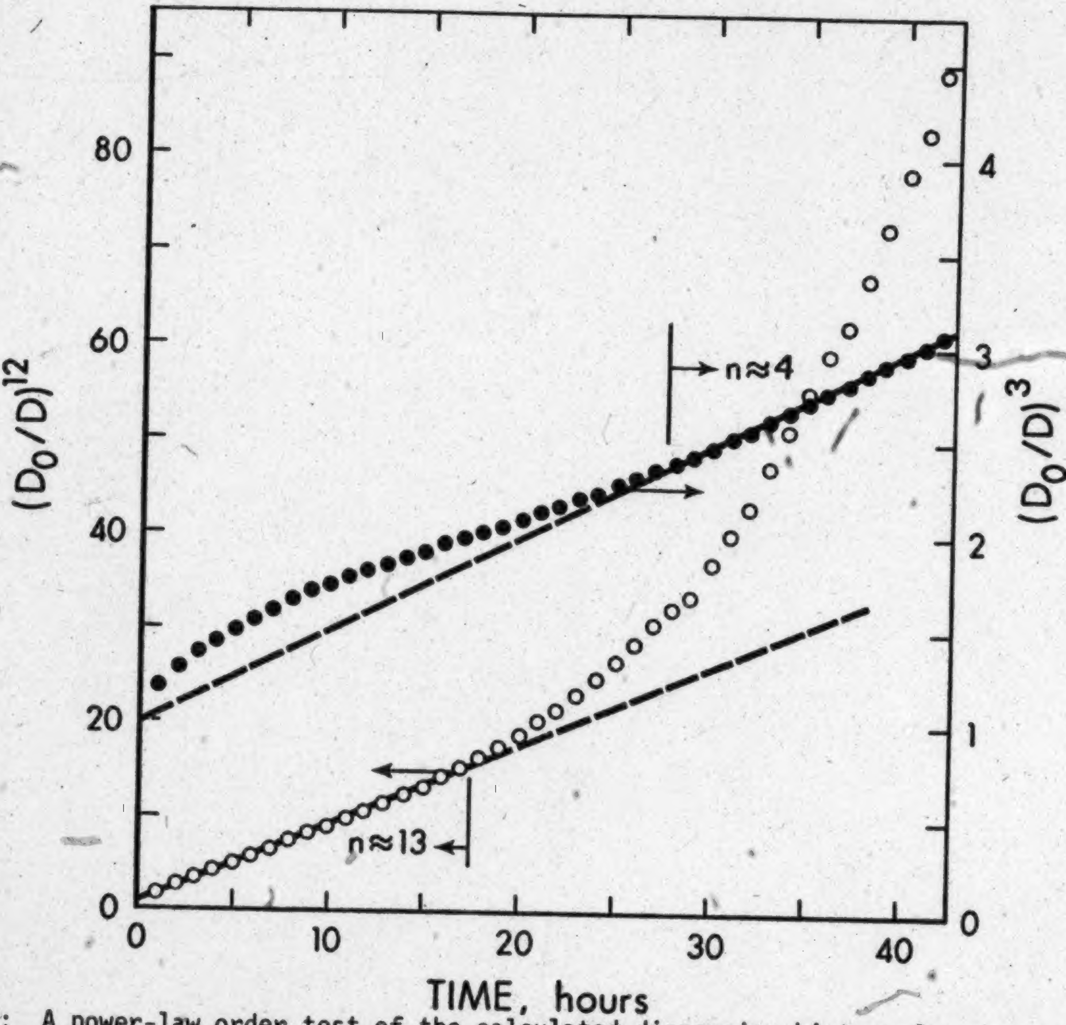

Figure 5.14: A power-law order test of the calculated dispersion history for the initial distribution of Wynblatt and Gjostein5.3, showing the fit to n = 13 for t <17 hours and n = 4 for t > 25 hours.

5.5.6 The Possibility of Multiple Mechanisms

Sintering behavior occurs over at least two orders of magnitude of particle size, from 0.5 to 50 nm, and over a range of atmospheres, temperatures, supports, and metal loadings. While this work has postulated interparticle atomic or molecular migration as an alternate to particle motion, the two mechanisms are not exclusive. Wynblatt and Gjostein[5.14] suggest particle migration may be prevalent for particles under 5 nm, but that some form of interparticle transport must take place at larger sizes to account for observed rates of sintering.

5.6 Conclusions

A model for the sintering of supported metal catalysts, based on the dissociation of individual atoms from the metal crystallites, has been developed. The model postulates that large interactions between the support and metal atoms may potentiate the escape of metal to the surface. Evidence of high interaction between metal and a support is found for oxygen atmospheres (on oxide supports), in defect regions, and in the presence of contaminants. The model has been applied to a variety of simulated catalysts. The model can account for a wide variety of experimental observations of sintering. These include a strong influence of atmosphere, a high apparent activation energy, possible redispersion, and a variation in order from < 2 to ≥ 13 when sintering behavior is fitted to a simple power-law equation.

The model predicts that the rate of sintering increases with increasing width of the initial PSD. Metal is transported from small to large particles, and transport is more rapid as the difference in size of particles is increased. This model predicts the presence of particles smaller than the initial minimum particle size as sintering progresses.

During the early stages of sintering the model predicts a buildup of a concentration of migrating metal atoms or molecules. If this buildup is substantial then redispersion of the catalyst will be significant. Factors affecting the extent of surface species buildup are migration velocity, collision accommodation, activation energy for escape from the particle to the support surface, temperature and metal loading. The first three factors would be influenced by the atmosphere in which sintering occurs.

This model predicts a considerable variation in order of fit to a power-law equation of sintering. Variation of the order is predicted within a given sintering experiment. Distribution width and initial particle size are especially critical parameters with respect to the power-law order.

A variety of improvements to the presented model can be made, such as: 1. using the Kelvin equation to calculate the rate of loss of atoms from larger crystallites rather than approximating this by a constant rate of loss per crystallite, 2. including variations in the concentration of migrating atoms with position, and 3. modelling the support surface as inhomogeneous. It is felt that at the present time improvements in the model along the above lines are unwarranted because insufficient information is available to *a priori* estimate the extra parameters in these extended models. These new parameters, such as interfacial tensions, energy distribution of inhomogeneous support surface, etc., in the refined models would be determined by fitting them to experimental data and any improvement in the fit over the simple model would be due to an increase in the number of adjustable parameters. One of the strengths of the presented model is that it contains only three parameters, *i.e.* α, A, and E_a, (in the case of equation 5.15 A and E_a are the only adjustable parameters) and it is easier to assign physical significance to these parameters and hence use their magnitude in designing catalysts with greater stability.

5.7 Nomenclature

A' and B - constants in equation 2.

A - pre-exponential factor in rate of loss equation (equation 3).

a_o - diameter of metal atom (0.277 nm for Pt).

D - dispersion.

D_i - effective collision size of crystallite i.

E_a - activation energy for atom moving from crystallite to support.

E_s - activation energy for metal atom migration over support surface.

F - cumulative distribution function.

F_s - number of metal atoms migrating on support surface.

$\overline{F}_s$ - average number of free surface atoms in time increment.

G_i - atoms gained by crystallite i.

H_a - heat of adsorption of single metal atoms on support.

K - rate constant in equation 1.

k - number of size increments used when generating intial PSD.

k_B - Boltzmann's constant.

L_i - atoms lost by crystallite i.

ℓ_i - particle size, the length of the cube edge.

ℓ_{CRIT} - the particle size above which increase and below which decrease in size occurs (function of time).

ℓ_{max} - the size of the largest particle in the initial PSD.

ℓ_{min} - the size of the smallest particle in the initial PSD.

M - total number of crystallites (function of time).

m - mass of metal atom.

N_i - number of atoms in crystallite.

N_t - total number of metal atoms in all crystallites.

$N_{s,i}$ - number of surface metal atoms in crystallite it.

n - order in the power-law model (equation 1).

P_k - number particles assigned to size increments when generating initial PSD.

q - the number of metal atom along cube edge minus one.

r - particle radius (equation 2).

S - metal surface area (equation 1).

S_o - support surface area per metal atom ($N_t S_o$ = total support surface area).

T - temperature.

t - time.

V - molar volume of metal.

v - velocity of atoms on support surface.

α - sticking probability of atoms colliding with crystallite.

β - defined by equation 3.

ν - frequency factor (10^{13} sec $^{-1}$).

ϕ - spreading pressure of metal on support surface.

5.8 References

5.1 Ruckenstein, E. and Pulvermacher, B., AIChE Jour. 19, 356 (1973).

5.2 Ruckenstein, E. and Pulvermacher, B., J. Catal. 29, 224 (1973).

5.3 Wynblatt, P. and Gjostein, N.A., Scripta Metal. 7, 969 (1973).

5.4 Somorjai, G.A. in "X-Ray and Electron Methods of Analysis" (H. van Olphen and W. Parrish, eds.) Chap. VI, Plenum Press, New York, 1968.

5.5 Weller, S.W. and Montagna, A.A., J. Catal. 20, 394 (1971).

5.6 Johnson, M.F.L. and Keith, C.D., J. Phys. Chem. 67, 200 (1963).

5.7 Chem. Abstr. 76 - 145405q (patent, Ger. Offen. 2, 137, 554).

5.8 Chem. Abstr. 68 - 31814b (patent, Neth. Appl. 6, 614, 074).

5.9 Herrmann, R.A., Adler, S.F., Goldstein, M.S. and De Baun, R.M., J. Phys. Chem. 65, 2189 (1961).

5.10 Geus, J.W. in "Chemisorption and Reactions on Metallic Films" (J.R. Anderson, ed.) Chap. 3, Academic Press, London, 1971.

5.11 Lewis, B., Sur. Sci. 21, 289 (1970).

5.12 Phillips, W.B., Deslodge, E.A. and Skofronick, J.G., J. Appl. Phys. 39, 3210 (1968).

5.13 Pashley, D.M., Stowell, M.J., Jacobs, M.H. and Law, T.J., Phil. Mag. 10, 127 (1964).

5.14 Wynblatt, P. and Gjostein, N.A., Prog. Sol. St. Chem. 9 (to be published).

5.15 Plante, E.R., Sessoms, A.B. and Fitch, K.R., J. Res. Nat. Bur. Stand., Sec. A, 74, 647 (1970).

5.16 Zinsmeister, G., "Proc. Intern. Symp. on Basic Problems in Thin Film Physics" (R.N. Mayer and H. Mayer, eds.) p. 33, 2nd ed., Vandenhoeck Ruprecht, Gottingen, 1966.

5.17 Lewis, B., Sur. Sci. 21, 273 (1970).

5.18 Poppa, H., J. Appl. Phys. 38, 3883 (1967).

5.19 Halpern, V., J. Appl. Phys. 40, 4627 (1969).

5.20 Neikam, W.C. and Vannice, M.A., "Proc. V Int. Cong. Catal." p. 609 North-Holland, Amsterdam, 1973.

5.21 Tabatadze, D.G., Myasnikov, I.A. and Evstigneeva, L.A., Russ. J. Phys. Chem. 46, 1488 (1972).

5.22 McLean, M. and Hondros, E.D., J. Matr. Sci. 6, 19 (1971).

5.23 "Handbook of Chemistry and Physics", 51st Ed., p. F-23, Chemical Rubber Company, Cleveland, 1970.

5.24 Gjostein, N.A., "Metal Surfaces", Chap. IV, Amer. Soc. for Metals, 1963.

5.25 Van Hardeveld, R., and Hartog, F., Sur. Sci. 15, 189 (1969).

5.26 Maat, H.J. and Moscou, L., "Proc. 3rd Int. Congr. Catal." p. 1277, North-Holland, Amsterdam, 1965.

5.27 Emelianova, G.I., and Hassau, S.A., "Proc. 4th Int. Congr. Catal.", p. 1329, Rice University Printing, Houston, 1969.

CHAPTER 6

EXPERIMENTAL STUDIES OF SINTERING OF SUPPORTED PLATINUM CATALYSTS

6.1 Survey

As discussed in Chapter 5, supported metal catalysts show changes in metal surface area during use or treatment at high temperatures, a process known as sintering. Sintering is of concern industrially because a loss of catalytic activity generally occurs, associated with an increase in the particle size of the metal. A number of patents have been issued for processes designed to redisperse sintered catalysts (*e.g.* references[6.1, 6.2]).

A number of investigators have studied catalyst systems under treatment conditions leading to sintering. In this chapter their work is briefly reviewed, and a series of experiments performed in this laboratory are described. From this data the sintering process appears to be extremely complex, and further experiments will be necessary to establish the critical parameters in this process.

Many authors[6.3 -6.10], in trying to describe the kinetics of sintering, have fitted data to the simple power law equation of the form

$$\frac{ds}{dt} = Ks^n \qquad 6.1$$

where s is the metal surface, n is generally reported as an integer, and an activation energy is lumped in the constant K. Both Herrmann *et al.*[6.3] and Matt and Moscou[6.4] report n values of 2 for Pt/Al_2O_3

catalysts in oxidizing environments. The latter authors examined their samples under the electron microscope before and after sintering. Initially the Pt in their catalysts consisted of particles in the 1 nm range. After treatment in air, they reported the presence of 1 to 50 nm particles. Somorjai[6.5] studied supported Pt catalysts sintered in an oxidizing atmosphere by small angle x-ray scattering. Based on data obtained by this technique, he proposed a modified growth law similar to that advanced by Wynblatt and Gjostein[6.6], of the same form as Equation 6.1 but with a K value which decreases exponentially with increasing average particle radius (see Equation 5.2). Somorjai[6.5] also estimated the activation energy to be 52 kcal for oxidizing atmospheres. However, small angle x-ray diffraction is not equally sensitive to all sizes of Pt particles.

Sintering kinetics change in a reducing environment, in general associated with a higher value of n. Somorjai[6.5] found a lower activation energy for an H_2 atmosphere, about 20 kcal, but a much lower rate pre-exponential factor, and hence a lower overall rate of sintering as compared to an oxidizing atmosphere. Gruber[6.7] and Hughes *et al.*[6.8] found n values in the 6 to 8 range for sintering at 500°C in the H_2 atmospheres.

Finally, two special studies have been made of Pt/Al_2O_3 systems. Wynblatt and Gjostein[6.6, 6.9] used electron microscopy to study Pt particles prepared on specially thin (10 nm) alumina substrates. They found minimal surface migration for a sample where Pt particles were larger than 5 nm, and cite interparticle transport for a mechanism in these and larger Pt particles. High values of n (>8) are attributed to facet inhibited growth; *i.e.*, expansion of a Pt particle must await nucleation of a ledge on a smooth face. Experimentally they observed n values from about 3 to 13 for sintering in air. Huang and Li[6.10] studied Ostwald ripening for large (>100 nm) Pt particles on α - Al_2O_3. Their n value of the order of 5 led them to conclude that surface diffusion is the mechanism of the growth process. Gregg and Howlett[6.11] similarly concluded that surface diffusion was the agglomeration process for the sintering of metal spheres observed under the optical microscope. Both Wynblatt and Gjostein[6.9] and Huang and Li[6.10] observed that the sintering rate increased with increases in oxygen concentration in an O_2/N_2 mixture.

As detailed in Chapter 5, two models have been developed to account for particle size changes occurring during sintering. Ruckenstein and Pulvermacher[6.12, 6.13] postulated crystallite migration and collision as a sintering mechanism and developed and solved a model for homogeneous and partially heterogeneous surfaces. This model can account for power law orders from 2 (rate controlled by fusion of particles) to about 8 (rate controlled by diffusion of particles). It also predicts that after a certain time a universal dimensionless curve will fit the particle size distribution of a catalyst. In Chapter 5 a model was developed which postulated the loss from particles of atomic or molecular species, followed by surface diffusion and recapture, as the sintering mechanism (see also references [6.14] and [6.15]). This model can account for power law orders less than zero (*i.e.* redispersion) up to 13 and higher. The order is found to depend heavily on the nature of the particle size distribution. While under either model the decrease in surface energy provides the driving force for metal agglomeration, the difference between transport as a crystallite or as an atomic species leads to significant differences in predicted growth kinetics. This point is discussed in further detail below in conjuction with some experimental results.

6.2 Results

Four series of experiments were conducted to explore the sintering behavior of supported Pt catalysts. In one series catalysts were sintered at varying temperatures for a fixed time period, and changes in the catalyst were monitored by electron microscopy and/or gas uptake. In a second series, the temperature was fixed and the time of sintering varied. In a third set of runs the sintering behavior of a catalyst batch into which a portion of pre-sintered catalyst containing large Pt particles was mixed was compared to that of an unmixed catalyst. Finally, electron micrographs were recorded of the same catalyst specimen area before and after reduction and sintering in an inert atmosphere.

6.2.1 Constant Time/Variable Temperature Treatments

Both commercial catalyst samples (Engelhard 0.5% Pt on Al_2O_3) and prepared specimens (4.76% Pt on Alon Al_2O_3) were heated 16 hours in oxygen at varying temperatures, and the dispersion or particle size were measured. In the case of the prepared catalyst, small samples (<0.5 g.) were used, and the progress of sintering was checked by electron micrographs. For the commercial catalyst, batches of sufficient size (8 - 10 g) were used to allow gas uptakes to be measured after sintering.

Figure 6.1 shows the size range of particles observed in the micrographs of several specimen areas of the Alon supported catalyst. The

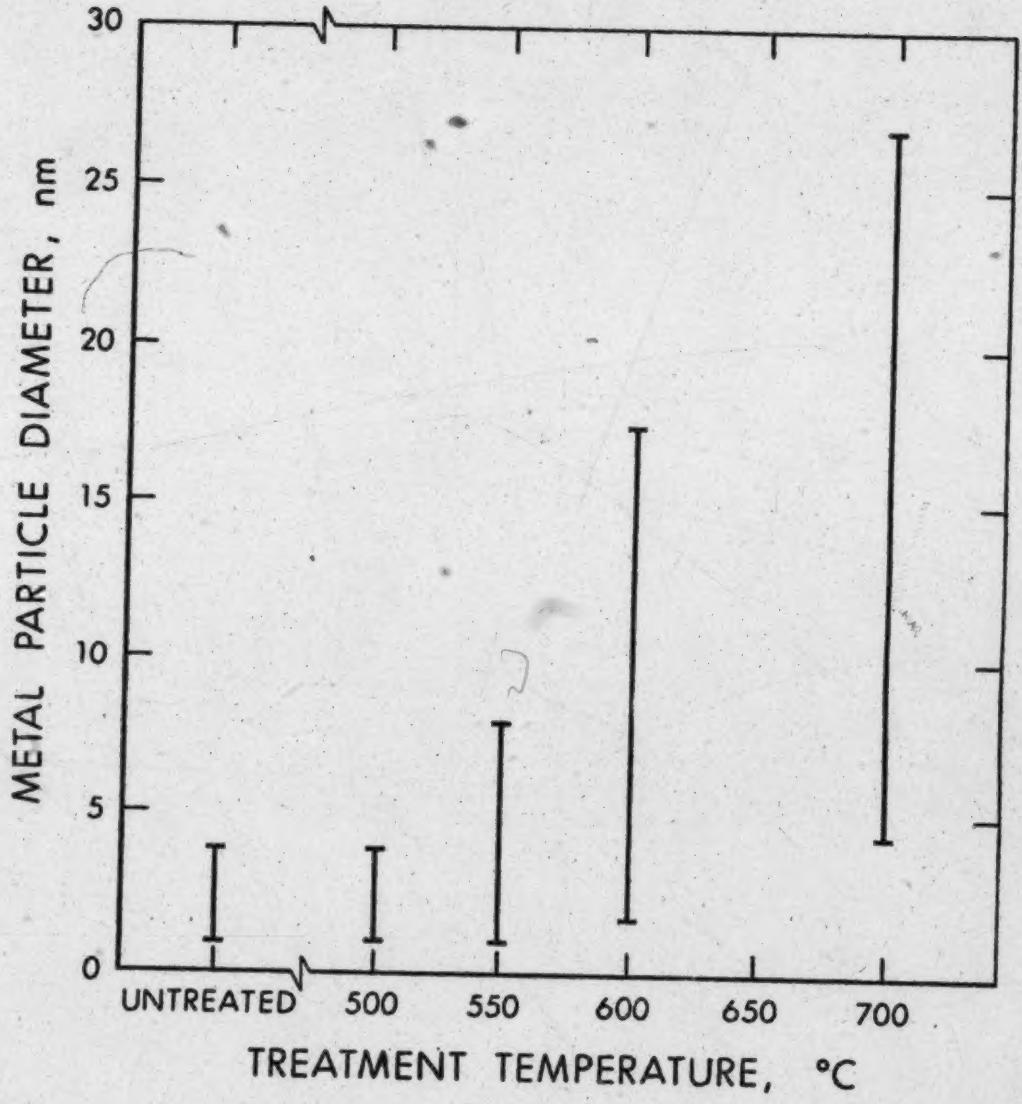

Figure 6.1: Effect of treatment temperature on metal particle size range, measured from electron micrographs. Batches of 4.76% Pt on Alon catalyst were heated 16 hr. in flowing oxygen at the indicated temperature.

lower limit of 1 nm shown in Figure 6.1 is considered the minimum size where metal size contrast can accurately be distinguished from the contrast inherent in the support (Chapter 3, reference [6.16]). No change was observed in the metal particle sizes following 16 hour heating in oxygen at 500°C. Significant particle growth was observed for 16 hour treatment at 550°C and for all higher temperatures. For the specimens sintered by 600° and 700°C, particle growth was sufficiently great to significantly lower the number of particles in a given field of view, hence the size ranges shown in Figure 6.1 for these two cases, based on about five fields of view, must be considered approximate. (Micrographs from this series of experiments are shown in Figure 5.1.) It is clear that the platinum particles grow to the same order of magnitude as the particles in the support, 10 to 30 nm, a point which will be discussed further below.

Figure 6.2 shows the variation of metal dispersion with treatment temperature for the 0.5% Pt commercial catalyst as measured by hydrogen and oxygen uptake at 0°C. The open triangles in Figure 6.2 show oxygen uptakes for the same catalyst sample, which was successively sintered overnight in flowing oxygen at 500°, 600° and 700°C. The circles in Figure 6.2 show oxygen uptakes (open circles) and hydrogen uptakes (solid circles) for separate batches of catalyst sintered at the indicated temperatures. Prior to gas adsorption measurements the catalysts were reduced by cooling or heating in flowing hydrogen from the indicated sintering temperature to 500°C, the sole exception being the 700°C successively sintered case where the catalyst was cooled to 600°C in oxygen and reduction was started at 600°C. Catalysts were outgassed in flowing helium for two hours (successively sintered cases)

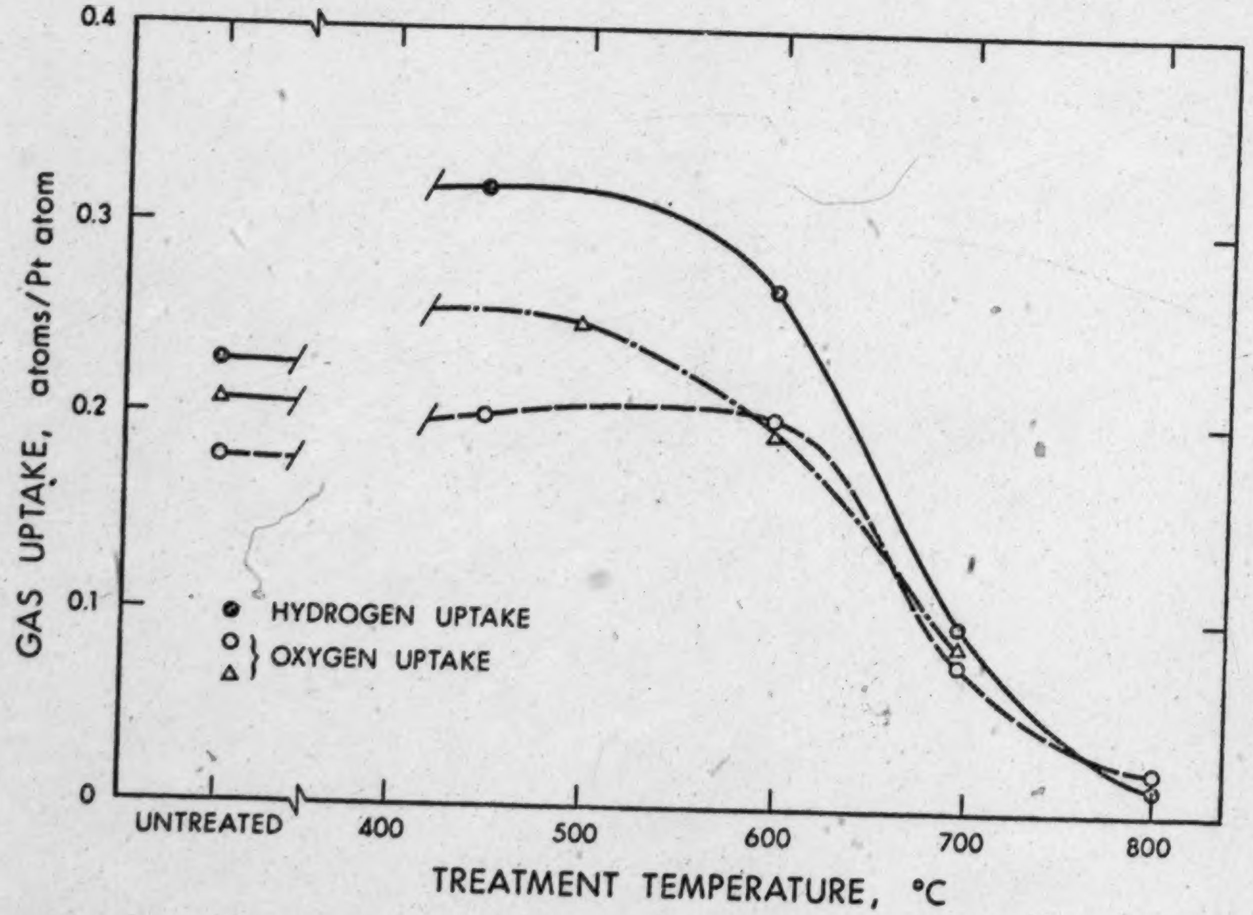

Figure 6.2: Effect of treatment temperature on metal dispersion for 0.5% Pt on Al_2O_3, by gas uptake. (See text for treatment conditions.

or one hour (separately sintered cases) at 500°C before being cooled for gas uptake measurement. Use of the catalysts for other experiments prior to the sintering study may account for the 15% difference in initial oxygen uptake observed for the untreated catalyst samples.

It is immediately evident from Figure 6.2 that at moderate sintering temperatures a redispersion of metal occurs for both catalysts. The increase in hydrogen uptake for the sample sintered at 450°C is far greater than the increase in oxygen uptake of the same sample. However, several authors (Chapter 4, references 6.17-6.19) have noted that relative to oxygen, hydrogen uptakes increase as dispersion increases. Hence, for redispersion, particularly to very small Pt particles, larger increases in hydrogen uptake as compared to oxygen would be expected.

It appears that changes in dispersion are strongly related to the atmosphere in which the catalyst is treated. For example, a portion of the 0.5% Pt on Al_2O_3 catalyst for which the oxygen uptake had been determined was used in another series of experiments, during which time it was exposed to flowing hydrogen at 500°C for a total of 10 hr, and to flowing helium at 500°C for 22 hr. The subsequent oxygen uptake increased by only 0.004 atoms/Pt atom (2% of the total uptake) from the initial oxygen uptakes, a value of the order of the accuracy of the uptake measurement. Comparing this with the results in Figure 6.2 indicates that dispersion changes are far more extensive for shorter treatment in oxygen, for which 16 hr treatment at 500°C gave a 19% increase in oxygen uptake.

6.2.2 Variable Time/Constant Temperature Treatments

Several samples of a second commercial catalyst (Engelhard 0.3%

Pt on Al_2O_3) were treated in air at 575°C for varying time periods, from 6 hr to over one month. Based on the results from overnight sintering reported above, it was felt that sintering at 575°C would provide a rate of change of dispersion sufficiently slow to allow monitoring of the kinetics. However, sintering was unexpectedly rapid; after 6 hr the uptake of oxygen had dropped from 0.350 atoms/atom Pt (for the unsintered specimen) to 0.019. At this low an uptake, gas adsorption measurements are subject to large relative error.

The unsintered catalyst was examined by electron microscopy, and metal particles were observed between 2 and 4 nm. Figure 6.3 shows the observed particle sizes for four of the sintered catalyst samples (6, 12, 120 and 360 hr of sintering). The rapid growth of large metal particles even after a six hour sintering period is evident from the observed metal particle sizes.

Comparison with the results of the earlier experiments involving the 0.5% Engelhard catalyst is difficult, however. Both catalysts are of the surface coated type, where the metal particles are in a thin layer on the outside of the alumina pellet. Thus while 0.3% and 0.5% are nominal metal loadings, the actual concentration of metal in the outer region is unknown and could vary from one catalyst lot to another.

6.2.3 Catalyst Mixture Experiments

A series of experiments were designed to check the effect of addition of a small portion of heavily pre-sintered catalysts on sintering kinetics. A portion of the 2.03% Pt on Alon alumina catalyst was heavily sintered (16 hr at 700°C in flowing oxygen) and had an oxygen uptake of 0.0313 atoms/Pt atom; examination of electron

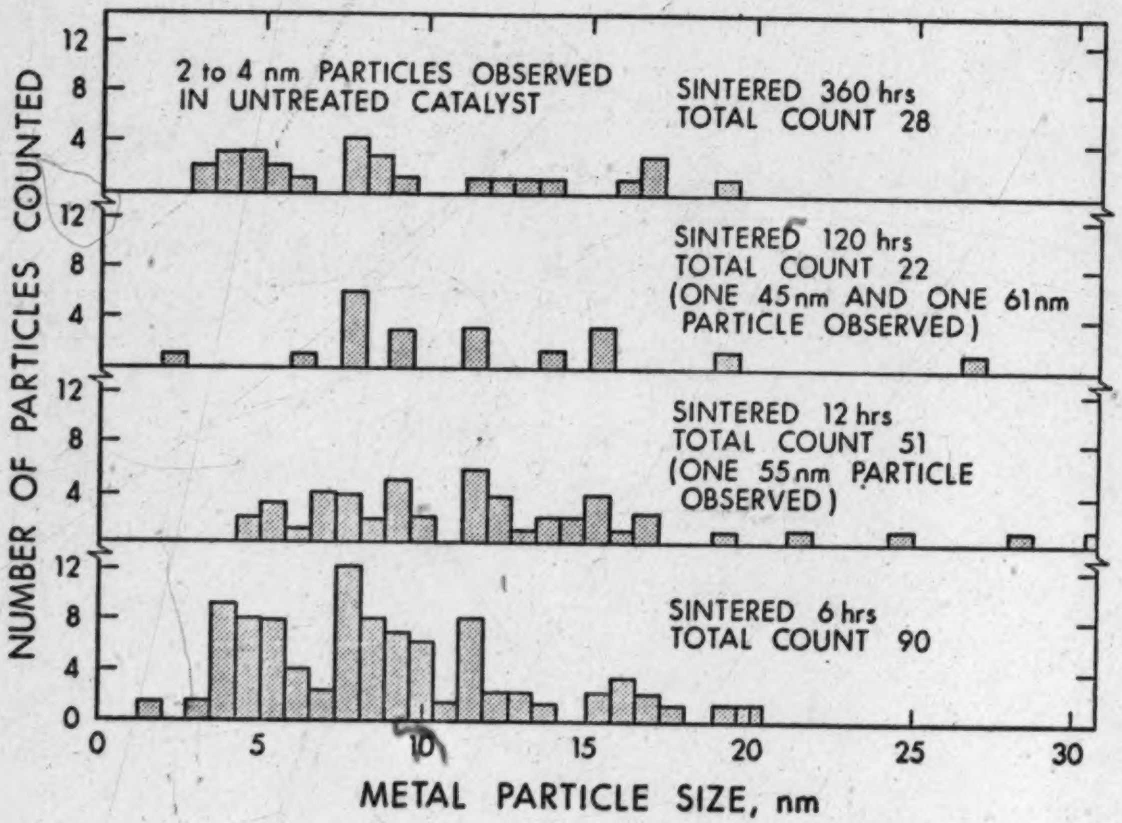

Figure 6.3: Particle size distribution from electron micrographs of a sintered Engelhard 0.3% Pt on Al_2O_3 catalyst. Batches were heated at 575°C in air for the indicated time.

micrographs confirmed the presence of large metal particles (range observed was 2.5 to 27 nm). The fresh catalyst had an initial oxygen uptake of 0.256 atoms oxygen/Pt atom.

Four batches of catalyst were then prepared; two of the fresh catalyst, and two of a mixture of 23.1 wt % of the heavily sintered catalyst and 76.9 wt % of the fresh catalyst. The batches of mixed catalyst were crushed, wetted and redried at 110°C to promote a thorough mixing of the sintered and unsintered portions. One mixed batch and one fresh batch were sintered 16 hr in flowing oxygen at 575°C and their oxygen uptakes were measured. These samples were subsequently sintered at 610°C for 16 hr, while the other two batches were sintered at 630°C for 16 hr. Samples were sintered, reduced (by cooling in flowing hydrogen from the sintering temperature to 500°C) and outgassed 1 hr (at 500°C in helium) under identical conditions, the exception being the mixed sample sintered at 610°C which was reduced and outgassed at 610°C.

Table 6.1 shows the initial oxygen uptakes for the four cases. The treatment at 575°C appeared to cause a slight redispersion in the samples. However, for the other two temperatures the mixed catalyst sinters significantly more extensively than the unmixed catalyst: after the 610°C treatment the unmixed catalyst had 66% of its original area compared to 43% for the mixed, after the 630°C treatment the unmixed catalyst had 29% of its original area compared to 3% for the mixed. From this data it appears that the presence of a portion of heavily sintered catalyst containing large metal particles speeds the sintering of a catalyst. The implications of this conclusion on proposed sintering mechanisms is discussed below.

Table 6.1: Effect of Addition of a Portion of Presintered Catalyst on Sintering Rate of a 2.03% Pt on Alon Catalyst

Treatment	Oxygen Uptake, atoms O/Pt atom	
	Unmixed	Mixed
Unsintered	0.256	0.204*
Sintered at 575°C	0.258	0.218
Sintered at 610°C	0.169	0.087
Sintered at 630°C	0.073	0.006

*By calculation from the dispersions of the unsintered and presintered samples.

Comparison of the results in Figure 6.1 and Table 6.1 indicates a dependence of sintering behavior on metal loading for the prepared catalysts. The two Alon supported catalysts (4.76% and 2.03% Pt) were similarly prepared, but the more heavily loaded catalyst shows sintering at 550°C (growth of Pt particles up to 80 nm), while the less heavily loaded catalyst shows no significant change in dispersion after similar treatment at 575°C. Pt particles from 1 to 3 nm were observed in the reduced 2.03% catalyst, compared to 1 to 4 nm for the reduced 4.76% catalyst.

6.2.4 Effect of Reduction and Sintering on Individual Metal Particles

Unreduced 2.03% Pt on Alon catalyst was deposited onto a specially prepared 'holey' film described in Chapter 2. Benchmarks on the grid made it possible to record electron micrographs of the same area before reduction, after reduction (1/2 hr in hydrogen at 300°C), and after various thermal treatments in flowing helium. Table 6.2 lists the details of treatment for the grids.

While the intention of these experiments was to follow the effect of various treatments on representative catalyst areas, caution must be used before conclusions based on these studies are drawn about catalyst sintering. In several important ways a catalyst supported on a holey carbon film mounted on a tungsten grid differs from a pure catalyst specimen. Other factors limit the accuracy of size and spatial position determinations of supported metal particles. For example:

a) Evidence appeared in about half the micrographs of small shifts (10 nm) in portions of the Alon substrate. In

Table 6.2: Grid Treatments

Grid	Areas Examined	Treatment History*
1	9	The grid was reduced at 300°C for 1/2 hr and some contamination was noted. After sintering 3 hr at 500°C (inserted in hot furnace), heavy contamination was noted. The film ruptured after a further 3 hr at 500°C.
2	9	The grid was reduced at 300°C for 1/2 hr and some contamination was noted. The film ruptured after 5 hr sintering at 500°C.
3	4	The grid was reduced at 300°C for 1/2 hr and some contamination was noted. The film ruptured after 4 hr sintering at 500°C.
4	4	The grid was reduced at 300°C for 1/2 hr and heavy contamination was noted; sintered 2.5 hr at 500°C, contamination reduced; film ruptured after 72 hr sintering at 550°C.
5	4	The grid was reduced at 300°C for 1/2 hr and deposits on grid noted. Subsequently the grid was discarded.
6	4	The grid was reduced at 300°C for 1/2 hr and some contamination was noted. After sintering 4 hr at 500°C, heavy contamination was noted. The grid was sintered an additional 4 hr at 500°C and a very heavy contamination was noted. After sintering 4 hr at 550°C, very heavy contamination was noted.

*All sintering treatments were in flowing helium and started in cold furnace unless otherwise noted; all reductions were in flowing hydrogen.

Table 6.2: (continued)

Grid	Areas Examined	Treatment History
7	3	The grid was reduced at 300°C for 1/2 hr and heavy contamination was noted. After sintering 4 hr at 500°C, some contamination was noted. The film ruptured after 4 hr sintering at 600°C.

addition, a few micrographs showed evidence of major movements (>10 nm) of the substrate. Thus the position of metal particles from micrograph to micrograph may in part be affected by movement in the substrate, arising from loss of H_2O during the reduction step (the first time the catalyst is heated above 110°C) or the high temperatures realized in thermal treatment.

b) Crushing the catalyst and dropping it on the grid gave catalyst clumps of various size. In selecting an area to be examined, a balance had to be struck between very thin clumps of catalyst, where electron microscope imaging clarity was good but the amount of catalyst was low, and thick clumps, where imaging clarity was reduced but the catalyst more closely approximated the bulk typical in a sintered catalyst. The result was a compromise which often reduced the quality of the image over what could be expected in ideal conditions. Where possible, thin regions at the edge of thick clumps were chosen, but this frequently led to a considerable range of elevation in the specimen, a factor which casues resolution and detection problems[6.16].

c) Contamination by carbon was far greater than that observed in conventional micrographs, both after reduction and after thermal treatment. There are two sources of carbon to contaminate the catalyst. One is from the cracking by the electron beam of residual hydrocarbon vapors within the microscope from the oil diffusion pump. However, under normal operation of the microscope, with a liquid nitrogen filled "cold finger" in the area of the sample, such contamination is quite low (see, for example, the micrographs in Chapter 3 and 5). The second source is the carbon in the film itself, which during reduction and sintering treatments may have migrated onto the catalyst from the film. Given the high contamination evident in many of the micrographs as compared to conventional micrographs, we suspect this latter source to be significant; if so, then catalysts treated on grids differ from ordinary catalysts due to the presence of mobile or vaporised carbon.

d) Evidence from micrographs also suggests that platinum can migrate onto the carbon, and may accumulate there in preference to remaining on the alumina. Figure 6.4 a shows two micrographs of the same specimen area of grid 6 at relatively low magnification, before reduction and after the second thermal treatment. The large dark region in the lower left hand corner of Figure 6.4 a appears to be a Pt crystal on the carbon. Similarly, Figure 6.4 b shows three micrographs of another region of grid 6 before reduction and after the second and third thermal treatments. Not only are the development of metal deposits (in the areas marked "a", "b", "c", and "d" in Figure 6.4 b, for example) evident after sintering, but their growth or decay with increasing sintering is also demonstrated. Access by the migrating platinum to the carbon film, and possibly to the metal grid, is a second major difference between grid treated catalysts and ordinary samples.

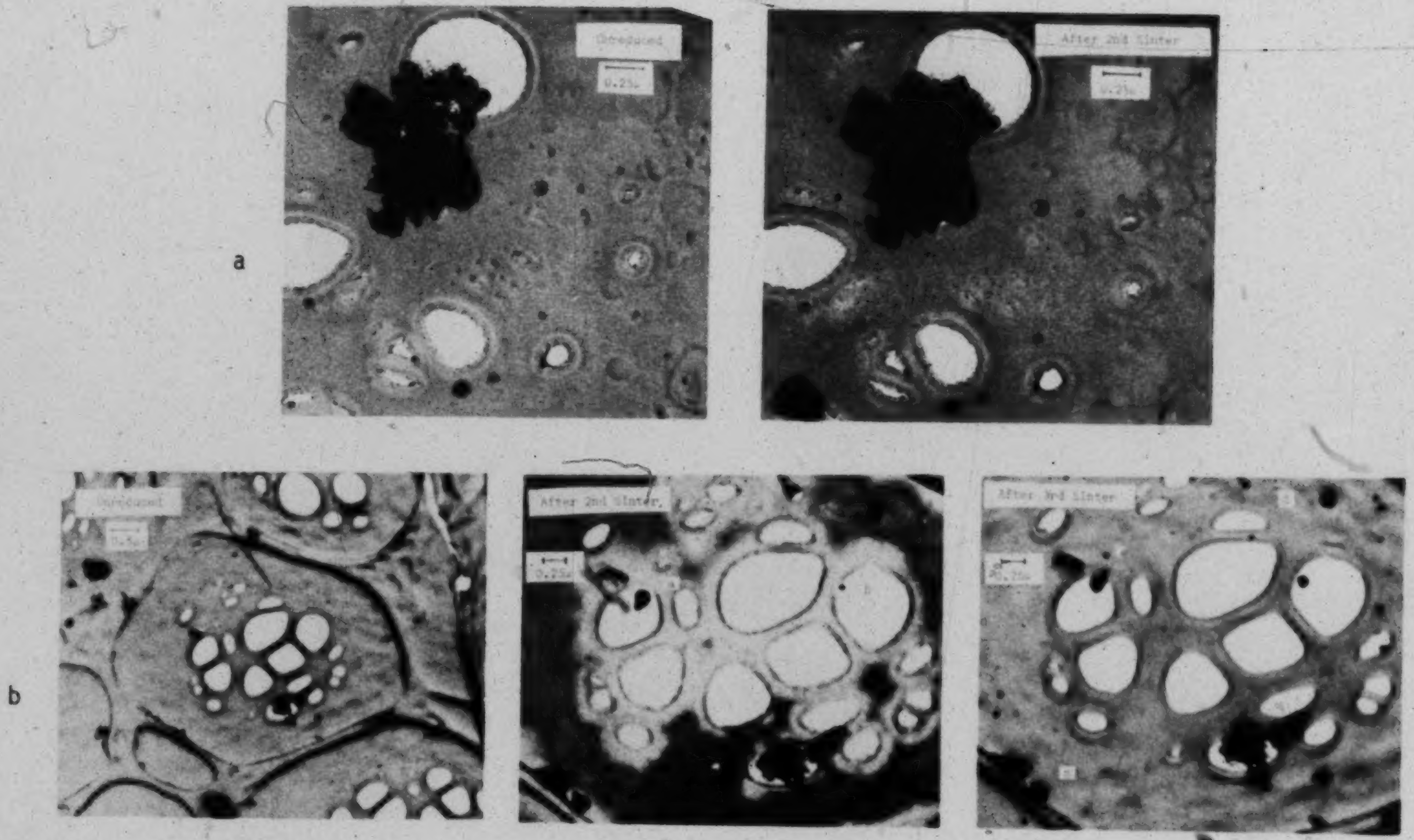
a
Unreduced
0.25µ
After 2nd Sinter
0.25µ
b
Unreduced
0.5µ
After 2nd Sinter.
0.25µ
After 3rd Sinter
0.25µ

Figure 6.4 (a), (b). Low magnification micrographs from grid 6 showing the accumulation of metal on the carbon film with successive thermal treatments.

With these cautions in mind, several observations about the growth of Pt particles on supported metal catalysts may be made from micrographs of the grid treated catalysts. (Photographic reproduction may have reduced the quality of the micrographs, especially for fine detail; prints of the original micrographs are availabe from the author on request.)

In the unreduced catalyst the Pt is extremely disperse. While typically Pt particles with images corresponding to 2 nm were noted, comparison of a sintered and unreduced catalyst (for example, Figure 6.5) shows that much of the Pt evident after sintering does not show up in the unreduced state, presumably because it is atomically dispersed and has not agglomerated into crystals. (In Chapter 3 the difficulty of relating image size to object size, particularly for detail smaller than 2.5 nm, was discussed. All size measurements reported here are image sizes corrected for magnification, with a probable variance of up to ± 1 nm from true object sizes.) In Figure 6.6 larger Pt crystallites than normal appear in the unreduced catalyst; this will be discussed below.

Some agglomeration of Pt takes place during reduction of the catalyst; examination of Figures 6.6, 6.7, and 6.8 illustrate this. In Figure 6.6, despite heavy carbon contamination in the micrograph of the reduced catalyst, growth of the Pt clusters as compared to the unreduced catalyst can be noted. In both Figures 6.7 and 6.8 numerous larger particles up to 4 nm appear, and a general agglomeration of Pt is evident. This agglomeration is somewhat remarkable considering the mild temperatures (300°C) used in the reduction step. Close inspection of Figures 6.7 and 6.8 show that some of the particles noted

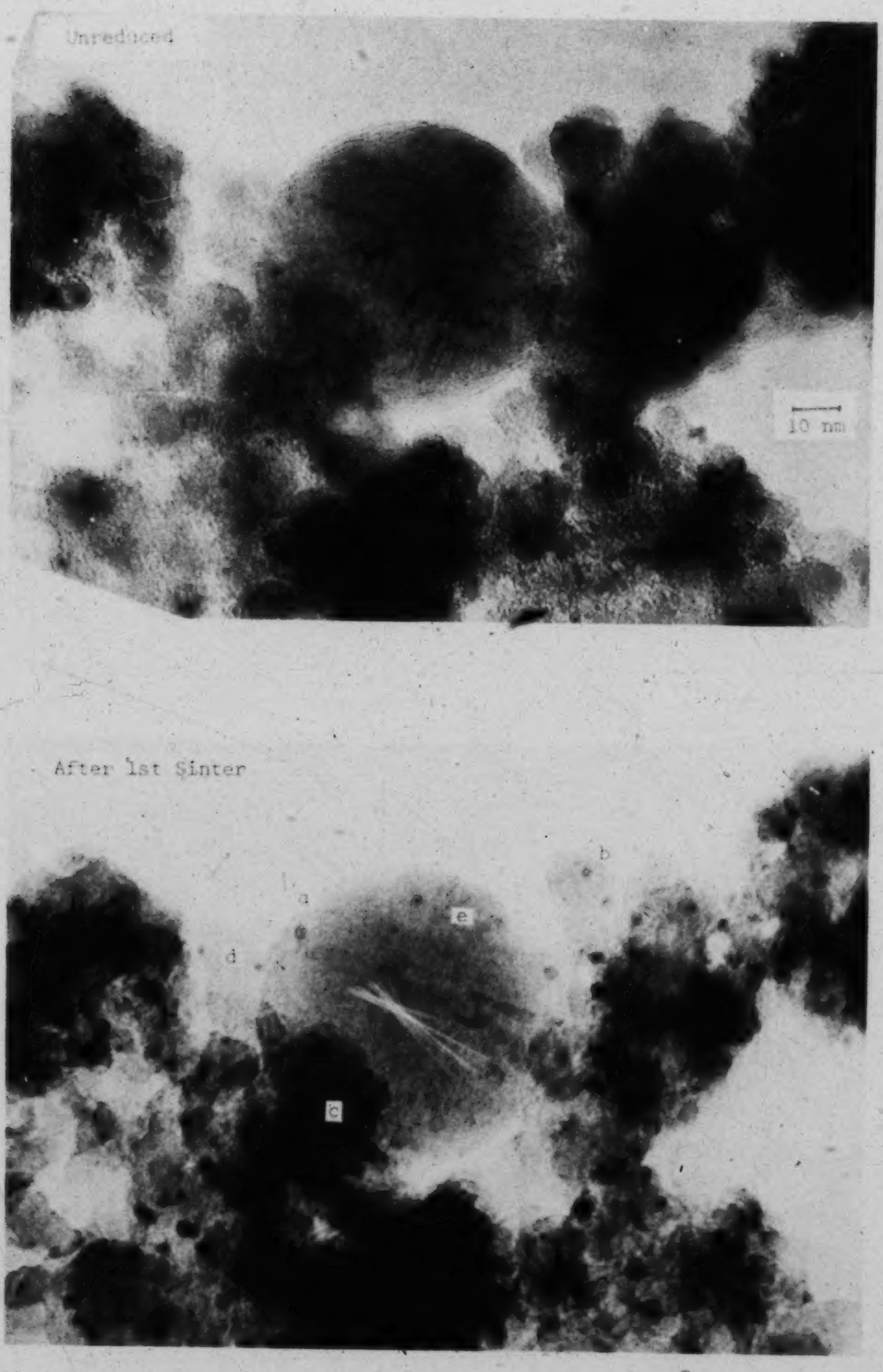
Unreduced
10 nm
After 1st Sinter
b
a
e
d
c

Figure 6.5 Micrographs from grid 4 showing the same area before reduction and after one thermal treatment at 500°C.

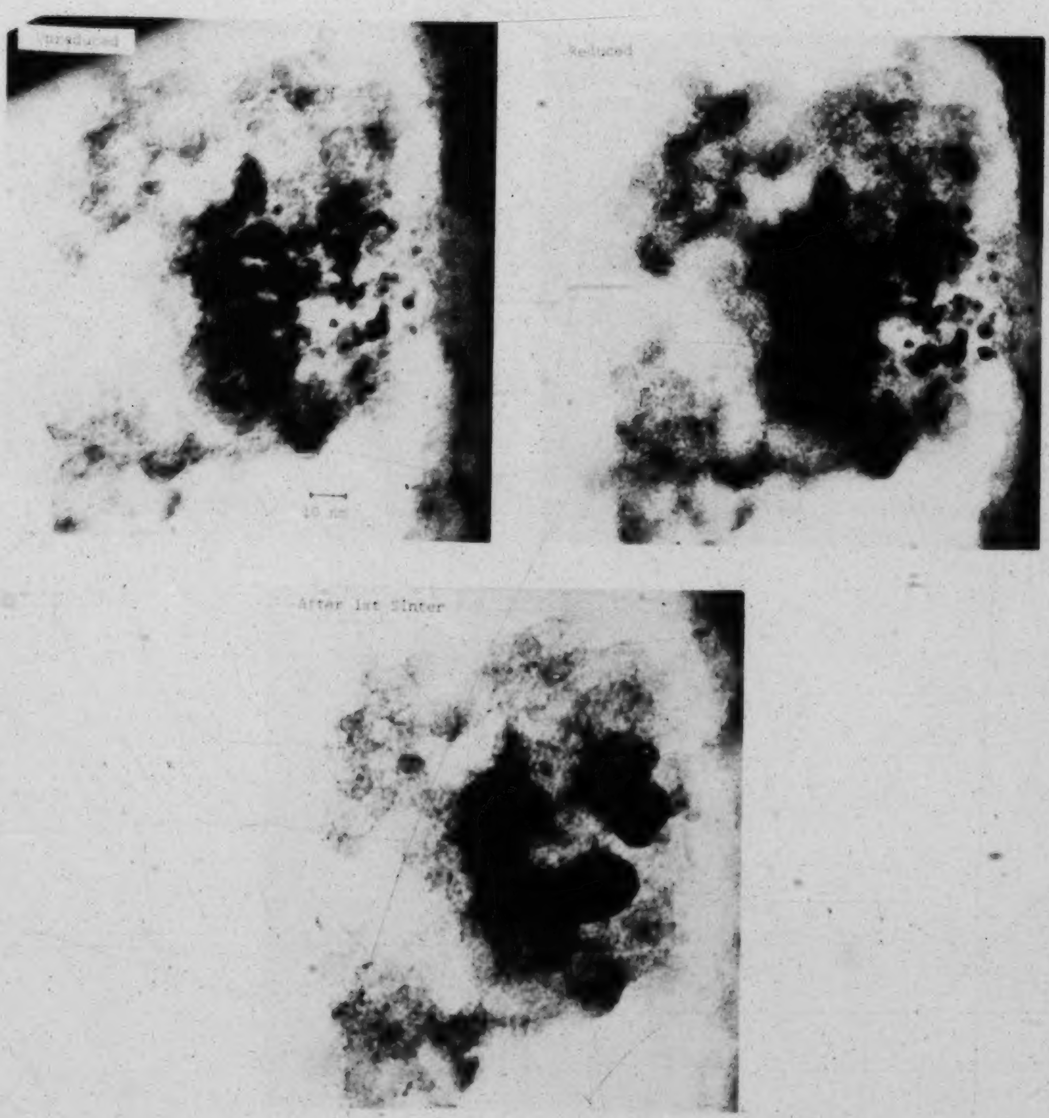
Unreduced
Reduced
10 nm
After 1st Sinter

Figure 6.6 Micrographs from grid 7 showing the same area before and after reduction and after one thermal treatment at 500°C.

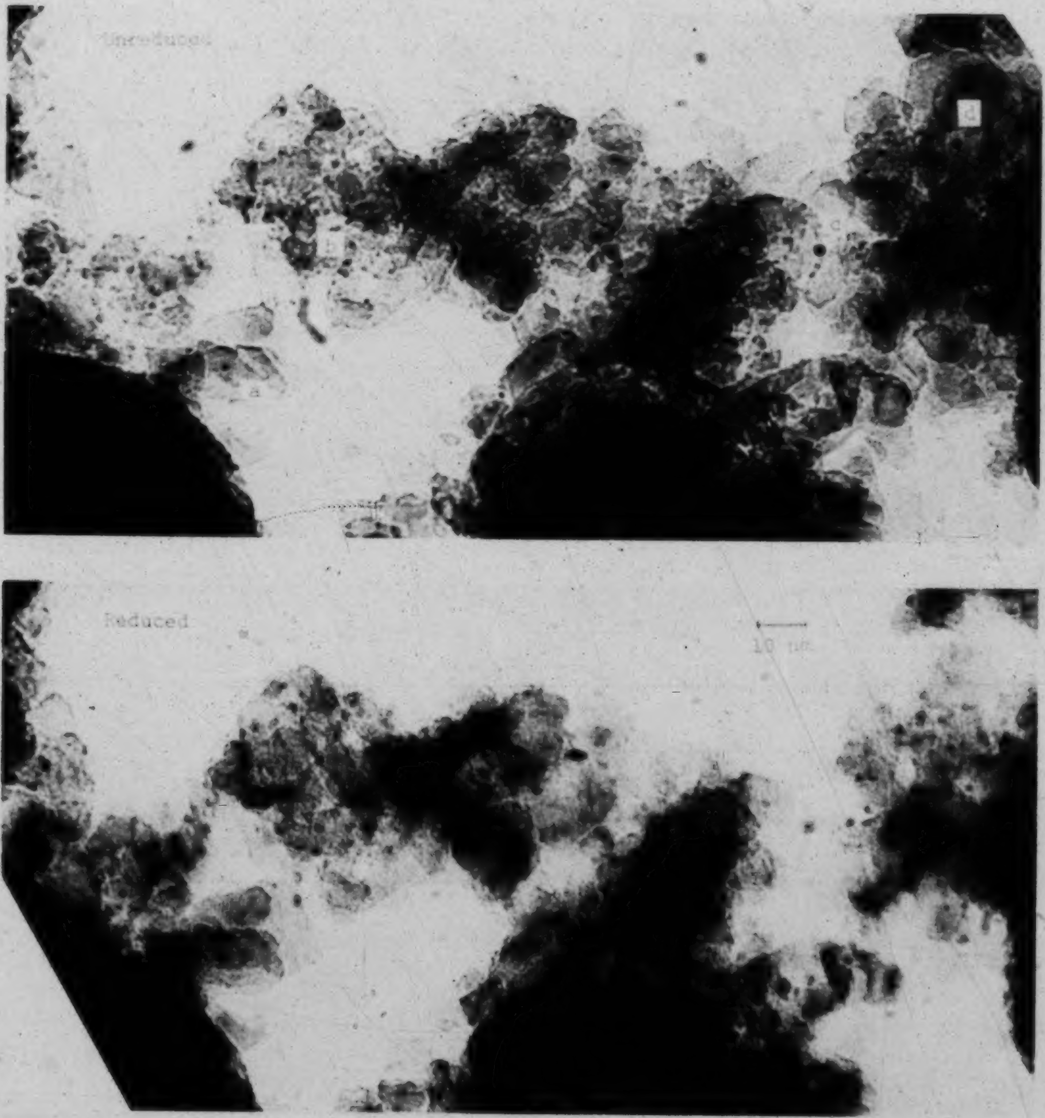
Unreduced
d
Reduced
10 µm

Figure 6.7 Micrographs from grid 2 showing the same area before and after reduction.

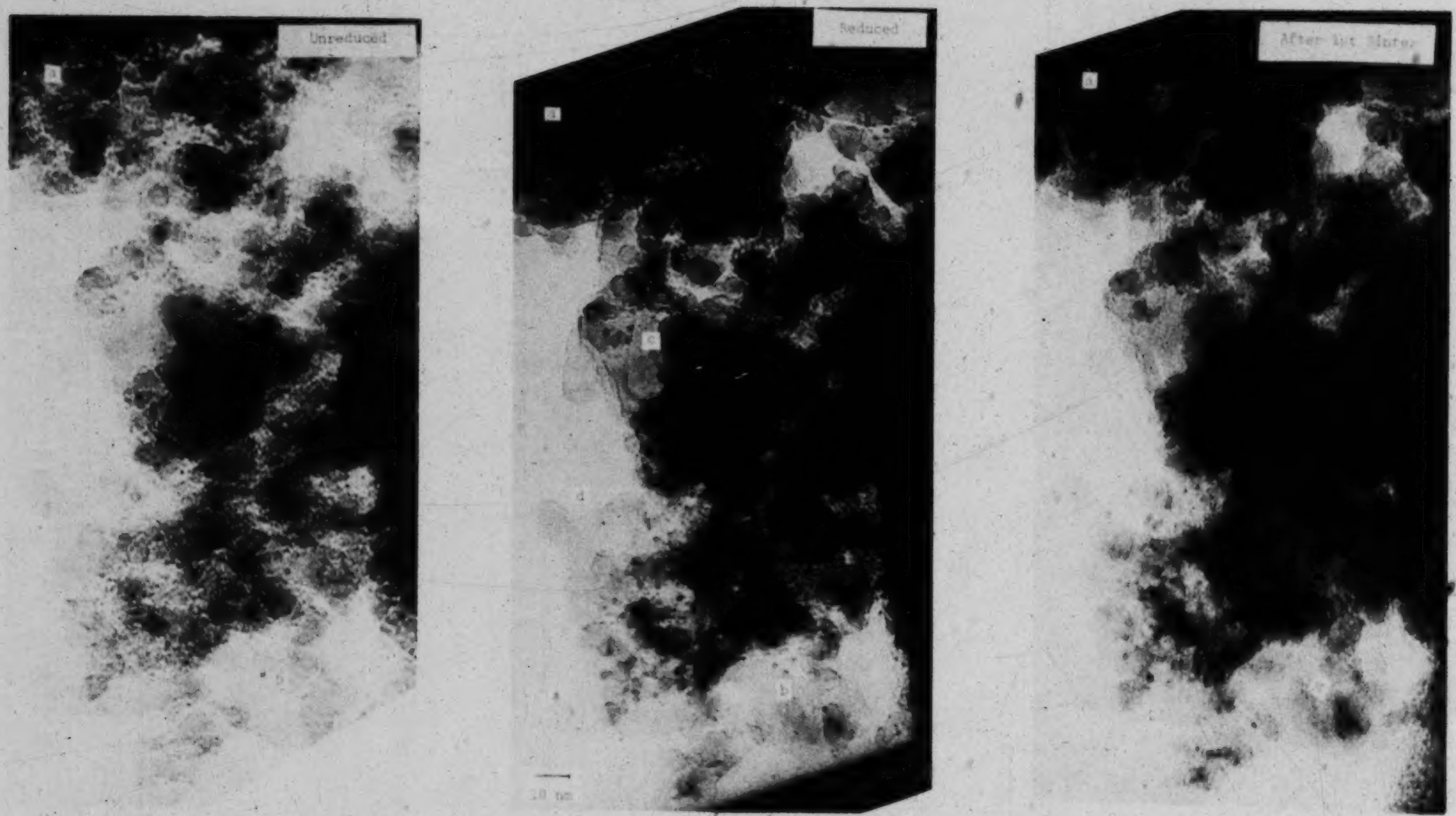
Unreduced
a
Reduced
a
c
d
b
10 nm
After 1st Sinter
a

Figure 6.8 Micrographs from grid 1 showing the same area before and after reduction and after one thermal treatment at 500°C.

in the unreduced catalyst remain fixed in location during reduction. In Figure 6.7, for example, five particles are illustrated (one each at "a", "b", and "c" and two at "d") which appear in both micrographs. Similarly, two particles each by regions "a" and "b" in Figure 6.8 appear before and after reduction. Not all particles in the reduced catalyst correspond to a particle in the unreduced catalyst; however, the small size of particles involved and the thickness of the specimen make simultaneous resolution of all small Pt particles unlikely[6.16].

Thermal treatment at 500°C leads to further agglomeration of Pt, as shown in Figure 6.6 and 6.8. In Figure 6.8, a consolidation of Pt particles is generally evident. In the region "c", a number of small particles evident in the reduced catalyst disappear and are replaced by one large (4 nm) particle in the sintered catalyst. A similar agglomeration is strikingly evident in Figure 6.6, where particles of the order of 20 nm in size appear after thermal treatment at 500°C. Once again, there is evidence of some particles remaining stationary during treatment. In Figure 6.5, particles observed after thermal treatment at regions "a", "b", and "c" correspond to particles observed in the unreduced state. This is not true of all the particles in Figure 6.5, however, such as those by "d" and "e". In these cases no particles are evident in the unreduced state, although the problem of detectability again exists for the very small unreduced particles. In Figure 6.8, the two particles each in regions "a" and "b" again remain stationary during thermal treatment at 500°C, although two apparently new particles appear by "d".

Both Figures 6.6 and 6.8 suggest that some localized effects are significant in the changes in metal particles associated with reduction and thermal treatments. For example, in Figure 6.6 an unusually high density of Pt exists in the unreduced catalyst in the catalyst area. While the reasons for this concentration of Pt salt are unknown, it results in Pt particles 5 to 10 times larger than normal after sintering. In light of the apparent influence of larger Pt crystallites on the overall sintering rate (see Section 6.2.3 above), such localized effects may be significant in the sintering of a catalyst. In Figure 6.8, the apparent agglomeration of the particles in region "c" to the large particle evident after thermal treatment again suggest a localized effect due to the close proximity of so many Pt particles.

In only one case, grid 6, did the holey carbon film in the areas micrographed survive more than one sintering treatment. Figure 6.9 shows the same specimen area after three thermal treatments (the middle micrograph is the mirror image of the other two because the grid was inverted). The extremely high carbon contamination, evident in all three micrographs, makes the distinction of individual Alon particles impossible, and severely impedes the clarity of the Pt crystallites. Despite this problem, the continued agglomeration of Pt can be noted for increasing thermal treatments: typical particle sizes change from 2.5 to 5 nm. While the poor clarity limits particle detection, we were able to note that some particles did not shift with the thermal treatment. Six particles noted in region "a" after the first sinter were identified in the micrograph taken after the second sinter. Similarly, five particles evident after a thermal treatment correspond to an existing particle in the same location prior to the treatment. The caution must also be re-emphasized that the catalyst on grid 6, contaminated by carbon (presumably from the holey film),

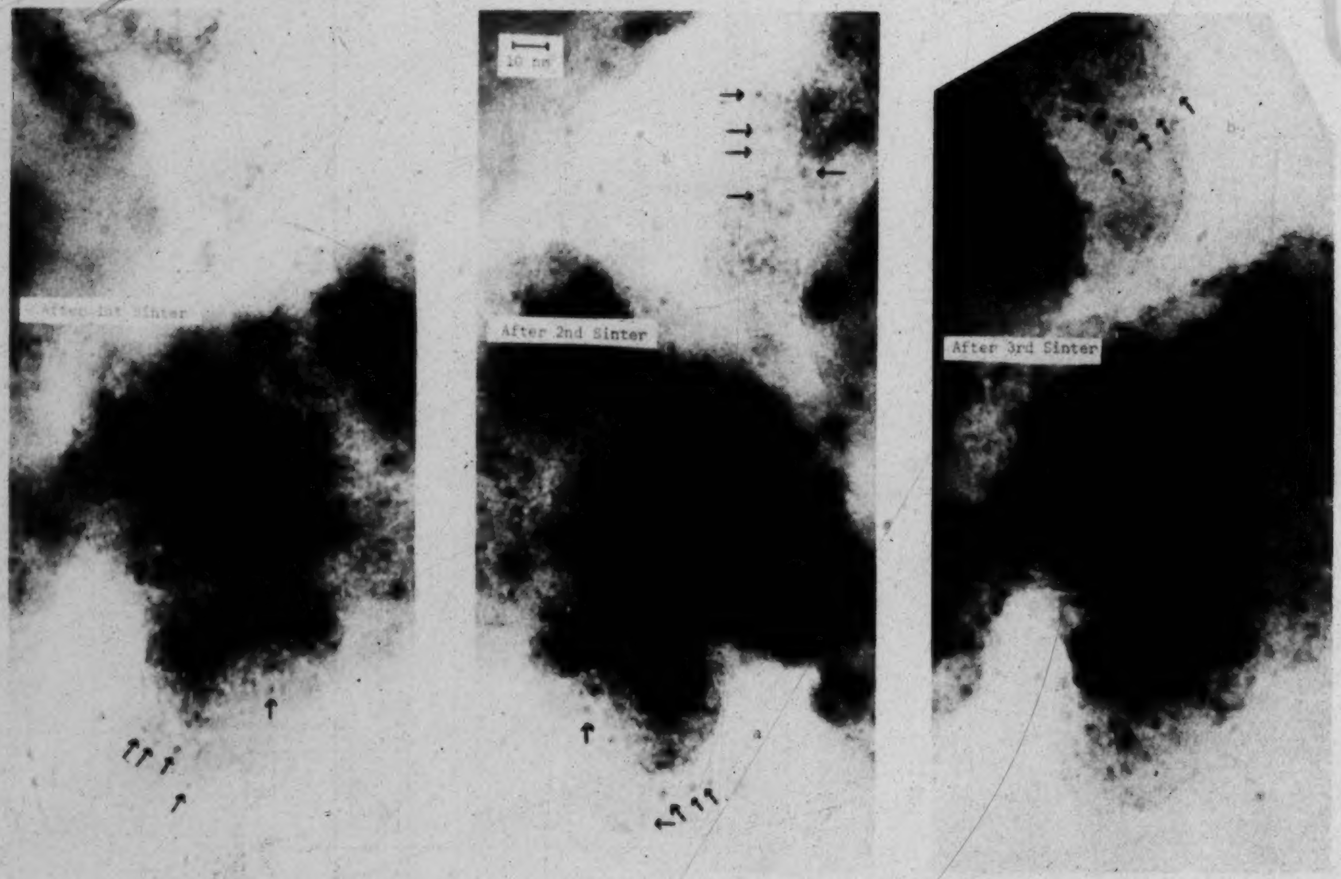
10 nm
After 1st Sinter
After 2nd Sinter
After 3rd Sinter

Figure 6.9 Micrographs from grid 6 showing the same area after thermal treatment at 500°C, a second thermal treatment at 500°C, and a third treatment at 550°C.

and losing metal to the film surface (shown in Figure 6.4), deviates substantially from a typical Pt/Al_2O_3 catalyst system.

6.3 Discussion

The purpose of these experiments was in part to try to establish the mechanism of sintering, specifically to distinguish between crystallite migration[6.12, 6.13] and atomic or molecular interparticle transport[6.14, 6.15] as the sintering process. This pursuit is by no means of academic interest only, since knowledge of the mechanism of Pt agglomeration would suggest appropriate schemes to control or reverse the loss of metal dispersion. Unfortunately, we do not consider the evidence gathered in this work to be sufficiently definitive to allow elimination of one or the other mechanism.

Sintering of the 4.76% Pt on Alon catalyst suggests strongly, however, that crystallite diffusion is not the sole mechanism of catalyst sintering, as previously noted (Chapter 5). The Alon substrate consists of 10 to 30 nm alumina particles; upon drying these appear to form irregular porous stacking arrangements. As Figure 6.1 shows, growth of Pt particles continues even when the metal crystallite size exceeds the size of a typical support particle; it is difficult to conceive of crystallite motion along the support surface continuing to occur in such a case.

Sintering of the commercial 0.5% Pt catalyst confirms the ability of supported metal catalysts to show an increase in dispersion (measured by gas uptake) with certain thermal treatments. The atomic surface diffusion model developed in Chapter 5[6.14, 6.15] accounts for redispersion as a transitory effect arising from the buildup of a high surface concentration of mobile metal species; cooling of a catalyst could "freeze" this metal as small crystallites or atomically dispersed atoms. Emelianova and Hassau[6.20] compared the dispersions of supported Pt catalysts which were rapidly and slowly cooled following otherwise identical thermal treatments. Their finding that the rapidly cooled catalyst always had a higher dispersion than the slowly cooled catalyst does suggest a "freezing" of the agglomeration process. Ruckenstein and Pulvermacher[6.12, 6.13] do not account for redispersion in their model, but propose to do this in a future work, attributing it to particle breakup caused by a spreading surface pressure. Attempts to determine whether redispersion is a transitory phenomenon followed by particle growth were frustrated when the 0.3% Pt commercial catalyst showed an unexpectedly high rate of sintering at 575°C.

The higher rate of sintering observed when presintered catalyst containing large Pt particles is added to a catalyst batch suggests that the large Pt particles speed agglomeration by acting as a "sink" for the transported metal. This in turn strongly suggests a highly mobile rapidly transported Pt species under the sintering conditions employed, since if the process were controlled by slowly diffusing Pt crystallites the effect of large metal particles on sintering rate would be minimal. The atomic diffusion model[6.14, 6.15] assumes a very rapid migration of metal atoms or molecules along the substrate such as is noted in film growth studies[6.21]. Ruckenstein and Pulvermacher [6.12, 6.13] describe a coalescence controlled condition, in which the rate of merger of metal particles is slower than their migration along the surface. However, Wynblatt and Gjostein[6.9] consider a sintering rate being coalescence controlled as impossible. If so, this suggests interparticle transport rather than crystallite migration as a sintering mechanism that can account for the influence of the added large Pt particles on the overall sintering rate.

An ideal way of distinguishing between crystallite migration and atomic diffusion mechanisms would be to sinter a catalyst while observing it in the electron microscope, using a heated grid holder. However, our attempts at this were frustrated because drift of the specimen, presumably due to thermal gradients in the grid, prevented resolution and recording of the metal particles of the order of 10 nm and less. The selection of an area of catalyst, to be examined after various treatments, was intended to approximate as closely as possible the *in situ* experiment. However, two detectability problems affected the electron micrograph studies of catalysts treated on grids. For small particles, the problem of simultaneous detection of all Pt crystallites[6.16] arises. For larger particles, carbon contamination, which we think arises from evaporation from the holey carbon film during thermal treatment, reduces the clarity of the micrographs. We conclude that at least some Pt particles remain in a fixed location during reduction and continued thermal treatments, and that agglomeration of Pt occurs during all of these steps. For a perfectly homogeneous surface, the crystallite migration model of sintering[6.12, 6.13] predicts all Pt particles will move, while the atomic surface diffusion model predicts none will (although some will disappear). On a heterogeneous surface, however, which probably more accurately describes a typical catalyst support, the former model can account for fixed particles and the latter can account for the appearance of particles at new locations. Hence these em studies do not allow either model to be definitively selected.

Contamination of the catalyst by material from the supporting grid would probably be reduced or disappear if a high boiling metal (such as tungsten) holey support film were used; Fukami *et al.*[6.22, 6.23] describe the preparation of these films. However, this would probably not reduce the transport of Pt to the support film, shown in Figure 6.4.

6.4 Conclusions

Sintering of supported metal catalysts was studied in a variety of experiments. For a 4.76% Pt on Alon catalyst, metal particle growth continued to a point where it exceeded the particle size of the support. Sintering of Engelhard 0.5% Pt on alumina catalysts in oxygen gave evidence of redispersion at lower temperatures (450° to 600°C) and loss of metal surface at higher temperatures (>600°C). The rate of sintering was found to be sensitive to the gas atmosphere and to the metal loading.

Including a portion of presintered catalyst in a catalyst batch to be sintered appears to substantially increase the overall rate of sintering. This is attributed to the large Pt particles found in the presintered specimen acting as a "sink" for transported metal.

Electron micrographs were recorded of the same catalyst area before reduction and after reduction and thermal treatments on the grid. Problems were noted with metal transport to the grid carbon support film and carbon transport to the catalyst. Agglomeration of Pt was noted after reduction in hydrogen at 300°C and after thermal treatments in helium at 500° and 550°C. Some metal particles kept a fixed location on the support during reduction and thermal treatments.

The data can be interpreted in terms of an interparticle transport sintering mechanism. While some of the data cast doubt upon crystallite migration as a sintering mechanism, we do not consider the results sufficiently conclusive to rule out this model as a possible mechanism of sintering.

6.5 References

6.1 Chem. Abstr. 76 - 145405q (Patent, Ger. Offen. 2, 137, 554).

6.2 Chem. Abstr. 68 - 31814b (Patent, Neth. Appl. 6, 614, 074).

6.3 Herrmann, R.A., Adler, S.F., Godlstein, M.S. and De Baun, R.M., J. Phys. Chem. 65, 2189 (1961).

6.4 Maat, H.J. and Moscou, L., "Proc. 3rd Int. Congr. Catal." p. 1277, North-Holland, Amsterdam, 1965.

6.5 Somorjai, G.A., in "X-Ray and Electron Methods of Analysis" (H. van Olphen and W. Parrish, eds.) Chap. VI, Plenum, New York, 1968.

6.6 Wynblatt, P. and Gjostein, N.A., Scripta Metal. 7, 969 (1973).

6.7 Gruber, H.L., J. Phys. Chem. 66, 48 (1962).

6.8 Hughes, T.R., Houston, R.J., and Sieg, R.P., Ind. Eng. Chem. Process Des. Develop. 1, 96 (1962).

6.9 Wynblatt, P., and Gjostein, N.A., Prog. Sol. St. Chem. 9 (to be published).

6.10 Huang, F.H., and Li, C.Y., Scrip. Metal. 7, 1239 (1973).

6.11 Gregg, S.J., and Howlett, B.J., in "Surface Phenomena of Metals", Society of Chemical Industry Monograph No. 28, London, 1968.

6.12 Ruckenstein, E., Pulvermacher, B., AIChE Jour. 19, 356 (1973).

6.13 Ruckenstein, E., and Pulvermacher, B., J. Catal. 29, 224 (1973).

6.14 Flynn, P.C., and Wanke, S.E., J. Catal. 34, (to be published).

6.15 Flynn, P.C., and Wanke, S.E., J. Catal. 34, (to be published).

6.16 Flynn, P.C., Wanke, S.E., and Turner, P.S., J. Catal. 33 233 (1974).

6.17 Kikuchi, E., Flynn, P.C., and Wanke, S.E., J. Catal. 34, 132 (1974).

6.18 Wilson, G.R., and Hall, W.K., J. Catal. 17, 190 (1970).

6.19 Dalla Betta, R.A., and Boudart, M., Proc. V. Int. Cong. Catal., 1972, 2, 96 - 1329.

6.20 Emelianova, G.I., and Hassau, S.A., "Proc. 4th Int. Congr. Catal.", p. 1329, Rice University Printing, Houston, 1969.

6.21 Geus, J.W. in "Chemisorption and Reactions on Metallic Films" (J.R. Anderson, ed.) Chap. 3, Academic Press, London, 1971.

6.22 Fukami, A., and Adachi, K., J. Electronmicrosc. 14, 112 (1965).

6.23 Fukami, A., Adachi, K., and Katok, M., J. Electronmicrosc. 21 19, (1972).

APPENDIX A

EXPERIMENTAL CONDITIONS

A-1 Catalysts and Preparations

Both commercial and prepared catalysts were used in this work.

Commercial catalysts were purchased from Engelhard Industries of Canada, Ltd. (512 King Street East, Toronto, Ontario). The catalysts were 1/8" alumina pellets with a surface coating of metal. 0.3% Pt (Lot 12, 514), 0.5% Pt (Lot 18, 381) and 0.5% Rhodium (Lot 17, 941) catalysts were employed. Specific pretreatments are noted with the experimental results.

Catalysts prepared in this laboratory were made with two different supports: Kaiser 201 Alumina spheres (Kaiser Chemicals, Baton Rouge, Louisiana, U.S.A.), and Alon fumed alumina,(Cabot Corporation, Boston, Mass., U.S.A.). The former was screened in this laboratory, and the 8-10 mesh range was used in all preparations. The latter was used as received.

Catalyst K1 (1.62% Pt on Kaiser 201 alumina) was prepared in the following fashion: to 24.8129 grams of Kaiser 201 alumina was added 30 ml of an H_2PtCl_6 solution containing 0.401 grams of Pt metal. This solution was prepared by dissolving Engelhard Platinum Chloride (40%) (Engelhard Industries, Toronto, Ontario) in distilled H_2O. After allowing to stand for 1/2 hour, the mixture was dryed at 110°C overnight, and then reduced in flowing hydrogen at 250°C for 1 hour. During crushing it was noted that the catalyst had a dark exterior ring, presumably Pt, that extended about 1/3 of the radius. The center of each alumina pellet was relatively free of Pt. Catalyst K2 (2.03% Pt on Kaiser 201 alumina) was prepared in a similar fashion except that the alumina was first wetted with pure H_2O, then the Pt solution was added. This mixture was allowed to stand 24 hours before being dried at 110°C. The dark ring of metal penetrated a shorter distance into the pellet for this catalyst, about 0.25 of the radius.

Catalysts A1 (0.10% Pt on Alon), A2 (0.51% Pt on Alon), A3 (1.00% Pt on Alon), A4 (2.03% Pt on Alon), A5 (2.46% Pt on Alon) and A6 (4.76% Pt on Alon) were prepared in a similar fashion. The alumina was wetted for form a thin paste, and then an appropriate amount of the platinum salt solution was added. This paste was dryed at 110°C, then reduced at 250°C in flowing hydrogen.

A-2 Gas Adsorption System

A-2.1 Calibration, Accuracy, and Sample Calculations

During normal operation of the dynamic system adsorbate gases were added to the continuously flowing carrier gas stream. This was achieved through the Carle sample valve described in Chapter 2, which has two loops that alternately hold a continuously flowing stream of sample gas. Switching of the valve passes the carrier gas through the loop and sweeps a pulse of the adsorbate gas past the catalyst.

The contents of the loops were calibrated by comparison to known volumes injected by syringe. Table A-1 shows the results of an O_2 calibration run (Run 4). For various oxygen flow rates through the loop (measured with a calibrated rotameter) the average peak size from a pulse passing through an empty sample tube is shown. The maximum variation observed among peak areas from the same loop and flow rate was

Table A-1: O_2 Calibration of Sample Loop Size

O_2 flow through sample loop (cc (STP)/min)	Average peak size (DISC integrator counts)
102.5	11,832
62.0	11,430
47.2	11,227
35.0	11,062
26.6	10,924
17.1	10,930
9.2	10,746

Injection volume	Number of pulses	Average area (DISC integrator counts)	Maximum deviation in peak area, %	Number of moles[1] injected
0.4 cc	5	8,486	0.58%	1.50×10^{-5}
0.5 cc	7	10,494	1.39%	1.87×10^{-5}
0.6 cc	6	12, 632	1.02%	2.25×10^{-5}
0.7 cc	3	14,708	0.11%	2.62×10^{-5}

[1] calculated from $n = \frac{PV}{RT}$, P = 691.6 mm Hg, T = 291°K

less than 0.75%. The maximum variation observed among peak areas from the two different loops was less than 2.1%; however, this is not necessarily due to differences in the size of the two loops. The carrier gas passes through small ports in the sample valve, and the alignment of the valve (set by hand) was slightly different for the two loops, leading to small variations in the carrier gas flow rate through the two loops. Thus as the valve was operated over a long period of time the relative areas of the peaks from the two loops varied. In the calculations the two loops were assumed to hold the same amount of adsorbate gas.

Table A-1 also shows the area as a function of size of O_2 pulse injected by syringe, with the maximum variation in peak areas indicated. Syringe contents were calculated from the ideal gas laws. From this data and the peak area as a function of flow through the loop, the size of an O_2 pulse was determined to be 20.3 ± 0.5 u moles at a flow rate of 60 cc (STP)/min through the loop. The variation in sample loop contents are from a variation in atmospheric pressure; which was 700 ± 10 mm Hg. In all standard runs O_2 flow through the sample valve was maintained at the rate of 60 cc (STP)/min, and the 20.3 u mole/pulse figure was used in uptake calculations.

Hydrogen, when used as a sample gas, was also flowed through the loop at 60 cc (SPT)/min, but the lower viscosity of hydrogen relative to oxygen lowered the absolute pressure, and hence the contents, in the sample loop. To calibrate the hydrogen contents, the pressure directly above and below one of the sample loops was measured by an H_2O U-tube manometer read by a cathatometer. The upper, lower, and average pressures are shown in Table A-2. Using 13.55 as the specific gravity of Hg, the results were converted to mm Hg. Using 700 mm Hg as the average barometric pressure (variation from 690 mm to 710 mm was actually observed), the hydrogen pulses are found to contain 0.92 as many moles as the O_2 pulses. In all standard runs where H_2 was to be adsorbed flow was maintained at 60 cc (STP)/min, and the 0.92 x 20.3 u moles/pulse figure was used in uptake calculations.

In some runs, the effect of rate of addition of O_2 on total uptake was checked by adding smaller O_2 pulses. This was achieved by mixing the O_2 with helium (the carrier gas) prior to flowing it through the sample loop. Most runs were made using a Type A or Type B dilution, and Table A-3 shows the calibration of the contents of each pulse in these two cases, calculated from the area of the two peaks through an empty sample tube. Two runs (5 and 15) were made at mixing rates for which final areas were not recorded. In these cases the contents of a pulse was estimated from the nominal composition of the sample gas and a total content of 20.3 u moles of gas in the sample pulse. This procedure is less accurate than the calibration by peak area used for the Type A and Type B dilute pulses.

During gas adsorption studies pulses were passed over the catalyst, and the output peak was recorded, taking two to five minutes per pulse. Pulses were continued until a steady output peak for each sample loop was achieved. The areas of these final peaks were assumed to represent 20.3 u moles of O_2 or 18.7 u moles of H_2, and the fractional output peaks were computed by comparison to these output areas, assuming a linear relationship between sample gas amount and peak area. Thus the variation of carrier gas flow rate did not affect the results, since

Table A-2: Hydrogen Calibration

Gas	Flow cc (STP)/min	P_{upper}, cm H_2O[1]	P_{lower}, cm H_2O[2]	P_{avg}, cm H_2O
H_2	60	35.6	34.8	35.2
O_2	60	117.5	114.7	116.1

Based on an average atmospheric pressure of 700 mm Hg and a specific gravity of 13.55 for Hg:

$$P_{H_2} = 700 + \frac{35.2 \times 10}{13.55} = 726 \text{ mm Hg}$$

$$P_{O_2} = 700 + \frac{116.1 \times 10}{13.55} = 786 \text{ mm Hg}$$

$$P_{H_2}/P_{O_2} = 726/786 = 0.92$$

[1] at upstream end of sample loop

[2] at downstream end of sample loop

Table A-3: Contents of Partial O_2 Pulses

	O_2 Flow[1] cc (STP)/min	He Flow[1] cc (STP)/min	Nominal O_2 Conc	Peak Area Disc Integrator Counts (corrected to the same attenuation)	O_2, u Moles in Pulse, by Area
Pure	60	0	100.0%	12,740	20.3[2]
Type A	12	49	19.7%	2,850	4.54
Type B	5	190	2.56%	493	0.79

[1] read from rotameter

[2] from previous correlation (see Table A-1)

an internal area standard was available. Figure A-1 shows a typical chart output for an oxygen run; the data are from Run 112. Table A-4 shows a typical calculation of oxygen uptake in atoms of O per atom Pt for this run.

Helium was always used as a carrier gas for oxygen pulses; both helium and nitrogen were employed for hydrogen pulses. Nitrogen has a much greater difference in thermal conductivity relative to hydrogen than helium. When used as a carrier gas for hydrogen pulses, a higher attenuation is used on the thermal conductivity cell output than when helium was used. This higher attenuation damped out noise and baseline drift due to temperature fluctuations and other uncontrollable factors; hence nitrogen carrier gas gave more accurate and drift free hydrogen uptake results. However, in titration runs, switching from helium to nitrogen as a carrier gas required about a one hour sweep period before a stable baseline was observed. For this reason, later runs employed helium only as a carrier gas. Hydrogen peak areas were checked and found to be linear with pulse size up to a full pulse. An attenuation of unity for H_2 output pulse meant that baseline drift reduced the accuracy of the H_2 peak areas relative to O_2 peak areas.

A second factor increasing the relative error in H_2 results was the presence of substantial tailing of the hydrogen peaks, attributed to reversible adsorption on the Pt catalyst of a portion of the H_2 pulse. Comparison of O_2 and blank tube peak areas showed virtually no retention of O_2 once the surface was saturated with O_2. The reversible hydrogen tail could be readily confused with baseline drift. For this reason O_2 uptakes in pulses are generally reported to two decimals (to one-one hundredth of a pulse) in Section A II 4, while

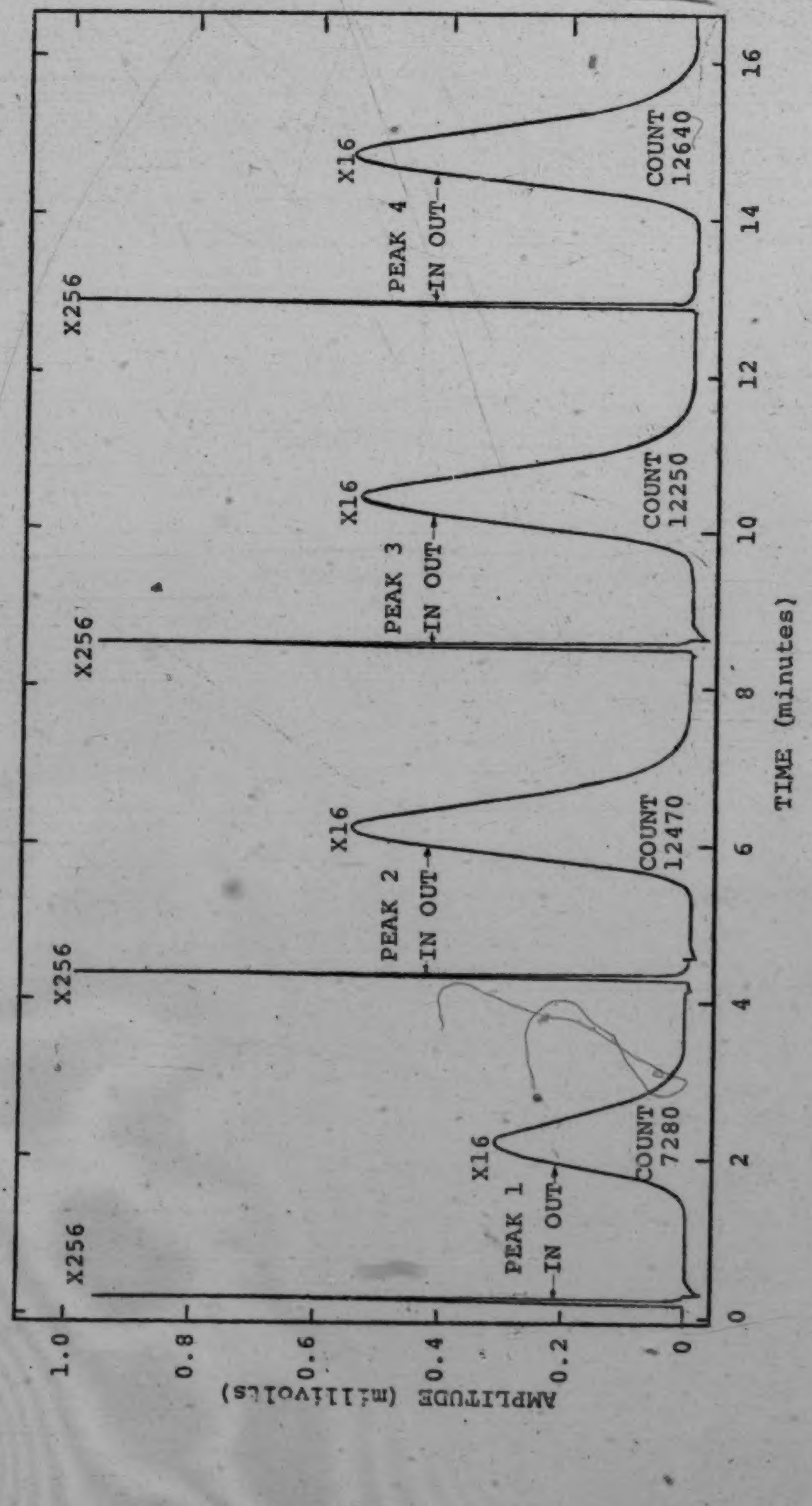

Figure A-1: Output from thermal conductivity cell from run 112.

Table A-4: Sample Calculations, Run 112

a) Catalyst Charge:

1.901 grams of catalyst A4 (2.03% Pt on Alon)

$$1.901 \text{ g} \times \frac{0.0203 \text{ g metal}}{\text{g catalyst}} \times \frac{1 \text{ mole}}{195.1 \text{ g Pt}} \times 10^6 \frac{\text{u moles}}{\text{mole}}$$

= 197 u moles of Pt atoms

b) Oxygen Uptake:

	Area, Disc Integratos Counts	Fraction Out
Peak 1	7,280	7280/12,250 = 0.594
Peak 2	12,470	12,470/12,640 = 0.985
Peak 3	12,250	1.000
Peak 4	12,640	1.000

Gross pulses in	4.000
Total pulses out	3.579
Net pulses in	0.421

$$0.421 \text{ pulses} \times \frac{20.3 \text{ u moles}}{\text{pulse}} \; O_2 \times \frac{2 \text{ atoms}}{\text{molecules}} = 17.1 \text{ u atoms O}$$

c) Uptake:

$$\frac{17.1 \text{ u atoms O}}{197 \text{ u atoms Pt}} = 0.087 \text{ atoms O/atom Pt}$$

H_2 results for an He carrier gas are reported to one decimal (one tenth of a pulse) unless manual integration of peaks was employed. Similar tailing was observed in adsorption of O_2 on supported Rhodium catalysts, indicating some reversible adsorption of O_2 in this case.

Exact repeatability of dynamic gas uptake can not be assessed, for two reasons. First, catalysts show some variation from sample to sample in terms of catalyst loading and dispersion, making exact parallel uptake determinations difficult. Second, each successive reduction and outgassing treatment can alter the surface of the metal catalyst. This latter effect seemed far more significant for the catalyst prepared on Alon than for the commercial catalysts or those prepared on Kaiser 201. For commercial catalysts oxygen uptakes were generally repeatable within 0.02 atoms O/atom Pt if the samples were run at about same time. Shelf ageing does appear to change gas adsorption amounts. Hydrogen uptakes were somewhat less repeatable than oxygen uptakes due to the lower measurement accuracy discussed above.

A-2.2 The Effect of Reduction and Outgassing Times on Gas Uptakes

Whether reduction time affects gas uptake appears to depend in part on the prior history of the catalyst sample. The Englehard 0.3% and 0.5% Pt on alumina catalysts were checked for gas uptake after various reduction treatments. Results of these experiments are shown in Table A-5. None of the 0.3% Pt samples had any prior reduction before the indicated treatment, which the 0.5% sample had been reduced overnight in flowing hydrogen at 500°C before the treatments shown in Table A-5. For the 0.3% catalysts, overnight reduction at 500°C

Table A-5: Effect of Reduction Conditions on Gas Uptake

Run	Catalyst[1]	Reduction Time, hr	Reduction Temperature, °C	O1, atoms/atom	H2, atoms/atom	Comments
97	E2	1	500	0.078	----	fresh catalyst
98	E2	overnight	500	0.352	----	fresh catalyst
95	E2	1	500	0.038	----	catalyst was sintered 3
100	E2	overnight	500	0.043	----	days in air at 575°C
101	E2	overnight	600	0.081	----	
46	E1	1.5	500	0.178	0.591	catalyst had previously
47	E1	4.0	500	0.178	0.581	been reduced overnight at
48	E1	14.5	500	0.180	0.581	500°C
56	E1	2.0	500	0.180	----	

[1] E1 = Englehard 0.5% Pt on alumina

E2 = Englehard 0.3% Pt on alumina

raises the gas uptake. Since the catalyst is treated in air by Englehard (temperature unknown), the long initial reduction may be necessary to convert bulk platinum oxides. The increase in uptake observed in run 101 for reduction at 600°C may be due to redispersion of the catalyst; as noted in Chapter 6, such increases in dispersion have been noted during sintering of catalysts in oxygen.

The results for the 0.5% Pt catalyst indicate that once the initial reduction is achieved, subsequent long term rereduction is not necessary. For the various reduction times, the deviation in initial oxygen uptake corresponds to about 0.01 pulses, the reliability of the peak measurements. Similarly, the titered hydrogen uptakes, measured for three of the runs, show a variance within the precision of the peak area measurements.

Changes in outgassing time cause a more substantial variation in initial oxygen uptake as shown in Table A-6. Again, the Englehard 0.5% Pt on alumina catalyst sample used in the study of reduction times was employed in these runs. Oxygen uptake decreases with increasing outgassing times, probably due to the desorption of surface hydrogen which otherwise consumes oxygen in a reaction to form H_2O. Table A-6 also shows the surface coverage by hydrogen, both in absolute amounts and as a fraction of the oxygen uptake. These were calculated assuming that the surface coverage by hydrogen is zero after 16 hours of outgassing; that the higher oxygen uptakes reacted partially with the hydrogen to form water, leaving the same surface coverage by oxygen, in all cases; and that the carrier gas did not contain any oxygen to build up on the surface. The ability of the catalyst to retain hydrogen even after two hours outgassing is evident from Table A-6.

Table A-6: Effect of Outgassing Time on Gas Uptake[1]

Run	Outgassing Time, hrs	01 atom/atom	Calculated Residual Hydrogen[2] atom/atom	fraction of surface
52	0.25	0.183	0.42	0.26
49	0.5	0.176	0.28	0.17
54	0.5	0.180	0.36	0.22
51	1.0	0.178	0.32	0.20
55	2.0	0.172	0.20	0.12
50	4.0	0.168	0.12	0.07
53	16.0	0.162	0	0

[1] Reduction time two hours in flowing hydrogen at 500°C

[2] Assuming:
a) no O_2 in carrier gas
b) all hydrogen consumed via $2H + \frac{1}{2} O_2 \rightarrow H_2O$
c) 16 hr outgassing gives "clean", *i.e.* hydrogen free, surface

The results from Runs 50 and 53 may also serve, with a different set of assumptions, as a test of the maximum oxygen content of the carrier gas. Thus one may assume that the metal surface is "clean" after four hours and that subsequent decreases in oxygen adsorption are due to the continual adsorption from the carrier gas of traces of oxygen during the degassing period. At the carrier gas flow rate of 53.5 cc (STP)/min, 1.72 moles of helium flowed over the catalyst in the 12 hours difference in outgassing time between the two runs. The decrease in oxygen uptake for Run 53 corresponds to 0.65 micro moles of oxygen, so the maximum oxygen in the carrier gas, assuming that all oxygen present would be adsorbed on the catalyst, would be 0.38 ppm. This value compares favorably to an upper limit of 0.4 ppm found by Meyer and Ronge (Reference 2.4 Chapter 2) in first testing out the Cu/CuO catalyst used in this work. A decrease of oxygen uptake with increasing outgassing time due solely to oxygen in the carrier gas would be linear with time. Since the results shown in Table A-6 do not correspond to a linear decline in oxygen uptake, at least part of the higher uptakes associated with shorter degassing times are attributed to residual surface hydrogen.

A-2.3 Effect of Rate of Addition of Oxygen on Oxygen Uptake

Supported platinum and rhodium catalysts were used to determine the sensitivity of oxygen uptake to the rate of addition of the oxygen to the catalyst. Since the adsorption of oxygen is exothermic and activated, it was anticipated that significant differences in localized heating might arise during the addition of adsorbate gas at different rates, leading to differences in uptake of the adsorbate gas.

In the first set of experiments the oxygen in the sample loop was diluted by mixing with the carrier gas (helium). The range of dilution in the sample loop was from pure O_2 to 4% O_2. The results of uptakes, for various stages of dilution for 0.5% platinum (E1) and rhodium (E3) catalysts are shown in Table A-7.

For the platinum catalyst runs, the uptakes at various dilutions are generally within 10% of each other, and show no consistent trend towards higher or lower uptakes for the diluted cases. For the one series where a rhodium catalyst was employed (Runs 13a to 19) significantly higher uptakes were observed for the very dilute pulses. However, as noted above, oxygen adsorption on supported rhodium catalysts includes a reversible slowly eluted adsorption. The high uptake for Run 13a is attributed to the failure to detect extremely broadened peaks. This run was terminated by adding a pure O_2 pulse after 330 dilute type B pulses were added. Total uptake included the 330 pulses and a small fraction of the final pure O_2 pulse. A portion of the first 330 pulses probably bled off without detection.

From these data it was concluded that dilution of a 0.5 cc oxygen pulse did not significantly affect the uptake of oxygen on the catalyst surface. However, even when a pure oxygen pulse is used, the pulse gets diluted by the carrier gas as it is swept into the specimen tube and over the catalyst. A second experiment was designed to see if uptake of oxygen varied when a pure oxygen stream was passed over the catalyst, as compared to an oxygen pulse.

The data, from Runs 93a, b, c, and d are shown in Table A-8; 2.03% Pt on Kaiser 201 catalyst was used. In Runs a and c, the catalyst was contacted with a stream of pure oxygen at about 1.2 atmospheres, then

Table A-7: Effect of Pulse Dilution on Oxygen Uptake

Run	Catalyst[1]	Temperature, °C	O_2 per Pulse[2], u Moles	Oxygen Uptake, atoms/atom
5	E1[3]	0	9.2	0.350
6			4.54	0.370
7			20.3	0.381
8			0.79	0.350
9	E1[3]	97	0.79	0.365
10			20.3	0.330
11			4.54	0.323
13a	E3	0	0.79	1.000
15			1.85	0.519
16			4.54	0.492
18			20.3	0.539
19			4.54	0.499
21	E1	96	0.79	0.299
22			4.54	0.254
23			20.3	0.256
24	E1	-98	0.79	0.197
25			4.54	0.186
26			20.3	0.198
27	E1	0	0.79	0.214

---

[1] E1 is Englehard 0.5% Pt on alumina
E3 is Englehard 0.5% Rh on alumina

[2] For details on calibration see Section A-2.1

[3] This sample of E1 had a varied thermal history in the early trials of the adsorption system and appears to have a significantly higher uptake than subsequent samples of E1.

Table A-7 (continued)

Run	Catalyst	Temperature, °C	O_2 per Pulse, u moles	Oxygen Uptake, atoms/atom
28			4.54	0.196
29			20.3	0.206
30a	E1	203	0.79	0.339
31			4.54	0.310
32			20.3	0.319
33			20.3	0.301
34	E1	97	0.79	0.270
35			4.54	0.277
36			20.3	0.278
37	E1 sintered at 500°C	0	0.79	0.268
38			20.3	0.254
39	E1 sintered at 600°C	0	20.3	0.197
40			0.79	0.195
41	E1 sintered at 700°C	0	0.79	0.082
42			20.3	0.075

Table A-8: Oxygen and Hydrogen Uptakes for Stream and Pulse Addition of Initial Oxygen

Run	Initial Oxygen Added by	O1, Initial Oxygen Uptake, atoms/atom	H2 Hydrogen Titer Uptake, atoms/atom	O3, Oxygen Titer Uptake, atoms/atom
93a	stream	0.276[1]	0.992	0.438
93b	pulse	0.226	0.891	0.434
93c	stream	0.251[2]	0.926	0.442
93d	pulse	0.225	0.874	0.431

[1] By calculation, assuming H2' (run a) = H2' (run b)

[2] By calculation, assuming H2' (run c) = H2' (run d)

hydrogen and oxygen titer steps were carried out. Runs b and d were identical to Runs a and c except that the initial oxygen was added by pulses for Runs b and d. If one assumes that the hydrogen left on the surface after titration (H2') is the same in Run a as in Run b, and similarly the same in Run c as in Run d, then the initial oxygen uptake (01) for Runs a and c may be calculated. Accounting for the water formed during titration, H2' (Run b) = 0.439 atoms/atom, so that 01 (Run a) = 0.276 atoms/atom. This represents about a 20% increase in initial oxygen uptake in Run a as compared to Run b. Similar calculations for Runs c and d give H2' (Run d) = 0.424 atoms/atom, 01 (Run c) = 0.251 atoms/atom, or about a 10% increase in initial oxygen uptake in Run c as compared to Run d.

Before concluding that oxygen uptake is significantly enhanced, a comment must be made on the assumption that H2 (Run a, c) is equal to H2 (Runs b, d). If the hydrogen uptake following titration is higher for a higher initial oxygen uptake, 01, then the calculated increase in 01 for Runs a and c will be correspondingly lower. One factor raising 01 for cases a and c is the higher partial pressure of oxygen when a pure O_2 stream is used. Whether localized heating effects are also involved cannot be determined from these four runs.

In conclusion, further dilution of the 0.5 cc pulses of oxygen used in this work appear to have no significant or consistent affect on oxygen uptake on support Pt catalysts. Use of a pure oxygen stream appears to increase oxygen uptake slightly as compared to addition of oxygen by pulses.

A-2.4 Experimental Conditions and Results

Table A-9 gives in summary form the experimental conditions and results for the dynamic gas adsorption system. Gas uptake results are in pulses of O_2 or H_2; O1 is an initial oxygen uptake, H_2 is the subsequent uptake of hydrogen uptake, etc. Thus the series O_2-H_2-O_2-H_2 leads to uptakes O1, H2, O3, and H4, while the series H_2-O_2-H_2-O_2 leads to uptakes H1, O2, H3, O4. The pulse contents are 20.3 u moles O_2 and 18.7 u moles H_2, as discussed in Section A-2.1.

Specific comments on each run follow Table A-9. The following codes are employed in the table:

Catalyst Code: (all concentrations are weight %)

E1	Englehard 0.5% Pt on alumina (commercial)
E2	Englehard 0.3% Pt on alumina (commercial)
E3	Englehard 0.5% Rh on alumina (commercial)
K1	1.62% Pt on Kaiser 201 alumina (prepared)
K2	2.03% Pt on Kaiser 201 alumina (prepared)
A1	0.10% Pt on Alon alumina (prepared)
A2	0.51% Pt on Alon alumina (prepared)
A3	1.00% Pt on Alon alumina (prepared)
A4	2.03% Pt on Alon alumina (prepared)
A5	2.46% Pt on Alon alumina (prepared)
A6	4.76% Pt on Alon alumina (prepared)

Reduction Code:

1 - Overnight (14 hr) in flowing H_2 at 500°C.

2 - 1 hour in flowing H_2 at 500°C.

3 - Other, see comments.

A - Reduction started in room temperature furnace, heatup rate was ~500°C per hour.

B - Reduction started at 500°C.

C - Reduction started at some other temperature. Unless otherwise noted, in these cases the temperature controller set point was 500°C, and the furnace was either heating or cooling to that temperature.

Outgassing Code:

1 - Two hours in flowing He at 500°C.

2 - One hour in flowing He at 500°C.

3 - Other, see comments.

Sample Gas Code:

A starred O_2 (O_2*) means that the oxygen pulses were diluted for this run; details of the dilution are in the comments. From Section A-2.1, a Type A dilute pulse contains 4.54 u moles O_2 per pulse, a Type B dilute pulse contains 0.79 u moles O_2 per pulse.

Table A-9: Results from Dynamic Adsorption System

Run	Catalyst	Catalyst Weight, Grams	Reduction	Out Gas	Carrier Gas	Sample Gas	Temperature °C	Uptakes, Pulses
1	----	----	----	----	He	O_2	----	----
2	----	----	----	----	He	O_2	----	----
3	E1	10.277	1C	1	He	O_2	0	----
4	----	----	----	----	He	O_2	----	----
5	E1	10.227	1C	1	He	O_2^*	0	01 = 4.98
6	E1	10.227	1C	1	He	O_2^*	0	01 = 10.7
7	E1	10.227	1C	1	He	O_2	0	01 = 2.46 01' = 0.68 01" = 0.396
8	E1	10.227	1C	1	He	O_2^*	0	01 = 58.0
9	E1	10.227	1C	1	He	O_2^*	97	01 = 60.5
10	E1	10.227	2A	1	He	O_2	97	01 = 2.13
11	E1	10.227	1C	1	He	O_2^*	97	01 = 9.32
12	E1	10.227	3A	1	He	O_2	0	01 = 1.90
13	E3	10.305	1C	1	He	O_2^*	0	----

Run	Catalyst	Catalyst Weight, Grams	Reduction	Out Gas	Carrier Gas	Sample Gas	Temperature °C	Uptakes, Pulses
13a	E3	10.305	2A	1	He	O_2*	0	01 = 319.6
14	----	----	----	----	He	O_2	0	----
15	E3	10.305	2A	1	He	O_2*	0	01 = 70.5
16	E3	10.305	2A	1	He	O_2*	0	01 = 27.6
17	E3	10.305	----	----	He	O_2	0	----
18	E3	10.305	2A	1	He	O_2	0	01 = 6.67
19	E3	10.305	2A	1	He	O_2*	0	01 = 27.2
20	E3	10.305	----	----	He	O_2	0 97 201	----
21	E1	9.836	1C	1	He	O_2*	96	01 = 47.7
22	E1	9.836	2A	1	He	O_2*	96	01 = 7.03
23	E1	9.836	2A	1	He	O_2	96	01 = 1.59
24	E1	10.125	1C	1	He	O_2*	-98	01 = 32.3
25	E1	10.125	2A	1	He	O_2*	-98	01 = 5.28
26	E1	10.125	2A	1	He	O_2	-98	01 = 1.26
27	E1	10.468	1C	1	He	O_2*	0	01 = 36.3
28	E1	10.468	2A	1	He	O_2*	0	01 = 5.77

Run	Catalyst	Catalyst Weight, Grams	Reduction	Out Gas	Carrier Gas	Sample Gas	Temperature °C	Uptakes, Pulses
29	E1	10.468	3B	1	He	O_2	0	01 = 1.36
30	E1	8.85	1C	1	He	O_2	203	----
30a	E1	8.85	2A	1	He	O_2^*	203	01 = 48.7
31	E1	8.85	2A	1	He	O_2^*	203	01 = 7.74
32	E1	8.85	2A	1	He	O_2	203	01 = 1.78
33	E1	8.85	2A	1	He	O_2	203	01 = 1.68
34	E1	8.065	1C	1	He	O_2^*	97	01 = 35.2
35	E1	8.065	3A	1	He	O_2^*	97	01 = 6.29
36	E1	8.065	2A	1	He	O_2	97	01 = 1.41
37	E1	8.065	3B	1	He	O_2^*	0	01 = 34.9
38	E1	8.065	2A	1	He	O_2	0	01 = 1.31
39	E1	10.468	3C	1	He	O_2^*	0	01 = 1.30
40	E1	10.468	2C	1	He	O_2^*	0	01 = 32.5
41	E1	8.85	4C	1	He	O_2^*	0	01 = 11.7
42	E1	8.85	2A	1	He	O_2	0	01 = 0.42
43	----	----	----	----	He	O_2	----	----

Run	Catalyst	Catalyst Weight, Grams	Reduction	Out Gas	Carrier Gas	Sample Gas	Temperature	Uptakes, Pulses
44	E3	----	1C	1	He	O_2	0	----
45	E1	----	1C	1	He	O_2	0	----
			3B	3	He	O_2	0	----
46	E1	8.459	3B	1	He	O_2	0	01 = 0.95 H2 = 3.43
47	E1	8.459	3B	1	He	O_2	0	01 = 0.95 H2 = 3.37
48	E1	8.459	3B	1	He	O_2	0	01 = 0.96 H2 = 3.37
49	E1	8.459	3B	3	He	O_2	0	01 = 0.94
50	E1	8.459	3B	3	He	O_2	0	01 = 0.90
51	E1	8.459	3B	2	He	O_2	0	01 = 0.95
52	E1	8.459	3B	3	He	O_2	0	01 = 0.98
53	E1	8.459	3B	3	He	O_2	0	01 = 0.87
54	E1	8.459	3B	3	He	O_2	0	01 = 0.96
55	E1	8.459	3B	1	He	O_2	0	01 = 0.91

Run	Catalyst	Catalyst Weight, Grams	Reduction	Out Gas	Carrier Gas	Sample Gas	Temperature °C	Uptakes, Pulses
56	E1	8.459	2B	2	N_2, He	H_2, O_2	0	H1 = 1.30 02 = 1.52
57	E1	8.459	2B	2	He, N_2	O_2, H_2	0	01 = 0.95 H2 = 3.34
58	E1	7.305	3C	2	He, N_2	O_2, H_2	0	01 = 0.81 H2 = 3.02
59	E1	7.305	2C	2	N_2, He	H_2, O_2	0	H1 = 1.18 02 = 1.35
60	E1	6.952	2C	2	He, N_2	O_2, N_2	0	01 = 0.88 H2 = 3.35
61	E1	6.952	2A	2	N_2, He	H_2, O_2	0	H1 = 1.52 02 = 1.51
62	E1	6.600	3C	2	N_2, He	H_2, O_2	0	H1 = 1.24 02 = 1.32
63	E1	6.600	2C	2	He, N_2	O_2, H_2	0	01 = 0.83 H2 = 2.59

Run	Catalyst	Catalyst Weight, Grams	Reduction	Out Gas	Carrier Gas	Sample Gas	Temperature °C	Uptakes, Pulses
64	E1	6.265	3C	2	He, N_2	O_2, H_2	0	01 = 0.36 H2 = 1.06
65	E1	6.265	2C	2	N_2, He	H_2, N_2	0	H1 = 0.39 02 = 0.47
66	E1	5.913	3A	2	He, N_2	H_2, O_2	0	01 - 0.24 H2 = 0.96
67	E1	5.913	3C	2	N_2, He	H_2, O_2	0	H1 = 0.032 02 = 0.135
68	E1	5.913	2C	2	He, N_2	O_2, H_2	0	01 = 0.087 H2 = 0.241
69	K1	8.5	2A	2	He, N_2	O_2, H_2	0	01 = 2.94 H2 = 8.5
70	K1	8.5	2A	2	N_2, He	H_2, O_2	0	H1 = 5.2 02 = 4.50
71	K1	8.5	2A	2	He, N_2	O_2, H_2	0	01 = 2.10 H2 = 9.1

Run	Catalyst	Catalyst Weight, Grams	Reduction	Out Gas	Carrier Gas	Sample Gas	Temperature °C	Uptakes, Pulses
72	K1	8.5	2C	2	He, N_2	O_2, H_2	98	O1 = 2.76 H2 = 9.0
73	pure Kaiser 201 alumina	----	3A	1	He, N_2	O_2, H_2	0	no uptake of O_2 or H_2 observed
74	K1	8.32	3A	2	He	O_2, H_2	RT	O1 = 2.02 H2 = 8.6
74a	K1	8.32	3A	2	He	H_2, O_2		H1 = 4.0 O2 = 3.74 H3 = 8.5 O4 = 3.84 H5 = 8.8 O6 = 3.99
75	K1	8.32	3A	2	He	H_2, O_2		H1 = 4.0 O2 = 3.67 H3 = 8.2 O4 = 3.72 H5 = 8.4 O6 = 3.82 H7 = 8.6 O8 = 3.89 H9 = 8.8 O10 = 3.88

Run	Catalyst	Catalyst Weight, Grams	Reduction	Out Gas	Carrier Gas	Sample Gas	Temperature °C	Uptakes, Pulses
75 con.	K1	8.32	3A	2	He	H_2, O_2		H11 = 8.9 012 = 3.98
								H13 = 9.0 014 = 3.96
								H15 = 9.0 016 = 4.05
								H17 = 9.0 018 = 4.07
								H19 = 9.0 020 = 4.07
								H21 = 9.0 022 = 4.09
								H23 = 9.0 024 = 4.08
								H25 = 9.1 026 = 4.08
								H27 = 9.0 028 = 4.11
								H29 = 9.0
76	K1	8.32	3A	2	He	H_2, O_2	0	
77	A3	4.01	2B	2	He	H_2, O_2	RT	H1 = 0.9 02 = 2.31
								H3 = 5.3 04 = 2.52
								H5 = 5.6 06 = 2.53
78	----	----	----	----	He	H_2	RT	----

Run	Catalyst	Catalyst Weight, Grams	Reduction	Out Gas	Carrier Gas	Sample Gas	Temperature °C	Uptakes, Pulses
79	A6	3.377	2B	2	He	H_2, O_2	RT	H1 = 8.0 O2 = 8.72 H3 = 19.5
80	A6	3.377	2B	2	He	O_2, H_2	RT	O1 = 5.24 H2 = 20.0 O3 = 8.70
81	A5	3.061	2B	2	He	O_2, H_2	RT	O1 = 2.40 H2 = 9.9 O2 = 4.56
82	A5	3.061	2B	2	He	H_2, O_2	RT	H1 = 4.0 O2 = 4.42 H3 = 9.95
83	E1	10.117	2B	2	He	H_2, O_2	-98	H1 = 2.64 O2 = 2.25 H3 = 2.50 O4 = 1.21
84	E1	10.117	2B	2	He	H2	0	H1 = 2.37
85	E1	10.117	2B	2	He	H_2, O_2	-196	H1 = ----
86	E1	10.117	2B	3	He	H_2, O_2	97	H1 = 1.56 O2 = 2.38 H3 = 5.38 O4 = 2.44 H5 = 5.46
87	E1	10.117	2B	2	He	H_2, O_2	206	H1 = 1.0 O2 = 2.53 H3 = 5.65

Run	Catalyst	Catalyst Weight, Grams	Reduction	Out Gas	Carrier Gas	Sample Gas	Temperature °C	Uptakes, Pulses
88	A6	1.595	2B	2	He	O_2	RT	01 = 2.15
89	E1	8.889	2B	2	He	H_2, O_2	-196	----
90	A1	2.49	2B	2	He	H_2, O_2	RT	H1 = 0.137 02 = 0.192 H3 = 0.445
90a	A1	2.49	2B	2	He	O_2, H_2	RT	01 = 0.84 H2 = 0.377 03 = 0.200
91	A6	----	----	----	He	H_2	RT	negligible uptake
92	A2	----	2B	2	He	H_2, O_2	RT	----
93a	K2	4.198	2A	2	He	H_2, O_2	RT	H2 = 11.6 03 = 4.72
93b	K2	4.198	2A	2	He	O_2, H_2	RT	01 = 2.43 H2 = 10.4 03 = 4.67
93c	K2	4.198	2A	2	He	H_2, O_2	RT	H2 = 10.8 03 = 4.75
93d	K2	4.198	2A	2	He	H_2, O_2	RT	01 = 2.42 H2 = 10.2 03 = 4.64
94	A4	4.960	2A	2	He	O_2	RT	----
95	E2	4.263	2B	2	He	O_2	RT	01 = 0.061

Run	Catalyst	Catalyst Weight, Grams	Reduction	Out Gas	Carrier Gas	Sample Gas	Temperature °C	Uptakes, Pulses
96	E2	4.791	2B	2	He	O_2	RT	01 = 0.051
97	E2	4.212	2B	2	He	O_2	RT	01 = 0.125
98	E2	4.705	1B	2	He	O_2, H_2	RT	01 = 0.626 H2 = 2.0
99	E2	3.972	1B	2	He	O_2	RT	01 = 0.028
100	E2	4.263	1B	2	He	O_2	RT	01 = 0.069
101	E2	4.263	3A	3	He	O_2	RT	01 = 0.130
102	A4	1.718	3C	3	He	O_2, H_2	RT	01 = 0.138 H2 = 1.05
103	A4	8.473	1A	2	He	O_2	RT	01 = 5.567
104	A5	3.066	2B	2	He	O_2	RT	01 = 1.5
105	A5	3.066	2A	2	He	H_2, O_2	RT	H1 = 3.1 02 = 3.25 H3 = 8.0
106	A5	3.066	2A	2	He	H_2, O_2	RT	H1 = 3.75 02 = 4.09 H3 = 9.4
107	A4	2.189	3C	2	He	O_2	RT	01 = 1.45
108	A4	2.006	3C	2	He	O_2	RT	01 = 1.12
109	A4	2.125	3C	2	He	O_2	RT	01 = 0.402

Run	Catalyst	Catalyst Weight, Grams	Reduction	Out Gas	Carrier Gas	Sample Gas	Temperature °C	Uptakes, Pulses
110	A4	1.948	3C	2	He	O_2	RT	01 = 0.031
111	A4	2.62	3C	2	He	O_2	RT	01 = 1.131
112	A4	1.901	3C	3	He	O_2	RT	01 = 0.421

Comments on Dynamic System Runs

Run

1. Calibration, injected 0.5 cc (STP)/min pulse O_2.
2. Calibration, injected 0.3, 0.5, 0.7 cc (STP)/min pulse O_2.
3. Recorder test, uptake not measured, reduction started at 250°C.
4. Calibration, injected 0.4, 0.5, 0.6, 0.7 cc (STP)/min pulse O_2.
5. Dilute O_2 pulse ($\sim 9.2 \times 10^{-6}$ moles O_2 per pulse), reduction started at 250°C.
6. Type A dilute O_2 pulse, reduction started at 250°C.
7. Pure O_2 pulse, reduction started at 250°C, 01' is after 2 hrs in He at 250°C, 01" is after subsequent overnight purge in He at 250°C, peak areas computed for four different flow rates.
8. Type B dilute O_2 pulse, reduction started at 250°C.
9. Type B dilute O_2 pulse, reduction started at 250°C.
10. Pure O_2 pulse.
11. Type A dilute O_2 pulse, reduction started at 250°C.
12. Reduced 6 hr in flowing H_2 at 500°C.
13. Type B dilute O_2 pulse, run aborted by plugged line, reduction started at 250°C.

13a. Type B dilute O_2 pulses (330); then pure O_2 pulse added.

14. Rhodium catalyst causes tailing in oxygen peak.
15. Dilute O_2 pulse ($\sim 1.85 \times 10^{-6}$ moles O_2 per pulse).
16. Type A dilute O_2 pulse.
17. Some desorption of O_2 observed at 200°C.
18. Pure O_2 pulse.
19. Type A dilute O_2 pulse.
20. Attempt to determine ΔH_a for reversible O_2 on Rh by getting holdup

for various temperatures; excessive mixing prevented accurate assessment of holdup.

21. Type B dilute O_2 pulse, reduction started at 250°C.

22. Type A dilute O_2 pulse.

23. Pure O_2 pulse.

24. Type B dilute O_2 pulse, reduction started at 250°C.

25. Type A dilute O_2 pulse.

26. Pure O_2 pulse.

27. Type B dilute O_2 pulse, reduction started at 250°C.

28. Type A dilute O_2 pulse.

29. Pure O_2 pulse, reduction time 1.75 hr.

30. Run aborted, reduction started at 250°C.

30a. Type B dilute O_2 pulse.

31. Type A dilute O_2 pulse.

32. Pure O_2 pulse.

33. Pure O_2 pulse.

34. Type B dilute O_2 pulse, reduction started at 250°C.

35. Type A dilute O_2 pulse, reduction time 0.6 hr.

36. Pure O_2 pulse.

37. Catalyst from Runs 34-36 was sintered in O_2 at 500°C overnight; Type B dilute O_2 pulse, reduction time 2 hr.

38. Same catalyst as Run 37, pure O_2 pulse.

39. Same catalyst from Runs 27-29 was sintered in O_2 at 600°C overnight; pure O_2 pulse; reduction started at 600°C, lasted 2 hr.

40. Same catalyst as Run 39, Type B dilute O_2 pulse, reduction started 150°C.

41. Same catalyst from Runs 30-33 was sintered in O_2 at 700°C

overnight; Type B dilue O_2 pulse; reduction started at 600°C, lasted 2 hr.

42. Same catalyst as Run 41; pure O_2 pulse.

43. Correlation of dilute peak sizes.

44. Check on tailing, reduction started at 250°C.

45. Reduction started at 250°C; run aborted due to open valve. Reduction time was 0.5 hr., outgassing time was 4 hrs; tube burst after this run, catalyst lost.

46. Reduction time 1.5 hr.

47. Reduction time 4.0 hr.

48. Reduction time 14.5 hr.

49. Outgas time 0.5 hr., reduction time 2 hr.

50. Outgas time 4.0 hr., reduction time 2 hr.

51. Outgas time 1.0 hr., reduction time 2 hr.

52. Outgas time 0.25 hr., reduction time 2 hr.

53. Outgas time 16.0 hr., reduction time 2 hr.

54. Outgas time 0.5 hr., reduction time 2 hr. A recheck of Run 49, no significant change in dispersion.

55. Outgas time 2.0 hr, reduction time 2 hr.

56. Titration, H_2 first.

57. Same catalyst as Run 56, titration, O_2 first.

58. Reduction started at 250°C, lasted 3 hr., titration, O_2 first.

59. Same catalyst Run 58, titration, H_2 first, reduction started at 250°C.

60. A portion of the catalyst used in Runs 58 and 59 is sintered overnight in flowing O_2 at 450°C. Titration, O_2 first. Reduction started at 450°C.

61. Same catalyst as Run 60, titration, H_2 first.

62. A portion of the catalyst used in Runs 60 and 61 is sintered overnight at 600°C. Titration, H_2 first. Reduction started at 600°C, lasted for 1 hr.

63. Same catalyst as Run 62, titration, O_2 first. Reduction started at 310°C.

64. A portion of the catalyst used in Runs 62 and 63 is sintered in O_2 overnight at 700°C. Titration, O_2 first. Reduction started at 700°C, lasted 1.5 hr.

65. Same catalyst as Run 64, titration, H_2 first. Reduction started at 300°C.

66. Same catalyst as Runs 64 and 65. Duplication of Run 64.

67. A portion of the Catalyst used in Runs 64 and 65 is sintered in O_2 overnight at 800°C. Titration, H_2 first. Reduction started at 800°C, lasted 1.4 hr.

68. Same catalyst as Run 67, titration, O_2 first. Reduction started at 200°C.

69. Titration, O_2 first.

70. Catalyst exposed to H_2 at 600°C prior to this run due to furnace malfunction, Same catalyst as Run 69, titration, H_2 first.

71. Same catalyst as Run 69, a repeat of that run.

72. Same sample as Run 69, titration, O_2 first, Reduction started at 100°C.

73. A test of adsorption on an alumina blank. Heated to 500°C in H_2.

74. A portion of the Catalyst used in Runs 69-72 is used in this run and run 75. Reduction 0.5 hr. Long term titration.

75. Carrier gas was passed through liquid nitrogen trap for this

long term titration. Reduction 0.5 hr., same catalyst as Run 74.

76. Same catalyst as Run 75. Reduction 0.15 hr., 0.2 cc of CCl_4 injected in carrier gas line prior to first adsorption, no uptake observed. Overnight degassing at room temperature does not lead to uptake, but reduction in H_2 at 500°C does.

77. Titration, H_2 first.

78. Test of linearity of peak size of H_2 to amount of H_2, using a blank tube and varying H_2 pulse sizes. Response was linear over region observed.

79. Titration, H_2 first.

80. Same sample as Run 79, titration, O_2 first.

81. Titration, O_2 first.

82. Same sample as Run 81, titration, H_2 first.

83. Titration, H_2 first, at -98°C.

84. Same catalyst as Run 83.

85. Same catalyst as Run 83. Peaks were too diffuse to be recorded.

86. Same catalyst as Run 83. Outgassed at 400°C for 1 hr., 500°C for 0.5 hr. Titration at 97°C.

87. Same catalyst as Run 83. Titration at 206°C. Reuptake of H_2 after 1 hr was 0.23 pulses.

88. A portion of the catalyst used in Runs 79 and 80 is finely crushed.

89. A portion of the catalyst used in Runs 83-87 was used in a duplication of Run 85. Again both H_2 and O_2 peaks were too diffuse to be measured.

90. Titration, both ways.

91. A portion of the catalyst from Runs 79 and 80 was sintered in O_2 overnight at 700°C, then cooled to room temperature without

reduction. No further uptake of hydrogen at room temperature was observed, however, the sample was small and extensively sintered (which EM pictures show).

92. Titration--run was aborted by malfunction in alignment of sample valve.

93a. Catalyst exposed to pure oxygen stream after cooling but before first hydrogen adsorption, hence first hydrogen adsorption is H_2.

93b. Same catalyst as 93a.

93c. Same catalyst and treatment as 93a.

93d. Same catalyst as 93a, a repeat of Run 93b.

94. Run aborted due to water in carrier gas line.

95. Catalyst was sintered three days in air at 575°C.

96. Catalyst was sintered 12 hr. in air at 575°C.

97. Unsintered catalyst.

98. Unsintered catalyst.

99. Catalyst was sintered 6 hr. in air at 575°C.

100. Same catalyst as Run 95.

101. Same catalyst as Runs 95 and 100, reduced overnight at 600°C and outgassed at 600°C.

102. Catalyst was sintered overnight at 700°C in O_2; reduction started at 700°C, lasted 1.5 hr., outgassing started at 520°C, lasted 1 hr.

103. Unsintered catalyst.

104. Catalyst wetted with 0.5 cc H_2O prior to adsorption.

105. Same catalyst as Run 104, catalyst wetted with 0.5 cc H_2O prior to adsorption.

106. Same catalyst as Runs 104 and 105.

107. A portion of the catalyst used in Run 103 is sintered at 575°C overnight in O_2. Reduction started at 575°C, lasted 1 hr.

108. A mixture of 23.1% of catalyst from Run 102 and 76.9% of catalyst from Run 103 is prepared and treated identically to the catalyst in Run 107.

109. Catalyst from Run 107 is sintered overnight in O_2 at 630°C. Reduction started at 630°C, lasted 1 hr.

110. Catalyst from Run 108 is treated identically to the catalyst in Run 109.

111. A portion of the catalyst used in Run 103 is sintered at 610°C overnight in O_2. Reduction started at 610°C, lasted 1 hr.

112. A mixture of 23.1% of catalyst from Run 102 and 76.9% of catalyst from Run 103 is sintered overnight in O_2 at 610°C. Reduction carried out at 610°C, lasted 1 hr., outgassing started at 610°C, lasted 1 hr.

APPENDIX B

CALCULATION OF PHASE CONTRAST IMAGES

Chapter 3 described the theory whereby phase contrast profiles in the image plane may be calculated for a variety of assemblies of scattering centers. The EMCON program was developed to perform this calculation.

Table B-1 gives the spatial coordinates of the scattering centers, which are based on a close packed spacing of 0.275 nm. These values were read into EMCON as XN(J) and YN(J), in Angstrom units. Table B-2 lists the parameters used in the EMCON program. The Doyle-Turner scattering equation is detailed in reference 3.17 (Chapter 3); the parameters for gold were used.

The EMCON program is listed. It uses the IMSL DRMBIU integration routine (Library 1, International Mathematical and Statistical Libraries, Inc., Houston, Texas, U.S.A.) and the SSP BESJ program for the zero order Bessel function value (IBM System 360 Scientific Subroutine Package Programmer's Manual (H20-0205), IBM, New York, N.Y., U.S.A.). The program determines the square of the wave function, ψ^2, as a function of the spatial position in the image plane. Thus a contrast profile of the atom or atoms scattering the electrons may be determined. Directly following the program a sample output from EMCON is also shown.

Table B-1: Atom Coordinate Positions Used in EMCON

Case	Atom number	Coordinates of atom, Å
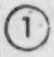	1	(0, 0)
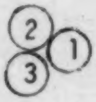	1	(58771, 0)
	2	(-0.79386, 1.375)
	3	(-0.79386, -1.375)
Identical to 3 atom case with 4th atom in center	1	(1,58771, 0)
	2	(-0.79386, 1.375)
	3	(-0.79386, -1.375)
	4	(0, 0)
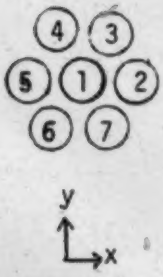	1	(0, 0)
	2	(2.75, 0)
	3	(1.375, 2.38157)
	4	(-1.375, 2.38157)
	5	(-2.75, 0)
	6	(-1.375, -2.38157)
	7	(1.375, -2.38157)

All reported profiles were stepped off in the +x direction.

Table B-2: Parameters Used in EMCON

All four cases were evaluated for the following input data:

WAVEL	(wavelength of incident electron)	0.037 Å
APER	(aperture size)	40 /microns
HMIN	(minimum integral step size)	5 x 10^{-7} radians
FOCLEN	(focal length of objective lens)	1.6 mm
TOL	(tolerance of integral in DRMBIU program)	0.005
DELRAD	(radial spatial increment)	0.5 Å
CSPH	(spherical aberration factor)	1.6 mm
DELFOC	(defocus in Angstroms)	-200. to +400. nm, in 20 nm increments
L1	(number of radial increments)	21

In addition, the single atom case was evaluated over the DELFOC range -20. to +200 nm, in 20 nm increments, for the above conditions with APER values of 32, 16, 8 and 4 microns.

```
C        EMCON DETERMINES THE CONTRAST BY CALCULATING THE WAVE FCT
C
C        DATA ARE
C        WAVEL      WAVELENGTH OF INCIDENT ELECTRON IN ANGSTROMS
C        APER       APERATURE SIZE IN MICRONS
C        HMIN       MINIMUM INTEGRAL STEP SIZE IN RADIANS
C        FOCLEN     FOCAL LENGTH OF OBJECTIVE LENS IN MM
C        TOL        TOLERANCE OF INTEGRAL
C        DELRAD     RADIAL INCREMENT IN ANGSTROMS
C        CSPH       SPHERICAL ABERATION CONSTANT IN MM
C        DELFOC     DEFOCUS IN ANGSTROMS
C        A1 THRU B4 ARE DOYLE/TURNER SCATTER FACTOR CONSTANTS
C        L1         NUMBER OF RADIAL INCREMENTS
C        L2         NUMBER OF ATOMS
C        XN(J) AND YN(J) ARE ATOM COORDINATES IN ANGSTROMS FROM CENTER
C
      EXTERNAL F
      DIMENSION WK(3000 ),XN(50),YN(50)
      COMMON  XN,YN,XI,YI,WAVEL,CSPH,DELFOC,A1,A2,A3,A4,B1,B2,B3,B4,LUNP
     1,L2,PI,C1,C2,C3,B1ADJ,B2ADJ,B3ADJ,B4ADJ,CO
      LUNR = 5
      LUNP = 6
    1 READ (LUNR,10) WAVEL,APER,HMIN,FOCLEN,TOL,DELRAD,CSPH,DELFOC
   10 FORMAT (8F10.0)
      IF (WAVEL) 1000,1000,40
   40 CONTINUE
      READ (LUNR,20) A1,B1,A2,B2,A3,B3,A4,B4
   20 FORMAT (8F10.0)
      READ (LUNR,30) L1,L2
   30 FORMAT ( 2I10)
      READ (LUNR,35) (XN(J),J = 1,L2)
      READ (LUNR,35) (YN(J),J = 1,L2)
   35 FORMAT (8F10.3)
      PI=3.141592
      CO = PI/2.
      C1 = 2.*PI/WAVEL
      C2 = 2.*PI*CSPH*10000000./(4.*WAVEL)
      B1ADJ = B1/(WAVEL**2)
      B2ADJ = B2/(WAVEL**2)
      B3ADJ = B3/(WAVEL**2)
      B4ADJ = B4/(WAVEL**2)
      ANGMAX = .001*APER/(2.*FOCLEN)
      HMAX = .02 * ANGMAX
      DO 999 K = 1,12
      DELFOC = -200.  + 200.*(K-1)
      C3 = 2.*PI*DELFOC/(2.*WAVEL)
      WRITE (LUNP,50) WAVEL,ANGMAX,TOL,CSPH,DELFOC,FOCLEN,APER,L2
   50 FORMAT (/////' BASIC DATA'/' WAVELENGTH OF ELECTRON =',F7.4,5X,' M
     1AXIMUM ANGLE IN RADIANS=',F8.5,5X,' TOLERANCE IN INTEGRAL =',F12.1
     20/' SPHERICAL ABERATION IN MM =',F5.2,5X,' DEFOCUS IN ANGSTROMS ='
     3, F7.1,5X,' OBJECTIVE LENS FOCAL LENGTH =',F6.2/' APERTURE IN MICR
     4ONS =', F5.1,5X,' NUMBER OF ATOMS =',I3///)
      DO 55 I = 1,L1
      XI = 0. + DELRAD*(I-1)
      YI = 0.
      R1 = DRMBIU(F,0.,ANGMAX,HMIN,HMAX,TOL,WK,IER)
      CALL UERTST(IER,'DRMBIU')
      PSISQD =    ( 1. + 4.*PI*1.196*R1/WAVEL)
      ABC = ABS  (PSISQD)
      PSI = SQRT (ABC)
      WRITE (LUNP,100) XI,YI,R1,PSI,PSISQD
      WRITE (7,    101)XI,PSISQD
   55 CONTINUE
  100 FORMAT (' POSITION IN ANGSTROMS, XI =',F6.2,2X,' YI =',F6.2,5X,' R
     1N =',F10.7,5X,' PSI =',F8.5,5X,' PSI SQUARED =',F8.5//)
  101 FORMAT (F10.3,F20.6 )
  999 CONTINUE
      GO TO 1
 1000 STOP
      END
      FUNCTION F(X)
      DIMENSION XN(50),YN(50)
      COMMON  XN,YN,XI,YI,WAVEL,CSPH,DELFOC,A1,A2,A3,A4,B1,B2,B3,B4,LUNP
     1,L2,PI,C1,C2,C3,B1ADJ,B2ADJ,B3ADJ,B4ADJ,CO
      BJSUM = 0.
      DO 250  K = 1,L2
      C = SORT ((XI+XN(K))**2  + (YI +YN(K))**2 )
      ICOUNT = 0
      PRECIS = .001
      IF ( C1*C*X ) 180,180,190
  180 BJ = 1.
      GO TO 200
  190 CALL BESJ ( C1*C*X ,0,BJ,PRECIS,JKL)
      IF (JKL)200,200,900
  900 PRECIS =  5. * PRECIS
      ICOUNT = ICOUNT + 1
      IF (ICOUNT - 4) 910,910,920
  910 WRITE(LUNP,901) JKL,PRECIS
  901 FORMAT (' SSP ERROR MESSAGE FOR BESJ IS',I2,5X,' NEW BESJ PRECISIO
     1N IS',F10.8)
      GO TO 190
  200 CONTINUE
      BJSUM = BJSUM + BJ
  250 CONTINUE
      F = COS (CO -C2*X**4. +C3*X**2) * (A1*EXP(-B1ADJ*(SIN(X/2.)**2)) +
     1A2*EXP(-B2ADJ*(SIN(X/2.)**2)) + A3*EXP(-B3ADJ*(SIN(X/2.)**2)) + A4
     2*EXP(-B4ADJ*(SIN(X/2.)**2))) * BJSUM * X
      RETURN
  920 STOP
      END
```

```
BASIC DATA
WAVELENGTH OF ELECTRON = 0.0370      MAXIMUM ANGLE IN RADIANS= 0.01250      TOLERANCE IN INTEGRAL =0.0049999990
SPHERICAL ABERATION IN MM = 1.60      DEFOCUS IN ANGSTROMS =  200.0      OBJECTIVE LENS FOCAL LENGTH =  1.60
APERTURE IN MICRONS = 40.0      NUMBER OF ATOMS =  7

*** I M S L(UERTST) ***  NON-DEFINED              DRMBIU     0
POSITION IN ANGSTROMS, XI =  0.0     YI =  0.0      RN =-0.0001531      PSI = 0.96841      PSI SQUARED = 0.93781

*** I M S L(UERTST) ***  NON-DEFINED              DRMBIU     0
POSITION IN ANGSTROMS, XI =  0.50    YI =  0.0      RN =-0.0001417      PSI = 0.97089      PSI SQUARED = 0.94265

*** I M S L(UERTST) ***  NON-DEFINED              DRMBIU     0
POSITION IN ANGSTROMS, XI =  1.00    YI =  0.0      RN =-0.0001102      PSI = 0.97736      PSI SQUARED = 0.95524

*** I M S L(UERTST) ***  NON-DEFINED              DRMBIU     0
POSITION IN ANGSTROMS, XI =  1.50    YI =  0.0      RN =-0.0000663      PSI = 0.98644      PSI SQUARED = 0.97307

*** I M S L(UERTST) ***  NON-DEFINED              DRMBIU     0
POSITION IN ANGSTROMS, XI =  2.00    YI =  0.0      RN =-0.0000208      PSI = 0.99577      PSI SQUARED = 0.99155

*** I M S L(UERTST) ***  NON-DEFINED              DRMBIU     0
POSITION IN ANGSTROMS, XI =  2.50    YI =  0.0      RN = 0.0000151      PSI = 1.00307      PSI SQUARED = 1.00615

*** I M S L(UERTST) ***  NON-DEFINED              DRMBIU     0
POSITION IN ANGSTROMS, XI =  3.00    YI =  0.0      RN = 0.0000335      PSI = 1.00678      PSI SQUARED = 1.01360

*** I M S L(UERTST) ***  NON-DEFINED              DRMBIU     0
POSITION IN ANGSTROMS, XI =  3.50    YI =  0.0      RN = 0.0000319      PSI = 1.00647      PSI SQUARED = 1.01297

*** I M S L(UERTST) ***  NON-DEFINED              DRMBIU     0
POSITION IN ANGSTROMS, XI =  4.00    YI =  0.0      RN = 0.0000148      PSI = 1.00300      PSI SQUARED = 1.00602

*** I M S L(UERTST) ***  NON-DEFINED              DRMBIU     0
POSITION IN ANGSTROMS, XI =  4.50    YI =  0.0      RN =-0.0000085      PSI = 0.99826      PSI SQUARED = 0.99653

*** I M S L(UERTST) ***  NON-DEFINED              DRMBIU     0
POSITION IN ANGSTROMS, XI =  5.00    YI =  0.0      RN =-0.0000272      PSI = 0.99447      PSI SQUARED = 0.98897
```

APPENDIX C

CALCULATION OF A SINTERING HISTORY

Chapter 5 outlines the equations which are postulated to describe the change in individual particle sizes during sintering. The SINTR programs were used to solve these equations, for the cases described in Chapter 5.

SINTR 1 was used for α/S_0 values $<10^{12}$ m^{-2}, where a trial and error solution is needed because F_s, the number of free surface atoms, is significant. In the case of $\alpha/S_0 > 10^{12}$ m^{-2}, F_s could be approximated as zero, a trial and error solution was no longer necessary, and SINTR 2 was used.

Both programs are reproduced here, along with a sample output from SINTR 2 which directly follows the listing of SINTR 2. Particle sizes for every tenth time increment were printed. The sample output shows only one of these complete particle size outputs after 1 hr. Computations were continued for 50 hrs (500 time increments) or until only one particle remained.

```
C   SINTR 1 PROGRAM
C
C   ***  DATA INPUT   ***
C
C   CARD 1 - NTIN = TOTAL NUMBER OF TIME INCREMENTS (1I10)
C   CARD 2 - DT = SIZE OF TIME INCREMENT (SEC)
C            SA = SURFACE AREA PER PT ATOM (SQ.A)
C            AC = ACTIVATION ENERGY (CAL/MOLE)
C            T = TEMPERATURE (K)
C            ACC = ACCOMMODATION COEFFICEINT
C            A = PRE-EXPONENTIAL FACTOR (1/SEC)
C        FORMAT FOR CARD 2  (4F10.1,2E10.2)
C   CARD 3 - INFORMATION ON INITIAL PARTICLE SIZE DISTRIBUTION
C            NI = NUMBER OF SIZE INCREMENTS
C            NY(I) = NUMBER OF PARTICLES IN EACH SIZE INCREMENT
C        FORMAT FOR CARD 3 - (27I3)
C   CARD 4 - SMIN = SIZE OF SMALLEST PARTICLE (A)
C                   (THIS IS THE SIZE ALONG THE EDGE OF CUBE)
C            DS = SIZE OF PARTICLE SIZE INCREMENT (A)
C        FORMAT FOR CARD 4 - (2F10.4)
C   CARD 5 - USUALLY THIS CARD IS BLANK UNLES SOME LARGE PARTICLES
C            ARE TO BE ADDED TO THE ORIGINAL DISTRIBUTION OF 121 PARTICLES
             NUMBER GIVES P(122),P(123),ETC.
C   CARD 6 - ANOTHER CARD FORMATED LIKE CARD 3 GIVES ANOTHER RUN WITH
             THE CARD 1 AND 2 CONDITIONS BUT A NEW PSD. OTHERWISE
             INSERT A BLANK CARD.
C          - IF BLANK THEN THE NEXT CARD SOULD BE A REPEAT OF CARD 1
C            OR BE A BLANK
C   CARD 7 - A CARD FORMATED LIKE CARD 1 STARTS A NEW RUN. A BLANK
             CARD CAUSES THE PROGRAM TO EXIT.
C
C   ************************************************
C
      DIMENSION NY(25),P(300),SS(300),DN(300)
       C3=14.32
       C4=7.84
      ULIM=0.1
C
C     ULIM = MAXIMUM CONVERGENCE ERROR IN NUMBER OF ATOMS BEFORE
C            PROGRAM PROCEEDS TO NEXT TIME INCREMENT.
C
  114   CONTINUE
C
C   READ IN DATA  (TO 5680)
C
      READ(5,555) NTIN
  555 FORMAT(1I10)
      READ(5,112) DT,SA,AC,T,ACC,A
      DTC=DT
      XYZ=T
      AC=-AC
  112 FORMAT(4F10.1,2F10.2)
      IF(DT-0.001)999,999,115
  115 CONTINUE
       READ(5,110) NI,(NY(I),I=1,NI)
      IF(NI)114,114,113
  113 CONTINUE
  110 FORMAT(27I3)
      READ(5,111)SMIN,DS ,DISPI,NPSD
  111 FORMAT(3F10.4,1I10)
      READ(5,5680) LP,(P(I) ,I=122,LP    )
 5680 FORMAT(1I10,7F13.0)
      DT=DTC
      T=XYZ
      TOTN=0.
      I=0
C
C   GENERATION OF INITIAL PARTICLE SIZE DISTRIBUTION (TO 2). EACH
C   PARTICLE HAS A DIFFERENT SIZE.
C
      DO 2 KK=1,NI
      NP=NY(KK)
      ZY=NP
      ZZ=KK
      DO 2 KP=1,NP
      I=I+1
      ZX=KP
      SI=SMIN+(ZZ-1.)*DS+(ZX-1.)/ZY*DS
C
C   SS(I) = SIZE OF PARTICLE 2, ANGSTROMS.
C   P(I) = NUMBER OF ATOMS IN PARTICLE 2.
C
      SS(I)=SI
       P(I)=0.5*(1.+(1.+(SI-2.77)/1.96)**3)
      TOTN=TOTN+P(I)
      L=I
  2   CONTINUE
C
C   LOOP ACTIVATED IF LARGE PARTICLES ARE ADDED TO DISTRIBUTION (TO 3681).
C
      IF(LP-10)3681,3681,3682
 3682 L=LP
      DO 3683 I=122,LP
      S=0.5*(1.+((2.*P(I)-1.)**0.3333))
      SS(I)=(S-1.)*3.92+2.77
 3683 TOTN=TOTN+P(I)
 3681 CONTINUE
C
C   SAS = TOTAL SURFACE AREA OF SUPPORT, SQ. CM.
C
      SAS=TOTN*SA*1.0E-16
      YY=(T-300.)/100.
      T1=T
C
C   PRINT OUTPUT HEADINGS (TO 40)
C
      WRITE(6,103)
  103 FORMAT('1',5X,'SINTERING MODEL')
```

```
      FN1=0.
      FN=0.
      JJ=0
      JJ=0
      WRITE(6,109) NPSD,DISPI
109   FORMAT(/,5X,'DISTRIBUTION NUMBER',1I5,10X,'INITIAL DISPERSION',1F
     110.2)
      WRITE(6,104)L,T,DT
104   FORMAT(/,5X,'INITIAL NO. OF PARTICLES -',1I8,/,5X,
     1'TEMPERATURE (KELVIN) -',1F10.1,/,5X,'TIME INCREMENT (SEC) -',
     21F7.0)
      WRITE(6,105) A,AC,SA,ACC
105   FORMAT(5X,'PRE-EXPONENTIAL FACTOR (1/SEC) -',1E9.2,//,5X,'ACTIVAT
     1ION ENERGY (E/R) KELVIN -' 1F15.0,/5X,'SURFACE AREA PER ATOM (SQ A
     2) -',1F9.1,/,5X,'ACCOMMODATION COEFFICIENT -',1E9.2)
      WRITE(6,401) TOTN,SAS
401   FORMAT(/,5X,'TOTAL ATOMS =',1F10.0,5X,'TOTAL AREA (SQ CM) =',
     11E9.3,/)
      WRITE(6,402)
402   FORMAT(5X,'INITIAL PARTICLE SIZES (ANGSTROMS)')
      WRITE(6,403) (SS(I),I=1,L)
403   FORMAT(5X,10F10.2)
      AL=DT*A*EXP(AC/T)
      WRITE(6,40) DT,AL
40    FORMAT(5X,'NUMBER OF ATOMS LEAVING PER PARTICLE IN',1F6.1,' SEC
     1=',1F10.1)
      LL=1
      DFN=0.
      TIME =0.
C
C   START OF THE TIME INCREMENT LOOP (TO 60).
C
      DO 60  J=1,NTIN
      DT=DTC
      DTT=DT
      YA=J
```

```
C
C   PROVISION OF HEATING AND COOLING PERIODS (TO 227).
C
      IF(J-101)225,225,226
  225 CONTINUE
      T=300.+YY*(YA-1.)
      DT=0.1*DTT
      GO TO 227
  226 IF(J+100-NTIN)227,227,228
  228 CONTINUE
      T=T-YY
      DT=0.1*DTT
  227 CONTINUE
      TIM=TIME
      TIME=TIME+DT
C
C   DFN AND DFN1 ARE THE CHANGE IN NUMBER OF FREE SURFACE ATOMS IN TIME
C   INCREMENT IN ITERATION I AND I+1
C
C   FN IS THE NUMBER OF FREE SURFACE ATOMS AT THE START OF TIME INTERVAL
C   FN1 IS THE AVERAGE NUMBER OF FREE SURFACE ATOMS DURING THE TIME INTERVAL
C   FN2 IS THE NUMBER OF FREE SURFACE ATOMS AT END OF TIME INTERVAL
C
      C1=A*EXP(AC/T)
      C2=1./SAS*818.3*SQRT(T)*ACC*1.0E-08
      DT9=DT
      DFN1=DFN
      FN2=FN +DFN
      IF(FN2)330,330,331
  330 FN2=0.
  331 FN1=(FN+FN2)/2.
      NOCO=0
      ICO=0
   22 CONTINUE
      NOCO=NOCO+1
      IF(300-NOCO)479,476,476
  479   WRITE(6,478)
  478   FORMAT(5X,'******* DOES NOT CONVERGE *******')
        GO TO 115
  476   CONTINUE
        SIGD=0.
C
C   CALCULATION OF CHANGE OF NUMBER OF ATOMS FOR EACH PARTICLE,DN(I),
C   (TO 3).
C
C   SIGD = NET CHANGE OF ATOMS IN ALL PARTICLES.
C   LL IS A COUNTER, ALL PARTICLES NUMBERED LESS THAN LL HAVE DISAPPEARED.
C
        DO 3I=LL,L
        DN(I)=  (C2*FN1*(C3+C4*(2.*P(I)-1.)**0.3333)-C1)*DT
        IF(DN(I)+P(I)) 470,470,471
  470   DN(I)=-P(I)
  471   SIGD=SIGD+DN(I)
  3     CONTINUE
        DFN=FN2-FN
        IF(ICO)800,601,602
  601   ERR1=SIGD+DFN
        ICO=1
        GO TO 728
  602   ERR1=ERROR
  728   ERROR=SIGD+DFN
        ABERR=ABS(ERROR)
C
C   CHECK TO SEE IF MATERIAL BALANCE ON TOTAL NUMBER OF ATOMS IS MET.
C
       IF(ABERR-ULIM)301,301,302
C
C   CORRECTION TO FN2 FOR NEXT ITERATION IF ULIM WAS EXCEEDED (TO 605+1)
C   THE METHOD OF OBTAINING THE NEXT GUESS FOR FN2 VARIES DEPENDING ON
C   THE VALUE OF  ERROR .
C
  302   IF(ERROR)411,411,412
  411   FN3=FN2
        FN2=FN2-ERROR
        FN1=(FN+FN2)/2.
        GO TO 22
  412   FN4=FN2
        IF(ERR1)425,425,414
  425   FN2=(FN3*ABS(ERROR)+FN4*ABS(ERR1))/(ABS(ERROR)+ABS(ERR1))
        FN1=(FN+FN2)/2.
        GO TO 22
  414   IF(FN2)603,603,604
C
C   IF FN2 OF LESS THAN ZERO (PHYSICALLY IMPOSSIBLE) WAS REQUIRED, THE
C   SIZE OF THE TIME INCREMENT WAS DECREASED BY A FACTOR OF 10.
C
  603   DT=DT/10.
  604   FN2=0.
        FN1=FN/2.
        GO TO 22
  605   FN1=(FN+FN2)/2.
        GO TO 22
  301   FN=FN+DFN
C
C   THE NUMBER OF ATOMS IN EACH PARTICLE AT THE END OF THE TIME INCREMENT IS
C   CALCULATED IN THIS LOOP.
C
        DO 307 I=LL,L
C
C   EACH PARTICLE CONTAINING LESS THAN 14 ATOMS IS MADE TO DISAPPEAR AND THE
C   ATOMS ARE ADDED TO FN.
C
        IF(P(I)+DN(I)-14.)308,307,310
  308   FN=FN+P(I) +DN(I)
        P(I)=0.
        DN(I)=0.
        GO TO 307
  310   P(I)=P(I)+DN(I)
  307  CONTINUE
C
C   CHECK WHETHER SIZE OF TIME INCREMENT HAD BEEN DECREASED DURING FN2 ITER-
C   ATIONS, (TO 452+2).
C
       TIM=TIM+DT
       DT1=TIME-TIM
       IF(DT1-1.0E-08)311,312,312
  312  DT=DT1
       FN2=FN+DFN1*DT/DT9
       IF(FN2)451,451,452
  451  FN2=0.
  452  FN1=(FN+FN2)/2.
       ICO=0
       GO TO 22
  311  CONTINUE
C
C   THIS LOOP COUNTS ALL PARTICLES THAT HAVE DISAPPEARED , I.E., IT
C   DETERMINES LL.
C
       DO 201 I=LL,L
       IF(P(I))800,201,210
  210  LL=I
       GO TO 15
  201   CONTINUE
  15   CONTINUE
C
C   INSTRUCTIONS TO PRINT IN INCREMENTS OF 10 TIME INTERVALS.
C
       JJ=JJ+1
       IF(JJ-10)78,71,78
  78   IF(P(L-1))800,71,60
  71   CONTINUE
       JJ=0
       TOTN=0.
       SURT=0.
```

```
C
C   CALCULATION OF PARTICLE SIZES AND DISPERSIONS(ONLY DONE FOR THE PRINTING
C   TIME INTERVAL).
C
        DO 70 I=1,L
         IF(P(I))800,79,73
  73    S=0.5*(1.+((2.*P(I)-1.)**0.3333))
        SS(I)=(S-1.)*3.92+2.77
        E=12.*S-24.
        PL=12.*S**2-36.*S+30.
        SURT=SURT+8.+E+PL
        TOTN=TOTN+P(I)
        GO TO 70
  79    SS(I)=0.
  70    CONTINUE
C
C   DIS1 IS THE DISPERSION OF PARTICLES ONLY, NOT TAKING FREE SURFACE ATOMS
C   INTO ACCOUNT
C   DIS IS  ISPERSION TAKING FREE SURFACE ATOMS INTO ACCOUNT
C
        DIS1=SURT/TOTN*100.
        TOTN=TOTN+FN
        DIS=(FN+SURT)/TOTN*100.
        WRITE(6,91)
  91    FORMAT(5X,'**************************')
        WRITE(6,32) TOTN,SURT,FN,DIS,DIS1
  32    FORMAT(//,5X,'TOTAL ATOMS',1F10.0,5X,'SURFACE ATOMS',1F10.0,
       15X,'FREE ATOMS AT END OF TIME INC.',1F10.0,/,5X,'DISPERSIONS',
       2 2F10.3,'  (WITH AND WITHOUT FREE ATOMS)',/)
        ACLO=A*DT*8.*EXP(AC/T)
        COLL=1./SAS*DT*818.3*SQRT(T)*ACC
        AVGG=COLL*80.*1.0E-08*FN2
        WRITE(6,698) T,DT,ACLO,AVGG
 698    FORMAT(5X,'TEMPERATURE =', 1F 8.1,5X,'TIME INC. =', 1F8.1,
       1 5X,   'CORNER LOSS PER PART.',1F 7.0,5X,'GAIN PER 20 A PART.',
       21F7.0,/)
```

```
      TIMES=TIME/3600.
      WRITE(6,33) J ,TIMES
   33 FORMAT(5X,'INC. NUMBER', 1I7,5X,'TOTAL ELAPSED TIME (HRS)',
     11F10.3,/)
      WRITE(6,403) (SS(I),I=1,L)
C
C INSTRUCTIONS TO GO TO NEXT PSD WHEN ONLY ONE PARTICLE REMAINS.
C
      IF(P(L-1))800,115,60
   60 CONTINUE
      GO TO 115
  800 WRITE(6,801)
  801 FORMAT(5X,'*** ERROR IN PROGRAM ***')
  999 CALL EXIT
      END
```

```
C     SINTR 2 PROGRAM
C     THE CONCENTRATION OF FREE SURFACE ATOMS IS ALWAYS SMALL
C     THIS PROGRAM IS FOR THE LIMITING CASE OF LOSS CONTROLLING
C
C     DATA INPUT AND INITIAL PSD GENERATION ARE THE SAME AS IN SINTR 1
C     SINTR 2 HAS NO HEATING OR COOLING PERIOD
C     INPUT AND OUTPUT FORMATS ARE PARALLEL TO SINTR 1.
C
      DIMENSION NY(30),SS(300),P(300)
  114  CONTINUE
      READ(5,555) NTIN
  555 FORMAT(1I10)
      READ(5,112) DT,SA,AC,T,ACC,A
      DTC=DT
      XYZ=T
      AC=-AC
  112 FORMAT(4F10.1,2F10.2)
      IF(DT-0.001)999,999,115
  115 CONTINUE
       READ(5,110) NI,(NY(I),I=1,NI)
      IF(NI)114,114,113
  113 CONTINUE
  110 FORMAT(27I3)
      READ(5,111)SMIN,DS ,DISPI,NPSD
  111 FORMAT(3F10.4,1I10)
      READ(5,5680) LP,( P(I),I=122,LP    )
 5680 FORMAT(1I10,7F13.0)
      T=XYZ
      SIGS=0.
      TOTN=0.
      I=0
      IF(NP)2,2,183
  183 CONTINUE
      DO 2 KK=1,NI
      NP=NY(KK)
      ZY=NP
      ZZ=KK
      DO 2 KP=1,NP
      I=I+1
      ZX=KP
      SI=SMIN+(ZZ-1.)*DS+(ZX-1.)/ZY*DS
      SS(I)=SI
      P(I) =0.5*(1.+(1.+(SI-2.77)/1.96)**3)
      TOTN=TOTN+P(I)
      SIGS=SIGS+SI+2.77
      L=I
 2    CONTINUE
      IF(LP-10)3681,3681,3682
3682  L=LP
      DO 3683 I=122,LP
         S =0.5*(1.+((2.*P(I) -1.)**0.3333))
      SS(I)=(S-1.)*3.92+2.77
      SIGS=SIGS+SS(I)+2.77
3683  TOTN=TOTN+P(I)
3681  CONTINUE
      SAS=TOTN*SA*1.0E-16
      YY=(T-300.)/100.
      T1=T
      WRITE(6,103)
 103  FORMAT('1',5X,'SINTERING MODEL')
      WRITE(6,109) NPSD,DISPI
 109  FORMAT(/,5X,'DISTRIBUTION NUMBER',1I5,10X,'INITIAL DISPERSION',1F
     110.2)
      WRITE(6,104)L,T,DT
 104  FORMAT(/,5X,'INITIAL NO. OF PARTICLES -',1I8,/,5X,
     1'TEMPERATURE (KELVIN) -',1F10.1,/,5X,'TIME INCREMENT (SEC) -',
     21F7.0)
      WRITE(6,105) A,AC,SA
 105  FORMAT(5X,'PRE-EXPONENTIAL FACTOR (1/SEC) -',1E9.2,//,5X,'ACTIVAT
     1ION ENERGY (E/R) KELVIN -' 1F15.0,/5X,'SURFACE AREA PER ATOM (SQ A
     2) -',1F9.1,/,5X,'ACCOMMODATION COEFFICIENT - VERY LARGE')
      WRITE(6,401) TOTN,SAS
```

```
  401 FORMAT(/,5X,'TOTAL ATOMS =',1F10.0,5X,'TOTAL AREA (SQ CM) =',
     11F9.3,/)
      WRITE(6,402)
  402 FORMAT(5X,'INITIAL PARTICLE SIZES (ANGSTROMS)')
      WRITE(6,403) (SS(I),I=1,L)
  403 FORMAT(5X,12F10.2)
      AL=DT*A*EXP(AC/T)
      WRITE(6,40) DT,AL
   40 FORMAT(5X,'NUMBER OF ATOMS LEAVING PER PARTICLE IN',1F6.1,' SEC
     1=',1F10.1)
      LL=L
      TIME=0.
C
C     START OF TIME INCREMENT LOOP (TO 60).
C     NO TRIAL AND ERROR CALCULATION NEEDED FOR THIS LOOP.
C
      DO 60  J=1,NTIN
      TIME=TIME+DT
      TOTN=0.
      SURT=0.
      AL=DT*A*EXP(AC/T)
      TOTP=LL
      SIGL=TOTP*AL
      IC=0
      NTOT=0.
   15 CONTINUE
      SIGS1=0.
      DO 3 I=1,L
      IF(P(I))800,3,4
    4 AG=SIGL*(SS(I)+2.77)/SIGS
      PA=P(I)-AL+AG
      IF(PA-14.)10,11,11
   10 SIGL=SIGL-AL+P(I)
      P(I)=0.
      SIGS=SIGS-SS(I)-2.77
      SS(I)=0.
      GO TO 3
11    CONTINUE
      S=0.5*(1.+((2.*PA  -1.)**0.3333))
      S1=(S-1.)*3.92+2.77
      IF(IC)12,12,13
12    SS(I)=(SS(I)+S1)/2.
      GO TO 14
13    SS(I)=S1
      P(I)=PA
14    SIGS1=SIGS1+SS(I)+2.77
3     CONTINUE
      SIGS=SIGS1
      IF(IC)16,16,17
16    IC=1
      GO TO 15
17    DO 20 I=1,L
      IF(P(I))800,20,21
21    LL=L-I+1
      GO TO 22
20     CONTINUE
22    JJ=JJ+1
      IF(LL-1)800,71,23
23    IF(JJ-10)60,71,60
71    CONTINUE
      JJ=0
      TOTN=0.
      SURT=0.
      DO 70 I=1,L
       IF(P(I))800,79,73
73    S=0.5*(1.+((2.*P(I)-1.)**0.3333))
      SS(I)=(S-1.)*3.92+2.77
      E=12.*S-24.
      PL=12.*S**2-36.*S+30.
      SURT=SURT+8.+E+PL
      TOTN=TOTN+P(I)
      GO TO 70
```

```
 79   SS(I)=0.
 70   CONTINUE
      DIS1=SURT/TOTN*100.
      WRITE(6,91)
 91   FORMAT(5X,'****************************')
      WRITE(6,32)TOTN,SURT,LL,DIS1
 32   FORMAT(//,5X,'TOTAL ATOMS',1F10.0,5X,'SURFACE ATOMS',1F10.0,
    15X,'REMAINING PARTICLES',1I5,/,85X,'DISPERSION',1F10.3)
      WRITE(6,698) T,DT
698   FORMAT(5X,'TEMPERATURE =', 1F 8.1,5X,'TIME INC. =', 1F8.1)
      TIMES=TIME/3600.
      WRITE(6,33) J ,TIMES
 33   FORMAT(5X,'INC. NUMBER', 1I7,5X,'TOTAL ELAPSED TIME (HRS)',
    11F10.3,/)
      WRITE(6,403) (SS(I),I=1,L)
      IF(P(L-1))800,115,60
 60   CONTINUE
      GO TO 115
800   WRITE(6,801)
801   FORMAT(5X,'*** ERROR IN PROGRAM ***')
999   CALL EXIT
      END
```

```
SINTERING MODEL

DISTRIBUTION NUMBER 1            INITIAL DISPERSION     35.00

INITIAL NO. OF PARTICLES -      121
TEMPERATURE (KELVIN) -     1000.0
TIME INCREMENT (SEC) -   360.
PRE-EXPONENTIAL FACTOR (1/SEC) - 0.80E 07

ACTIVATION ENERGY (E/R) KELVIN -          -15000.
SURFACE AREA PER ATOM (SQ A) -     100.0
ACCOMMODATION COEFFICIENT - VERY LARGE

TOTAL ATOMS =    201105.     TOTAL AREA (SQ CM) =0.201E-08

INITIAL PARTICLE SIZES (ANGSTROMS)
     27.00     27.28     27.42     27.57     27.66     27.76     27.85     27.92     27.99     28.07     28.14     28.19
     28.25     28.31     28.37     28.42     28.47     28.52     28.57     28.61     28.66     28.71     28.75     28.79
     28.83     28.87     28.91     28.95     28.99     29.03     29.07     29.10     29.14     29.17     29.21     29.24
     29.28     29.31     29.34     29.38     29.41     29.44     29.47     29.50     29.53     29.57     29.59     29.62
     29.65     29.68     29.71     29.74     29.77     29.79     29.82     29.85     29.88     29.91     29.94     29.97
     29.99     30.02     30.05     30.08     30.11     30.14     30.17     30.19     30.22     30.25     30.28     30.31
     30.34     30.37     30.39     30.42     30.46     30.49     30.52     30.55     30.58     30.61     30.65     30.68
     30.71     30.74     30.78     30.82     30.85     30.89     30.92     30.96     30.99     31.04     31.08     31.12
     31.16     31.20     31.24     31.28     31.33     31.38     31.42     31.47     31.52     31.57     31.62     31.68
     31.74     31.79     31.85     31.92     31.99     32.07     32.14     32.23     32.33     32.42     32.57     32.71
     32.99
NUMBER OF ATOMS LEAVING PER PARTICLE IN 360.0 SEC  =     880.9
****************************


TOTAL ATOMS   201110.     SURFACE ATOMS    65954.     REMAINING PARTICLES  106
                                                                             DISPERSION    32.795

TEMPERATURE =  1000.0     TIME INC. =   360.0
INC. NUMBER      10    TOTAL ELAPSED TIME (HRS)      1.000

      0.00      0.00      0.00      0.00      0.00      0.00      0.00      0.00      0.00      0.00      0.00      0.00
      0.00      0.00      0.00      7.90     12.87     15.21     16.84     18.11     19.16     20.06     20.74     21.36
     21.93     22.46     22.95     23.41     23.85     24.21     24.55     24.88     25.19     25.49     25.78     26.07
     26.34     26.57     26.80     27.02     27.23     27.44     27.65     27.85     28.05     28.24     28.40     28.57
     28.73     28.89     29.05     29.20     29.35     29.50     29.65     29.79     29.93     30.07     30.21     30.34
     30.48     30.61     30.74     30.87     30.99     31.12     31.24     31.36     31.48     31.60     31.72     31.83
     31.95     32.06     32.17     32.28     32.41     32.53     32.64     32.76     32.88     32.99     33.11     33.22
     33.33     33.45     33.57     33.69     33.81     33.93     34.05     34.16     34.28     34.41     34.54     34.66
     34.79     34.91     35.03     35.15     35.29     35.43     35.57     35.70     35.83     35.97     36.12     36.28
     36.43     36.58     36.73     36.91     37.09     37.27     37.45     37.68     37.90     38.13     38.45     38.77
     39.39
******************************
```